

CONVERSION ELECTRONS IN $^{154,156}\text{GD}$

A Dissertation

Submitted to the Graduate School
of the University of Notre Dame
in Partial Fulfillment of the Requirements
for the Degree of

Doctor of Philosophy

by
Sabrina Yve Strauss

Ani Aprahamian, Director

Graduate Program in Physics

Notre Dame, Indiana

March 2020

© Copyright by

Sabrina Strauss

2020

CC-BY-4.0

CONVERSION ELECTRONS IN $^{154,156}\text{GD}$

Abstract

by

Sabrina Yve Strauss

One of the open questions of nuclear structure is the nature of excited 0^+ states. Probing the 0^+ states in nuclei requires spectroscopy of the 0^+ states with respect to other states. One such probe is conversion electrons. The transitions between two 0^+ states can only be seen via E0 transitions, which are forbidden via γ -rays. Further, E0 components of $J^\pi \rightarrow J^\pi$ transitions can give similar probes of relationships between bands. Information on E0 components are challenging to measure and sparse in nuclear databases.

The rare-earth region provides a rich landscape to probe pure and mixed E0 transitions. The deformed nature of nuclei in the area leads to a large number of nuclear structure phenomena. In ^{154}Gd , 16 0^+ states have been seen in previous studies, the nature of many are unknown. The first excited 0^+ state is of great interest, due to its large E0 strength to the ground state. There is a question of the nature of this state and its potential role as an example of β -vibration, or an indication of shape coexistence. ^{156}Gd is one of the most well-studied nuclei in the rare-earth region. It has a large number of known levels, lifetimes and mixing ratios, allowing for the study of mixed E0 transitions.

This work reports on results for transitions in $^{154,156}\text{Gd}$ following the $^{152,154}\text{Sm}(\alpha,2n)$ reaction using the Internal Conversion Electron Ball (ICEBall) array in coincidence with γ -rays at the University of Notre Dame Nuclear Science Laboratory (NSL).

ICEBall was re-implemented at the NSL 8 years ago and the γ -rays were detected by GEORGINA, a HPGe array at the NSL, and Clovershare, segmented HPGe detectors purchased by the Yale Nuclear Structure Laboratory that are shared by a consortium of universities and laboratories for experimental campaigns.

To my parents, who always encouraged my love of science.

To Jolie, who introduced me to nuclear physics research.

To Ani, who helped keep me from going too far down side paths.

To all the people who put up with my mood swings.

CONTENTS

Figures	vi
Tables	xvi
Chapter 1: Introduction	1
1.1 Nuclear Excitations	11
1.1.1 Collective Excitations	11
1.1.2 Shape Coexistence	14
1.2 Multipole Radiation	16
1.3 Internal Conversion	20
1.3.1 E0 Transitions	25
1.4 The Rare Earth Region: $N = 90, Z = 60$	28
Chapter 2: Experimental Setup	30
2.1 Overview	30
2.2 Nuclear Science Laboratory at Notre Dame	33
2.3 Beam Production	35
2.3.1 Talys Calculations	36
2.3.2 Test Analysis and Results	37
2.4 Electron Detection	41
2.4.1 Internal Conversion Electron Ball Spectrometer	43
2.4.1.1 Mini-Orange Spectrometer	45
2.4.2 Calibration	48
2.5 Gamma Detection	49
2.5.1 GEORGINA	51
2.5.2 CloverShare	52
2.5.3 Calibration	53
2.6 Target Fabrication	56
2.7 Experimental Configuration and Operation	59
2.7.1 Experimental Beam Operation	59
2.7.2 GEORGINA Configuration and Electronics	59
2.7.3 Clovershare Configuration and Electronics	63

Chapter 3: Analysis	71
3.1 Fitting Spectra	71
3.2 Gating	73
3.3 Systematic Effects	81
3.3.1 Electronics-based Integral Non-Linearities	81
3.3.2 Run-based Calibration Corrections	82
3.3.3 Angular Distributions and Angular Correlations	84
3.4 Upper Limits	87
3.5 Error Analysis	89
 Chapter 4: ^{154}Gd Results	91
4.1 Ground State Band Confirmation	94
4.2 Gates on the Ground State Band	98
4.3 Conversion Coefficients from Singles	102
4.4 $J^\pi \rightarrow J^\pi$ Transitions	125
4.4.1 $0^+ \rightarrow 0^+$ Identification and Population	125
4.4.2 $J^\pi \rightarrow J^\pi$ Transitions	127
4.4.2.1 $K^\pi = 0_2^+$, First Excited 0^+ Band, 680.6673 keV	135
4.4.2.2 $K^\pi = 0_3^+$, Second Excited 0^+ Band, 1182.091 keV	142
4.4.2.3 $K^\pi = 0_6^+$, Fifth Excited 0^+ Band, 1573.9 keV	143
4.4.2.4 $K^\pi = 0_7^+$, Sixth Excited 0^+ Band, 1650.3 keV	143
4.4.2.5 $K^\pi = 2^+$, γ Band, 996.264 keV	144
4.4.2.6 $K^\pi = 2_2^+$, Second Excited 2^+ Band, 1531.305 keV	145
4.4.2.7 $K^\pi = 4_1^+$, First Excited 4^+ Band, 1645.814 keV	145
 Chapter 5: ^{156}Gd Results	147
5.1 Ground State Band Confirmation	147
5.2 Gates on the Ground State Band	150
5.3 Conversion Coefficients from Singles	166
5.4 $J^\pi \rightarrow J^\pi$ Transitions	167
5.4.1 $0^+ \rightarrow 0^+$ Identification and Population	167
5.4.2 $J^\pi \rightarrow J^\pi$ Transitions	175
5.4.2.1 $K^\pi = 0_3^+$, Second Excited 0^+ Band, 1168.186 keV	180
5.4.2.2 $K^\pi = 2_2^+$, Second Excited 2^+ Band, 1827.841 keV	183
5.4.2.3 $K^\pi = 4_1^+$, First Excited 4^+ Band, 1510.594 keV	183
 Chapter 6: Discussion	184
6.1 Dynamic Symmetries in Nuclei	184
6.2 Dynamic Moments of Inertia	185
6.3 ^{154}Gd Results	187
6.3.1 $K^\pi = 0_2^+$, First Excited 0^+ Band, 680.6673 keV	191
6.3.2 $K^\pi = 0_3^+$, Second Excited 0^+ Band, 1182.091 keV	195
6.3.3 $K^\pi = 0_6^+$, Fifth Excited 0^+ Band, 1573.9 keV	197

6.3.4	$K^\pi = 0_7^+$, Sixth Excited 0^+ Band, 1650.3 keV	200
6.3.5	$K^\pi = 2^+$, γ Band, 996.264 keV	202
6.3.6	$K^\pi = 2_2^+$, Second Excited 2^+ Band, 1531.305 keV	206
6.3.7	$K^\pi = 4^+$, First Excited 4^+ Band, 1645.814 keV	209
6.3.8	Summary and Conclusions	212
6.4	^{156}Gd Results	212
6.4.1	$K^\pi = 0_2^+$, First Excited 0^+ Band, 1049.487 keV	217
6.4.2	$K^\pi = 0_3^+$, Second Excited 0^+ Band, 1168.186 keV	219
6.4.3	$K^\pi = 2^+$, γ Band, 1065.1781 keV	221
6.4.4	$K^\pi = 2^+$, Second Excited 2^+ Band, 1827.841 keV	223
6.4.5	$K^\pi = 4^+$, First Excited 4^+ Band, 1510.594 keV	225
6.4.6	Summary and Conclusions	228
Chapter 7: Future Work		230
7.1	Detector Upgrades	230
7.1.1	fIREBAll	230
7.1.2	Magnet Designs	232
7.2	Target Upgrades	233
7.3	Electronics	240
7.4	Additional Experiments	241
7.5	Outlook	241
Bibliography		244

FIGURES

- 1.1 The chart of nuclides. The x -axis is increasing in neutron number from left to right, and the y -axis is increasing in proton number from bottom to top. The lower leftmost corner is the lightest elements, while the upper right are the heaviest, including superheavy elements. Black boxes indicate stable or extremely long lived nuclei. These nuclei are in the "center" of the chart, and known colloquially as the valley of stability. To either side of these stable nuclei are radioactive nuclei, which become shorter lived the farther they are from the valley, indicated by the lightening color. The black boxes are at neutron and proton numbers 8, 20, 28, 50, 82 and 126, marking closed shells for spherical nuclei, and are discussed in further depth within the text.

1.2 The evolution of the shell model and the creation of the closed shells of a spherical nucleus. On the left is the spherical harmonic oscillator. By changing the potential to the Woods-Saxon potential, creating a flat centered potential well, the degenerate states of the harmonic oscillator separate in energy. By further adding a spin-coupling term, the levels separate with energy spacings that create the closed shells and the magic numbers.

1.3 The energy of the first excited 2^+ state, plotted in isotopic chains by mass, distinguished by color. Areas of high excitation energy, around $A \sim 90, 140, 210$ all correspond to doubly magic areas. The areas around $A \sim 110, 170$ have much lower excitation energies and correspond to areas of deformation.

1.4 The Nilsson diagram, showing the evolution of the shell levels of the nucleus with respect to the deformation parameter β . As the nucleus gets more deformed, the closed shells break down. Taken from [22]. .

1.5 Illustration of different kinds of deformation, where spherical symmetry is lost. Treating the vertical as the axis of symmetry, the prolate nucleus is contracted along this axis, but is still axially symmetric. The oblate nucleus is elongated along this axis, but otherwise axially symmetric. It is also possible for the nucleus to lose axial symmetry. .

1.6	Plot of the norm of the quadrupole deformation parameter β_2 along isotopic chains. Deformation can be seen setting in, as isotopic chains transition from spherical to deformed. β_2 is the quadrupole deformation parameter. The norm of β_2 is used, as the method used to calculate β_2 only gives a magnitude, not a sign. A secondary method is needed to distinguish between prolate and oblate.	9
1.7	Plot of the ratio of the first 4^+ excited state energy to the first 2^+ excited state energy in even-even nuclei. On the right, the ratio is broken down into sections, based on structure. This ratio is an excellent diagnostic of the general nuclear structure.	10
1.8	Cartoon of what excited states built upon different types of nuclei looks like. The closed shell has a large gap between the ground state and first excited state. In the vibrator model, this gap is lower, and a gap of comparable size exists before a cluster of states occurs. In the rotor model, the spacing follows a spacing pattern of $J_f(J_f + 1) - J_i(J_i + 1)$, with γ and β vibrations also coming into play. The transitional area between vibrator and rotor shows a shift between the two, with the clustered states of the vibrator model beginning to space out. . . .	13
1.9	Cartoon of the potential well of a nucleus with shape coexistence. A second minima appears at a different β , the deformation parameter. Both of these minima can have excitations built on top of them, leading to shape coexistence. A representation of the shape at β is shown in each minima.	14
1.10	The theoretical K-shell conversion coefficients for the magnetic and electric multipoles for $l = 1, 2, 3$, calculated using BrICC [40]. Each of the multipoles is distinct. Further distinction between multipoles can be seen by plotting the intensity ratios between different electronic shells.	21
2.1	Image of the assembled experimental configuration with Clovershare. One HPGe detector is not visible from this angle. The red line indicates the beam direction.	31
2.2	Comparison between the cross sections of the (α, xn) reactions on ^{154}Sm , calculated using Talys[44]. The less neutrons being lost, the lower the energy before the reaction occurs. Maximizing the cross section with respect to the neutron flux can be done by finding an energy where the desired reaction, $(\alpha, 2n)$ can be maximized, while minimizing the (α, n) and $(\alpha, 3n)$ reactions. Specifically, this means finding an energy before the $3n$ reaction has significant strength, while maximizing the $2n$ reaction, as the n reaction is nearly the same across the energy regime of interest.	32

2.3	Current layout of the Nuclear Science Laboratory at Notre Dame. The red line indicates the path taken by the beam, from ion source, through the accelerator and analyzing magnet, before being sent to ICEBall.	34
2.4	A schematic of how the Helium Ion Source works.	35
2.5	Talys calculation of the highest cross sections divided by the total neutron yield in the natural Samarium target. Only the largest contributors are included, as there are a large number of products possible between the isotopes of Samarium in the target and the reactions channels open for each. All of the largest contributors are Gadolinium isotopes. The ratios for the isotopes of interest appear to plateau around 20-22 MeV.	37
2.6	A cartoon illustration of pulse shape based on radiation type, in the same detecting material. The different types of radiation interact with the detecting material creating a fast and slow excitation. The ratio of these fast and slow excitations is based on the radiation, and expressed in the length of the decay tail. Picture taken from [42].	38
2.7	Plot of the pulse height vs the decay time in the NE212 detectors. Two clear areas are seen. The leftmost, with the shorter decay time, is the gammas, while the more spread out peak on the right is neutrons.	39
2.8	Cartoon of how the bandgap works for insulators, conductors, and semiconductors. Insulators have a large band gap, conductors overlap, and semiconductors have a small bandgap.	42
2.9	Image of ICEBall, open for servicing. The beam would go from left to right in the picture. The target ladder is blank, in the center of ICEBall.	44
2.10	Graphic of the mini-orange filter. The central blocker keeps γ -rays from hitting the detector. The magnets bend electrons toward the detectors, and positrons away from the detectors. Being permanent magnets, they are optimized for a range of electron energies, and can cause overbending or underbending of electrons outside of that energy range, making the magnetic filter a factor in the efficiency. Taken from [53].	45
2.11	An efficiency comparison of magnetic filters of two different strengths. The weak filter has been weakened by 70% compared to the strong filter, using the Pitt split-pole spectrograph. Data from [52].	47
2.12	Linear and quadratic energy calibrations of one Si(Li) detector, using the electron energies listed in Table 2.7. The top graphs show the calibrations, while the graphs beneath show the respective residuals. The calibration is in much better agreement in the quadratic fit, as seen in the residuals.	50

2.13 An example of one of the GEORGINA detectors. The crystal is at a 90° from the cold finger, allowing the long side of the crystal to be placed next to the target, to optimize solid angle coverage. In the experiment, the circular face of the crystal was placed toward the target.	51
2.14 Example of one of the CloverShare detectors.	52
2.15 A characteristic fit of the Clovershare detector efficiencies. The points with large error bars are the ^{152}Eu points, as the scaling of the points caused a large uncertainty, compared to the ^{207}Bi and ^{133}Ba	56
2.16 Efficiency of a CloverShare detector, with the individual leaves' efficiency summed together, compared to the efficiency of the leaves calibrated and summed together. The different colors/shapes indicate the different sources, as labeled.	57
2.17 A look at the energy calibration of an individual leaf in an HPGe Clover detector. The upper graph is a linear calibration. The lower graph is a look at the residuals. For HPGe detectors, ± 0.4 keV is not a good energy calibration. Here, the sawtooth fit that was derived from the differential non-linearity in the electronics is seen fitted to the data.	58
2.18 Plot of the HPGe 1 detector time minus the buncher time. Two distinct peaks can be seen in the spectrum, the main timing peak close to channel 800, and the much smaller secondary peak, coming from a second, later bunching signal. The bunching signal only acts as a stop signal for the timing. It can also be used as a veto, as events without a valid buncher time are not real, or are background.	60
2.19 A schematic of the electronics for the ICEBall-GEORGINA set up. See section 2.7.2 for a detailed explanation. Taken from [8].	62
2.20 ICEBall modeled in Autodesk Inventor [5] with the Clovershare detectors placed around it in locations to optimize efficiency. Once ICEBall had been modeled, the detectors were moved around to make sure they were not behind the tungsten blockers. The beamline was also modeled to know where obstructions existed that prevent the Clovershare detectors from being place there.	63
2.21 The signal processing done by the XIA Pixie-16 electronics. All the processing is done within the module. Taken from [82].	65

3.1	A plot of the energy-gated timing for a HPGe-Si(Li) detector pairing. The HPGe detector was gated at 247.9 keV, one of the ground state band transitions in the ^{145}Gd nucleus. The conversion electrons for other transitions in the ground state band were gated on in the Si(Li) detector. Plotted here are the time differences between the two detectors when both peaks were seen in the respective detectors. The 123LM peak was used instead of the K peak due to the high threshold of this detector. As can be seen, the timing has an energy dependence. This dependence is most prominent at lower energies.	79
3.2	Timing between two of the Clovershare detectors, with one detector gated on 123 keV, the lowest transition in the ground state band of ^{154}Gd . In this data, the gates all looked similarly symmetric, and the timing gates did not need to be varied as they had for the GEORGINA set up.	80
3.3	The difference between the literature value and the calibrated value (before run-by-run correction) of the naturally occurring ^{40}K background peak at 1460 keV, plotted by run for one leaf of one HPGe detector. The red line shows $\Delta E = 0$	83
3.4	An example of the subtraction used to removed the ground state band peaks from spectra. To subtract the conversion electron peak off, the area of the corresponding gamma peak was taken from the same gate. Using the conversion coefficient and the efficiencies of both detectors, the area of the peak could be calculated. From there, this value, along with fixed R , β , σ , and centroid were used to subtract the peak off. The black line is the function used for subtraction. The blue line is the original spectrum, and the red line is after subtraction. This code can be found in Appendix ??	88
3.5	An example of the global background fit used for peaks that could not be fit using the skewed gaussian function. The areas on either side of the peak are selected by the user. Once the background fit is done, the central area between the two sections is treated as the peak and the background is subtracted off to give a peak area. The red line shows the fit for the background area, and the two sections used for the background fit. See Appendix ?? for the global-fit function used.	89
4.1	Systematics of the Gadolinium isotopes. ^{154}Gd has an anomalously large connection between the first excited 0^+ state and the ground state. The arrows shown are the $B(E2)$ components of the transitions, in single particle Weisskopf units [57, 63–65]. The $R_{4/2}$ values beneath each nucleus are a ratio of the energies of the first excited 2^+ and 4^+ states, both in the ground state band. This ratio gives a rough measure of deformation.	92

- 4.8 Electron singles for ^{154}Gd . The energies of transitions between 0^+ states are marked in the plot. The most prominent is the $0_2^+ \rightarrow 0_{gs}^+$ transition. The $0_7^+ \rightarrow 0_3^+$ transition is at the energy of the $10_{gs}^+ \rightarrow 8_{gs}^+$ K-electron energy, and the $0_6^+ \rightarrow 0_3^+$ transition is between the $8_{gs}^+ \rightarrow 6_{gs}^+$ L and M electron energies. The $0_7^+ \rightarrow 0_6^+$ transition may be present, but sits on the low energy tail of the $2_{gs}^+ \rightarrow 0_{gs}^+$ L electron peak. 127
- 5.1 Singles spectra of ^{156}Gd . Spectra are labeled with the particles being detected, the energies of the γ and electron spectra aligned for identification. In the γ spectrum, several lines of note are labeled. The large peak in the electron spectrum at low energy is cut off due to the threshold. It is a combination of background and the 89L peak. Transitions in the higher energy regime of the γ spectrum cannot be determined without gating, due to additional background from the experimental room. The electron spectrum only goes to 1250 keV, as that is the limit of the detectors. 148
- 5.2 (a) Level Scheme of ^{156}Gd . The gamma ray of the $2_{gs}^+ \rightarrow 0_{gs}^+$ (89 keV) transition in the ground state was gated on. It was then compared with the gated spectrum from the gamma ray of the $4_{gs}^+ \rightarrow 2_{gs}^+$ (199 keV) transition in the ground state. Peaks only appearing in the first gate were assumed to go into the 2_{gs}^+ state, and assignments were made. Due to the low energy of the $2_{gs}^+ \rightarrow 0_{gs}^+$ transition, the efficiency was lower, and it is likely that transitions into the 2_{gs}^+ state were missed. The levels are organized by band. The lower levels of the band, unseen by gamma rays in this gate, are in blue. (b) Gamma spectrum gated on 89 keV, corresponding to the $2_{gs}^+ \rightarrow 0_{gs}^+$ transition. Several transitions are marked according to the level scheme. 153
- 5.3 (a) Level Scheme of ^{156}Gd . The gamma ray of the $4_{gs}^+ \rightarrow 2_{gs}^+$ (199 keV) transition in the ground state was gated on. It was then compared with the gated spectrum from the gamma ray of the $6_{gs}^+ \rightarrow 4_{gs}^+$ (296 keV) transition in the ground state. Peaks only appearing in the first gate were assumed to go into the 4_{gs}^+ state, and assignments were made. Additionally, these peaks were also gated on, to look for cascades leading into the 4_{gs}^+ state, which were found in several cases. The levels are organized by band. The lower levels of the band, unseen by gamma rays in this gate, are in blue. (b) Gamma spectrum gated on 199 keV, corresponding to the $4_{gs}^+ \rightarrow 2_{gs}^+$ transition. Several transitions are marked according to the level scheme. 156

5.4 (a) Level Scheme of ^{156}Gd . The gamma ray of the $6_{gs}^+ \rightarrow 4_{gs}^+$ (296 keV) transition in the ground state was gated on. It was then compared with the gated spectrum from the gamma ray of the $8_{gs}^+ \rightarrow 6_{gs}^+$ (380 keV) transition in the ground state. Peaks only appearing in the first gate were assumed to go into the 6_{gs}^+ state, and assignments were made. Additionally, these peaks were also gated on, to look for cascades leading into the 6_{gs}^+ state, which were found in several cases. The levels are organized by band. The lower levels of the band, unseen by gamma rays in this gate, are in blue. (b) Gamma spectrum gated on 296 keV, corresponding to the $6_{gs}^+ \rightarrow 4_{gs}^+$ transition. Several transitions are marked according to the level scheme.	159
5.5 (a) Level Scheme of ^{156}Gd . The gamma ray of the $8_{gs}^+ \rightarrow 6_{gs}^+$ (380 keV) transition in the ground state was gated on. It was then compared with the gated spectrum from the gamma ray of the $10_{gs}^+ \rightarrow 8_{gs}^+$ (451 keV) transition in the ground state. Peaks only appearing in the first gate were assumed to go into the 8_{gs}^+ state, and assignments were made. Additionally, these peaks were also gated on, to look for cascades leading into the 8_{gs}^+ state, which were found in several cases. The levels are organized by band. The lower levels of the band, unseen by gamma rays in this gate, are in blue. (b) Gamma spectrum gated on 380 keV, corresponding to the $8_{gs}^+ \rightarrow 6_{gs}^+$ transition. Several transitions are marked according to the level scheme.	162
5.6 Example of comparing gates for level population confirmation	165
5.7 Electron singles for ^{156}Gd . The energies of transitions between 0^+ states are marked in the plot. In this spectrum, the $0_3^+ \rightarrow 0_{gs}^+$ transition is the most prominent. The $0_2^+ \rightarrow 0_{gs}^+$ and $0_4^+ \rightarrow 0_3^+$ transitions appears to have some strength, but are obscured by other conversion electrons in the data. The $0_3^+ \rightarrow 0_2^+$ transition is at too low an energy to distinguish from the high background at low energies.	176
6.1 The interacting boson model symmetry triangle. The critical point symmetries described by Iachello[33] are marked.	185
6.2 The dynamic moments of inertia of the non- 0^+ bands seen in the experiment. As is seen visually and with the slopes, the ground state band and the γ band have similar moments of inertia. However, they do not overlap within their standard deviations.	188
6.3 The dynamic moments of inertia of the four 0^+ bands seen in the experiment. As is seen visually and with the slopes, the ground state band and the first excited 0^+ band have very similar moments of inertia.	189

6.4	The dynamic moments of inertia of the non- 0^+ bands seen in the experiment. As is seen visually and with the slopes, the ground state band and the γ band have similar moments of inertia, and overlap within two standard deviations.	214
6.5	The dynamic moments of inertia of the four 0^+ bands seen in the experiment. As is seen visually and with the slopes, the ground state band and the first excited 0^+ band have very similar moments of inertia.	215
7.1	A comparison of the singles spectrum of one Si(Li) detector between the GEORGINA and Clovershare experiments. The resolution of the Si(Li) detector has deteriorated between the two experiments (the GEORGINA one was performed first). The LM peaks at ~ 240 keV and ~ 330 keV show this most clearly. The peaks are distinguishable in the GEORGINA data, but not in the Clovershare data.	231
7.2	Map of the magnetic field lines, created through the use of COMSOL, for the original magnetic design [26].	233
7.3	Initial tests of the cross shapes. The left-side of the shape would be the side against the blocker. Two extremes were chosen, with intermediate steps being tested between the two. These are the three sets of extremes used: large triangle to square, triangle with the base against the blocker to triangle with the point against the blocker, and square to truncated diamond.	234
7.4	Sampling of the different hybrid cross shapes tested while examining magnetic designs. The left side of the shape would be the side against the central blocker.	235
7.5	Various width profiles tested for the magnets. The left figure shows the cross-shape for the width profiles. The left side goes against the central blocker. Variable gradients were looked at, starting with linear slopes, but evolving into step functions and piecewise linear slopes as the simulations expanded.	236
7.6	The final shapes chosen for testing. The left side goes against the central blocker. The top design has the best overall efficiency, the middle design has the best high energy efficiency, and the bottom design has the best low energy efficiency. These designs have been commissioned for testing.	237
7.7	Comparison of the thick (self-supporting) and thin (carbon-backed) targets. The spectra were taken during the same experiment. At low energies, the resolution is better in the thin target. Further, the energies of the peaks shift based on which target it is. This spectrum is not energy calibrated.	238

7.8	Trigger rate of the background with respect to time, after running on one of the carbon-backed targets. There is a clear indication of an exponential decay, shown by the fit. The slope corresponds to a half-life of 133(5) seconds. ^{15}O has a half-life of 122 seconds, within an acceptable error with the low statistics of the run.	239
7.9	A schematic representation of the MDPP-16 software in SCP mode. The amplitude and timing are separated out into individual signals. Signal properties, shaping time, and the threshold can all be adjusted. Taken from [50].	241

TABLES

2.1	Isotope Distribution of Natural Samarium	36
2.2	$4^+ \rightarrow 2^+$ K-Electrons by Isotope	40
2.3	Summary of Energy Tests	41
2.4	ICEBall Detector Locations	44
2.5	ICEBall Magnetic Strengths with GEORGINA	46
2.6	ICEBall Magnetic Strengths with Clovershare	47
2.7	ICEBall Calibration Sources	48
2.8	GEORGINA Calibration Sources	54
2.9	^{56}Co Calibration Information	55
2.10	Target Enrichment and Thickness	59
2.11	GEORGINA Detector Locations	61
2.12	Clovershare Detector Locations	64
2.13	Data Event - MADC32 (32 Bit Word)	67
2.14	Data Event - V775 (32 Bit Word)	68
2.15	Data Event - V830 (32 Bit Word)	69
2.16	Data Event - Pixie-16 (32 Bit Word)	70
3.1	Si(Li) Efficiencies in GEORGINA Configuration	74
3.2	GEORGINA Efficiency Parameters	74
3.3	Si(Li) Efficiencies in Clovershare Configuration	75
3.4	Clovershare March Run Efficiency Parameters	75
3.5	Clovershare May Run Efficiency Parameters	76
3.6	Timing Gates by Detector Pairing for the ICEBall-GEORGINA Experiment	77
3.7	Relative Angles of Detectors	85
4.1	^{154}Gd Ground State Band $6^+ \rightarrow 4^+$ and $8^+ \rightarrow 6^+$ Extra Electron Peak Contributions in Singles	99

4.2	^{154}Gd Ground State Band Internal Conversion Coefficients from Singles	100
4.3	^{154}Gd Internal Conversion Coefficients from Singles	117
4.4	Uncorrected ^{154}Gd Internal Conversion Coefficients from Singles	119
4.5	^{154}Gd Internal Conversion Electrons without Assigned Multipolarities	122
4.6	0^+ States in ^{154}Gd	126
4.7	$0^+ \rightarrow 0^+$ Transitions in ^{154}Gd	129
4.8	$2^+ \rightarrow 2^+$ Transitions in ^{154}Gd	130
4.9	$4^+ \rightarrow 4^+$ Transitions in ^{154}Gd	132
4.10	$6^+ \rightarrow 6^+$ Transitions in ^{154}Gd	134
4.11	$E0$ Contributions for $J^\pi \rightarrow J^\pi$ Transitions	136
4.12	$q_K^2(E0/E2)$ for $0^+ \rightarrow 0^+$ Transitions	138
4.13	$E0$ Contributions for $J^\pi \rightarrow J^\pi$ Transitions with Known Mixing Ratios	139
4.14	$B(E0)$ Ratios for $J^\pi \rightarrow J^\pi$ Transitions	140
5.1	^{156}Gd Ground State Band Internal Conversion Coefficients from Singles	151
5.2	0^+ States in ^{156}Gd	168
5.3	^{156}Gd Internal Conversion Coefficients from Singles	169
5.4	Uncorrected ^{156}Gd Internal Conversion Coefficients from Singles	170
5.5	^{156}Gd Internal Conversion Electrons without Assigned Multipolarities	174
5.6	$0^+ \rightarrow 0^+$ Transitions in ^{156}Gd	177
5.7	$2^+ \rightarrow 2^+$ Transitions in ^{156}Gd	178
5.8	$4^+ \rightarrow 4^+$ Transitions in ^{156}Gd	179
5.9	$E0$ Contributions for $J^\pi \rightarrow J^\pi$ Transitions	181
5.10	$B(E0)$ Ratios for $J^\pi \rightarrow J^\pi$ Transitions	181
5.11	$E0$ Contributions for $J^\pi \rightarrow J^\pi$ Transitions	182
6.1	Dynamic Moments of Inertia of Bands seen in ^{154}Gd	190
6.2	^{154}Gd $K_i = 0_2^+$ Internal Conversion Coefficients from Singles	192
6.3	$J^\pi \rightarrow J^\pi$ Transitions for $K_i = 0_2^+$ in ^{154}Gd	194
6.4	$J^\pi \rightarrow J^\pi$ Transitions for $K_i = 0_3^+$ in ^{154}Gd	196
6.5	^{154}Gd $K_i = 0_6^+$, Internal Conversion Coefficients from Singles	198
6.6	$J^\pi \rightarrow J^\pi$ Transitions for $K_i = 0_6^+$ in ^{154}Gd	199
6.7	$J^\pi \rightarrow J^\pi$ Transitions for $K_i = 0_7^+$ in ^{154}Gd	201

6.8	^{154}Gd $K_i = 2_1^+$, γ Internal Conversion Coefficients from Singles	203
6.9	$J^\pi \rightarrow J^\pi$ Transitions for $K_i = 2_1^+$, γ in ^{154}Gd	205
6.10	^{154}Gd $K_i = 2_2^+$, Internal Conversion Coefficients from Singles	207
6.11	$J^\pi \rightarrow J^\pi$ Transitions for $K_i = 2_2^+$ in ^{154}Gd	208
6.12	^{154}Gd $K_i = 4_1^+$, Internal Conversion Coefficients from Singles	210
6.13	$J^\pi \rightarrow J^\pi$ Transitions for $K_i = 4_1^+$ in ^{154}Gd	211
6.14	Summary of 0^+ State Information in ^{154}Gd	213
6.15	Dynamic Moments of Inertia of Bands seen in ^{156}Gd	216
6.16	^{156}Gd $K_i = 0_2^+$ Internal Conversion Coefficients from Singles	218
6.17	$J^\pi \rightarrow J^\pi$ Transitions for $K_i = 0_3^+$ in ^{154}Gd	220
6.18	^{156}Gd $K_i = 2_1^+$, γ Internal Conversion Coefficients from Singles	222
6.19	$J^\pi \rightarrow J^\pi$ Transitions for $K_i = 2_2^+$ in ^{154}Gd	224
6.20	^{156}Gd $K_i = 2_1^+$, γ Internal Conversion Coefficients from Singles	226
6.21	$J^\pi \rightarrow J^\pi$ Transitions for $K_i = 4_1^+$ in ^{156}Gd	227
6.22	Summary of 0^+ State Information in ^{156}Gd	229
7.1	Data Event - MDPP-16 (32 Bit Word)	243

CHAPTER 1

INTRODUCTION

Visible matter comprises ~ 5 percent of the universe. This matter makes up all living things and ecosystems, including the stars and planets. This matter exists entirely within the atom, with the nucleus holding more than 99.9 % of all matter. The nucleus is comprised of protons and neutrons in different configurations, held together by the strong force. Understanding this essential building block of the universe is at the heart of understanding how matter is formed and evolves.

The periodicity of phenomena on the atomic level and higher is well documented near stability, from the lattice structures of crystals, to the periodic table of the elements, organized in a way that groups elements that behave similarly due to the structure of the orbiting atomic electrons. The periodic table organizes elements based on similar properties, such as the halogens and noble gases. The elements can be neatly grouped by similar chemical properties. But, this periodic table does not delve into the subatomic level. The periodic table separates out atoms by the number of protons, which equates with the atomic number, but the number of neutrons in a nucleus can also vary, creating different isotopes of an element that is otherwise chemically identical. When mapping these two, we create Figure 1.1, known as the chart of nuclides. These nucleons are held together by the strong force, which has a short range. In the low-mass region of the chart, this creates a linear trend for the line of stability. As mass and the total number of nucleons increases, the line of stability trends toward the neutron side, due to repulsion by the coulomb force in the protons. As the neutrons do not contribute significantly to the coulomb force, the

addition of more neutrons creates larger separation between protons, decreasing the coulomb contribution.

The chart of nuclides has several notable features in this form. The color coding in Figure 1.1 is representative of the lifetimes of the isotopes represented in each box: lighter boxes are shorter-lived, while darker boxes are longer lived, with black boxes being stable isotopes. This creates a black line going up at approximately $N = Z$, known as the valley of stability. Additionally in this figure, several rows and columns are singled out. These rows and columns are a series of numbers referred to as the "magic" numbers, and highlight a form of periodicity in nuclei.

This periodic nature is explained through the shell model. Based on the same idea as atomic electrons, the "shells" occur due to the energy gap in levels. The neutrons and protons each have separate potential wells and levels populated. When examining solutions to this potential well, the magic numbers naturally form after including angular momentum and taking the spin-orbit interaction into account, as seen in Figure 1.2. These magic numbers represent closed shells of a spherical nucleus model. It is of note that a doubly-magic nucleus, that is, a nucleus with both neutron and proton closed shells, is spherical. However, a nucleus with only a single closed shell is not, necessarily, spherical. These closed shells cause a variety of effects, including high energy of the first excited 2^+ state at closed shells, seen in Figure 1.3. The high energy of the first excited 2^+ state near the closed shells is due to the large energy gaps that occur at closed shells, seen on the right side of Figure 1.2.

Outside of these closed shells, there are large regions that do not work within the paradigm created by this phenomenon. Nuclei near the closed shells are generally expected to be spherical in nature. However, the shell model becomes extremely complex away from the closed shells. In some cases, the magic numbers themselves appear to change. This change can be charted using the Nilsson model, which evolves the spherical shell model as it deforms into an ellipsoid. The model uses the deformation

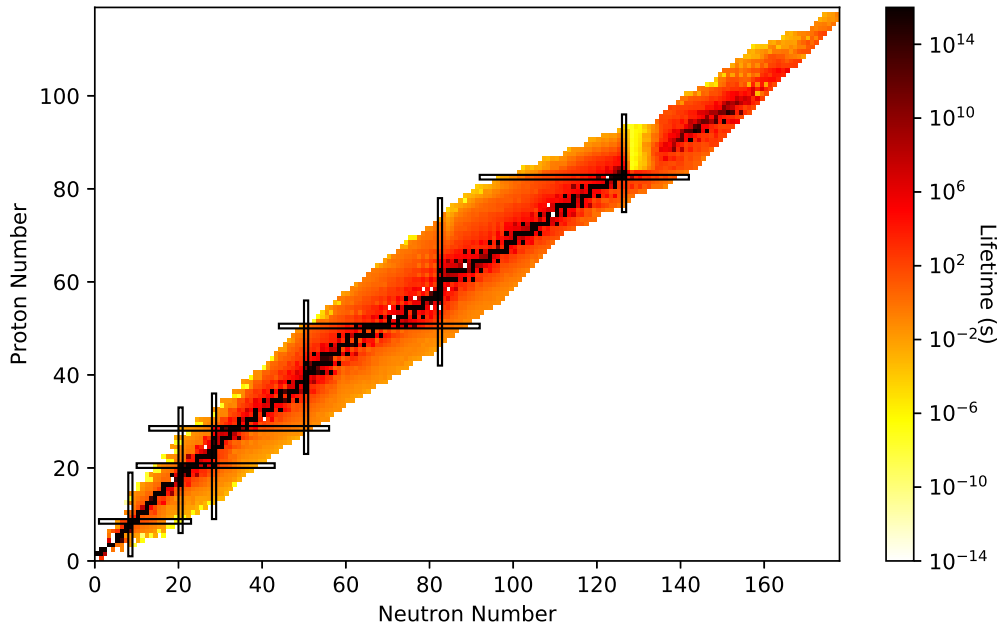


Figure 1.1. The chart of nuclides. The x -axis is increasing in neutron number from left to right, and the y -axis is increasing in proton number from bottom to top. The lower leftmost corner is the lightest elements, while the upper right are the heaviest, including superheavy elements. Black boxes indicate stable or extremely long lived nuclei. These nuclei are in the "center" of the chart, and known colloquially as the valley of stability. To either side of these stable nuclei are radioactive nuclei, which become shorter lived the farther they are from the valley, indicated by the lightening color. The black boxes are at neutron and proton numbers 8, 20, 28, 50, 82 and 126, marking closed shells for spherical nuclei, and are discussed in further depth within the text.

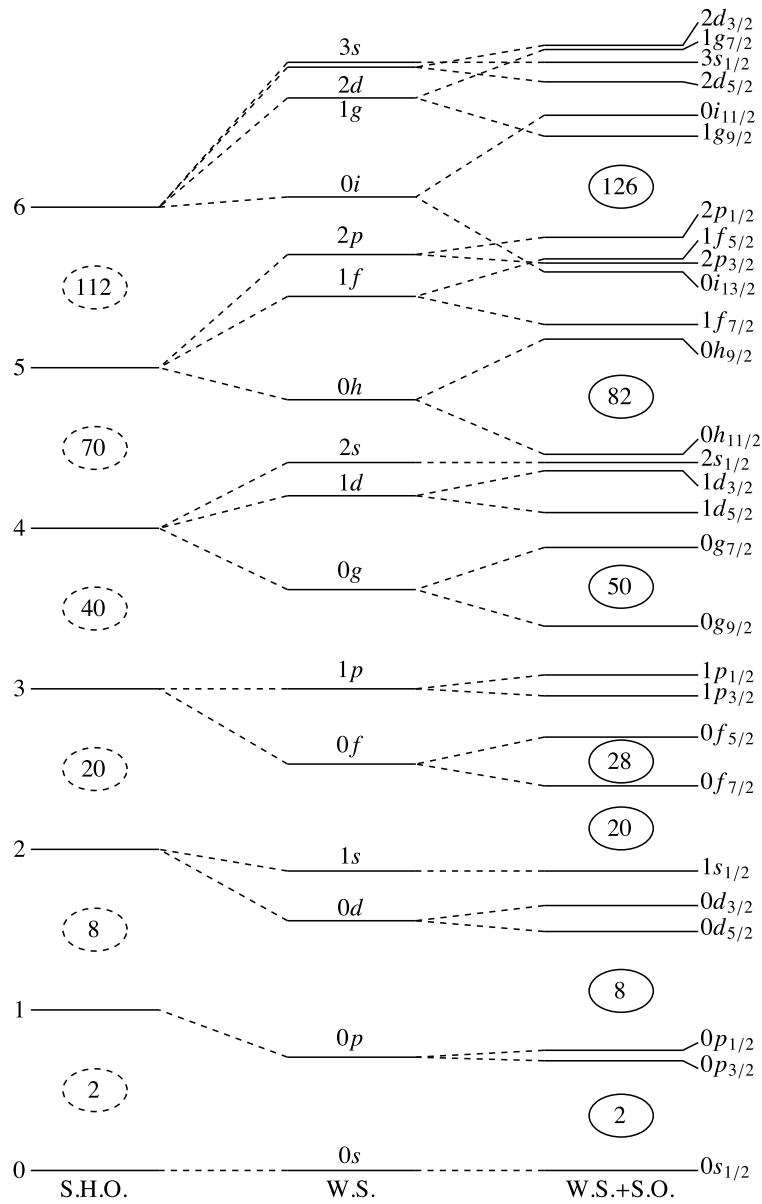


Figure 1.2. The evolution of the shell model and the creation of the closed shells of a spherical nucleus. On the left is the spherical harmonic oscillator. By changing the potential to the Woods-Saxon potential, creating a flat centered potential well, the degenerate states of the harmonic oscillator separate in energy. By further adding a spin-coupling term, the levels separate with energy spacings that create the closed shells and the magic numbers.

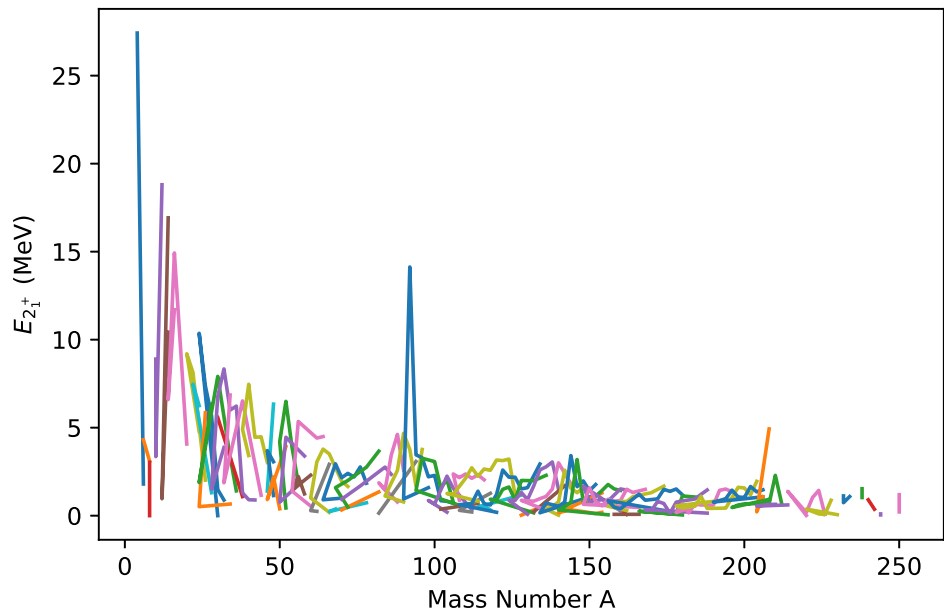


Figure 1.3. The energy of the first excited 2^+ state, plotted in isotopic chains by mass, distinguished by color. Areas of high excitation energy, around $A \sim 90, 140, 210$ all correspond to doubly magic areas. The areas around $A \sim 110, 170$ have much lower excitation energies and correspond to areas of deformation.

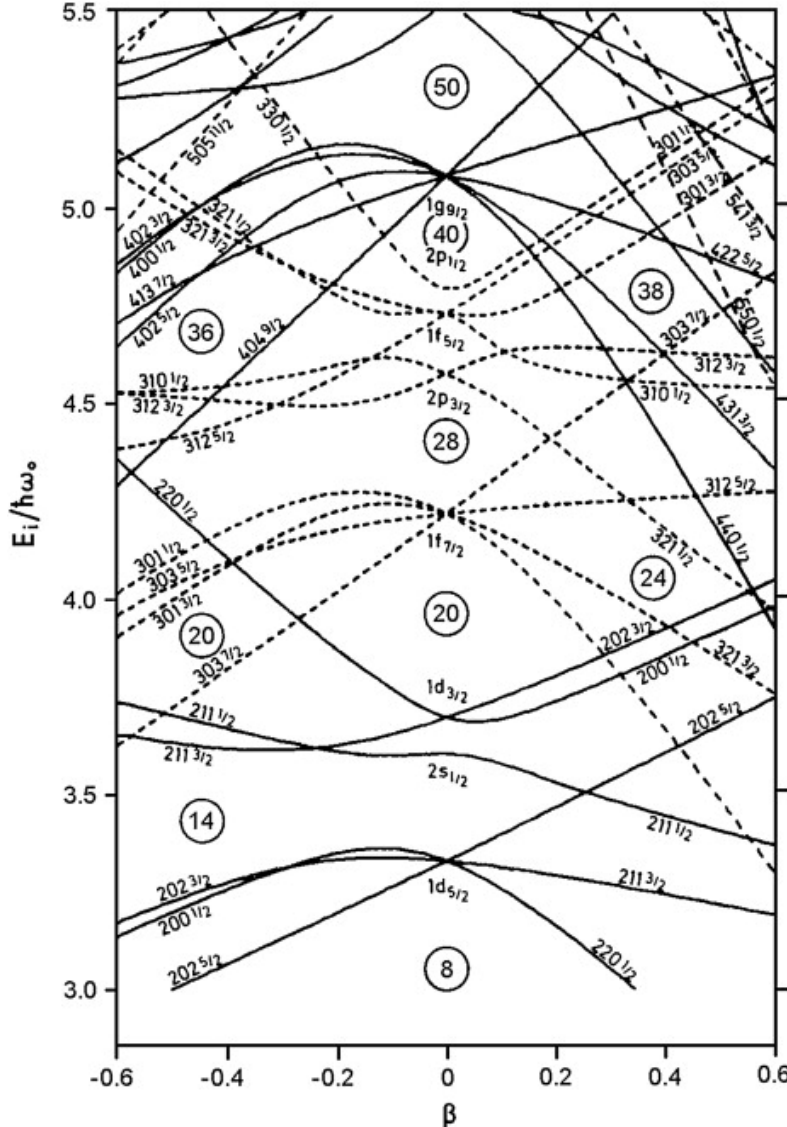


Figure 1.4. The Nilsson diagram, showing the evolution of the shell levels of the nucleus with respect to the deformation parameter β . As the nucleus gets more deformed, the closed shells break down. Taken from [22].

parameter β in the Hamiltonian, allowing the level energies to be seen as a function of β . This leads to a collapse and change of the magic numbers, as seen in Figure 1.4.

In the area around $Z = 60$ and $N = 90$, away from the closed shells, nuclei are not spherical in their ground state. They lose symmetry on the major axes, becoming

asymmetric, i.e. $\langle r_x \rangle = \langle r_y \rangle \neq \langle r_z \rangle$ or $\langle r_x \rangle \neq \langle r_y \rangle \neq \langle r_z \rangle$. The former case, known as axial symmetry, has two forms: oblate (pancake-like) or prolate (football-like) depending on whether the nucleus appears compressed (oblate) or elongated (prolate) along the symmetry axis (z), as seen in Figure 1.5. In Figure 1.4, the negative β corresponds to oblate nuclei, while positive β corresponds to prolate nuclei. There are more exotic deformations when the latter asymmetry is true, where symmetry is broken around two or more axes, resulting in triaxial shapes, pear-shapes and other exotic deformations.

There are several ways to look for deformation in a nucleus. If we assume the nuclear shape is an axially-symmetric rigid ellipsoid with a surface parametrized by

$$r = R_0(1 + \beta_2 Y_{20}(\theta, \phi)) \quad (1.1)$$

where R_0 is the mean radius, Y_{20} is the spherical harmonic of rank 2, and β_2 (also referred to as β) is the quadrupole deformation parameter, the moment of inertia is

$$I = \frac{2}{5} A M R_0^2 \beta_2 (1 + 0.31\beta_2) + \mathcal{O}(\beta_2^3) \quad (1.2)$$

and the intrinsic electric quadrupole moment is

$$Q_0 = \frac{3}{\sqrt{5}\pi} Z R_0^2 \beta_2 (1 + 0.16\beta_2) + \mathcal{O}(\beta_2^3) \quad (1.3)$$

where Z is the atomic number and A is the number of nucleons [20]. This can be measured in even-even nuclei using the transition between the 0^+ ground state and the first excited 2^+ state. The onset of deformation can be seen in Figure 1.6, via the rapid increase in β_2 . The equation used to calculate β_2 for this figure is

$$\beta_2 = \frac{4\pi}{3Z R_0^2} [B(E2; 0_1^+ \rightarrow 2_1^+)]^{1/2}. \quad (1.4)$$

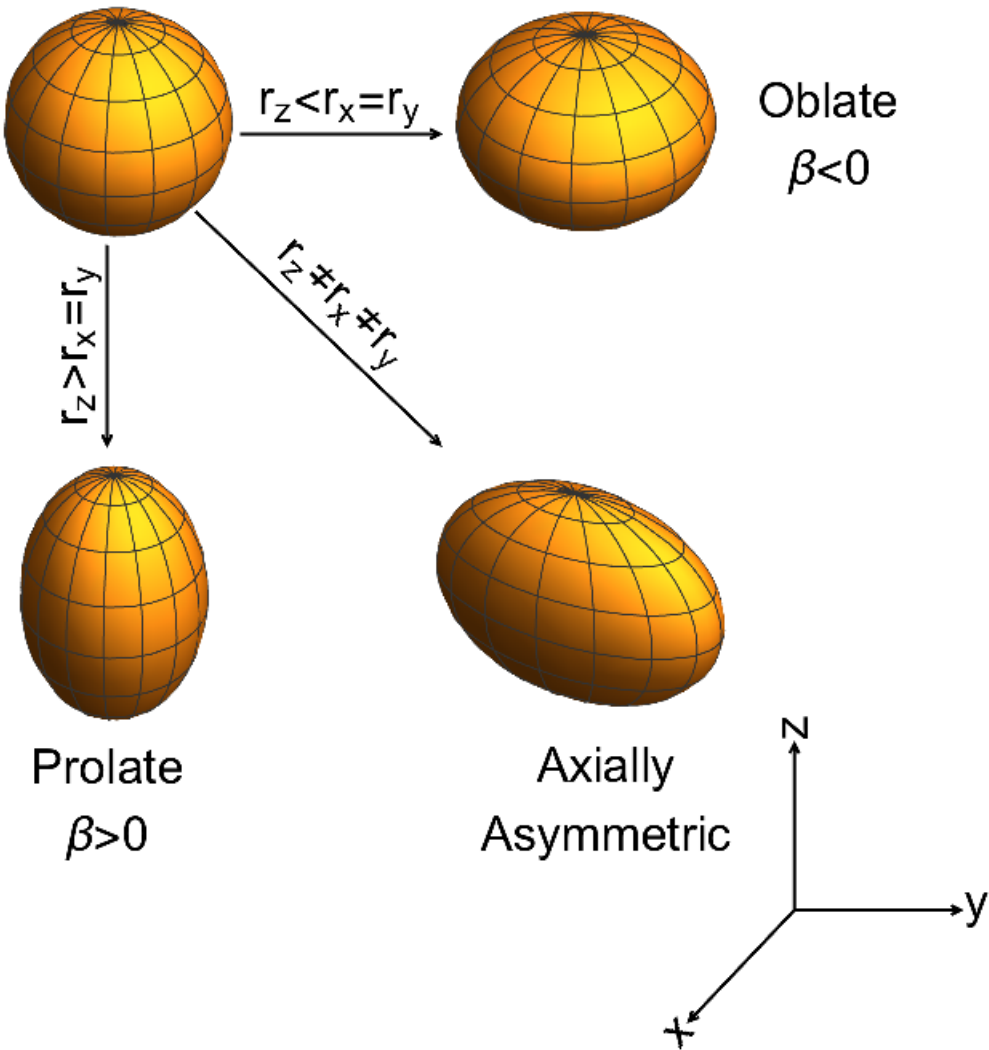


Figure 1.5. Illustration of different kinds of deformation, where spherical symmetry is lost. Treating the vertical as the axis of symmetry, the prolate nucleus is contracted along this axis, but is still axially symmetric. The oblate nucleus is elongated along this axis, but otherwise axially symmetric. It is also possible for the nucleus to lose axial symmetry.

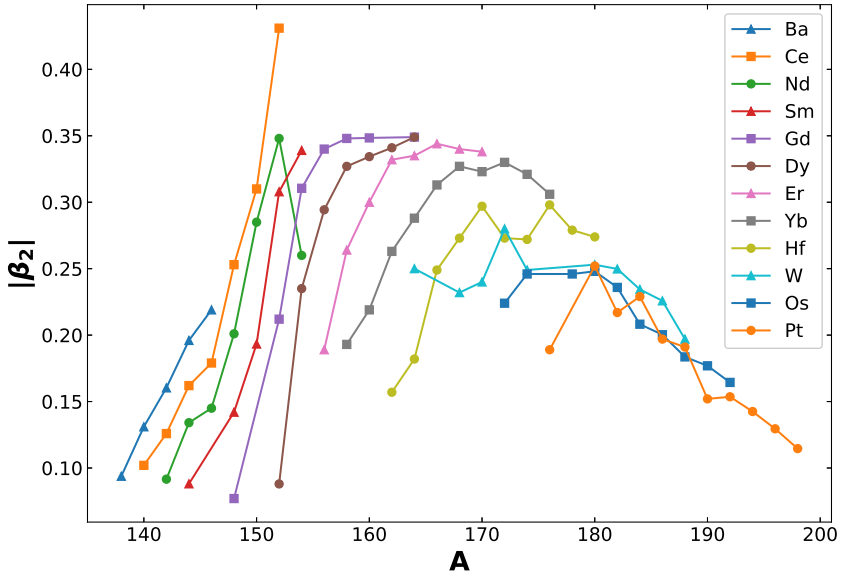


Figure 1.6. Plot of the norm of the quadrupole deformation parameter β_2 along isotopic chains. Deformation can be seen setting in, as isotopic chains transition from spherical to deformed. β_2 is the quadrupole deformation parameter. The norm of β_2 is used, as the method used to calculate β_2 only gives a magnitude, not a sign. A secondary method is needed to distinguish between prolate and oblate.

The only assumption for this equation is that of a uniform charge distribution[62]. There is no way to distinguish prolate and oblate using this calculation, as the sign comes from the choice of sign on the root. The choice cannot be determined solely from the $B(E2)$.

In the lanthanide region, there are multiple stable isotopes of several elements, including Samarium ($Z = 62$) and Gadolinium ($Z = 64$). Studies across these elements show the onset of deformation through systematics like the energy of the first excited 2^+ state, and the ratio between the energies of the first 4^+ and 2^+ excited states, seen in Figure 1.7. The $E_{4_1^+}/E_{2_1^+}$ ratio theoretically tops out at 3.3. This ratio gives a measure of the moment of inertia of the ground-state band of the nucleus, as,

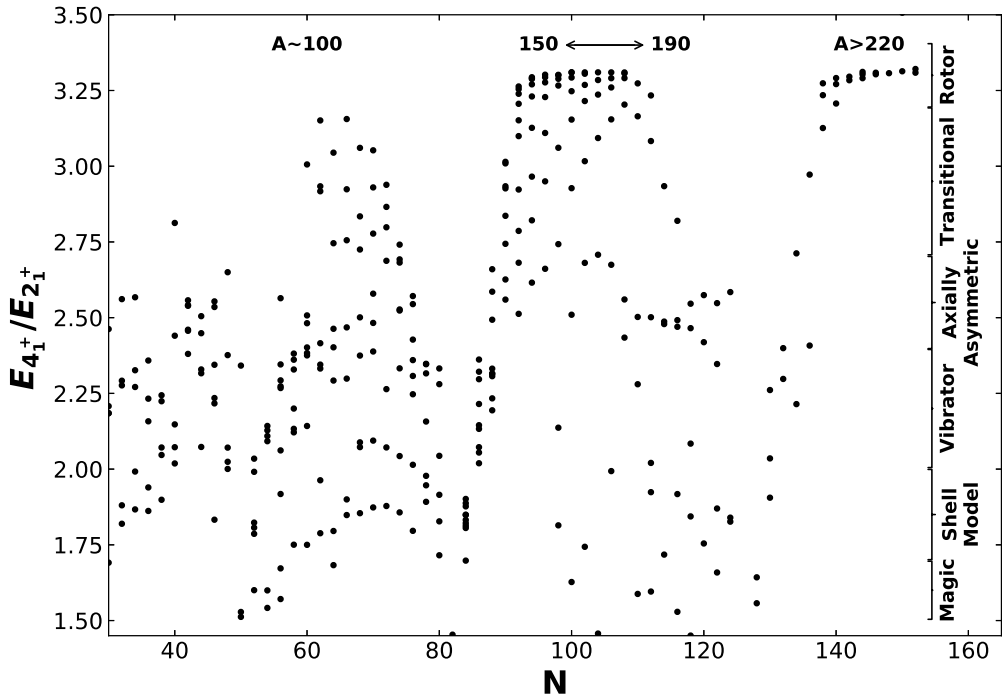


Figure 1.7. Plot of the ratio of the first 4^+ excited state energy to the first 2^+ excited state energy in even-even nuclei. On the right, the ratio is broken down into sections, based on structure. This ratio is an excellent diagnostic of the general nuclear structure.

for a rigid rotor,

$$E = \frac{\hbar^2}{2\mathcal{J}_{eff}} J(J+1). \quad (1.5)$$

The moment of inertia, \mathcal{J}_{eff} , varies as energy increases. In a perfect rigid rotor, this would not be the case, and $\mathcal{J}_{eff} = \mathcal{J}_{rigid} = \frac{2}{5}Am_{\mathcal{N}}r_0^2A^{2/3}$. Taking the ratio of two energy levels, $J = 4$ and $J = 2$ in this case, would give a ratio of $10/3$, or 3.3. However, if it is not a rigid rotor, this number deviates from 3.3, as the change in the effective moment of inertia changes. The model used by Bohr and Mottelson shows that \mathcal{J}_{eff} is proportional to the square of the deformation parameter, β_2 , at low deformation, and approaches that of a rigid body at high deformation [14].

Many of these nuclei are successfully modelled with deformation in theoretical calculations [27]. These models can also open up new questions, when a previously identified feature does not fit with the assignment in an otherwise well described system.

1.1 Nuclear Excitations

There are many different ways a nucleus can be excited. While the types of excitations available depend on shape, there are two extremes to consider: a single particle excitation, and a collective excitation. The single particle excitation can be described as a single neutron, proton, or hole from a closed shell being excited to a different level. A collective excitation is usually thought of on a macroscopic level, looking at large numbers of nucleons moving together. These are only extremes, and there are excitations that can be described as multi-particle that would fit in-between. All of these excitations can exist within a nucleus.

1.1.1 Collective Excitations

Two types of collective excitations are rotational and vibrational excitations. Rotational excitations occur in deformed nuclei where spherical symmetry is broken, i.e. $\langle r_x \rangle = \langle r_y \rangle \neq \langle r_z \rangle$ or $\langle r_x \rangle \neq \langle r_y \rangle \neq \langle r_z \rangle$. These are caused by the rotation of the nucleus about the axis of symmetry. Vibrational excitations involve the compression and expansion of the nucleus as a whole. These come in different modes, and have a characteristic even spacing, seen in Figure 1.8. Two theorized forms of vibrational excitations are β and γ quadrupole excitations in a deformed nucleus[70]. In a spherical nucleus, there is only one type of quadrupole excitation. The deformation breaks

the degeneracy, creating two possible modes. We can write the radius as

$$r(\theta) = r_0 \left[1 + \sum_{\mu} \alpha_{2\mu}^* Y_{2\mu}(\theta) \right] + O(\alpha^2) \quad (1.6)$$

where $\alpha_{2\mu}$ are the set of deformation parameters and $Y_{2\mu}(\theta)$ are the spherical harmonics of order 2. The axes can be defined such that

$$\begin{aligned} \alpha_{21} &= \alpha_{2-1} = 0, \\ \text{and } \alpha_{22} &= \alpha_{2-2} \end{aligned} \quad (1.7)$$

leaving two shape parameters, α_{20} and α_{22} . These two parameters can be written in terms of β and γ , such that

$$\begin{aligned} \alpha_{20} &= \beta \cos \gamma \\ \alpha_{22} &= \frac{1}{\sqrt{2}} \beta \sin \gamma \end{aligned} \quad (1.8)$$

In an axially symmetric nucleus, $\gamma = 0$. From equation 1.8, β vibrations are described as oscillations in α_{20} , and γ vibrations are described as oscillations in α_{22} [70].

There are several ways to tell the difference between these types of excitations. The collective models have well-described spacing of the levels, seen in Figure 1.8. Vibrational excitations will be spaced regularly as $n\hbar\omega$, while rotational excitations will have increasing spacing between the levels as J increases. The reduced transition probabilities also give information about the difference between two different levels. The single-particle strengths for these transitions can be calculated and are known as Weisskopf estimates. The reduced transition probability can then be written in Weisskopf units using the estimate, which gives a measure of the collectivity of the transition. This does have limitations, however, as the Weisskopf estimate assumes a spherical nuclear model. Predictions of the relative strengths of reduced transitions probabilities, specifically $B(E2)$, can be used to determine the collective nature of an

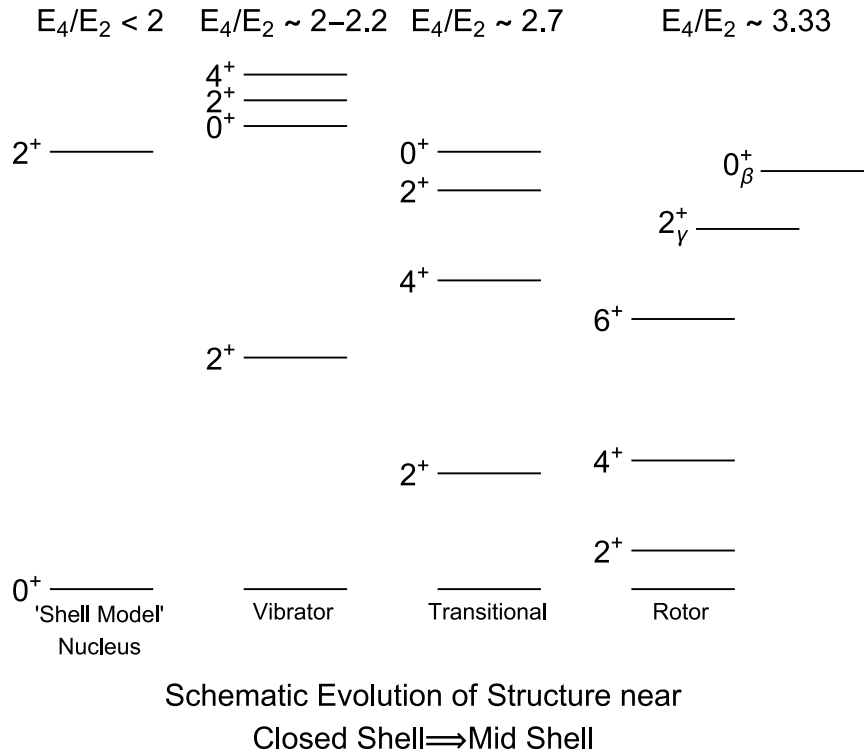


Figure 1.8. Cartoon of what excited states built upon different types of nuclei looks like. The closed shell has a large gap between the ground state and first excited state. In the vibrator model, this gap is lower, and a gap of comparable size exists before a cluster of states occurs. In the rotor model, the spacing follows a spacing pattern of $J_f(J_f + 1) - J_i(J_i + 1)$, with γ and β vibrations also coming into play. The transitional area between vibrator and rotor shows a shift between the two, with the clustered states of the vibrator model beginning to space out.

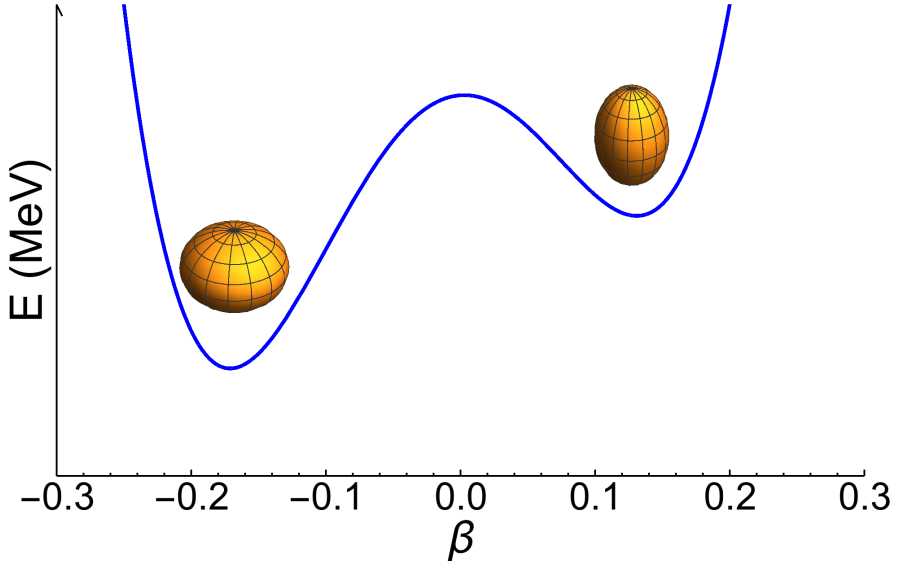


Figure 1.9. Cartoon of the potential well of a nucleus with shape coexistence. A second minima appears at a different β , the deformation parameter. Both of these minima can have excitations built on top of them, leading to shape coexistence. A representation of the shape at β is shown in each minima.

excited band[71].

1.1.2 Shape Coexistence

In the previous discussion, we have considered only shapes and excitations of the ground state. However, as excitation energy increases, multiple equilibrium shapes can be found within a single nucleus. A simple model for this shape coexistence imagines a potential as a function of deformation parameter; each local minimum will correspond to an equilibrium shape as illustrated in Figure 1.9. Each minimum can also have excitations built upon them. If the energy barrier between minima is small enough, the shapes can also interact, causing shape mixing effects.

In an even-even nucleus, the lowest energy state of a given coexisting shape should have $J^\pi = 0^+$. In the lowest configuration for a shape, all the particles (or holes) should be paired. Thus, a possible signature of shape coexistence is the presence of additional 0^+ states beyond the ground state. There are two main theoretical approaches to shape coexistence in nuclei: microscopic shell-model and mean-field descriptions [32]. These two approaches compliment each other.

In the shell-model approach, additional shapes come from np - nh configurations. Ground state deformation evolves across a shell from preferential population of different m_j -substates as more particles are added. Within a finite number of particles, similar filling can be achieved by moving particles amongst m_j -substates. Naïvely, one might expect that many 0^+ np - nh configurations would be at very high excitation energies. However, upon correcting for monopole interaction energy, and then coupling different np - nh subspaces together, lower energy 0^+ states are calculated [21]. In this approach, intruder states from even-even particle-hole excitations can create shape-coexisting 0^+ states.

The mean-field approach uses the self-consistent Hartree-Fock-Bogoliubov (HFB) theory. The effective forces are tuned to describe global nuclear properties. When minimizing the energy, deformation in the nuclear shape can result, much like in Figure 1.9. Various mean-field states are found, which have broken symmetries needed within the nucleus. These states are projected onto the proper particle numbers, isospin, and angular momentum to produce the physical 0^+ states observed [32]. To compare with experimental data, the Hamiltonian must be re-diagonalized in terms of the physical, projected states.

Shape coexistence, like the collective excitations, has spectroscopic fingerprints that can help determine its existence. As with deformation, large reduced transition rates are a possible sign of shape coexistence, but do not distinguish between static and dynamic deformation [32]. The diagonal $E2$ matrix elements, i.e. the quadrupole

moments, can distinguish between the dynamic and static. The $E0$ transitions present in $J^\pi \rightarrow J^\pi$ may also be an indirect fingerprint of shape coexistence, as it is related to the change in the mean radius of the nucleus, as discussed in Section 1.3.1[80]. The low-lying states of interest can be difficult to observe, as they are not populated strongly in reactions.

1.2 Multipole Radiation

When the nucleus is in an excited state, with energy in excess of its ground state, it is then capable of de-exciting in different ways. With enough energy, the nucleus will preferentially emit particles, such as neutrons or protons, as it is mediated by the strong interaction. In the case that enough energy is not present for particle emission, the electromagnetic force becomes the dominant mode of de-excitation, via photon emission in the form of γ -rays. Because nuclei have well-defined angular momentum, the simplest way of describing the electromagnetic radiation is in terms of electromagnetic fields with well defined-angular momentum. This is done by expansion in spherical harmonics of the electromagnetic fields. This expansion is commonly referred to as multipole expansion. Discussion and derivation can be found in detail in many references [13, 15, 39, 84].

To get the transition rate or transition probability, Fermi's golden rule,

$$w_{if} = \frac{2\pi}{\hbar} |\langle f | H_{int} | i \rangle|^2 \rho, \quad (1.9)$$

is used where H_{int} is the interaction Hamiltonian from the generated field and ρ is the density of states. The Hamiltonian for electromagnetic radiation is

$$H(\mathbf{r}) = -\frac{e}{2mc} \{g_l [\mathbf{A}(\mathbf{r}) \cdot \mathbf{p} + \mathbf{p} \cdot \mathbf{A}(\mathbf{r})] + g_s \hbar \mathbf{s} \cdot \nabla \times \mathbf{A}(\mathbf{r})\} \quad (1.10)$$

in terms of the spin (\mathbf{s}) and momentum (\mathbf{p}) operators and the magnetic vector potential $\mathbf{A}(\mathbf{r})$ [15]. The factors g_l and g_s are the orbital and spin g -factors, respectively. The magnetic vector potential can be defined as

$$\mathbf{A}_q(\mathbf{k}, \mathbf{r}) = \mathbf{e}_q e^{i\mathbf{k}\cdot\mathbf{r}} = \frac{1}{\sqrt{2}} \sum_{lm} (q \mathbf{A}_{lm}^M(\mathbf{r}) + \mathbf{A}_{lm}^E(\mathbf{r})) \mathcal{D}_{mq}^l(R) \quad (1.11)$$

where $\mathcal{D}_{mq}^l(R)$ is the rotation matrix with R taking the z-axis to the \mathbf{k} direction and $q = \pm 1$ is the polarization factor. The vector potential is split into $\mathbf{A}_{lm}^E(\mathbf{r})$ and $\mathbf{A}_{lm}^M(\mathbf{r})$, the transverse solutions to the equation

$$\nabla^2 \mathbf{A} + k^2 \mathbf{A} = 0, \quad (1.12)$$

which is the wave equation derived from Maxwell's equations in free space. These two solutions are linearly independent and have opposite parities $\pi(\mathbf{A}_{lm}^E) = (-1)^l$ and $\pi(\mathbf{A}_{lm}^M) = (-1)^{l-1}$. The two solutions can then be written as

$$\sqrt{\{l(l+1)\}} \mathbf{A}_{lm}^M = i^l (2l+1) j_l(kr) \mathbf{L} \left(\frac{2l+1}{4\pi} \right)^{\frac{1}{2}} Y_{lm}, \text{ and} \quad (1.13a)$$

$$\mathbf{A}_{lm}^E = (1/k) \nabla \times \mathbf{A}_{lm}^M \quad (1.13b)$$

where Y_{lm} are the spherical harmonics, and $j_l(kr)$ are the spherical Bessel functions. The spherical Bessel functions can be approximated using the long wavelength approximation

$$j_l(kr) \approx (kr)^l / (2l+1)!! , \text{ if } kr \ll 1, \quad (1.14)$$

The Hamiltonian can then be rewritten as

$$H'_q(\mathbf{k}, \mathbf{r}) = - \sum_{lm} \frac{i^l k^l}{(2l-1)!!} \sqrt{\frac{2l+1}{2l}} \mathcal{D}_{mq}^l(R) \{(Q_{lm} + Q'_{lm}) - iq(M_{lm} + M'_{lm})\} \quad (1.15)$$

where Q_{lm} , Q'_{lm} , M_{lm} , and M'_{lm} are the electric (Q) and magnetic (M) multipole operators. They are defined

$$Q_{lm}(\mathbf{r}) = eg_l \left[\left(\frac{2l+1}{4\pi} \right)^{\frac{1}{2}} r^l Y_{lm} \right] \quad (1.16a)$$

$$Q'_{lm}(\mathbf{r}) = -k\beta g_s \mathbf{L} \left[\left(\frac{2l+1}{4\pi} \right)^{\frac{1}{2}} r^l Y_{lm} \right] \cdot \mathbf{S} / (l+1) \quad (1.16b)$$

$$M_{lm}(\mathbf{r}) = -2\beta g_l \nabla \left[\left(\frac{2l+1}{4\pi} \right)^{\frac{1}{2}} \mathbf{r}^l Y_{lm} \right] \cdot \mathbf{L} / (l+1) \quad (1.16c)$$

$$M'_{lm}(\mathbf{r}) = \beta g_s \nabla \left[\left(\frac{2l+1}{4\pi} \right)^{\frac{1}{2}} r^l Y_{lm} \right] \cdot \mathbf{S} \quad (1.16d)$$

with β being the magneton $\beta = e\hbar/2mc$ [15]. Using this form of the Hamiltonian in equation 1.9, the transition probabilities are

$$T^E(l, m) = \frac{8\pi(l+1)}{l[(2l+1)!!]^2} \frac{k^{2l+1}}{\hbar} |\langle f | Q_{lm} | i \rangle + \langle f | Q'_{lm} | i \rangle|^2 \quad (1.17a)$$

$$T^M(l, m) = \frac{8\pi(l+1)}{l[(2l+1)!!]^2} \frac{k^{2l+1}}{\hbar} |\langle f | M_{lm} | i \rangle + \langle f | M'_{lm} | i \rangle|^2 \quad (1.17b)$$

Of note from this, the transition probability decreases with increasing l , making lower angular momentum transitions more favorable. Additionally, looking at the multipole operators, once the wave equations have been added in, all but the Q_{lm} multipole operator has a factor of β , which is very small. This makes the electric transition stronger than the magnetic transition of the same l .

There are limitations for the types of multipole radiation that can be emitted from a transition, known as selection rules. One such limitation is that all of the multipole

operators of equations 1.16 are proportional to the identity operators and $\langle f|i \rangle = 0$ by orthogonality for $f \neq i$. Other rules are based on two pieces of information about the initial and final states: the spins and parities of the states. The spins, J , of the states select the allowable l , using the range $|J_i - J_f| \leq l \leq J_i + J_f$, meaning the change in angular momentum cannot exceed the sum of the spins of the two states, or be smaller than the difference of the spins of the two states. For example, a transition between two states of spins 4 and 2 would allow l from 2 to 6. The parity selection now helps select the set of solutions. With the first selection rule, in the example, the possibilities are E2, M2 ... E6, M6. If the parity stays the same between the two states, so positive to positive or negative to negative, the solutions are even El and odd Ml. If the parity changes, the solutions are odd El and even Ml. In an equation form, the parity change is

$$\pi(\text{El}) = (-1)^l \quad \pi(\text{Ml}) = (-1)^{l-1} \quad (1.18)$$

While not a selection rule, multipoles of lower order are stronger, and electric multipoles are stronger than magnetic multipoles, with Ml having about the same intensity as E($l+1$). There are also forbidden transitions to consider. The name is a misnomer, as these transitions are not strictly forbidden, but are highly suppressed, or must occur through a different mechanism. A relevant example to this text is that of the $l = 0$ transition, previously noted as forbidden. Photons carry an angular momentum of 1, so any transitions that occur via photon emission must have a $\Delta J \geq 1$, so l must be at least 1. An E0 transition has $l = 0$, making it forbidden by single photon emission. However, it can still occur several different ways, including internal conversion.

1.3 Internal Conversion

Not all transitions are equal, with certain multipolarities being preferred or excluded via selection rules. This makes transitions between some states highly improbable or, in the case of photon emission, impossible. The $0^+ \rightarrow 0^+$ transition cannot occur via photon emission due to $\Delta J = 0$. To study these transitions, another type of de-excitation that occurs using the mechanisms in electromagnetic radiation must occur, assuming particle emission does not take place. Above 1.022 MeV of excitation, the nucleus can also de-excite via pair-production, the creation of an electron-positron pair. Below this energy, there are two processes to de-excite the nucleus: the aforementioned photon emission and internal conversion. Internal conversion is also an electromagnetic processing, occurring internally within the atom, with the excitation energy being transferred to an orbiting atomic electron. The electron is then ejected from its bound state, as the energy it has been given exceeds the electron binding energy, giving the electron a kinetic energy of

$$T_e = E_\gamma - B_i \quad (1.19)$$

where B_i is the binding energy of the i^{th} atomic shell of the electron, and E_γ is the transition energy. The electron carries information about the multipolarity of the transition it was ejected from, as a photon would if emitted for the same transition. Unlike photon emission, it is not bound by a change in angular momentum, creating a process through which E0 transitions can occur, thus giving a method to study such transitions and states. Figure 1.10 shows the internal conversion coefficients of the K-shell electron for several multipolarities in Gadolinium, plotted against energy.

Both of these processes come from the same overall mechanism, that of the electromagnetic field, but internal conversion also has a component from the nuclear interaction. As a result, internal conversion can be described with the conversion

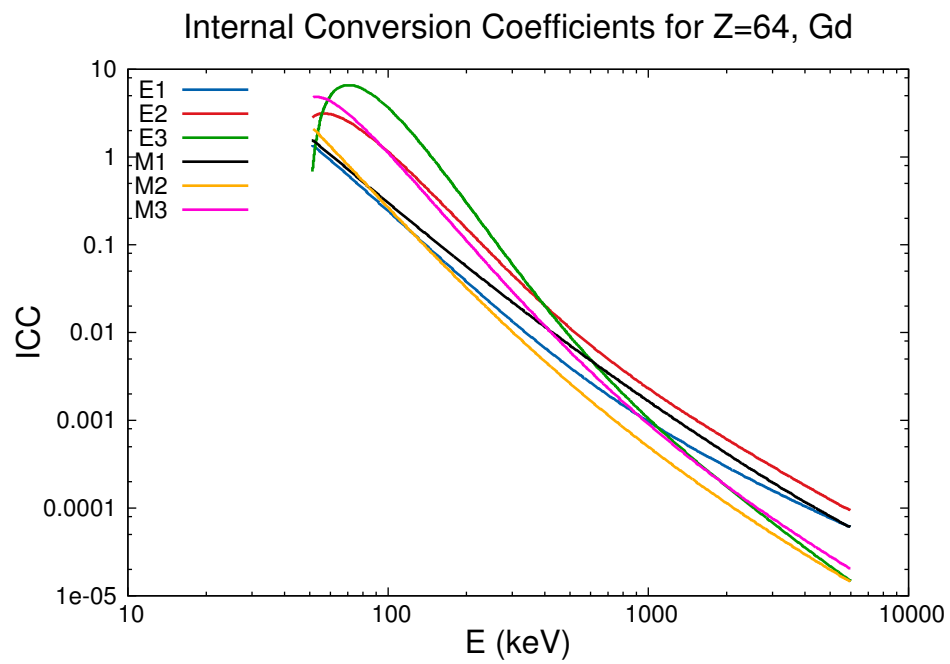


Figure 1.10. The theoretical K-shell conversion coefficients for the magnetic and electric multipoles for $l = 1, 2, 3$, calculated using BrICC [40]. Each of the multipoles is distinct. Further distinction between multipoles can be seen by plotting the intensity ratios between different electronic shells.

coefficient

$$\alpha = \frac{w_e}{w_\gamma} \quad (1.20)$$

where w_e is the transition probability due to internal conversion and w_γ is the transition probability due to single photon emission for the same transition.

Internal conversion is a result of the interaction of the electron's wavefunction with that of the nucleus. The probability for internal conversion can be derived using Fermi's Golden rule, equation 1.9, where H_{int} is the electromagnetic interaction of the combined initial nuclear and electron states ($\phi_i = \psi_i \varphi_i$), to the combined final nuclear state and free electron ($\phi_f = \psi_f \varphi_f$), and ρ is the accessible energy state density for the ejected electron. For simplicity, this derivation will be specifically for K -shell electrons, and look at the area outside of the nuclear radius [13, 72, 73].

Taking into account there are two electrons in the K -shell, the probability w_{if} can then be rewritten as

$$w_{if} = 2 \frac{2\pi}{\hbar} z(k) \int |\langle f | H_{int} | i \rangle|^2 d\Omega \quad (1.21)$$

where $d\Omega$ is the electron direction within the solid angle, and the density of final states has been rewritten in terms of the wave vector \mathbf{k} of the electron after ejection as

$$\rho = z(k)d\Omega, \text{ where} \quad (1.22)$$

$$z(k) = V \frac{m\hbar k}{(2\pi\hbar)^3}. \quad (1.23)$$

The electron can be treated as a plane wave once it has been ejected from the K shell, assuming the electron energy is large compared to the binding energy. This

makes the initial and final states of the electron

$$\psi_i = \left(\pi \left(\frac{a_0}{Z} \right)^3 \right)^{-1/2} e^{-\frac{RZ}{a_0}} \text{ and} \quad (1.24a)$$

$$\psi_f = V^{-1/2} e^{i\mathbf{k} \cdot \mathbf{R}} \quad (1.24b)$$

where $a_0 = \hbar^2/me^2$ is the Bohr radius of the hydrogen atom, \mathbf{R} is the position vector between the electron and the center of the nucleus and V is the volume of the "box", which will be taken to ∞ .

By assuming the interaction is occurring outside of the nucleus, the Hamiltonian can be assumed to be the electrostatic interaction between the protons of the nucleus and the electron or

$$H = \sum_{n=1}^Z \frac{e^2}{|\mathbf{R} - \mathbf{r}_n|} \quad (1.25)$$

where \mathbf{R} is as described above, and \mathbf{r}_n is the proton position from the center of the nucleus¹. Then the matrix element is

$$|\langle f | H_{int} | i \rangle| = \left(V \pi \left(\frac{a_0}{Z} \right)^3 \right)^{-1/2} \sum_{n=1}^Z \int e^{-i\mathbf{k} \cdot \mathbf{R}} \varphi_f^* \frac{e^2}{|\mathbf{R} - \mathbf{r}_n|} e^{-\frac{RZ}{a_0}} \varphi_i d\omega \quad (1.26)$$

with φ_i and φ_f being the initial and final wave functions of the nucleus, respectively. The integration must occur over both the coordinates of the ejected electron and over the coordinates in the nuclear wave functions, such that $d\omega = d^3R d\tau$ where τ represents the nuclear coordinates.

¹For this derivation, the electric multipoles are being considered, so only the electrostatic interaction is being used. By using the magnetic interaction instead, the magnetic multipoles can also be derived.

$|\mathbf{R} - \mathbf{r}_n|^{-1}$ can be expanded in terms of spherical harmonics such that

$$\frac{1}{|\mathbf{R} - \mathbf{r}_n|} = \begin{cases} \sum_{l=0}^{\infty} \sum_{m=-l}^l \frac{4\pi}{2l+1} \frac{r_n^l}{R^{l+1}} Y_{lm}(\Theta, \Phi) Y_{lm}^*(\theta_n, \phi_n), & \mathbf{R} > \mathbf{r}_n \\ \sum_{l=0}^{\infty} \sum_{m=-l}^l \frac{4\pi}{2l+1} \frac{R^l}{r_n^{l+1}} Y_{lm}^*(\Theta, \Phi) Y_{lm}(\theta_n, \phi_n), & \mathbf{R} < \mathbf{r}_n \end{cases} \quad (1.27)$$

where Θ and Φ are the polar vector of \mathbf{R} and θ_n and ϕ_n are the same for \mathbf{r}_n . The main contribution to the integral is going to come from $\mathbf{R} > \mathbf{r}_n$ in all cases but $l = 0$, as the term $\frac{R^l}{r_i^{l+1}}$ will go to zero. Substituting this into equation 1.26 gives

$$|\langle f | H_{int} | i \rangle| = \frac{e}{\left(V\pi \left(\frac{a_0}{Z}\right)^3\right)^{1/2}} \sum_{l=0}^{\infty} \sum_{m=-l}^l \frac{4\pi}{2l+1} \langle f | Q_{lm} | i \rangle J_{lm} \quad (1.28)$$

where $\langle f | Q_{lm} | i \rangle$ is the electric multipole matrix element and J_{lm} is the integral

$$J_{lm} \equiv \int e^{-\frac{RZ}{a_0}} e^{-i\mathbf{k} \cdot \mathbf{R}} R^{-(l+1)} Y_{lm}(\Theta, \Phi) d^3R. \quad (1.29)$$

Because of the earlier assumption of the outgoing electron being a plane wave by assuming the energy is sufficiently large, such that $ka_0/Z \gg 1$, $e^{-\frac{RZ}{a_0}} \simeq 1$ and the integral can be evaluated. Treating θ and ϕ as polar angles for \mathbf{k} ,

$$J_{lm} = 4\pi i^{-l} \frac{k^{l-2}}{(2l-1)!!} Y_{lm}(\theta, \phi). \quad (1.30)$$

Substituting all of this into 1.9, the transition probability is

$$w_{if} = 128\pi \frac{me^2 Z^3}{\hbar^2 a_0^3} \sum_{l=0}^{\infty} \sum_{m=-l}^l \frac{k^{2l-3}}{[(2l-1)!!]^2} |\langle f | Q_{lm} | i \rangle|^2. \quad (1.31)$$

There is a strong dependence on atomic number Z and the multipole order l . The magnetic transition follows a similar derivation, with a solution distinct from the electric one just derived. Thus, measuring the conversion coefficient of a transition

can be used to determine the multipolarity of the transition. The theoretical K -shell conversion coefficients for $l = 1, 2, 3$ are plotted in Figure 1.10 for comparison.

1.3.1 E0 Transitions

Like the electromagnetic radiation, $l = 0$ transitions are still forbidden in the internal conversion proof above, as the rate directly depends on $\langle f | Q_{lm} | i \rangle$, which goes to 0 for $l = 0$, which is relevant to transitions where the initial and final spins are the same. This, however, arises from the previous assumption of looking only outside of the nucleus. While the majority of the interaction between nucleus and electron occurs outside of the nucleus, when this goes to zero, as is the case for $l = 0$, the correction term from inside the nucleus must be taken into account, i.e. $R < r_i$. This leads to the second equation of 1.27. Revisiting equation 1.26, and setting $l = 0$ it becomes

$$|\langle f | H_{int} | i \rangle| = \frac{e}{\left(V\pi\left(\frac{a_0}{Z}\right)^3\right)^{1/2}} \sum_{n=1}^Z \int d\tau \varphi_f^* \frac{1}{r_n} \varphi_i \int_{R < r_n} d^3 R e^{-i\mathbf{k} \cdot \mathbf{R}} e^{-\frac{RZ}{a_0}} \quad (1.32)$$

As integration over \mathbf{R} extends only to very small numbers, the exponentials on the right can be approximated as 1, simplifying the integral to just $d^3 R$, making it $4\pi r_n^3/3$. The matrix element is now

$$|\langle f | H_{int} | i \rangle| = \frac{4\pi}{3} \frac{e}{\left(V\pi\left(\frac{a_0}{Z}\right)^3\right)^{1/2}} \sum_{n=1}^Z \int d\tau \varphi_f^* r_n^2 \varphi_i \quad (1.33)$$

The sum is of the order of magnitude of the square of the nuclear charge radius, denoted by \mathcal{R}^2 . Substituting 1.33 into 1.21, the probability for an electric multipole of order $l = 0$ becomes

$$w_{if} = \frac{32}{9} \frac{e^2}{\hbar c} Z^3 \left(\frac{\mathcal{R}^2}{a_0^2}\right)^2 \left(2 \frac{\Delta E}{mc^2}\right)^{1/2} \frac{mc^2}{\hbar} \quad (1.34)$$

where $\Delta E = E_f - E_i - B_K$ is the energy of the electron, with B_K indicating the atomic binding energy of the K -shell. At first glance, this indicates the $l = 0$ (E0) component is a measure of the change in the nuclear charge radius. The diagonal components of the E0 operator are measures of the mean-square charge radius [80]. The off-diagonal terms, which would be the terms probed by conversion electron spectroscopy are a direct probe of the nuclear dynamic. The interpretation of E0 components does not have a complete consensus [35].

One common way to rewrite the E0 transition probability is $\mathcal{W} = \Omega \rho^2$, where Ω are non-nuclear factors, i.e. $\Omega = \sum_i \Omega_i$ where i is the electron subshell, defined by Church and Wesener [24]. This contains the nuclear factors to ρ^2 , referred to as the nuclear strength parameter [23, 80]. In practice, ρ^2 tends to fall between $10^{-1} - 10^{-3}$, so it is standard to quote $\rho^2 \times 10^3$. For a given transition,

$$\rho_{if}^2 = \left| \frac{\langle f | \sum_n e_n r_n^2 | i \rangle}{e R_0^2} \right|^2 \quad (1.35)$$

This makes ρ^2 unitless, due to the division by $e R_0^2$, where $R_0 = 1.2A^{1/3}\text{fm}$ is the standard nuclear radial approximation. With this, ρ^2 can be scaled in terms of mass, allowing for comparisons across the nuclear chart [80]. The term $\langle f | \sum_n e_n r_n^2 | i \rangle$ shows two main contributions to the magnitude of ρ^2 : the nuclear matrix element of the initial and final states, and δr , the change in the nuclear radius. For large ρ^2 , both of these must be large. For small ρ^2 , the matrix element may be large, with only a small change in δr , or the opposite may be true. All of these possibilities give insight into the nuclear structure.

Experimentally, this strength parameter can be determined by the equation

$$\rho^2(E0) = q_K^2(E0/E2) \times \mathcal{W}(E2) \times \frac{\alpha_K(E2)}{\Omega_K(E0)} \quad (1.36)$$

where the E2 being referenced is the transition from the 0^+ state to the 2^+ state in

the ground state band. $\mathcal{W}_\gamma(E2)$ is the transition rate, the inverse of the partial mean life of the γ -component of the E2 transition. $q_K^2(E0/E2)$ is a ratio of the intensity of the E0 and E2 electrons and $\alpha_K(E2)$ is the theoretical conversion coefficient of the E2 transition. This electronic factor has an energy dependence. This strength parameter is directly related to the reduced transition probability $B(E0)$ by

$$B(E0) = \rho^2(E0)e^2R^4. \quad (1.37)$$

In a mixed transition with an E0 component, the E2 in equation 1.36 would be the E2 component of the transition, and would be calculated using the gamma rays and the theoretical E2 internal conversion coefficient[24]. A second mixing term, ϵ would be used to represent the ratio between the E0 electrons and E2 gamma-ray components, and would be defined as

$$\epsilon^2 = (\alpha_{exp} - \alpha(E2)) - \delta^2(\alpha(M1) - \alpha_{exp}) \quad (1.38)$$

where δ is the mixing ratio between E2 and M1, obtained from gamma-gamma directional correlation experiments, and the theoretical conversion coefficients for pure M1 and E2 transitions are used. δ is defined as the ratio of $(l + 1)$ to l , using the convention from Krane [45]. ϵ^2 is related to $q_K^2(E0/E2)$ via $\epsilon^2 = q_K^2(E0/E2)\alpha_K(E2)$.

These transitions have been predicted via a variety of models, including the shell model, collective models, shape mixing i.e. shape coexistence and intruder states[80]. Depending upon which phenomenon is responsible for a given E0 transition will change ρ^2 , of which estimates can be calculated. Many of these models lead to small E0 rates, the exception being shape mixing. Due to the dominant nature of shape mixing in E0 decays, it is difficult to compare these models with experimental ρ^2 values unless shape-mixing effects have been removed [80].

1.4 The Rare Earth Region: $N = 90, Z = 60$

The region around $N = 90, Z = 60$ is far away from the closed shells, and constitutes the largest region of deformed nuclei in the chart of nuclides. This region of nuclei has a variety of interesting structure features that are not fully characterized, including a large number of bound 0^+ states outside of the ground state [54]. Many of these states have not been fully characterized, including gamma-spectroscopy, electron-spectroscopy and lifetime measurements. With this large number of 0^+ states, electron-spectroscopy becomes vital, as transitions between two 0^+ states must be E0 in nature, which cannot occur via gamma radiation.

The isotopic chains of the rare earth region can be seen plotted against the magnitude of the deformation parameter β in Figure 1.6. There is a large amount of deformation in the region, and several isotopes with large numbers of 0^+ states, including ^{152}Gd , ^{156}Gd , ^{162}Dy , and ^{168}Er , all of which have more than 10 0^+ states below 3 MeV [54], with ^{154}Gd having the most, at 16 states. In addition, ^{158}Gd also has a large number of 0^+ states at 13 [47]. This makes the Gd isotopic chain excellent for studying the nature of these excited 0^+ states in deformed nuclei.

In section 1.1, collective excitations and shape coexistence were discussed. In these deformed nuclei, there are a large number of collective excitations, the nature of which is unknown. E0 transitions in the region have been seen to have large transition strengths, and have been associated with shape coexistence [80]. Confirming shape coexistence cannot be done with a single measurement. Heyde and Wood give an in-depth look at the spectroscopic fingerprints needed to identify shape coexistence [32]. Direct fingerprints for deformation include the diagonal E2 matrix elements, which can be done via Coulomb excitation experiments. Reduced transition probabilities for E2 transitions also show deformation. Such values largely require lifetime measurements, of which there are a variety of possible methods, dependent on the range of the lifetimes being measured, including doppler broadening

and doppler shift methods.

While an indirect fingerprint, with the large number of 0^+ states present in this region of the nuclear chart, E0 strengths become a vital spectroscopic fingerprint in interpretation and understanding [32]. These transitions give a model-independent view of the configurations underlying the transition. Other hints to shape coexistence include changes in masses, mean-square radii, and pair occupancies. Systematic patterns in the more direct fingerprints can also hint at possible shape coexistence. Fully understanding the 0^+ states in nuclei will require a systematic study of E0 transition strengths including those from $\Delta J \neq 0$.

CHAPTER 2

EXPERIMENTAL SETUP

2.1 Overview

For E0 transitions, two types of radiation must be measured: conversion electrons and gamma rays. As conversion electron transitions and intensities are usually tabulated as conversion coefficients, which compare the electron intensities to the respective gamma-rays from the transition, both conversion electrons and gamma-rays must be measured in this experiment. Further, to identify pure E0 transitions, the experiment must show no corresponding gamma rays.

Due to the high level density of nuclei in the rare-earth region, detectors with high resolution are favored for these experiments. The detectors must also be placed in a way that allows for simultaneous measurement of both particles and gamma-rays. For good resolution, high purity germanium (HPGe) detectors are the standard for gamma-rays. For electron detection, silicon-based detectors have the best resolution. The electron energies of interest range from less than 100 keV to over 1 MeV. Standard silicon detectors do not have an energy range that high for electrons, so lithium-drifted silicon (Si(Li)) detectors were used, which have a higher top-end electron energy.

To make these measurements, three separate experiments were performed at the Nuclear Science Laboratory (NSL) at the University of Notre Dame using the Internal Conversion Electron Ball (ICEBall) Spectrometer paired with two configurations of HPGe detectors: GEORGINA and Clovershare (Figure 2.1).

The $(\alpha, 2n)$ reaction favors populating states of low, even- J and positive parity. These states, including the 0^+ states, are the ones of interest in this study, making

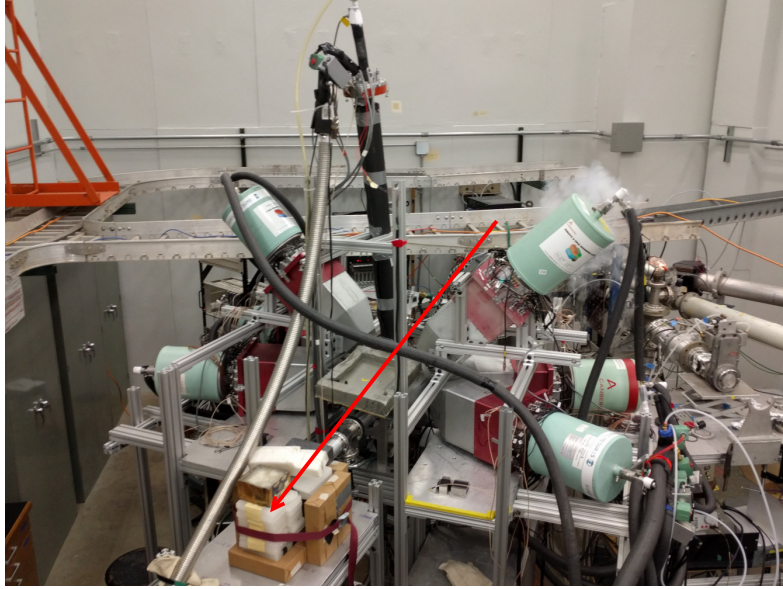


Figure 2.1. Image of the assembled experimental configuration with Clovershare. One HPGe detector is not visible from this angle. The red line indicates the beam direction.

this a natural reaction to select for the experiment. The Q value for this reaction is -14.774 MeV for ^{154}Gd and -13.638 MeV for ^{156}Gd , meaning an alpha beam of the necessary energy for the reaction to occur is well within the capability of the NSL.

A $\text{Sm}(\alpha, 2n)\text{Gd}$ reaction was used with different enriched targets to create the desired Gd isotope, with an α beam of 20 MeV. A bunched beam was used to create timing for coincidence identification. This beam energy was determined by a measurement using a natural Sm target, with ICEBall and two neutron detectors. TALYS was run to determine a range of energies to maximize the cross section of the desired reaction, while minimizing the neutron flux, as neutrons can damage HPGe detectors. Figure 2.2 shows the cross sections for the (α, xn) reactions for ^{154}Sm in the α energy range of interest. Beam energies from 16 MeV to 21 MeV were tested. Measurements were done at 1 MeV intervals. The cross section was calculated using conversion electron measurements from ICEBall, and compared with the neutron flux

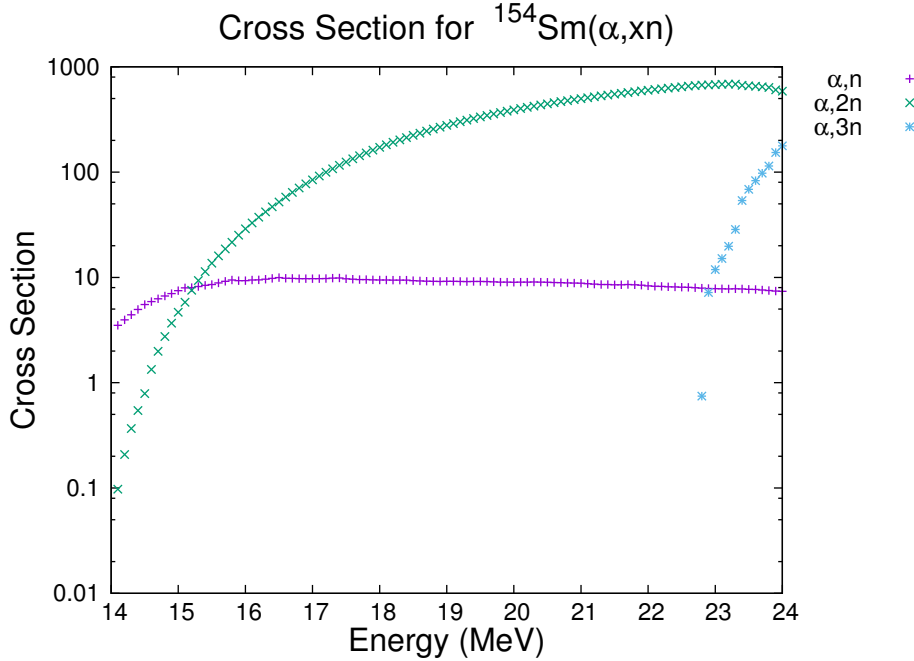


Figure 2.2. Comparison between the cross sections of the (α, xn) reactions on ^{154}Sm , calculated using Talys[44]. The less neutrons being lost, the lower the energy before the reaction occurs. Maximizing the cross section with respect to the neutron flux can be done by finding an energy where the desired reaction, $(\alpha, 2n)$ can be maximized, while minimizing the (α, n) and $(\alpha, 3n)$ reactions. Specifically, this means finding an energy before the $3n$ reaction has significant strength, while maximizing the $2n$ reaction, as the n reaction is nearly the same across the energy regime of interest.

at that energy.

Two different forms of electronics were used for the data acquisition system. The data acquisition systems used were based on the NSCL DAQ[56, 60]. The electronics used with GEORGINA were shaped by NIM modules before going through ADC VME modules to the computer [17, 48]. The Clovershare data used the XIA Pixie-16 modules, which take the place of the NIM and VME modules for shaping and converting the signals to digital data [82].

The digital files were converted to files for the analysis software using `evt2root` [74]. Analysis, reported in Chapter 3, was done using the CERN Root Data Analysis

Framework and Radware [16, 61].

2.2 Nuclear Science Laboratory at Notre Dame

The Nuclear Science Laboratory at the University of Notre Dame has been in operation since the 1934, with accelerators in operation since 1937. Currently, the NSL operates locally with three accelerators: the FN Tandem, the 5 MV Single-Ended Sta. Ana accelerator, and the 3 MV 9S Tandem. There is also a fourth accelerator, a 1 MV machine called CASPAR, located in the Homestake Mines in South Dakota. The experiments in this dissertation were performed on the FN Tandem. Figure 2.3 is the current layout of the NSL. The accelerator in the top right of the figure is the FN Tandem.

The FN Tandem has two ion sources: the Helium Ion Source (HIS) and the Multi-Cathode Source of Negative Ions Using Cesium Sputtering (MC-SNICS). Most elements can absorb the electrons from cesium to create negative ions. Helium cannot and needs a special source, as discussed below. For the experiments described, the HIS was used.

Due to the electron binding energy of helium, the HIS uses a duoplasmatron. Within the duoplasmatron, a thin tungsten wire is heated while surrounded by the source gas (helium). The tungsten wire emits electrons, and positively ionizes the helium. This helium is extracted from the duoplasmatron and focused by an einzel lens, where it then goes through the lithium charge exchange. This section of the HIS works as a small two stage acceleration system, although the charge exchange works by adding electrons instead of stripping them. The positively charged ions are accelerated through a lithium vapor, and some gain electrons, becoming neutral or negatively charged. Those ions that become negatively charged are accelerated out the other end of the HIS, before being sent to the FN Tandem. Figure 2.4 is a schematic of this system.

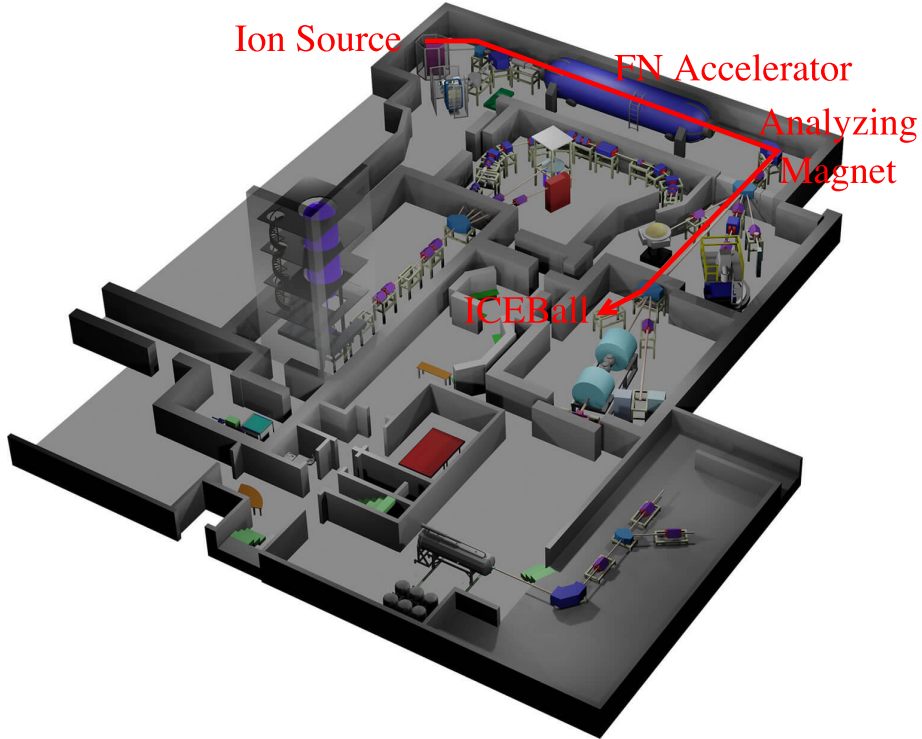


Figure 2.3. Current layout of the Nuclear Science Laboratory at Notre Dame. The red line indicates the path taken by the beam, from ion source, through the accelerator and analyzing magnet, before being sent to ICEBall.

The FN Tandem has been in operation since 1968. It is a Van de Graaff. Charging chains carrying a static charge deposit the charge on a terminal in the center of the machine. The charging chains are a pelletron type, upgraded from the original insulated rubber belt system in 2000. The pelletron chain consists of metal pellets connected using nylon, allowing for each pellet to be electrically isolated as it carries electrical charge to the terminal [55]. The beamline is kept at vacuum, but the area outside of the beamline and within the accelerator tank, is filled with a mixture of CO₂ and dry nitrogen gas, at approximately 200 PSI. To create a more uniform acceleration field, the terminal is brought to ground along the beamline using resistor-lined tubes. The resistors create a uniform electrical field down the tube, allowing

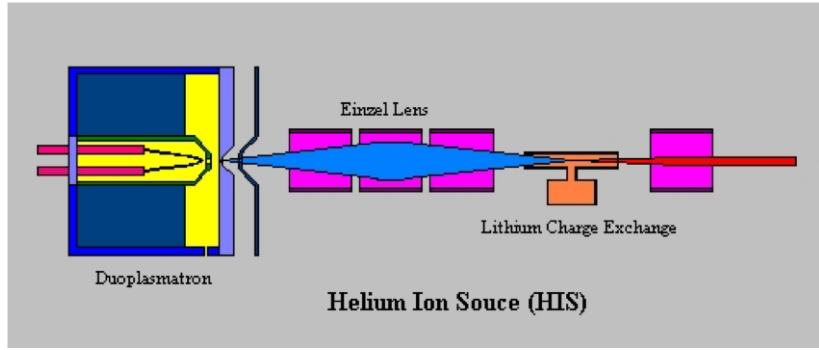


Figure 2.4. A schematic of how the Helium Ion Source works.

for uniform acceleration.

It is known as a tandem because the system is a two-stage acceleration. Negatively charged ions enter the system, accelerating toward a positively charged terminal shell. Inside of the shell, the ions go through carbon stripping foils $3 \mu\text{g}/\text{cm}^2$ thick, becoming positively charged as electrons are pulled off. The ions then accelerate away from the terminal for the second stage. The total energy gained by the ions is the terminal voltage times the quantity of one plus the final charge state.

After being sent through the accelerator, the beam goes through the analyzing magnet. This magnet is set for the specific species, energy, and charge state to bend 90 degrees to the experimental set ups.

2.3 Beam Production

Because of the use of HPGe detectors in an $(\alpha, 2n)$ reaction, the neutron flux must be minimized in comparison to the cross section of the reaction, as the (α, n) reaction is also open. The neutrons being produced will interact with everything, including the HPGe detectors, which can be damaged by the (n, γ) reaction on germanium. To do this minimization, a range of energies to test were selected by looking at theoretical cross sections in Talys[44]. These energies were then tested with natural Sm targets,

TABLE 2.1
ISOTOPE DISTRIBUTION OF NATURAL SAMARIUM

Isotope	Lifetime (y)	Abundance (%)
^{144}Sm	Stable	3.08
^{147}Sm	1.06×10^{11}	15.00
^{148}Sm	7×10^{15}	11.25
^{149}Sm	Stable	13.82
^{150}Sm	Stable	7.37
^{152}Sm	Stable	26.74
^{154}Sm	Stable	22.74

ICEBall, and two liquid scintillators to detect neutrons.

Samarium, as with many even-Z elements in the lanthanide region, has many stable isotopes. A total of five stable isotopes of Samarium exist, with two other isotopes being long-lived. Table 2.1 summarizes the abundances and lifetimes of the various isotopes found in natural Samarium. The two isotopes used our enriched targets are the ones that have the highest natural abundances, $^{152,154}\text{Sm}$.

2.3.1 Talys Calculations

Talys [44] is code for simulation of nuclear reactions dynamically with neutrons. Cross sections can be estimated using Talys to guide where an experiment may want to run to optimize production, as is the case presently.

Both natural and enriched Samarium targets were used and modelled within Talys. A range of energies, from 14 MeV to 24 MeV α -particles were run. These energies allowed a large number of potential reaction products from elastic, inelas-

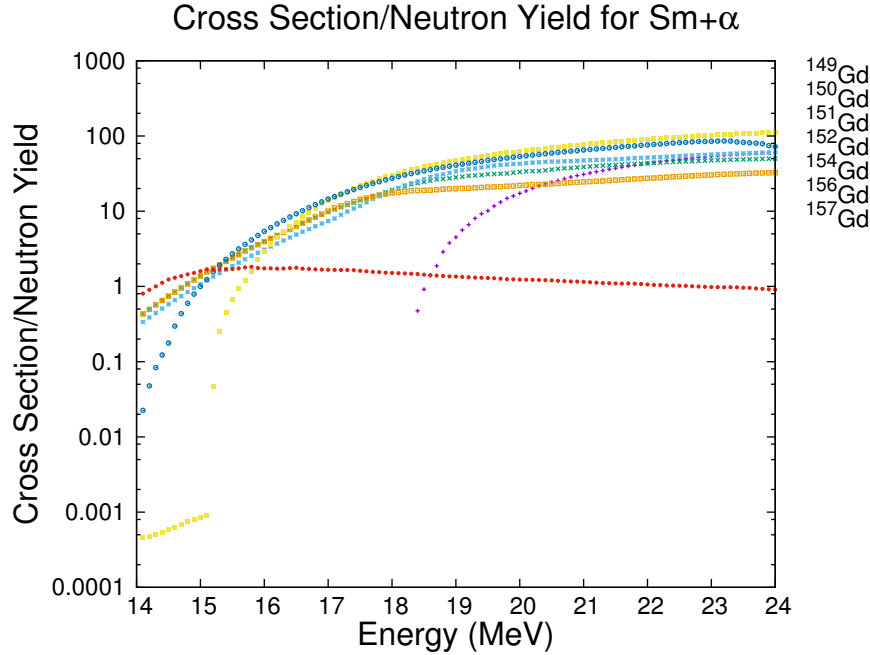


Figure 2.5. Talys calculation of the highest cross sections divided by the total neutron yield in the natural Samarium target. Only the largest contributors are included, as there are a large number of products possible between the isotopes of Samarium in the target and the reactions channels open for each. All of the largest contributors are Gadolinium isotopes. The ratios for the isotopes of interest appear to plateau around 20-22 MeV.

tic, transfer, and knockout reactions. Figure 2.5 is a visual summary of the strongest modelled reactions in the natural Samarium target. It was decided to test the energies between 16-21 MeV.

2.3.2 Test Analysis and Results

To test these Talys calculations and determine the best running energy, the cross section and neutron flux had to be measured at each energy without the use of the HPGe detectors. This was done using a natural Samarium target. ICEBall was used to measure the cross section by examining the K-electrons from ground-state band transitions in the reactions of interest, as the ground-state band is the most

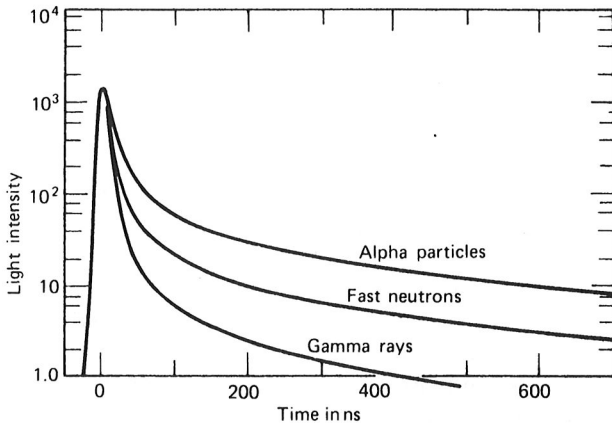


Figure 2.6. A cartoon illustration of pulse shape based on radiation type, in the same detecting material. The different types of radiation interact with the detecting material creating a fast and slow excitation. The ratio of these fast and slow excitations is based on the radiation, and expressed in the length of the decay tail. Picture taken from [42].

significantly populated band in the reaction. The DAQ described in Section 2.7.2 was used. Spectra from ICEBall were fit using the methods described in Section 3.1. The peaks were identified under the assumption the ground-state band transitions would be the strongest peaks in the spectra, and populate quickly.

The neutrons were measured using two NE213 liquid organic scintillators. In these detectors, it is possible to do pulse shape discrimination, as the neutrons have longer decay times than the gammas in these detectors due to the nature of the interaction with the scintillating liquid [42]. This produces longer trails in the detectors, leading to different decay shapes, see Figure 2.6.

By plotting the pulse height against the decay tail time, neutrons and gammas can be separated. In this setup, this was done by sending the signal to a Mesytec MPD-4 (Multi-channel Pulse Discriminator) [49]. This is a module built for pulse discrimination. It splits the signal, amplifies for the pulse height, and sends the other signal to a constant fraction discriminator (CFD), which converts the value to

17 MeV Neutron Detector

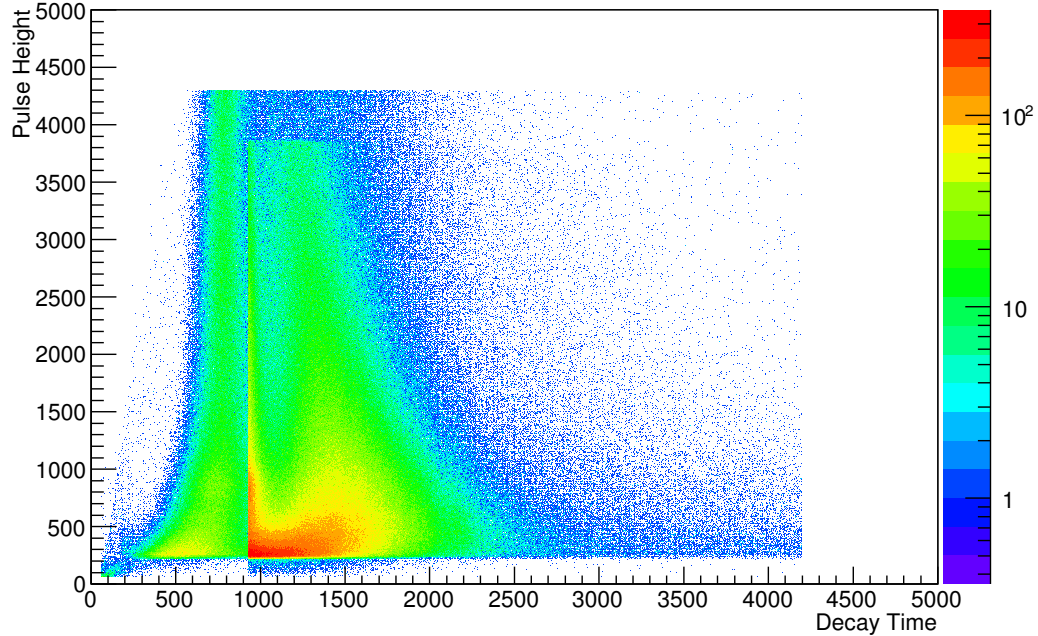


Figure 2.7. Plot of the pulse height vs the decay time in the NE212 detectors. Two clear areas are seen. The leftmost, with the shorter decay time, is the gammas, while the more spread out peak on the right is neutrons.

an amplitude using a time to analog converter (TAC). A CFD works by measuring the time it takes for a pulse to decrease to a fraction of its original height. Both of these signals (the pulse amplitude and the TAC amplitude) are recorded in the data. Plotting these values in a two-dimensional plot distinguishes the gammas and neutrons, as in Figure 2.7. There is a threshold cut off that removed most gammas from the spectrum.

Once the detectors were calibrated, each energy was run, with a total of four different targets across six energies. For each energy, the peaks in the electron spectra were identified with their respective isotopes, working under the assumption that only the lowest-lying states and the ground-state band would be populated significantly enough to see the electrons. These peaks are representative of the reaction cross

TABLE 2.2

 $4^+ \rightarrow 2^+$ K-ELECTRONS BY ISOTOPE

Isotope	Energy (keV)
^{154}Gd	197
^{156}Gd	149

section for that isotope. The K-electron of the $4^+ \rightarrow 2^+$ ground state transition for both nuclei of interest was clearly visible and clean at all energies, listed in Table 2.2. These K-electrons were used for the cross-section calculation.

To calculate the cross section, the formula

$$\sigma = \frac{Yield}{\delta x * Q * \epsilon} \quad (2.1)$$

was used, where δx is the target thickness, Q is the integrated charge, and ϵ is the efficiency of the Si(Li) detector at the electron energy. The *Yield* is the area under the curve.

This then had to be compared with the neutron production cross section. A bunched beam was used to get a time-of-flight. Calculating the neutron flux was done using the formula

$$\sigma_n = \frac{Neutrons}{\delta x * Q} \quad (2.2)$$

where δx and Q are the same as used for the cross section. The neutron yield is obtained by pulse shape discrimination, as seen in Figure 2.7. The left-most line is the gamma-flash that comes from the prompt gammas. The secondary gathering of counts, to the right, is the neutron peak. This area can be integrated over to get the number of neutrons seen during the run.

TABLE 2.3
SUMMARY OF ENERGY TESTS

Energy (MeV)	Cross Section (mb)		Neutron Flux (neutrons/s)	Ratio (σ/Φ_n)	
	^{154}Gd	^{156}Gd		^{154}Gd	^{156}Gd
16	0.126 (13)	0.334 (25)	1.247 (4)	0.101 (10)	0.268 (20)
17	0.554 (54)	1.273 (91)	2.142 (13)	0.259 (25)	0.594 (43)
18	3.124 (133)	5.427 (233)	4.281 (30)	0.730 (31)	1.268 (55)
19	3.030 (172)	5.327 (217)	4.205 (25)	0.721 (41)	1.267 (52)
20	5.618 (167)	9.438 (275)	5.806 (36)	0.968 (29)	1.626 (48)
21	7.438 (267)	12.827 (419)	7.410 (54)	1.004 (37)	1.731 (58)

Table 2.3 summarizes the results at each energy. Note, that the cross section is not reflective of the full cross section of the isotopes, but of the K-electrons for that transition. This ratio, of the cross-section to the neutron flux, was ultimately used to determine the running energy. The two higher energies, 20 and 21 MeV, have a ratio that agrees within error for both isotopes, indicating a plateau, in agreement with the expectation from Talys. Ultimately, 20 MeV was chosen for two reasons: to minimize any higher energy reaction channels, and because the neutron flux was lower in rate.

2.4 Electron Detection

Silicon detectors are a commonly used particle detector, with good energy resolution. The detectors are semiconductors, using a $p - n$ junction to create a depletion region, which becomes the active detection region[42]. Semiconductors have a bandgap around 1eV. A cartoon of the bandgap can be seen in Figure 2.8. The

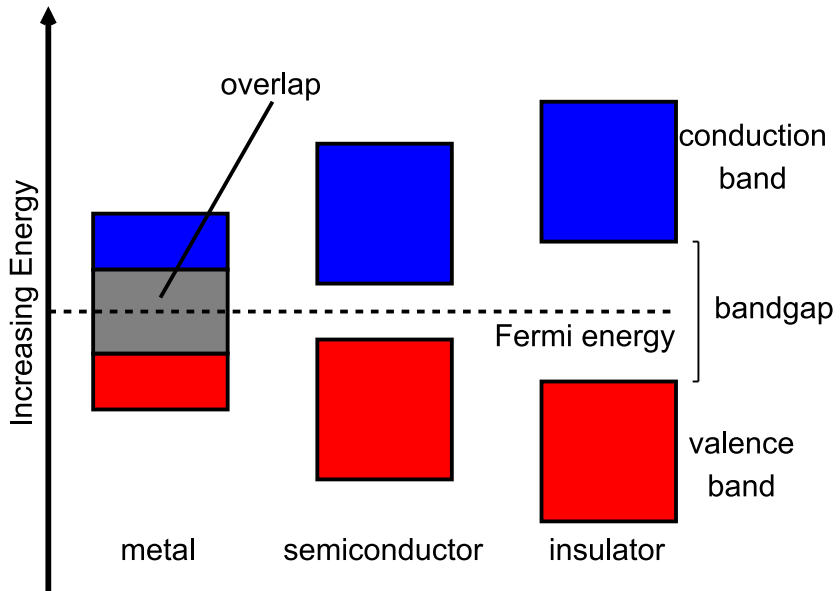


Figure 2.8. Cartoon of how the bandgap works for insulators, conductors, and semiconductors. Insulators have a large band gap, conductors overlap, and semiconductors have a small bandgap.

p–*n* junction takes two semi-conductor materials, one of *p*-type (an excess of holes in the valence band) and one of *n*-type (an excess of electrons in the conduction band) together. The holes and electrons mix, creating a depletion region, which becomes the active detection area. This region can be enlarged to some extent by putting a bias across the detector.

Because electrons are much more penetrative than protons or alphas of the same kinetic energy, it takes much more material to fully stop electrons. Silicon detectors only have active regions of 1mm-2mm thick, due to impurities, and cannot be made thick enough for the purposes of measuring electrons in the energy range of interest. Lithium-drifted silicon, colloquially Si(Li), detectors operate under the same principles as silicon detectors, but can be manufactured with larger depletion regions and a larger detectable energy range of electrons. These work by specifically introducing impurities, or doping, in this case lithium, to the detector, drifting it to create a

$p - i - n$ junction. The i region is also known as the intrinsic region, and is created by the drifting of the lithium, creating a highly purified region. The thickness of these detectors is only limited by the distance across which the lithium can be successfully drifted.

2.4.1 Internal Conversion Electron Ball Spectrometer

The Internal Conversion Electron Ball Spectrometer (ICEBall) was developed at the University of Pittsburgh by Metlay et al. [52, 53]. Originally at the Spin Spectrometer at Oak Ridge National Laboratory, it was later stationed at the Wright Nuclear Structure Laboratory at Yale University with the YRAST Ball, until being brought to the University of Notre Dame and stationed in the Nuclear Science Laboratory West Target Room, on a dedicated beamline [8].

Originally designed to go inside of large gamma detector arrays, ICEBall consists of six mini-orange spectrometers, cooled using liquid nitrogen for ideal energy resolution. The liquid nitrogen is administered using an autofill system with two thermal sensors for a start and stop signal. When the sensor closest to the detectors warms enough, liquid nitrogen is pumped into the system. A second sensor at the top of the dewar is used to stop the fill of liquid nitrogen before it overflows. This system fills in 15 to 20 minute intervals. ICEBall can be seen in Figure 2.9, open for servicing.

The Si(Li) detectors inside of ICEBall are 5 mm thick, with a surface area of 750 mm^2 [53]. Table 2.4 summarizes the locations of the six Si(Li) detectors inside of ICEBall, using spherical coordinates. A thin aluminized mylar foil is placed in front of the Si(Li) detectors to block low-energy electrons and δ -rays that successfully make it past the mini-orange filter (discussed in Section 2.4.1.1).



Figure 2.9. Image of ICEBall, open for servicing. The beam would go from left to right in the picture. The target ladder is blank, in the center of ICEBall.

TABLE 2.4
ICEBALL DETECTOR LOCATIONS

Detector	θ	ϕ
1	90	79.2
2	270	100.8
3	172	129.9
4	198	31.7
5	18	148.3
6	355	50.1

The beam axis is the z-axis. θ is the angle in the xy-plane, where 0 degrees is beam left. ϕ is the azimuthal angle, with respect to the beam axis. All values are in degrees.

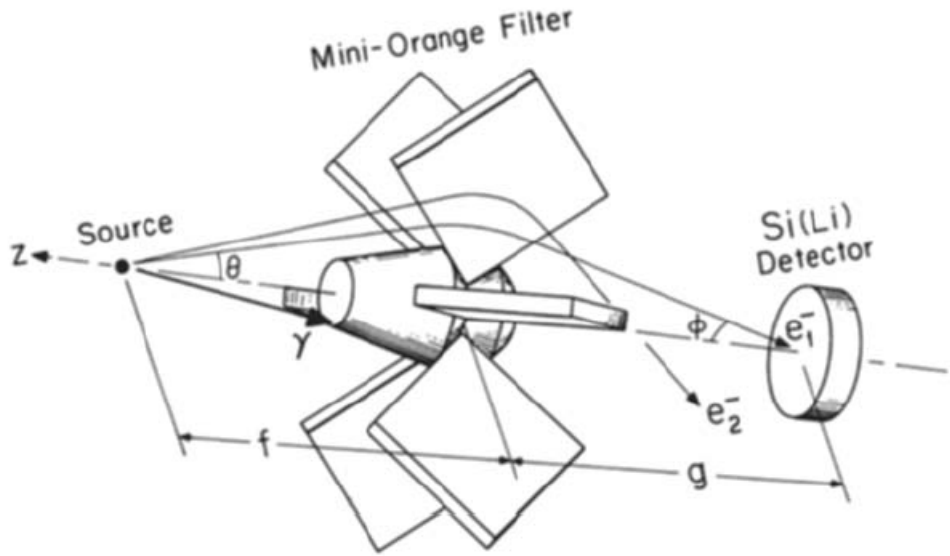


Figure 2.10. Graphic of the mini-orange filter. The central blocker keeps γ -rays from hitting the detector. The magnets bend electrons toward the detectors, and positrons away from the detectors. Being permanent magnets, they are optimized for a range of electron energies, and can cause overbending or underbending of electrons outside of that energy range, making the magnetic filter a factor in the efficiency. Taken from [53].

2.4.1.1 Mini-Orange Spectrometer

Between the detectors and the target are mini-orange filters. First designed in the 1970s, mini-orange filters are a permanent magnet array surrounding a high-Z material, as seen in Figure 2.10 [37, 38]. In ICEBall, this material is tungsten, and the magnets are made of SmCo₅, and arranged in groups of 3. The tungsten acts as a blocker, lowering background from the target that can be due to γ rays and heavy charged particles. The magnets create a field that bends electrons toward the detector, while bending positrons away from the detector, further lowering background noise.

Compared to conventional spectrometers that sweep over electron energies by changing the magnetic field of the spectrometer, the mini-orange spectrometers are

TABLE 2.5
ICEBALL MAGNETIC STRENGTHS WITH GEORGINA

Detector	Filter	Strengths
1	M13	815,740,830
2	M15	939,911,949
3	M21	850,875,900
4	M14	972,911,992
5	M18	856,913,963
6	M22	845,900,900

Magnetic strengths of the mini-orange filters used in the GEORGINA experiments, listed in Gauss. All the magnetic strengths are similar and geared for efficiency peaking at approximately 300-400 keV.

able to cover a wide range of energies at once. A drawback of this is the permanent magnets. The field is optimized for a range of energies, and must be pre-selected before the experiment. Switching magnets mid-experiment is not feasible, due to the downtime needed to warm-up the system, bring it to atmosphere, replace the filter, and then return the system to data taking conditions. Additionally, the efficiency of the system is a convolution of the detector's efficiency and the mini-orange filter in front of it, meaning each configuration must have a separate efficiency measurement. Tables 2.5 and 2.6 summarize the magnetic configurations of the mini-orange filters used in the experiments. The higher the magnetic strengths, the higher energy the peak efficiency of the mini-orange spectrometer, seen in Figure 2.11. For the GEORGINA configuration, the magnetic strengths were all of similar values. For the Clovershare configuration, the filters were replaced on three detectors to enhance electron efficiency at higher energies.

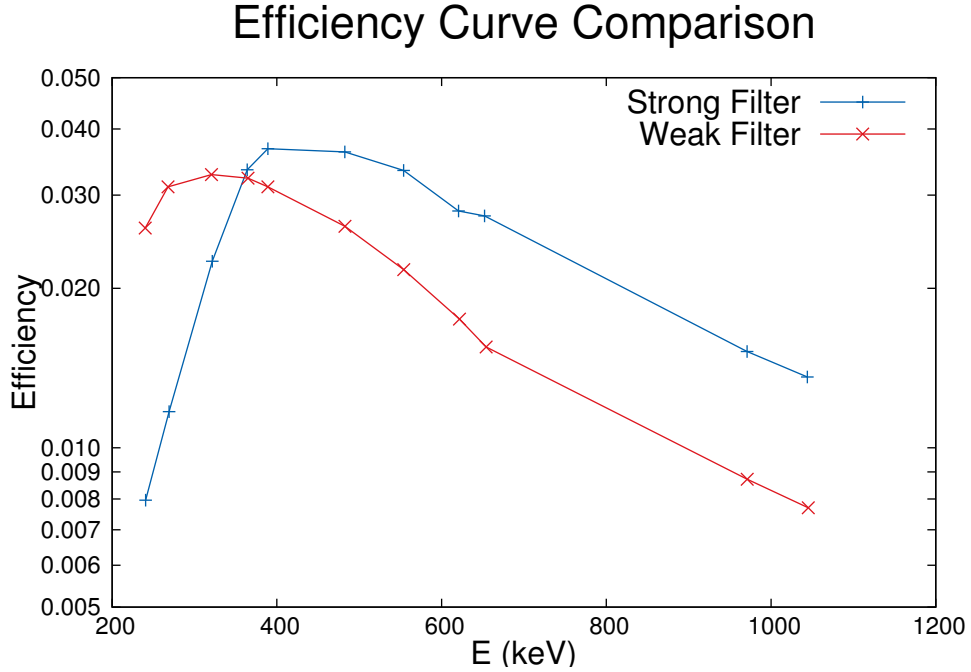


Figure 2.11. An efficiency comparison of magnetic filters of two different strengths. The weak filter has been weakened by 70% compared to the strong filter, using the Pitt split-pole spectrograph. Data from [52].

TABLE 2.6
ICEBALL MAGNETIC STRENGTHS WITH CLOVERSHARE

Detector	Filter	Strengths
1	M13	815,740,830
2	M20	1228,1292,1265
3	M21	850,875,900
4	M2	1411,1420,1410
5	M16	1286,1340,1285
6	M22	845,900,900

Magnetic strengths of the mini-orange filters used in the Clovershare experiments, listed in Gauss.
The magnetic strengths are mid-energy range and high-energy range for efficiency.

TABLE 2.7
ICEBALL CALIBRATION SOURCES

Source	Activity	Electron Energy (keV)	Intensity (%)
^{133}Ba	0.331(7) μCi ¹	240.413	0.331
		266.868	0.698
		320.032	1.308
		347.866	0.370
^{207}Bi	0.306(8) μCi ²	481.697	1.562
		554.4	0.469
		975.657	7.243
		1048.1	1.838

Calibration source information for ICEBall. The energies and the respective intensities are listed for each source. Intensities are taken from [77]. The intensity of the 347 keV line in ^{133}Ba is both the 384K and 356L intensities combined.

2.4.2 Calibration

ICEBall is energy and efficiency calibrated using two sources: ^{133}Ba and ^{207}Bi . The specific properties of the two sources are listed in Table 2.7. The ^{207}Bi covers the high-energy regime, with lines around 500 keV and 1000 keV. The ^{133}Ba covered energies from 200 to 400 keV. Both sources are low activity, preventing incomplete or overlapping charge collection from hindering the resolution of the detectors during calibration runs.

The energy calibration is assumed to be quadratic in nature, although both linear and quadratic calibrations are performed. Figure 2.12 shows both of these fits and

¹Measured on May-4-2012

²Measured on May-4-2012

their respective residuals for one of the Si(Li) detectors. These values are summarized in the next chapter for each experiment.

The efficiency calibration is fitted to equation

$$\ln(\epsilon) = p_1 + p_2 \ln(E) + p_3 E. \quad (2.3)$$

The efficiency is a convolution of the magnetic configuration and the inherent detector efficiency. Using the efficiency points, the analytic expression for the efficiency was determined empirically in previous work [8]. These experimental values are summarized in the next chapter for each experiment.

2.5 Gamma Detection

Gamma radiation is highly penetrating, making semiconductor detectors of normal purity unusable, as they have limitations on the depth of the depletion region that are nowhere near the necessary depths needed for fully stopping gamma radiation. The depletion depth is inversely proportional to the number of impurities in the material [42]. High-purity germanium, also known as intrinsic germanium, detectors decrease these impurities to increase the depletion depth, resulting in depths of several centimeters.

Like other semi-conductor detectors, there are dead zones that attenuate the radiation. Generally, this attenuation is negligible above 200 keV. These detectors have a high resolution due to the small bandgap of 0.7 eV in germanium. This small bandgap comes at a price, and HPGe detectors can only be operated at liquid nitrogen temperatures, as putting any voltage on a room temperature HPGe would result in high leakage currents and noise, making detection impossible.

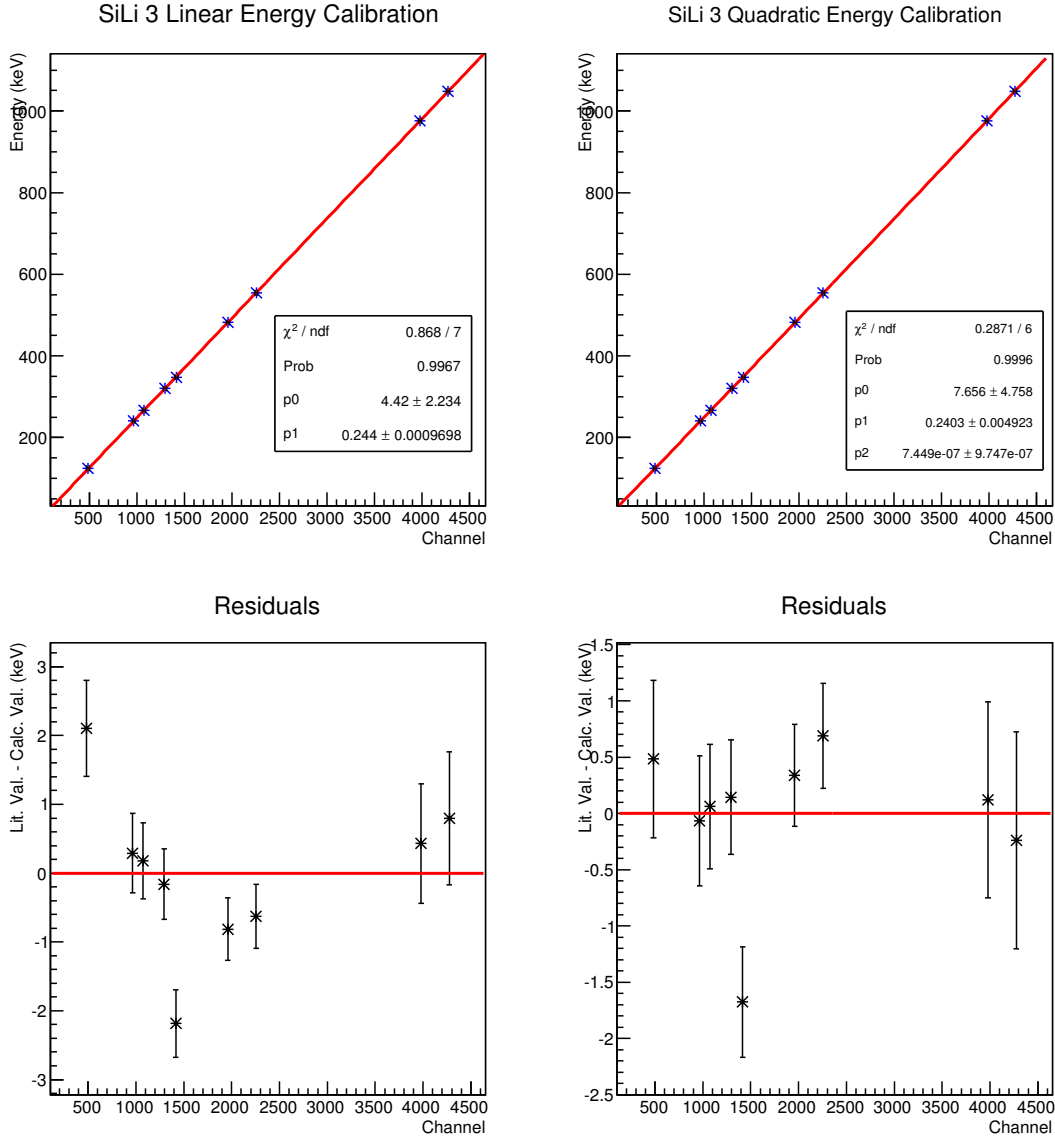


Figure 2.12. Linear and quadratic energy calibrations of one Si(Li) detector, using the electron energies listed in Table 2.7. The top graphs show the calibrations, while the graphs beneath show the respective residuals. The calibration is in much better agreement in the quadratic fit, as seen in the residuals.



Figure 2.13. An example of one of the GEORGINA detectors. The crystal is at a 90° from the cold finger, allowing the long side of the crystal to be placed next to the target, to optimize solid angle coverage. In the experiment, the circular face of the crystal was placed toward the target.

2.5.1 GEORGINA

The GErmanium detector Online aRray for Gamma ray spectroscopy in Nuclear Astrophysics (GEORGINA) is a compact array of high-purity germanium (HPGe) detectors for γ -ray experiments[36]. The detectors are 100% relative efficiency (as compared with a $3'' \times 3''$ NaI detector at 1332 keV). These detectors were designed for use with low cross-section astrophysical capture reactions, meant to cover a large solid angle. There are a total of five detectors. The detectors were designed with the crystal at a 90° from the cold-finger, as seen in Figure 2.13.

One of the two detectors had Bismuth Germanate (BGO) detectors from Argonne National Laboratory around it to cut down on background from incomplete charge collection. BGO detectors have a high efficiency, but poor resolution, and are good to use as a veto system. In the event that a gamma-ray does not deposit its full energy in the HPGe crystal, the BGO detectors surrounding the crystal should pick up the remaining energy. This indicates the event was incomplete in energy and should be excluded from the data. This is a manual cut made during the analysis procedure by looking at the data from the BGO detectors.



Figure 2.14. Example of one of the CloverShare detectors.

2.5.2 CloverShare

CloverShare is a group of nine HPGe clover detectors with BGO shields, that originated at Yale University as part of the YRAST Ball array [9]. They were sent to various laboratories and universities for series of experiments, including the NSL. Two campaigns of experiments were run with CloverShare, each one involving an ICEBall experiment.

The CloverShare detectors are large, segmented HPGe detectors, with fitted BGO shields, seen in Figure 2.14. Each detector is segmented into four crystals, resembling a clover. Due to the "add-back" capability of these detectors, summing over the close-proximity crystals, the detectors each have a total relative efficiency $\tilde{1}50\%$, whereas each individual crystal is approximately 20% efficient. In the first of the two experiments, 7 detectors were used. In the second, 5 were used, as two experienced pre-amplifier problems during the previous campaign. The detectors used biases between -3000 and -4000 V, and were kept cold using a liquid nitrogen autofill system.

2.5.3 Calibration

Both sets of detectors were calibrated using a ^{152}Eu source, in addition to the ICEBall sources. The information about the sources is in Table 2.8. The ^{152}Eu source was not designed to sit perfectly on the target ladder, while the two ICEBall sources were. So, even though the Eu source was attached to the target ladder for the GEORGINA calibration, using it as a measure of absolute efficiency was not possible. For the CloverShare calibration, the ^{152}Eu source was placed on the individual detectors instead of centered in ICEBall. To use the ^{152}Eu for the efficiency, a linear extrapolation of the efficiency of the 344 keV line was done using the 303 keV and 356 keV lines in ^{133}Ba . All points in the Eu were then scaled based on this. Additionally, several background lines could be used to extend the energy calibration up to 2700 keV. The energy calibration was fit to a polynomial, and fits up to the fifth order were done to find the best calibration without overfitting. For examples of these fits, see the next chapter. All points in the Eu were then scaled based on this. A characteristic fit of the efficiency of these detectors can be seen in Figure 2.15.

The efficiency calibration is fitted to equation

$$\ln(\epsilon) = a_0 - (a_1 + a_2 \times e^{-a_3 \times E}) \times E^{-a_4 \times E} \times \ln(E) \quad (2.4)$$

A characteristic fit can be seen in Figure 2.15. The CloverShare detectors were also calibrated using a ^{56}Co source that was created on the FN accelerator days before the experiment. The information about the source is in Table 2.9.

As the clovers are comprised of four separate crystals, the efficiency was taken for the individual leaves, and once the detectors had been calibrated, they were

³Measured on May-4-2012

⁴Measured on May-4-2012

⁵Measured on Mar-16-2016

TABLE 2.8
GEORGINA CALIBRATION SOURCES

Source	Activity	γ Energy (keV)	Intensity (%)
^{133}Ba	0.331(7) μCi^3	80.997	0.3406
		276.398	7.164
		302.853	18.33
		356.017	62.05
		383.851	8.94
^{207}Bi	0.306(8) μCi^4	569.702	97.75
		1063.662	74.09
^{152}Eu		121.7825	28.65
		244.6989	7.582
		344.281	26.6
		411.115	2.262
		443.965	3.125
		778.903	13.017
		867.39	4.26
		964.055	14.758
		1085.842	10.062
		1089.7	1.738
		1112.087	13.587
		1408.022	20.945

Calibration source information for GEORGINA. The energies and the respective intensities are listed for each source. Intensities are taken from [77]. The ^{152}Eu does not have activity and intensity, as it was normalized to the ^{133}Ba .

TABLE 2.9
 ^{56}CO CALIBRATION INFORMATION

Activity	γ Energy (keV)
6.44 μCi^5	846.77
	977.372
	1037.843
	1175.101
	1238.288
	1360.212
	1771.357
	2015.215
	2034.791
	2598.5

Energies used in ^{56}Co for calibration, as well as activity.

summed together. Figure 2.16 shows the comparison. As is expected, there is a small improvement in the higher energies. This is due to the summation of otherwise incomplete charge collection due to compton scattering within individual crystals. This did cause the efficiency at lower energies to appear lower, but this is due to the summing of cascades of energies over the segments. The summed crystals were used for analysis, and will be used in spectra from here on forward.

Each leaf of the clovers was energy calibrated. An unusual trend in the residuals was found in all cases, as seen in Figure 2.17. This trend could not be corrected for by using a higher-order polynomial, as is usually the case for integral non-linearities in multi-channel analyzers [42]. Instead, this appears to be a differential non-linearity in the electronics, resulting in discontinuities. The electronics used for the experiment

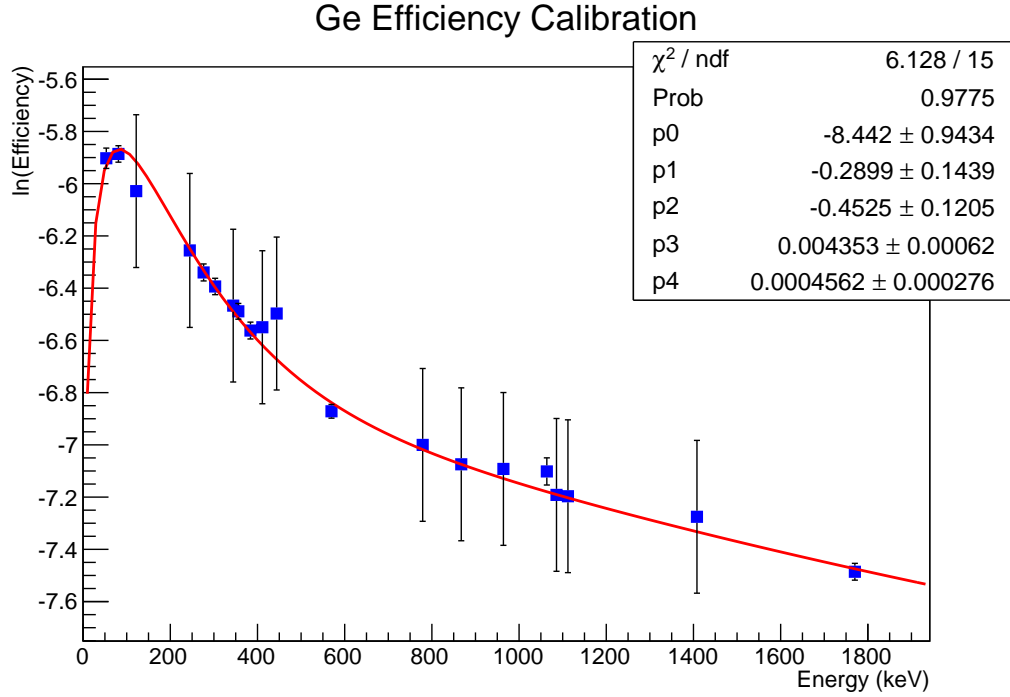


Figure 2.15. A characteristic fit of the Clovershare detector efficiencies. The points with large error bars are the ^{152}Eu points, as the scaling of the points caused a large uncertainty, compared to the ^{207}Bi and ^{133}Ba .

are not primarily used with detectors of this sensitivity.

2.6 Target Fabrication

Electrons must escape the target for detection. All materials have some stopping power for radiation, based on the material, thickness, and type of particle. The Beta-Bloch formula can be used to calculate this stopping power, with several programs, including SRIM, created to make and tabulate these values[86]. A thicker target causes energy loss and straggling effects, blurring out the conversion electron spectrum, meaning a thinner target is a more ideal situation.

Enriched, self-supporting Samarium targets were used for this experiment. Table 2.10 has the enrichment and thickness of the targets used. The material started as

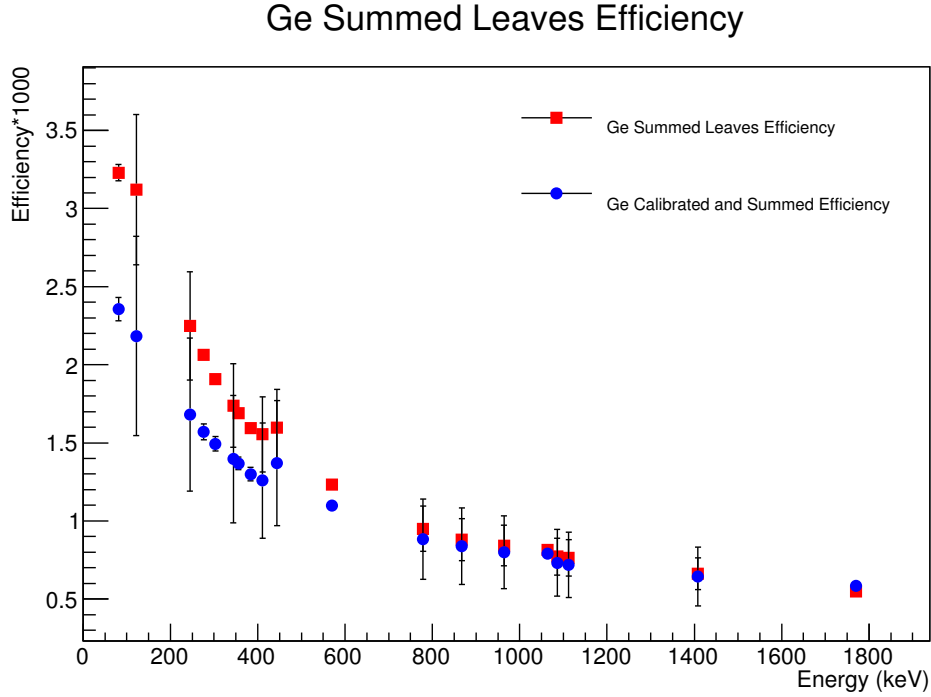
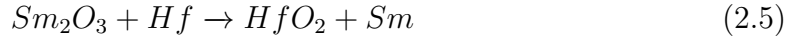


Figure 2.16. Efficiency of a CloverShare detector, with the individual leaves' efficiency summed together, compared to the efficiency of the leaves calibrated and summed together. The different colors/shapes indicate the different sources, as labeled.

Sm_2O_3 . Using the reaction



at a temperature of 1520-1820 K the Samarium was extracted as a metal [25]. Once cooled, it was rolled as thin as possible. Samarium easily oxidizes, stagnating the rolling process, as too much work on the material at once could cause instantaneous oxidation, resulting in the loss of the target. Rolling had to be done incrementally, giving the material time to rest.

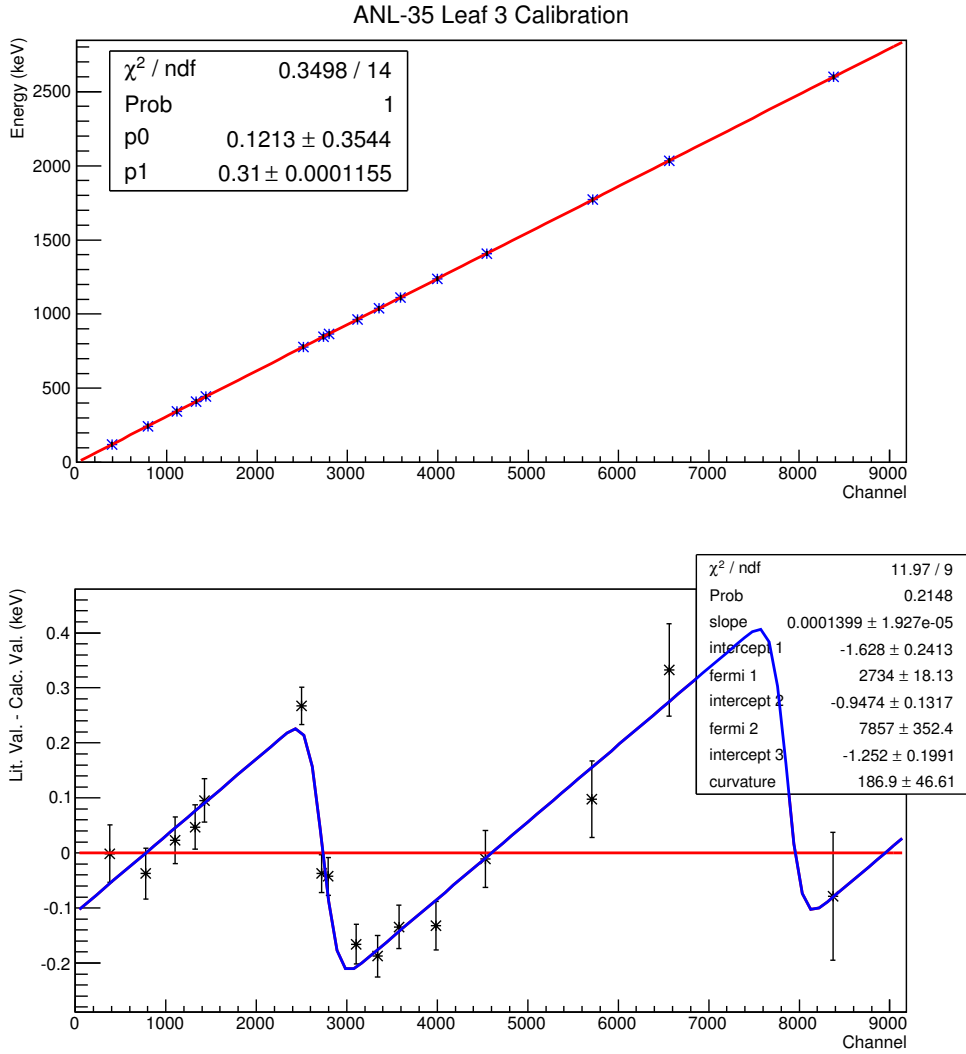


Figure 2.17. A look at the energy calibration of an individual leaf in an HPGe Clover detector. The upper graph is a linear calibration. The lower graph is a look at the residuals. For HPGe detectors, ± 0.4 keV is not a good energy calibration. Here, the sawtooth fit that was derived from the differential non-linearity in the electronics is seen fitted to the data.

TABLE 2.10
TARGET ENRICHMENT AND THICKNESS

Isotope	Enrichment (%)	Thickness (mg/cm ²)
¹⁵² Sm	> 98	1.44
¹⁵⁴ Sm	> 98	1.7

2.7 Experimental Configuration and Operation

2.7.1 Experimental Beam Operation

The experiments with GEORGINA were done using a bunched beam, creating a set timing signal to help with coincidence. The beam was bunched before the accelerator, with a time separation of 600 ns between bunches and a full-width half-maximum of 16 ns for the bunch. The timing of these bunches is shown in Figure 2.18. Clear separation in of the bunches is visible. The accelerator was run with a terminal voltage of 6.64 MV, with ⁴He²⁺ being sent through the machine, resulting in a beam of energy 20 MeV, including the initial 60 kV kick from the HIS.

2.7.2 GEORGINA Configuration and Electronics

While the GEORGINA detectors were designed for large efficiency up to 12 MeV, they were used in this experiment for energies up to 4 MeV. Two GEORGINA detectors were used in the experiment with ICEBall. The location of the detectors is given in Table 2.11. They were placed with the face of the detector against ICEBall.

The ICEBall-GEORGINA data was taken the electronics set-up from previous experiments[8]. Signals from the Si(Li), HPGe, and BGO detectors were split into two signals, one for timing and one for energy, as seen in Figure 2.19. For the Si(Li) and

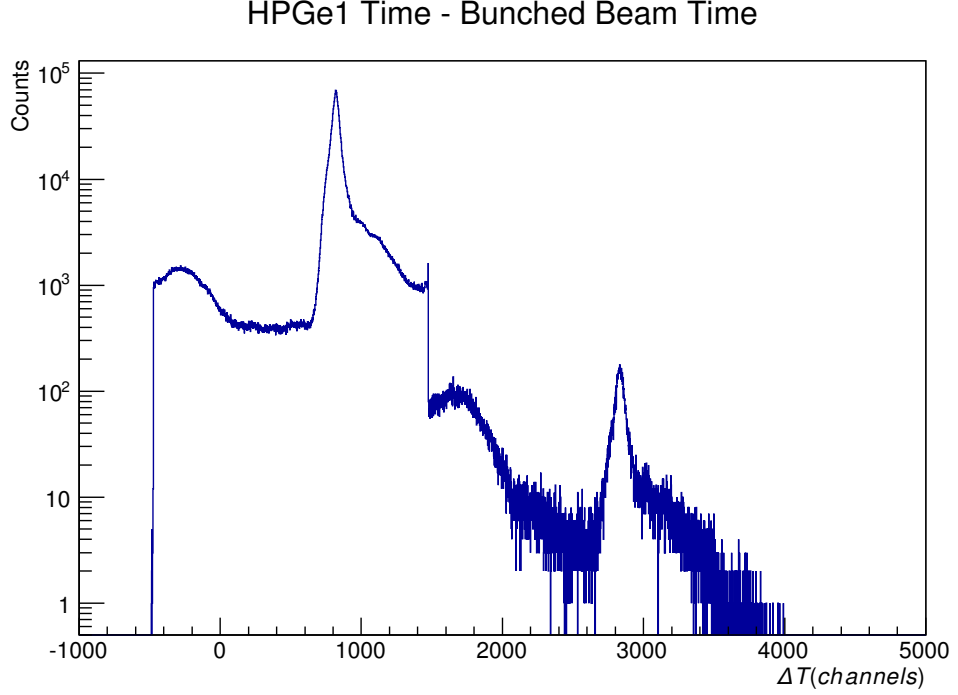


Figure 2.18. Plot of the HPGe 1 detector time minus the buncher time. Two distinct peaks can be seen in the spectrum, the main timing peak close to channel 800, and the much smaller secondary peak, coming from a second, later bunching signal. The bunching signal only acts as a stop signal for the timing. It can also be used as a veto, as events without a valid buncher time are not real, or are background.

HPGe, the energy signals are run through an amplifier NIM (Nuclear Instrumentation Modules) before being fed into the Mesytec analog-to-digital converter (MADC-32) VME (Versa Module Europa) bus module for analog-to-digital conversion [48]. This module has 13 bit resolution. The timing signals went through a Timing Filter Amplifier (TFA) NIM and a Constant Fraction Discriminator (CFD) NIM to clean the signal before being converted using a Caen V775 time-to-digital converter (TDC) module, with 12 bit resolution[17]. The TFA module shapes the pulse signal and amplifies it. The CFD module allows for triggering on the same part of the slope of a signal, regardless of the height of the signal, giving more consistent timing. A

TABLE 2.11
GEORGINA DETECTOR LOCATIONS

Detector	θ	ϕ
1	0	90
2	180	90

The beam axis is the z-axis. θ is the angle in the xy-plane, where 0 degrees is beam left. ϕ is the azimuthal angle, with respect to the beam axis. All values are in degrees.

third module, the Caen V830 32 Channel Latching Scaler, was used to keep track of detector rates for deadtime, beam current, and trigger rates[18] via a second signal sent from the CFD module. Logic was done using a third signal from the CFD module and logic NIM modules that employ an emitter-couple logic circuit. These can be adjusted for either "and" or "or" logic. This logic created the trigger that acted as the start signal. The data structures of the events in these modules are explicitly written in Tables 2.13, 2.14, 2.15.

The BGO detectors went through an amplifier before being fed directly into the MADC-32. Both the Si(Li)s and the HPGe detectors went into a preamplifier before going into an amplifier, and then the MADC-32. The amplifier allowed for the adjustment of the gain, to optimize the energy regime of interest. The timing signals were sent through a TFA before going through a CFD and being delayed and sent as timing stop signals, as well as being recorded into the scalers. The stop signal was delayed by 500ns to prevent self-triggering. Start timing signals were put into a logic coincidence for the trigger. The trigger could be adjusted if the count rate were too high, but the ideal case was the "OR" coincidence, where a Si(Li) or HPGe detector could trigger the start. When this occurred, the signal was sent to a trigger, which sent the TDC a start signal. Stop signals could come from any of the three types of

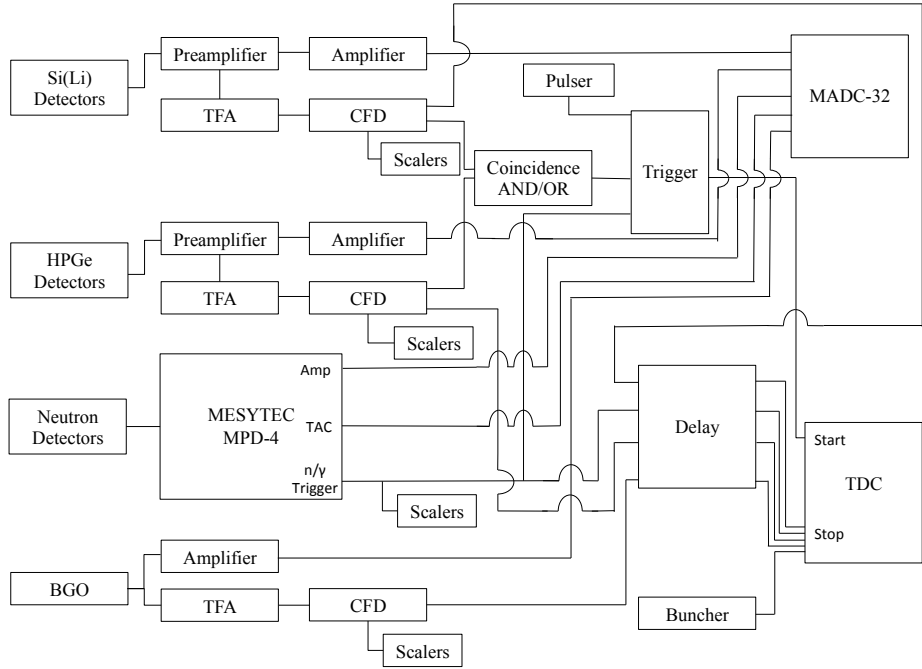


Figure 2.19. A schematic of the electronics for the ICEBall-GEORGINA set up. See section 2.7.2 for a detailed explanation. Taken from [8].

detectors, or the bunched beam being used.

The data was collected from the VME modules using the Michigan State University NSCL data acquisition system (DAQ)[56]. The data file, known as an event or "evt" file, is only compatible with the analysis software SpecTcl[56]. For online analysis, SpecTcl was used. However, for the purposes of gating and fitting, it is inadequate. These evt files were instead converted into "root" files, for use with the CERN Root Data Analysis Framework[16]. This open source software is programmable through C++, allowing for a robust set of features. This conversion was done using a program called `evt2root`[74].

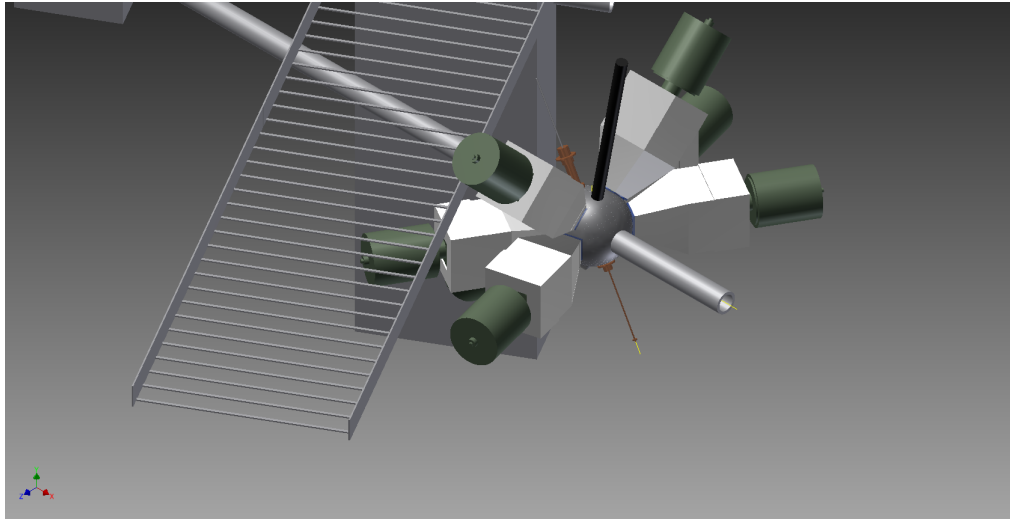


Figure 2.20. ICEBall modeled in Autodesk Inventor [5] with the Clovershare detectors placed around it in locations to optimize efficiency. Once ICEBall had been modeled, the detectors were moved around to make sure they were not behind the tungsten blockers. The beamline was also modeled to know where obstructions existed that prevent the Clovershare detectors from being placed there.

2.7.3 Clovershare Configuration and Electronics

Due to the fixed nature of the ICEBall detectors, the clovers were limited in the angles they could be placed at to optimize efficiency. With the tungsten blockers in front of the Si(Li) detectors to block gamma-rays and x-rays, placing the clovers behind these detectors would drastically reduce efficiency. The system was modeled in AutoDesk Inventor [5] to visualize the detector placement, and find an ideal setup to optimize the HPGe detectors. Figure 2.20 shows the resulting model and placements, as well as several unmoveable obstructions, like cable trays, that needed to be worked around. Figure 2.1 shows the final placements for the seven-detector configuration, in the experimental hall. Table 2.12 lists the detector placements for the seven and five detector configurations, labeled as Experiments 1 and 2.

The electronics used for the Clovershare series of experiments were designed for

TABLE 2.12
CLOVERSHARE DETECTOR LOCATIONS

	Experiment 1		Experiment 2	
Detector	θ	ϕ	θ	ϕ
ANL-35	270	145	270	145
LBL-7	0	111	0	111
ANL-23	0	66	Not Used	
LBL-6	180	111	Not Used	
LBL-10	180	66	180	71
ANL-31	45	90	45	90
ANL-18	135	90	180	111

The detectors are listed by identification name. The angles for the detectors are given for both experiments run with the Clovershare detectors. ANL-23 and LBL-6 were not used in the second experiment due to preamplifier issues. The beam axis is the z-axis. θ is the angle in the xy-plane, where 0 degrees is beam left. ϕ is the azimuthal angle, with respect to the beam axis. All values are in degrees.

use with the High Efficiency TOTal absorption spectrometeR (HECTOR), a NaI(Tl) detector array[66]. The HECTOR data acquisition system is based on the Michigan State University NSCL digital data acquisition system (DDAS). This system uses three XIA Pixie-16 modules [82] which are 16 channel 14-bit 100 MSPS digitizers. The data structure of this system can be seen in Table 2.16. Signals from detectors were fed directly from the preamplifiers to the Pixie modules, which did the amplification, shaping, timing, and logic triggers within the module through adjustments on the data acquisition computer, seen in Figure 2.21. In the ICEBall setup, these functions were done using the NIM electronics. NaI(Tl) detectors have far lower resolution than HPGe detectors, so the differential non-linearities are not noticeable in the HECTOR data.

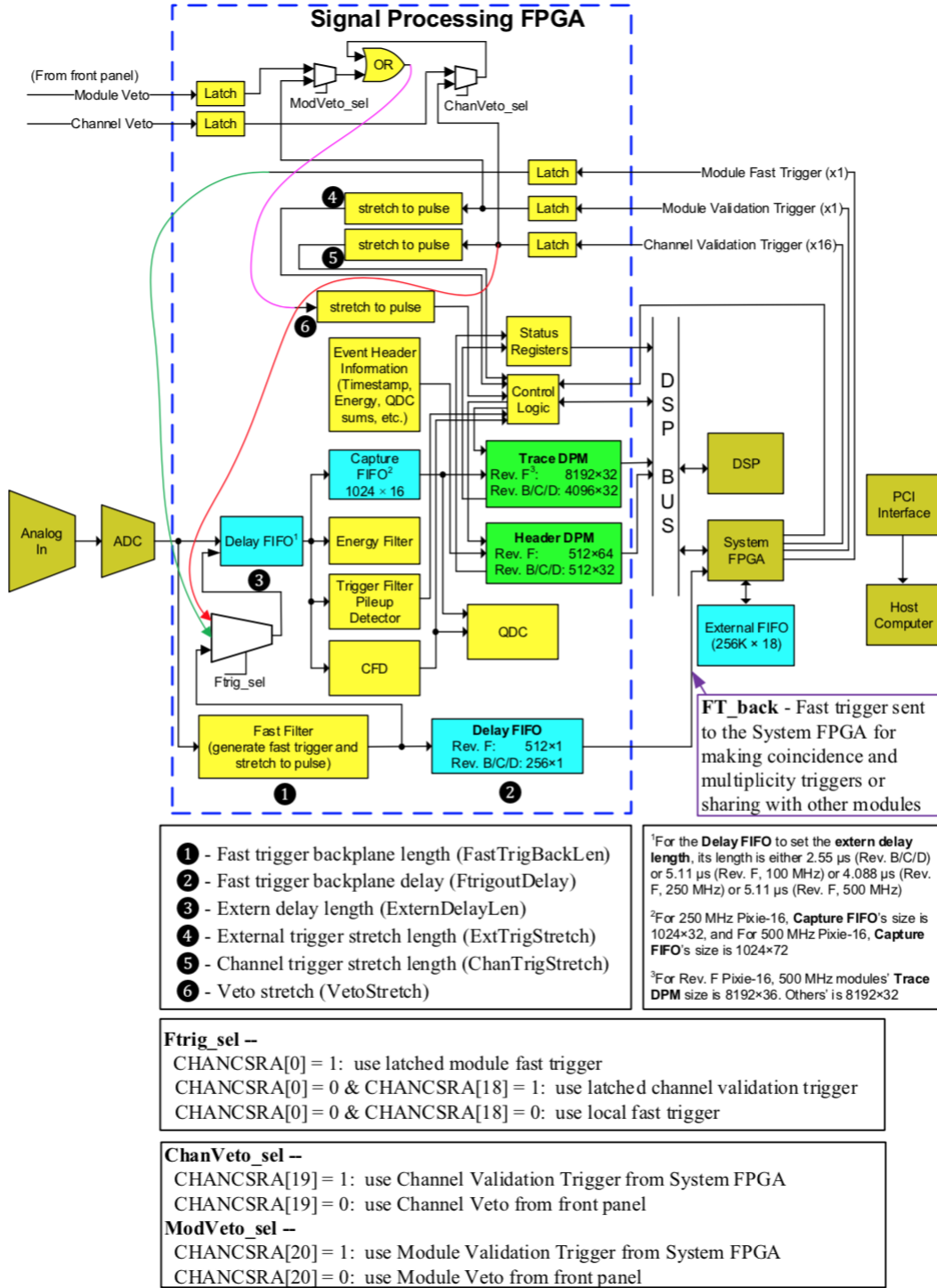


Figure 2.21. The signal processing done by the XIA Pixie-16 electronics.
 All the processing is done within the module. Taken from [82].

The Pixie modules were unable to produce enough gain in the amplifier section for the Si(Li) detectors to cover a significant number of channels for resolution, so the detectors' signals were put through fast filter amplifiers [3] to boost the signal before being fed into the DDAS. Fast amplifiers were used due to the fast timing and acquisition nature of the Pixie-16 modules and DDAS.

As with the ICEBall data, these files were event files that were then converted in root files for further analysis.

TABLE 2.13

DATA EVENT - MADC32 (32 BIT WORD)

Header						
2	6	8	1	3	2	10
header signature	subheader	module id	output format	adc resolution		number of data words
b01	b000000		bx	bxxx	b00	number of 32 bit data words
Data Word						
2	9	5	1	1	1..3	11..13
data-sig				out of range		
b00	00 0100 000	channel number	b0	Oor	b00	ADC Amplitude
End of Event						
2				30		
b11					event counter/time stamp	

Table of the 32-bit word data structure of the MADC. The headers, event word structure, and end of event structure, where needed, are all listed. In the tables, the first row in a given block is the number of bits used by that piece of data, while the second row is a description of the data. Bits go in descending order from left to right.

TABLE 2.14

DATA EVENT - V775 (32 BIT WORD)

Header							
5	3	8	2	6			8
Geo Address[5]	010	Crate Number[8]	00	Converted Channels[6]			
Data Word							
5	3	3	5	1	1	1	12
Geo Address[5]	000		Channel Number	Valid	Under-Threshold	Overflow	ADC Amplitude[12]
End of Block							
5	3					24	
Geo Address[5]	100					Event Counter[24]	

Table of the 32-bit word data structure of the CAEN 775 TDC. The headers, event word structure, and end of event structure, where needed, are all listed. In the tables, the first row in a given block is the number of bits used by that piece of data, while the second row is a description of the data. Bits go in descending order from left to right.

DATA EVENT - V830 (32 BIT WORD)

TABLE 2.15

Header					
5	1	2	6	2	16
Geo Address	1		Number of Enabled Channels	Source	Trigger Number
Geo Address	1			Source	
Data Word					
<hr/>					
32					
<hr/>					
Channel Counter[32]					

Table of the 32-bit word data structure of the CAEN V830 Scaler. The headers, event word structure, and end of event structure, where needed, are all listed. In the tables, the first row in a given block is the number of bits used by that piece of data, while the second row is a description of the data. Bits go in descending order from left to right.

TABLE 2.16

DATA EVENT - PIXIE-16 (32 BIT WORD)

Index	Header						
0	1	14	5	4	4	4	
	Finish Code	Event Length	Header Length	CrateID	SlotID	Chan#	
1	32						
	EVTTIME_LO[32]						
2	1	15		16			
	CFD forced trigger bit	CFD Fractional Time[15] x 32768		EVTTIME_HI[16]			
3	1	15		16			
	Trace Out-of-Range Flag	Trace Length		Event Energy			
Data Word							
n	16			16			
	ADC Data #(2n+1)[16]			ADC Data #(2n)[16]			

Table of the 32-bit word data structure of the Xia Pixie-16. The headers, event word structure, and end of event structure, where needed, are all listed. In the tables, the first row in a given block is the number of bits used by that piece of data, while the second row is a description of the data. Bits go in descending order from left to right.

CHAPTER 3

ANALYSIS

The acquisition of the data, as discussed in the previous chapter, was done using the NSCL DAQ [56, 60]. These files were converted into files compatible with ROOT [16]. In ROOT, calibrations, gates, and fitting were done. Fits of the peaks were also done in RADWARE [61] and compared. RADWARE was used as the main fitting tool, as the built-in framework for the Fano factor [29] created more consistent global fits, and a better estimate of the skew factors for the conversion electron spectra. Appendix ?? contains the analysis code used, and Appendix ?? contains the ROOT macros discussed in the text.

3.1 Fitting Spectra

Whenever possible, all data were fit using the same methodology. If another methodology needed to be used (as will be discussed in Section 3.4) the methodology was tested. This was done by taking both fitting routines to the same peaks and comparing the results. If they were in agreement, the secondary method could be used where the primary method failed.

In a completely ideal scenario, the spectrum from an experiment should look like a series of delta functions. This is never the case in a real experiment, as detectors do not have infinite resolution, and do not cover an infinitesimal angle. Instead, an ideal experimental spectrum would have the peaks look like gaussian functions. The normal gaussian formula is

$$f(x) = he^{-\left(\frac{x-\mu}{\sqrt{2}\sigma}\right)^2} \quad (3.1)$$

where h is the height of the peak, μ is the centroid of the peak, and σ^2 is the variation of the peak. This function can be renormalized using the integral to give the area as a fitting parameter instead of the height as

$$A = h\sigma\sqrt{2\pi} \quad (3.2)$$

The HPGe spectra were fitted using the gaussian formula. Fitting multiple peaks at once in a spectrum requires a secondary consideration: the Fano factor. The Fano factor is a measure of dispersion within a detector[29]. It takes into account that the energy loss in the detector is not purely statistical, as the gaussian distribution would assume. This goes into the resolution of the detector, which is related to the energy of the particle being detected. As a result, the resolution changes with energy. This is reflected in the variation (σ^2) in the fit. To do this in ROOT, the fitting function must be written to reflect this information, tying the width of every peak together under certain assumptions. As there is not an iterative way to create such a function in ROOT for x number of peaks, an individual fitting function must be written for each number x of peaks to fit. This becomes exceedingly tedious. However, RADWARE has this energy adjustment built into the fitting code, allowing the correlation between peaks to be turned off if needed for up to 35 peaks. If there are background peaks that should not have a correlation, such as the case of a Compton peak, it can be turned off for individual peaks.

In the previous chapter, the results of the calibrations were discussed, without going into detail into the calibrations themselves. In particular, the calibrations of the Si(Li) detectors were important for the fitting of data peaks. Due to incomplete charge collection, the Si(Li) detectors have a pronounced low-energy tail that can be modeled using a skewed gaussian. This skewed gaussian formula adds two more fitting parameters: R and β . R is the ratio of the tail height to the peak height, and β is a "skewedness" parameter. Both of these values are floated during the calibrations

to find optimal values, and then fixed from these values for the data fits. The skewed gaussian formula is

$$f(x) = h \left(1 - \frac{R}{100} \right) e^{-\left(\frac{x-\mu}{\sqrt{2}\sigma}\right)^2} + h \left(\frac{R}{100} \right) e^{\frac{x-\mu}{\beta}} \operatorname{erfc} \left(\frac{x-\mu}{\sqrt{2}\sigma} + \frac{\sigma}{\sqrt{2}\beta} \right) \quad (3.3)$$

with the variables as previously discussed. Of note, R can only range from 0 to 100, and β must be non-zero when used. In general, β should be positive. Similar to the Fano factor, R and β are related to the detector. R may vary slightly with energy, but can be held fixed, while β is usually fixed for the detector.

A third component, a smoothed step function, can also be used to increase the background on the low energy side of the peak that occurs from the Compton scattering of photons into the detector. This adds one more fitting parameter, the step height, to the fitting function, that would need to be fixed from the calibration data. Fits were done with and without this floating in the calibration data. It made no impact, and in some cases, found a negative step height, which is unphysical. The step height was therefore fixed to zero.

The peak fits in RADWARE were used to get the efficiency parameters for the equations 2.3 and 2.4. The parameters for the ICEBall-GEORGINA set up are in Tables 3.1 and 3.2. The parameters for the ICEBall-Clovershare runs are in Tables 3.3, 3.4 and 3.5. The Si(Li) efficiencies did not change between the two Clovershare runs, but the HPGe detectors were changed and moved, resulting in different values.

3.2 Gating

Two types of gates were used in the analysis: energy and timing. Energy gates were used to look for coincidence with specific transitions. This allowed for confirmation of excited state population using known level schemes. Generally, the energy gates were used on the gamma-ray spectra, defined using the centroid of the gamma

TABLE 3.1
SI(LI) EFFICIENCIES IN GEORGINA CONFIGURATION

Detector	p_1	p_2	p_3
1	-9.753	1.127	-0.003429
2	-20.33	3.155	-0.006227
3	-15.96	2.309	-0.004813
4	-8.542	0.9793	-0.003405
5	-14.39	2.186	-0.006035
6	-11.41	1.485	-0.003527

TABLE 3.2
GEORGINA EFFICIENCY PARAMETERS

Detector	a_0	a_1	a_2	a_3	a_4
0	-8.247	-0.4383	-0.2526	0.003371	0.000269
1	-8.581	-0.5057	-0.3439	0.003742	0.000235

TABLE 3.3
SI(LI) EFFICIENCIES IN CLOVERSHARE CONFIGURATION

Detector	p_1	p_2	p_3
1	-11.39	1.424	-0.003961
2	-17.75	2.542	-0.003829
3	-14.55	2.101	-0.004718
4	-20.39	3.16	-0.005671
5	-16.79	2.426	-0.004415
6	-15.88	2.331	-0.004863

TABLE 3.4
CLOVERSHARE MARCH RUN EFFICIENCY PARAMETERS

Detector	a_0	a_1	a_2	a_3	a_4
0	-8.193	-0.3404	-0.4493	0.005554	0.0007445
1	-7.43975	-0.289389	-0.374205	0.00649538	0.000929357
2	-8.317	-0.2887	-0.5504	0.008845	0.0008342
3	-9.611	-0.4577	-0.5905	0.004659	0.0004296
4	-7.863	-0.327	-0.447	0.008795	0.00098
5	-8.297	-0.3503	-0.4463	0.006396	0.0007243
6	-8.225	-0.3443	-0.4478	0.005464	0.0007393

TABLE 3.5

CLOVERSHARE MAY RUN EFFICIENCY PARAMETERS

Detector	a_0	a_1	a_2	a_3	a_4
0	-8.185	-0.3043	-0.4174	0.004383	0.0006837
1	-7.286	-0.3525	-0.334	0.007523	0.001481
4	Not calculated due to detector malfunction				
5	-7.724	-0.2955	-0.2346	0.004545	0.0001513
6	-15.55	-1.496	-1.132	0.004681	0.0001785

and a range of $\pm 2\sigma$. Only one HPGe detector would be gated on so both gamma-ray and conversion electron spectra could be viewed with the same constraints. The Si(Li) detectors were gated on, but both due to the low-energy skewed tails and the lower resolution of the Si(Li) detectors, clean gates were not achievable. A background energy gate was also used, gating on an area in the energy spectrum, near the peak of interest, with no identifiable peaks. This gate gives a measure of the background spectrum due to incidental coincidence.

The timing gates were unique to pairs of detectors. In the GEORGINA data, a pulsed beam was used, allowing for a distinct timing structure, shown in Figure 2.18 from the previous chapter. As is seen, the structure is complicated. By using an energy gate, the background is cut down, and the timing structure becomes much clearer, as seen in Figure 3.1. There is an energy dependence, also shown in the figure. Thus, the timing gates were made to cover the full range of possibilities. A second timing gate, covering a different region of the same time length, is used to subtract off the background the timing gate does not exclude. Table 3.6 summarizes the gates for the different detector pairings. In some cases, the background gates

TABLE 3.6
 TIMING GATES BY DETECTOR PAIRING FOR THE
 ICEBALL-GEORGINA EXPERIMENT

Detector 1	Detector 2	Main Gate		Background Gate	
		Start	End	Start	End
HPGe-HPGe Pairings					
0	1	-1500	1000	-2500	-1500
				1000	2500
HPGe-Si(Li) Pairings					
0	0	-1500	0	0	1500
0	1	-600	1000	1000	2000
				-1600	-1000
0	2	-400	1000	1000	2400
0	3	-500	1000	1000	2500
0	4	-200	1100	-1300	-200
0	5	-700	1000	1000	2000
				-1400	-700
1	0	-1200	1200	-2400	-1200
				1200	2400
1	1	-600	1500	1500	2100
				-2100	-600
1	2	-200	1400	1400	1600
				-1600	-200
1	3	-500	1400	-1900	-500
				1400	1900

TABLE 3.6 (CONTINUED)

Detector 1	Detector 2	Main Gate		Background Gate	
		Start	End	Start	End
1	4	-100	1600	-1700	-100
				1600	1700
1	5	-600	1500	-2100	-600
				1500	2100
Si(Li)-Si(Li) Pairings					
1	2	-200	200	200	600
1	3	-200	200	200	600
1	4	0	200	200	400
1	5	-600	600	600	1800
1	0	-1200	200	200	1600
2	3	-100	100	100	300
2	4	0	200	200	400
2	5	-600	200	200	1000
2	0	-1200	200	200	1600
3	4	0	200	200	400
3	5	-600	400	400	1000
3	0	-1200	200	200	1600
4	5	-700	100	100	900
4	0	-1200	100	100	1400
5	0	-1200	200	200	1600

A table of the timing gates used in the GEORGINA experiment. Detectors are indexed as the code read them in. The indexes worked in both orders, to avoid redundancy issues, i.e. (0,1) and (1,0) are the same as far as the code is concerned. All start and end values are channel number, and in several cases, there are two background gates, due to the size of the main gate and the available channel range.

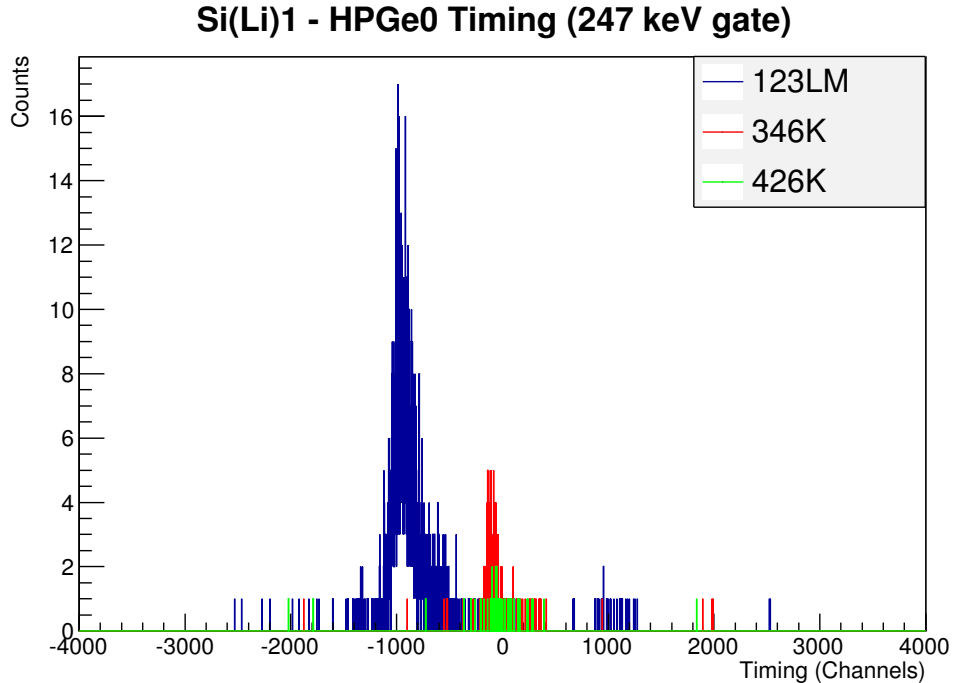


Figure 3.1. A plot of the energy-gated timing for a HPGe-Si(Li) detector pairing. The HPGe detector was gated at 247.9 keV, one of the ground state band transitions in the ^{145}Gd nucleus. The conversion electrons for other transitions in the ground state band were gated on in the Si(Li) detector. Plotted here are the time differences between the two detectors when both peaks were seen in the respective detectors. The 123LM peak was used instead of the K peak due to the high threshold of this detector. As can be seen, the timing has an energy dependence. This dependence is most prominent at lower energies.

needed two sections, to cover the same range as the original timing gate.

In the Clovershare data, the timing was done within the electronics, leading to an clean structure, seen in Figure 3.2. Although the same code structure was used for the timing, the gates were all the same within the Clovershare data. The main gate used was ± 0.3 and the background ranged from 0.3 to 0.9, using the same scaling as seen in Figure 3.2.

Background was taken into account via the energy and timing background gates. The energy background (E_b) gate would be subtracted off the main energy gate

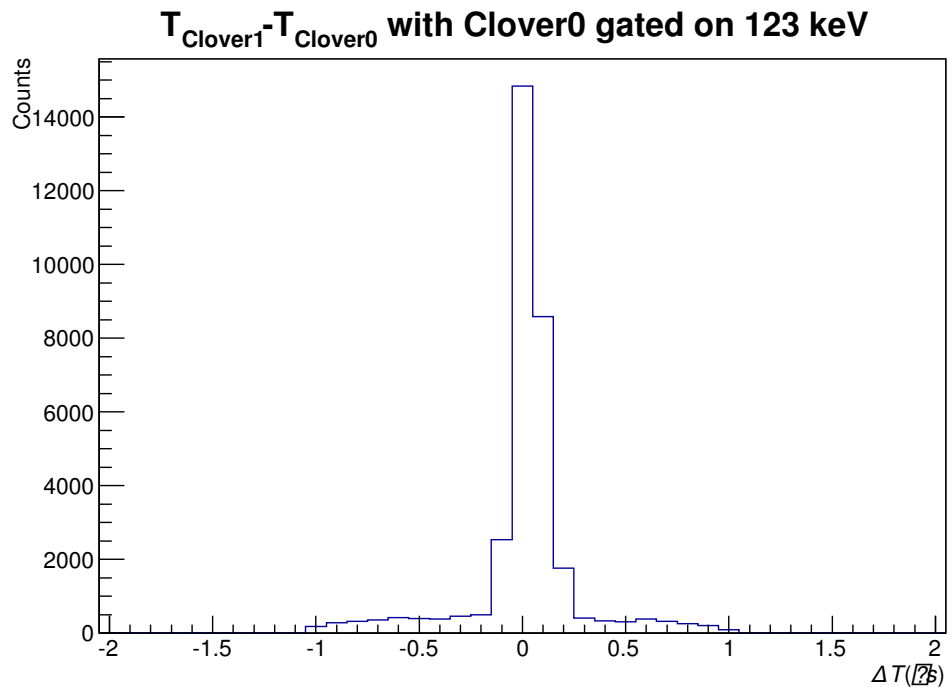


Figure 3.2. Timing between two of the Clovershare detectors, with one detector gated on 123 keV, the lowest transition in the ground state band of ^{154}Gd . In this data, the gates all looked similarly symmetric, and the timing gates did not need to be varied as they had for the GEORGINA set up.

(E). These two energy gates were repeated with the main timing(t), and background timing(t_b). The resulting $E - E_b$ spectra, one on the main timing gate, and one on the background timing gate, were then also subtracted as $t - t_b$ to remove any random coincidence from the timing gate.

3.3 Systematic Effects

Several systematic effects had to be taken into account at various stages of analysis. Each will be discussed in further detail in this section. At the calibration stage, there are two major corrections in the Clovershare data. The first, as discussed in section 2.5.3, is due to the integral non-linearities of the electronics. Second, the instability of the Clovershare detectors required a run-by-run calibration correction.

In the analysis stage, corrections on extracted values needed to be done based on the angular correlations due to the detectors being at different angles relative to each other. If the angle between the two HPGe detectors were the same as the angle between the HPGe detector and Si(Li) detector(s), this correction would divide out and be unneeded.

3.3.1 Electronics-based Integral Non-Linearities

There are two kinds of non-linearities from electronics: integral and differential [42]. These two non-linearities are interrelated. Integral linearity is most easily seen in the energy calibration. Differential non-linearity can be seen by looking at the count rate with respect to channel number. Generally, the non-linearity can be expressed in calibration by a higher order correction to an otherwise linear calibration. In the GEORGINA detectors, this was the case. In the Clovershare detectors, this was not the case.

The Pixie-16 MCA used in the Clovershare experiments has non-linearity specifications for 12-bit and 14-bit modes, but not 16-bit, according to the XIA datasheet

[82]. These are listed in terms of the difference of the least significant bit (LSB). In an ideal ADC, this number is 0, meaning the difference between two adjacent channels is exactly one LSB. A larger number means the gap is that much greater than one, and a negative number is that much less. When such non-linearities exist, a best case scenario is for the difference to be constant, leading to the polynomial correction. In the case of the Clovershare experiments, the LSB difference between channels does not appear to be constant.

Plotting the residuals of the calibration after doing a linear fit shows what appears to be a sawtooth pattern to the energy points, as seen in Figure 2.17. To fit this sawtooth pattern, it was assumed that the upward slope of the various sections was the same, and the sections were connected via the error function and complimentary error function, to allow for smoothing of the discontinuity. This results in the function

$$E_{res} = m * x + b_1 * \operatorname{Erfc}\left(\frac{x - f_1}{c}\right) + b_2 * \operatorname{Erf}\left(\frac{x - f_1}{c}\right) * \operatorname{Erfc}\left(\frac{x - f_2}{c}\right) + b_3 * \operatorname{Erfc}\left(\frac{x - f_2}{c}\right) \quad (3.4)$$

where m is the slope, b_i are the various intercepts to shift the correction, f_i is the location of the shift, and c is the curvature of the error function.

3.3.2 Run-based Calibration Corrections

Run-by-run corrections are usually needed when there is drift or instability in the electronics or pre-amplifier. In the Si(Li) and GEORGINA detectors, there was no noticeable drift. The Clovershare data does appear to need a correction for the HPGe detectors. The best way to track these instabilities was to look at known lines in each run, and plot the residuals after calibration, compared to the known value. This can be seen in Figure 3.3. Several well defined peaks were taken in run to define a linear correction for each run. These linear corrections were done on top of the original energy calibration and correction.

Clover 0 Residuals by Run

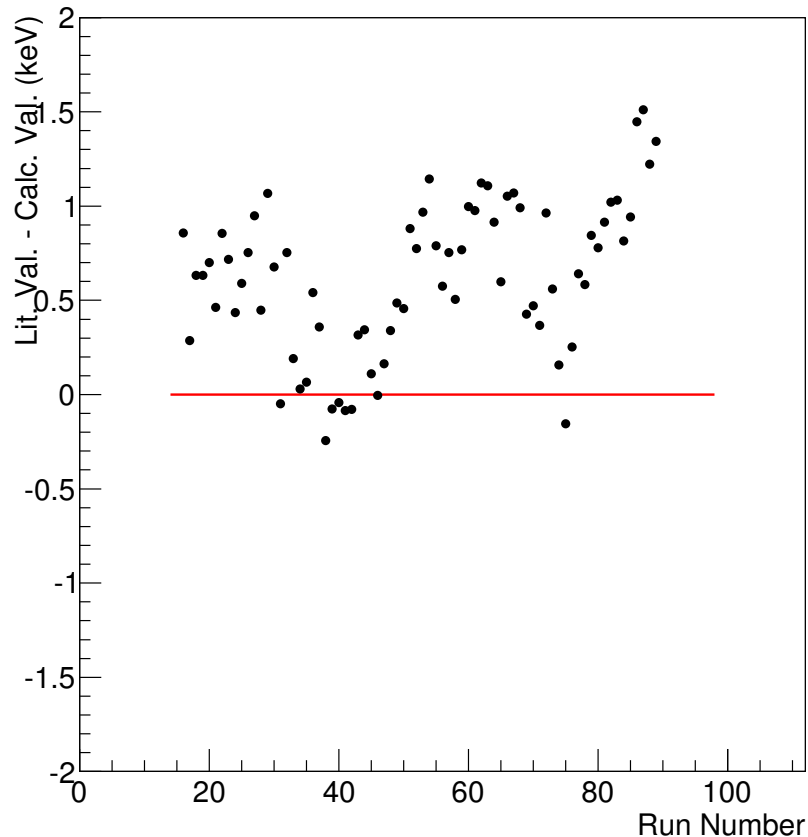


Figure 3.3. The difference between the literature value and the calibrated value (before run-by-run correction) of the naturally occurring ^{40}K background peak at 1460 keV, plotted by run for one leaf of one HPGe detector. The red line shows $\Delta E = 0$.

The peaks used for the run-by-run correction were a combination of the ground-state band peaks in the isotope of interest at low energies, and background gammas at higher energies, such as 1460 keV from ^{40}K and 1764 keV from ^{214}Bi . These are naturally occurring from the concrete walls of the NSL.

3.3.3 Angular Distributions and Angular Correlations

Angular correlations are a well studied phenomenon that arises when trying to look at two types of radiation in coincidence. A thorough exploration of different radiation pairings is explored in [11]. For this work, the pairings of interest are $\gamma - \gamma$ and $\gamma - e$. Triple correlations were also explored, as there were several cases where the intermediate transition was not seen.

Because the detectors are at different angles with respect to each other, when computing conversion coefficients, or subtracting off conversion electrons from the ground state band within the spectra, a correlation must be made based on these relative angles. Table 3.7 lists these angles from the ICEBall-Georgina setup, with respect to Detector 1.

These angles can be calculated using

$$\theta' = \cos^{-1}\left(\frac{\sin\theta_1\cos\phi_1\sin\theta_2\cos\phi_2 + \cos\theta_1\cos\phi_1\cos\theta_2\cos\phi_2 + \sin\phi_1\sin\phi_2}{\sqrt{2}}\right) \quad (3.5)$$

with the previous definitions given for the angles in Tables 2.4 and 2.11.

Angular correlation functions for $\gamma - \gamma$ are usually written as a series of Legendre polynomials, multiplied by a correlation coefficient A_ν , or

$$w(\beta) = \sum_\nu A_\nu P_\nu(\cos\beta) \quad (3.6)$$

TABLE 3.7
RELATIVE ANGLES OF DETECTORS

Detector	θ'
HPGe 2	180
SiLi 1	90
SiLi 2	90
SiLi 3	122.5
SiLi 4	110.7
SiLi 5	69.3
SiLi 6	57.3

Relative angles of the detectors with respect to HPGe 1 in the ICEBall-GEORGINA set up. The angles were calculated using Tables 2.4 and 2.11 and equation 3.5. All angles are in degrees.

In the case of $\gamma - e$ correlations, the equation becomes

$$w_m(\beta) = \sum_{\nu} b_{\nu}(LLm) A_{\nu} P_{\nu}(\cos\beta), \quad (3.7)$$

$$w_e(\beta) = \sum_{\nu} b_{\nu}(L+1, L+1, e) A_{\nu} P_{\nu}(\cos\beta)$$

depending on if the radiation is electric or magnetic in nature. The b_{ν} values are based off the same matrix elements used to calculate theoretical conversion coefficients, and are well understood[68, 69].

Both of these cases assume pure multipole transitions. In the case of mixed transitions, the correlation function becomes

$$W = w_I + \delta^2 w_{II} + 2\delta w_{III} \quad (3.8)$$

where w_I and w_{II} are the pure multipole correlation functions, and w_{III} is a correlation mixing the two multipoles. The variable δ is known as the mixing ratio.

These correlations can be further extrapolated to look at cases not just of direct correlations, but of indirect correlations, such as three γ -rays in cascade. If the middle radiation is not observed, the first and third radiations still have a determinable correlation. This is derived for pure multipoles by [11] and for mixed transitions by [58, 67].

For the experiments in this text, the ratios of these angular correlations at the detectors respective angles is needed to adjust for angular effects. Thus, the ratio becomes a factor, C_\angle , the ratio of the Si(Li) detector angle to the HPGe detector angle with respect to the detector gated on. The conversion coefficient is divided by this factor for correction.

In the singles, a similar value, based on the angular distribution instead of the angular correlation, must be used for correction. Correlations rise out of the angular distribution caused by the multipolarity of different types of radiation, so the angular distribution can also factor into the singles data, with the beam direction acting as the origin angle, making C_\angle , the ratio of the Si(Li) detector angle to the HPGe detector angle with respect to the beam axis.

The correction must further be adjusted by the solid angle the detector subtends. Only the azimuthal angle of the detector changes the distribution, so integration over slices of the detector with respect to angle can give a weighted average, i.e.

$$\overline{W} = \frac{1}{\pi r^2} \int_{-\tan^{-1}(r/d)}^{\tan^{-1}(r/d)} W(\eta + \omega) \left[2\sqrt{r^2 - (d \times \tan(\omega))^2} \right] \frac{d\delta\omega}{\cos^2(\omega)} \quad (3.9)$$

where $W(\theta)$ is the angular distribution function, η is the azimuthal angle center of the detector, d is the distance of the detector from the target, and r is the radius of the detector, in the same units as d . For the Si(Li) detectors, these distances were

taken as the maximal coverage of the mini-orange filters, and the distance between the target and the center of the blocker. Compared to treating the detectors as points, the effects were small, but the solid angle values were used in the singles.

3.4 Upper Limits

In ^{156}Gd , there were several possible transitions of interest at energies less than 250 keV. In that energy range, the ground-state band transitions cover much of the spectrum. Some transitions could be removed through the use of gating on gamma-rays of parallel transitions, but not all the transitions could be removed. This was due, in part, to the gate transitions being in sequence with some of the ground-state band.

To get an upper limit for the transitions of interest, the ground state band transitions that were in sequence with the gate transition were subtracted off of the conversion electron spectrum through the following method. An example of this subtraction can be seen in Figure 3.4. The skewed gaussian fitting function described earlier was given parameters derived from the data and subtracted from the conversion electron spectrum.

The area of the skewed gaussian is obtained by getting the area of the gamma peak, and adjusting by several factors: efficiencies (ϵ), conversion coefficient (α , as derived from theory), and correlation coefficients (W). This gives the following:

$$A_{ce} = A_\gamma \times \frac{\epsilon_{ce}}{\epsilon_\gamma} \times \alpha \times \frac{W_{ce}}{W_\gamma}. \quad (3.10)$$

The height of the skewed gaussian can be derived in terms of the area, R , σ and β to be

$$H = A \frac{100}{2 * e^{-\frac{\sigma^2}{2\beta^2}} R\sigma - \sqrt{2\pi}(R - 100)\sigma}; \quad (3.11)$$

These three variables are all unique to the detector, and come directly from fitting

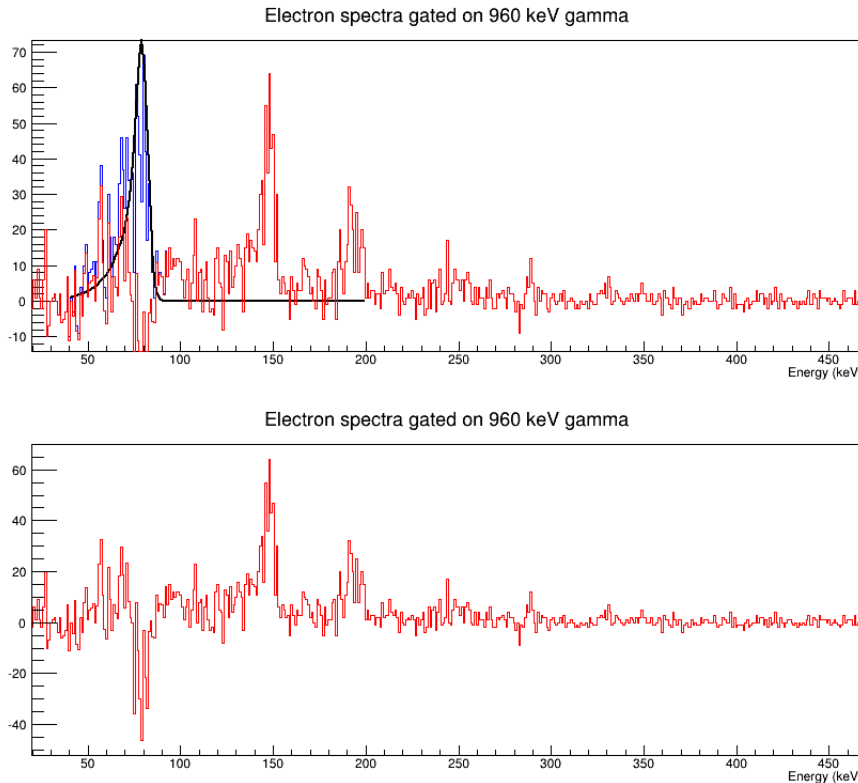


Figure 3.4. An example of the subtraction used to removed the ground state band peaks from spectra. To subtract the conversion electron peak off, the area of the corresponding gamma peak was taken from the same gate. Using the conversion coefficient and the efficiencies of both detectors, the area of the peak could be calculated. From there, this value, along with fixed R , β , σ , and centroid were used to subtract the peak off. The black line is the function used for subtraction. The blue line is the original spectrum, and the red line is after subtraction. This code can be found in Appendix ??

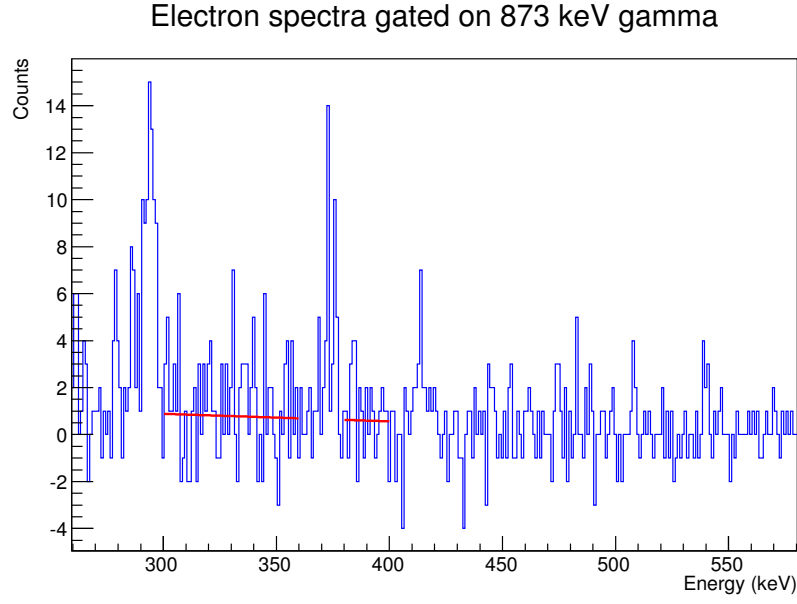


Figure 3.5. An example of the global background fit used for peaks that could not be fit using the skewed gaussian function. The areas on either side of the peak are selected by the user. Once the background fit is done, the central area between the two sections is treated as the peak and the background is subtracted off to give a peak area. The red line shows the fit for the background area, and the two sections used for the background fit.

See Appendix ?? for the global-fit function used.

the calibration data, as previously discussed. From there, the parameters can be fed into the equation, along with the centroid of the peak, and subtracted directly off the spectrum. Any remaining counts are counted by taking sections on either side of the area of interest and using a global linear fit for the background, as seen in Figure 3.5. This linear fit is subtracted off bin-by-bin in the region of interest. The remaining area is then taken as an upper limit on the transition of interest.

3.5 Error Analysis

When areas of peaks were found, the error is found with the fit. In the cases of the peaks that needed to be fit by estimating the background and subtracting it off,

the error of the area is assumed to be the square root of the counts in the peak added in quadrature with the error in the background.

These areas are propagated through calculations via the equation

$$\sigma_f^2 = \sum_i \left(\sigma_{x_i} \frac{\delta f}{\delta x_i} \right)^2 \quad (3.12)$$

where f is a function of all x_i in the sum [10]. If the function is related to all variables via some form of a polynomial, i.e. $(x_i)^a$ where a is a constant, then it can be rewritten as

$$\sigma_f^2 = f * \sum_i \left(\frac{\sigma_{x_i}}{a * x_i} \right)^2 \quad (3.13)$$

Errors on the areas of both gamma-rays and electrons were propagated through the data. The error on the efficiency was estimated by shifting the efficiency value $\pm 0.5\sigma$ and calculating upper and lower limit functions for the efficiency.

In the final results, the uncertainties were kept separate into statistical and systematic effects. Statistical effects are caused by the areas of the peaks. Systematic effects are from the uncertainty in the efficiency of both the HPGe and Si(Li) detectors, as well as an uncertainty in the angular correlations, based on the solid angle covered by the detectors.

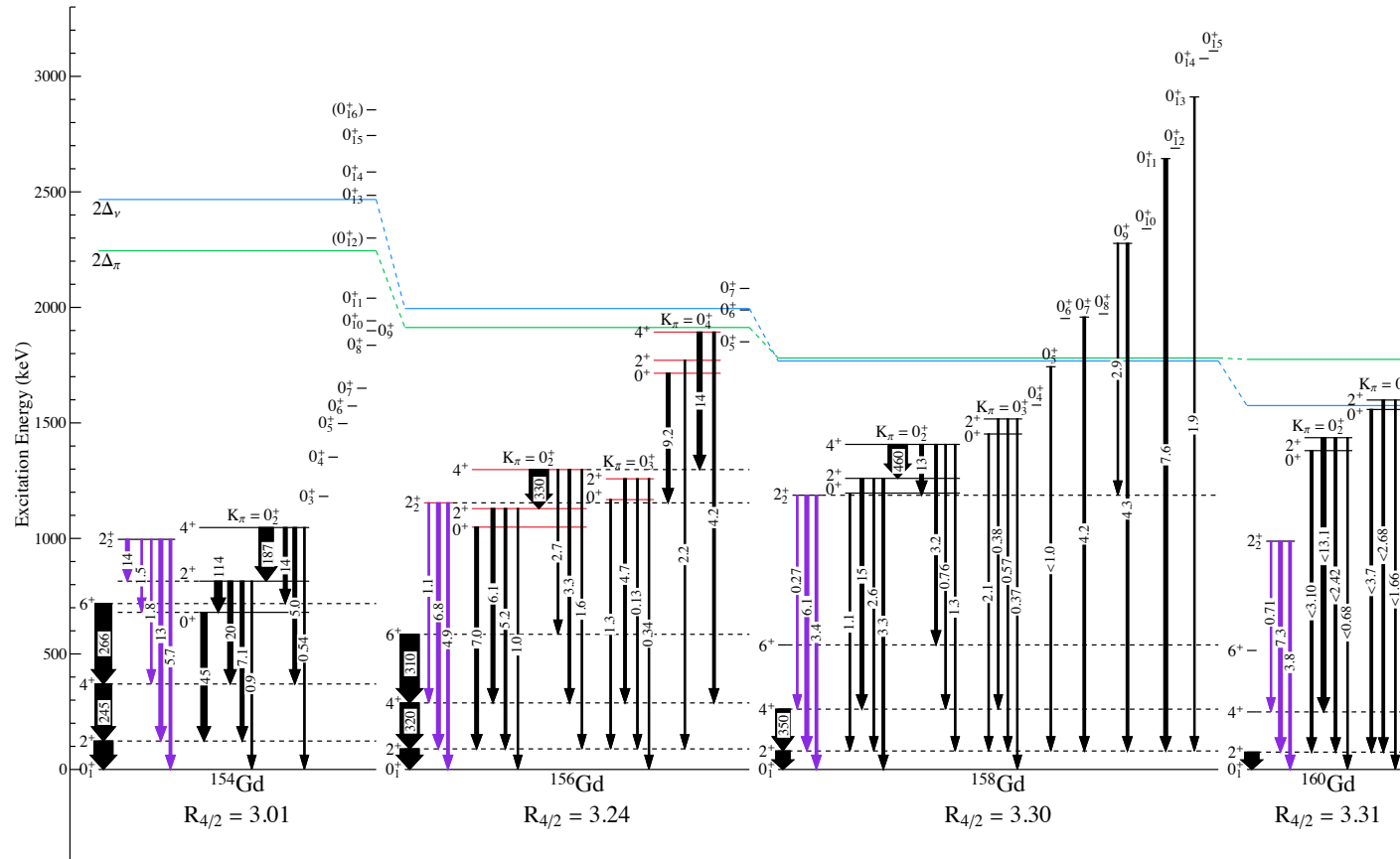
CHAPTER 4

^{154}GD RESULTS

^{154}Gd is a transitional nucleus ($\beta_2 = 0.3105$) with a large number of 0^+ states, 16, under 3 MeV. Eleven of these 0^+ states are below the pairing gap, as seen in Figure 4.1. The nature of these 0^+ states is of interest for this study. The lowest lying excited 0^+ state in the nucleus has an anomalously large transition to the ground state, as compared with other nuclei in the region, shown in Figure 4.1. For this 0^+ state, there is a question of the state being a β -vibration build on the ground state, or the minimum of another shape configuration.

The ^{154}Gd data was taken across three separate runs; one with ICEBall and GEORGINA, and two with ICEBall and Clovershare, in two different configurations, as discussed in Chapter 2. The GEORGINA experiment allowed for the HPGe detectors to be closer to the target, at a distance of 30 cm. This experiment yielded the most conversion electron data, and results in this chapter are quoted from that data. Although the Clovershare detectors had to be placed 5-10 cm farther from the target, the larger number of detectors, 7 for the first run and 5 for the second, the $\gamma - \gamma$ coincidence data was better, so identification of transition placements and level populations are confirmed. All of the experiments used the same enriched ^{152}Sm target of 1.44 mg/cm^2 thickness, discussed in Chapter 2 and shown in Table 2.10. A complete catalog of spectra used in analysis can be found in Appendix ??.

Figure 4.1. Systematics of the Gadolinium isotopes. ^{154}Gd has an anomalously large connection between the first excited 0^+ state and the ground state. The arrows shown are the $B(E2)$ components of the transitions, in single particle Weisskopf units [57, 63–65]. The $R_{4/2}$ values beneath each nucleus are a ratio of the energies of the first excited 2^+ and 4^+ states, both in the ground state band. This ratio gives a rough measure of deformation.



4.1 Ground State Band Confirmation

In the singles spectrum several prominent peaks stand out, seen in Figure 4.2. In the γ -spectrum, there are four prominent peaks from 100 to 500 keV. These peaks are the ground state band. The strong peak just beyond 500 keV is the 511 keV annihilation peak, and the peaks below 100 keV are x-rays. In the conversion electron spectrum of Figure 4.2, there are distinguishable peaks until approximately 400 keV in, and then again in the range of 550 keV to 650 keV. The peaks up to 400 keV correspond to these same ground-state lines that are prominent in the γ -spectrum. The K peaks are 51 keV less than the γ -peak, due to electron binding energy. The L peaks are 8 keV less, while the M peaks and higher electron shells are 1 keV or less different, compared to the energy of the γ -peak. The peaks in the range of 550 keV to 650 keV correspond to a strong series of $J^\pi \rightarrow J^\pi$ transitions from the first excited 0^+ band.

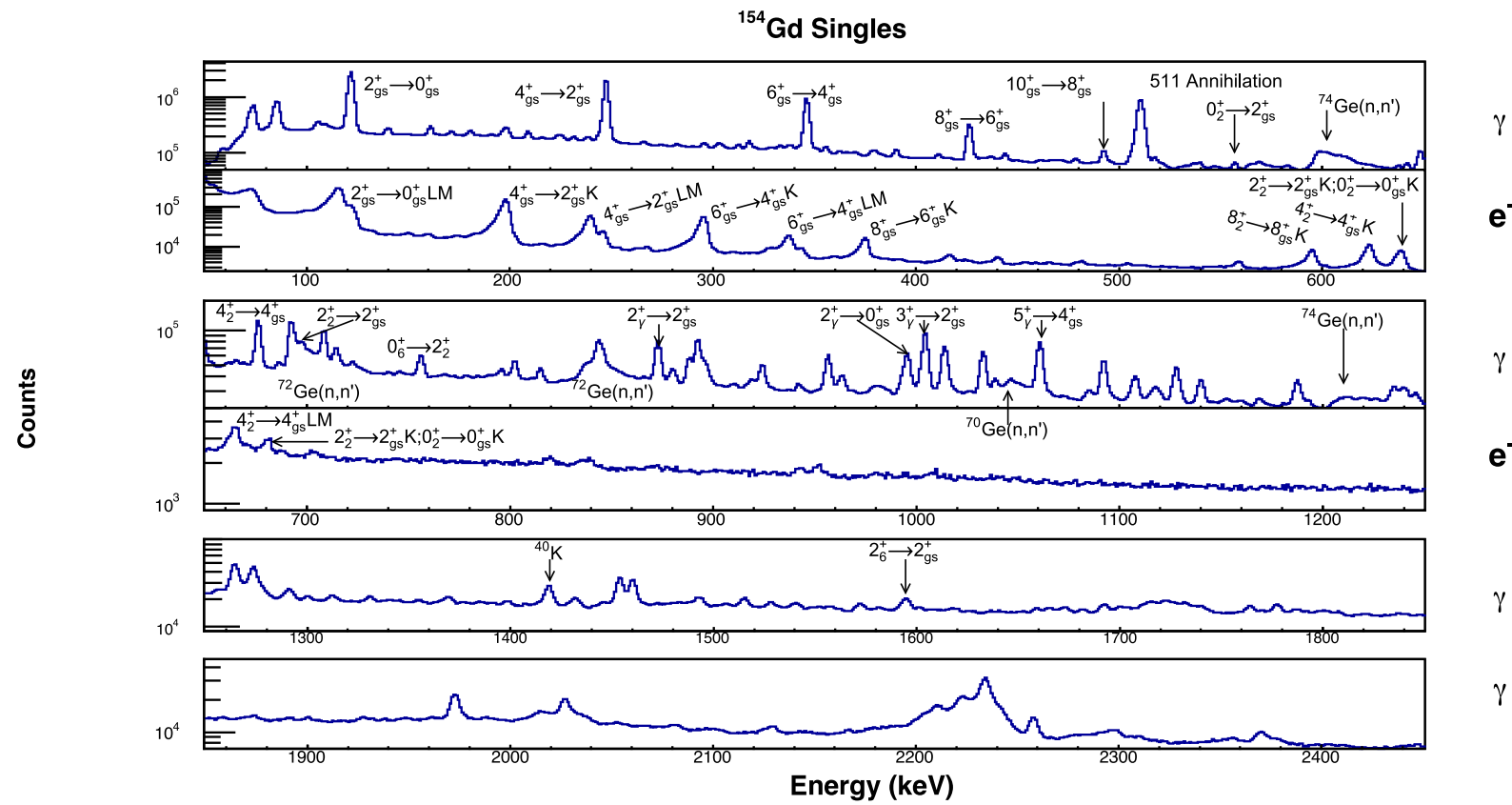
These ground state band transitions are known to be pure E2 multipoles, and have been previously measured and identified as such. This makes them excellent for calibration and comparison with calculated theoretical conversion coefficients.

In gated spectra, the internal conversion coefficients for the ground state band were in agreement with theory, after the angular correlation correction, discussed in Section 3.3.3, was applied. The peaks corresponding to the ground state band did not have contributions from other transitions when gated. In the singles, two of the four ground state band lines overestimated the conversion coefficient, indicating electron contributions from other transitions. To remove the contributions from other transitions, the γ -ray had to be distinguishable and identifiable. The conversion coefficient was then assumed from theory, and the contribution to the area was calculated to be

$$A_e = \alpha \epsilon_e \frac{A_\gamma}{\epsilon_\gamma} C_L \quad (4.1)$$

Figure 4.2. Singles spectra of ^{154}Gd . Spectra are labeled with the particles being detected, the energies of the γ and electron spectra aligned for identification. In the γ spectrum, several lines of note are labeled. The large peak at low energy in the electron spectrum is cut off due to the threshold. It is a combination of background and the 123K peak.

Transitions in the higher energy regime of the γ spectrum cannot be determined without gating, due to additional background from the experimental room. The electron detectors have a maximum energy of approximately 1250 keV, so there are no conversion electron spectra paired with the higher energy gamma spectra.



where ϵ_i are the efficiencies of the electrons and gammas respectively. C_{\angle} is the angular correction for this particular transition, discussed in Section 3.3.3.

For the $6_{gs}^+ \rightarrow 4_{gs}^+$ and $8_{gs}^+ \rightarrow 6_{gs}^+$ transitions, electron contributions from smaller gamma lines of similar energy had to be subtracted. Looking at Figure 4.2, it is clear there are many transitions around the same energy, making determination of the contributing peaks important. Only lines from reactions in the target material will contribute. Potential contribution lines needed to be identified as coming from the reaction. This is done by gating on the lines and identifying them within the known level scheme, as is discussed in Section 4.2. For instance, the 390.73 keV line in Table 4.1, was seen in coincidence with the $4_{gs}^+ \rightarrow 2_{gs}^+$, $6_{gs}^+ \rightarrow 4_{gs}^+$, $4_{0_2^+}^+ \rightarrow 2_{gs}^+$, $6_{0_2^+}^+ \rightarrow 6_{gs}^+$, $4_{0_2^+}^+ \rightarrow 4_{gs}^+$, $6_{0_2^+}^+ \rightarrow 4_{0_2^+}^+$, and $10_{0_2^+}^+ \rightarrow 8_{0_2^+}^+$ transitions. The transitions involving the ground state band gave context for approximate J^π , as no ground state band lines were seen above the 6^+ state. The transitions between the 0_2^+ band and the ground state band indicates the 390.73 keV line is part of the 0_2^+ band. Finally, seeing both the $6_{0_2^+}^+ \rightarrow 4_{0_2^+}^+$, and $10_{0_2^+}^+ \rightarrow 8_{0_2^+}^+$ transitions without the intermediate transition, which matched in energy, gave firm identification. Multipolarities could then be assigned based on the known data, and the contribution to the electron peak of interest could be calculated based on the gamma area and theoretical conversion coefficient. Contributions were subtracted off the fitted area of the electron peak, before the conversion coefficient of the ground state line was calculated. The error also includes contributions from the errors of these extra transitions' gamma peaks and the errors on the theoretical α values.

There were two types of transitions that acted as contributions to the conversion electron peak areas: those of similar energy, and higher energies whose K-electron energies were similar to the L and M peaks of the lines of interest. The peaks are summarized in Table 4.1. The electron-shell of the transition is listed in each case, and total L and M contributions are used, without need to look at subshell

contributions. In several transitions, the mixing ratio had to be assumed to get a conversion coefficient for the subtraction.

The $6_{gs}^+ \rightarrow 4_{gs}^+$ K-conversion coefficient was $0.0546(1)(14)$ before contributions from other transitions were taken into account. After subtracting the transitions in Table 4.1, the new value is $0.0335(1)^{+11}_{-10}$, in agreement with previous measurements and theory from BrICC[40]. Similarly, the $8_{gs}^+ \rightarrow 6_{gs}^+$ K-conversion coefficient went $0.0271(2)(7)$ to $0.0180(2)(5)$, also in agreement with theory calculations. The contributing transitions that were subtracted are summarized in Table 4.1. The conversion coefficient was then calculated, with an angular distribution correction based on the multipolarity of the transition. The transitions up to the 10_{gs}^+ are summarized and compared with theory in Table 4.2.

4.2 Gates on the Ground State Band

To confirm the levels populated in the experiment, the γ -rays of the ground state transitions were used as energy gates. Figures 4.4, 4.5, 4.6, and 4.7 are the result of these gates. Band structure in these figures was taken from the data sheets[64]. No band assignments were made in this work. In the cases of cascades, secondary gates were done to confirm assignments. The spectra from these gates are available in Appendix ??.

Determining which transitions went uniquely into a given ground state level was done by comparing the outgoing ground state transition for that level with the incoming transition i.e. for the 2^+ level, the $2_{gs}^+ \rightarrow 0_{gs}^+$ (123 keV) gate was compared directly with the $4_{gs}^+ \rightarrow 2_{gs}^+$ (247 keV) gate. The γ -spectra corresponding to two of these gates can be seen in Figure 4.3. Lines in the gamma spectrum that were present only in the outgoing spectrum, but not the incoming, were assumed to be populating that level. For example, in Figure 4.3, several areas have been highlighted. The line at 557 keV is present in the $2_{gs}^+ \rightarrow 0_{gs}^+$ gate, but not the $4_{gs}^+ \rightarrow 2_{gs}^+$ gate. This line

TABLE 4.1

^{154}GD GROUND STATE BAND $6^+ \rightarrow 4^+$ AND $8^+ \rightarrow 6^+$ EXTRA
ELECTRON PEAK CONTRIBUTIONS IN SINGLES

E	E_i	E_f	$J_i \rightarrow J_f$	Multipolarity	δ	Shell	α
346.59 keV, $6^+ \rightarrow 4^+$							
338.28	1770	1432	$5_{4^+}^+ \rightarrow 5_\gamma^+$	E0,E2,M1	-0.004	K	0.10 (1)
					$\frac{K(E0)}{K(E2)} \approx 1.0$	L	0.01210 (12)
						M	0.00180 (3)
342.18	2254	1911	$8_{4^+}^+ \rightarrow 6_{4^+}^+$	E2		K	0.0315 (5)
						L	0.0069 (1)
						M	0.001554 (22)
390.73	1756	1366	$8_{0_2^+}^+ \rightarrow 6_{0_2^+}^+$	E2		K	0.0218 (3)
426.84 keV, $8^+ \rightarrow 6^+$							
422.12	1418	996	$2_{0_3^+}^+ \rightarrow 2_\gamma^+$	E0,E2,M1	Assumed ≈ 1	K	0.114 (16)
						L	0.0161 (23)
						M	0.0049 (12)
466.99	1719	1251	$2_{2^-}^- \rightarrow 3_{0^-}^-$	M1,E2	Assumed ≈ 1	K	0.019 (6)
478.27	1719	1241	$2_{2^-}^- \rightarrow 1_{0^-}^-$	E2		K	0.01272 (18)

Table 4.1: A list of the transitions in the ^{154}Gd Singles data that were contributing to the electron peaks corresponding to the ground state band lines. Conversion coefficients were assumed using BrICC[40]. The bands for each level are listed as subscripts.

TABLE 4.2

^{154}GD GROUND STATE BAND INTERNAL CONVERSION
COEFFICIENTS FROM SINGLES

E (keV)	$J^\pi \rightarrow J^\pi$	E_i (keV)	E_f (keV)	$T_{1/2}$ (fs)	Multipolarity	Shell	α (This Work)	α (Th)[40]	α (Spits)[75]	α (Gono)[31]
122.23	$2^+ \rightarrow 0^+$	123.0709	0	1184000	E2	K	$0.7759 (34) {}^{+148}_{-146}$	0.656 (10)	0.61 (3)	
						L	$0.3788 (26) {}^{+81}_{-80}$	0.411 (6)		
						M	$0.1323 (3) (29)$	0.0963 (14)		
247.85	$4^+ \rightarrow 2^+$	370.9998	123.0709	45600	E2	K	$0.1044 (2) {}^{+31}_{-30}$	0.1000 (12)	0.080 (3)	0.0827 (119)
						L	$0.0272 (1) (8)$	0.0225 (4)		
						M	$0.0096 (1) (3)$	0.00513 (8)		
346.59 [†]	$6^+ \rightarrow 4^+$	717.662	370.9998	8260	E2	K	$0.0335 (1) {}^{+11}_{-10}$	0.0304 (5)	0.029 (1)	0.0306*
						L	$0.0087 (1) (3)$	0.00662 (10)		
						M	$0.0027 (1) (1)$	0.001491 (21)		
426.84 [†]	$8^+ \rightarrow 6^+$	1144.44	717.662	2570	[E2]	K	$0.0180 (2) (5)$	0.01716 (24)		0.0170 (22)
						L	$0.0030 (1) (1)$	0.00332 (5)		
						M	$0.0008 (1) (1)$	0.000741 (11)		

TABLE 4.2 (CONTINUED)

E (keV)	$J^\pi \rightarrow J^\pi$	E_i (keV)	E_f (keV)	$T_{1/2}$ (fs)	Multipolarity	Shell	α (This Work)	α (Th)[40]	α (Spits)[75]	α (Gono)[31]
493.171	$10^+ \rightarrow 8^+$	1637.05	1144.44	1110	E2	K	0.0124 (4) (4)	0.01179 (17)		0.0124 (21)
						L	0.0067 (4) (2)	0.00213 (3)		

Table 4.2: A list of ground state band conversion coefficients from ^{154}Gd . Multipolarities and mixing ratios were taken from the data sheets[64]. Unless otherwise stated, the α values are α_K . An angular distribution correction has been applied based on multipolarities for pure transitions, and those with known mixing ratios. The first error is statistical, the second is systematic. Numbers are compared with Spits et al.[75] and Gono et al.[31]. The starred value was used as an absolute calibration of the conversion electron detector in the Gono work. The dagger lines had contaminant lines subtracted from the conversion electrons. See the text for more details.

corresponds to the $0_2^+ \rightarrow 2_{gs}^+$ transition, putting it in parallel with the $4_{gs}^+ \rightarrow 2_{gs}^+$ transition, explaining why it remains unseen. These identified transitions were then gated on to confirm the assignment, and to search for cascades from higher states.

There were nine bands seen in the gating, 4 of which are bands with excited 0^+ band heads. These are seen in the $2_{gs}^+ \rightarrow 0_{gs}^+$ gate (Figure 4.4). Three of these bands are seen in the $4_{gs}^+ \rightarrow 2_{gs}^+$ gate (Figure 4.5), and two are seen in the $6_{gs}^+ \rightarrow 4_{gs}^+$ gate (Figure 4.6). Only one is seen in the $8_{gs}^+ \rightarrow 6_{gs}^+$ gate (Figure 4.7). This drop off is unsurprising for multiple reasons. Studies have shown the $(\alpha, 2n)$ reaction to stop populating spin states with a significant cross section beyond $J^\pi = 12^+$ [81]. In the ground state band of ^{154}Gd , the 12^+ state sits at 2184.69 keV, giving an approximate cut off for populating higher energy states in the nucleus. Additionally, due to the lack of known higher spin states in the higher energy 0^+ bands, identification of populating such bands in the higher gates becomes difficult.

4.3 Conversion Coefficients from Singles

Conversion coefficients were calculated from the singles spectra. Transitions that could be clearly identified and distinguished are found in Table 4.3. Several transitions with E0 components can be found in Table 4.3. Most of the conversion electrons seen are the K -shell electron. These transitions were corrected for angular effects based on the multipolarity of the transition.

Table 4.4 conversion coefficients have been left uncorrected in the singles for one of two reasons: either there were multiple known assignments to the gamma-ray energy, or the transition is considered a mixed transition, but no mixing ratio, δ has been previously measured. For the $3_\gamma^+ \rightarrow 2_{0_2^+}^+$ transition, a mixing ratio, δ , could be calculated by solving the equation

$$\alpha_{exp} C_L(\delta) = \frac{1}{1 + \delta^2} (\alpha(E2) + \delta^2 \alpha(M1)) \quad (4.2)$$

Figure 4.3. Spectra gated on 123 keV ($2_{gs}^+ \rightarrow 0_{gs}^+$) and 247 keV ($4_{gs}^+ \rightarrow 2_{gs}^+$), the first two ground state band lines of ^{154}Gd . As can be seen, some lines do not appear in different gates. Comparison of these gates, yields a list of transitions that directly populate the interim level (in this example, the 2^+ state). Several peaks are circled in green that appear in the $2_{gs}^+ \rightarrow 0_{gs}^+$ and not the $4_{gs}^+ \rightarrow 2_{gs}^+$ transition.

Spectra gated on Ground State Band Transitions

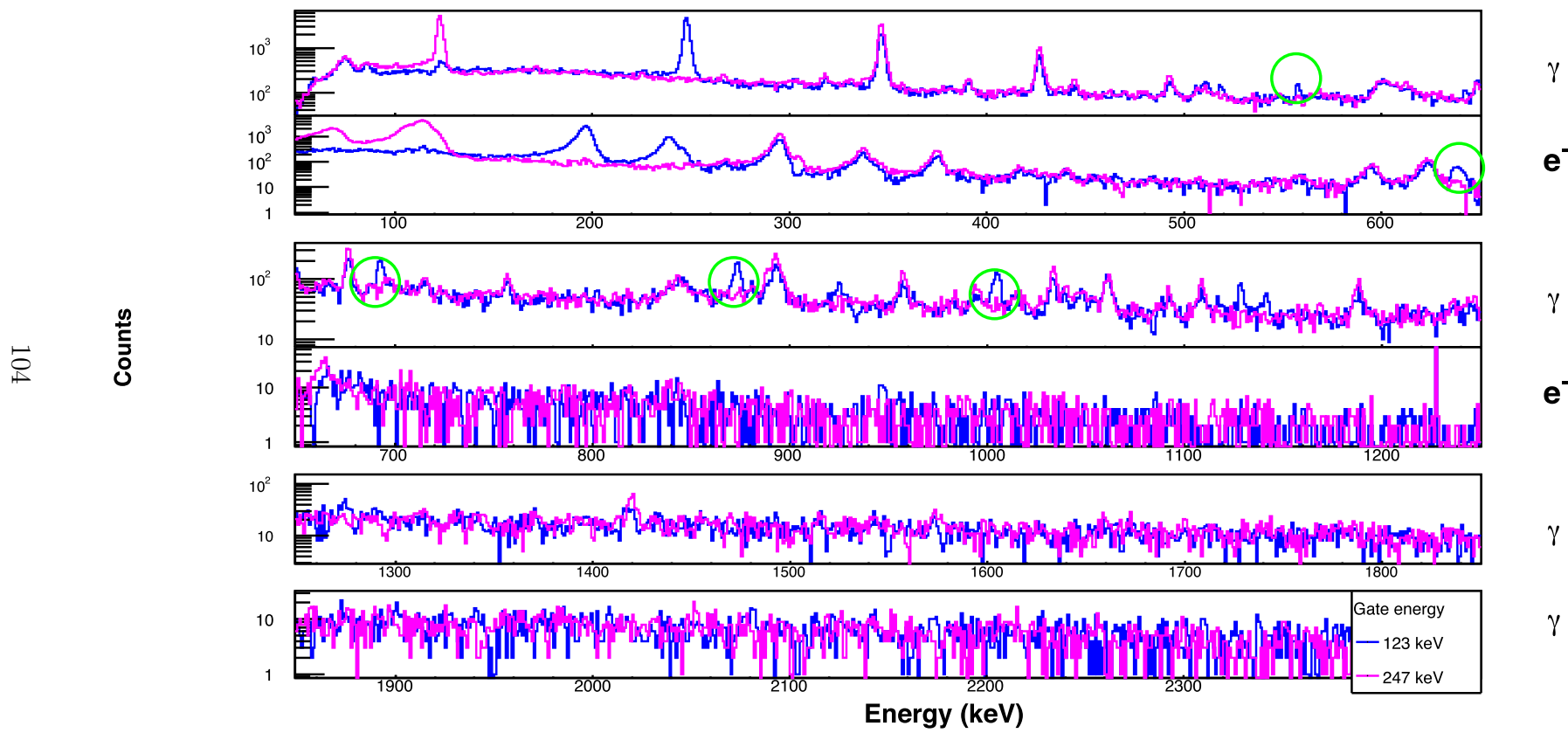
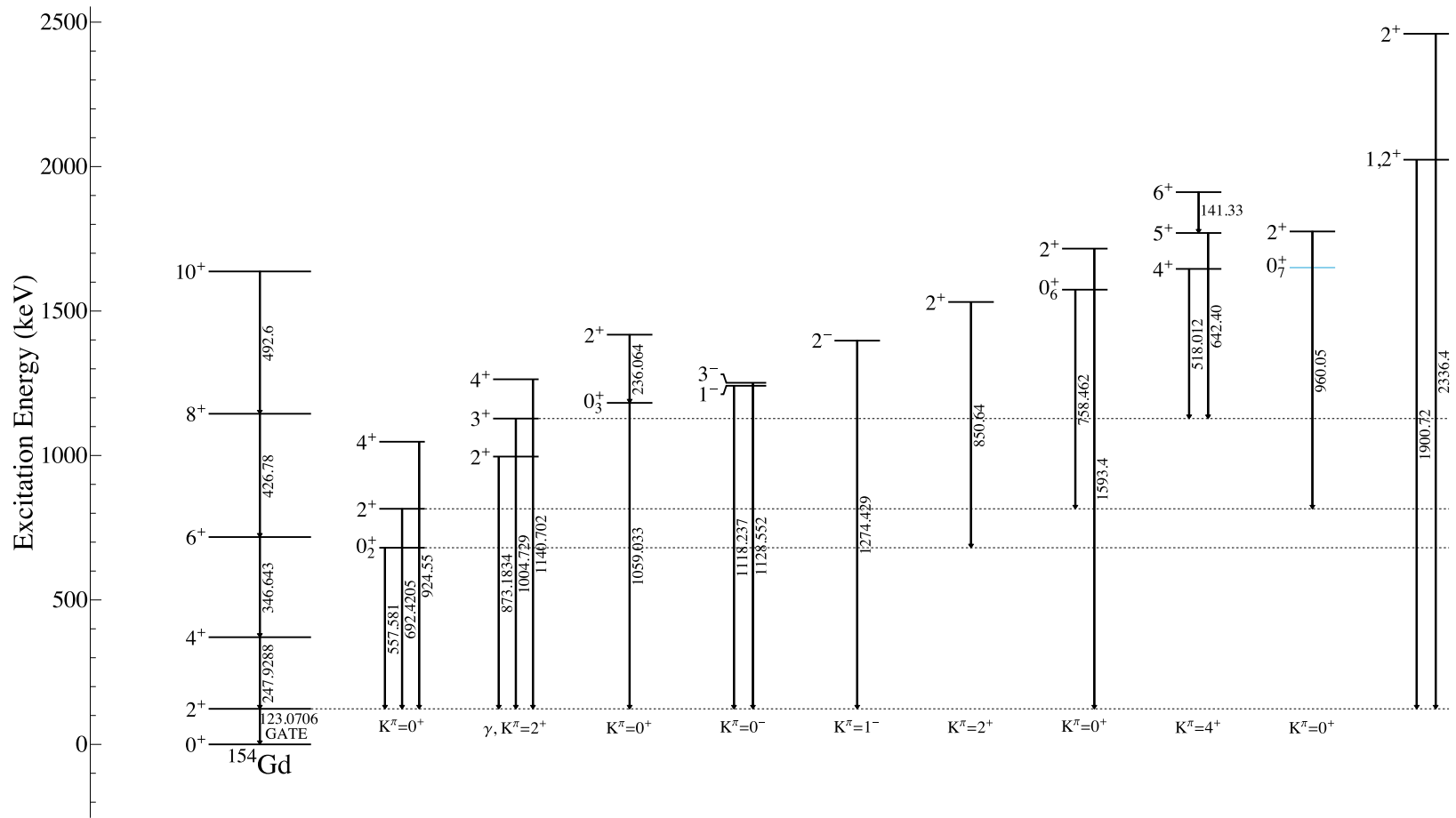


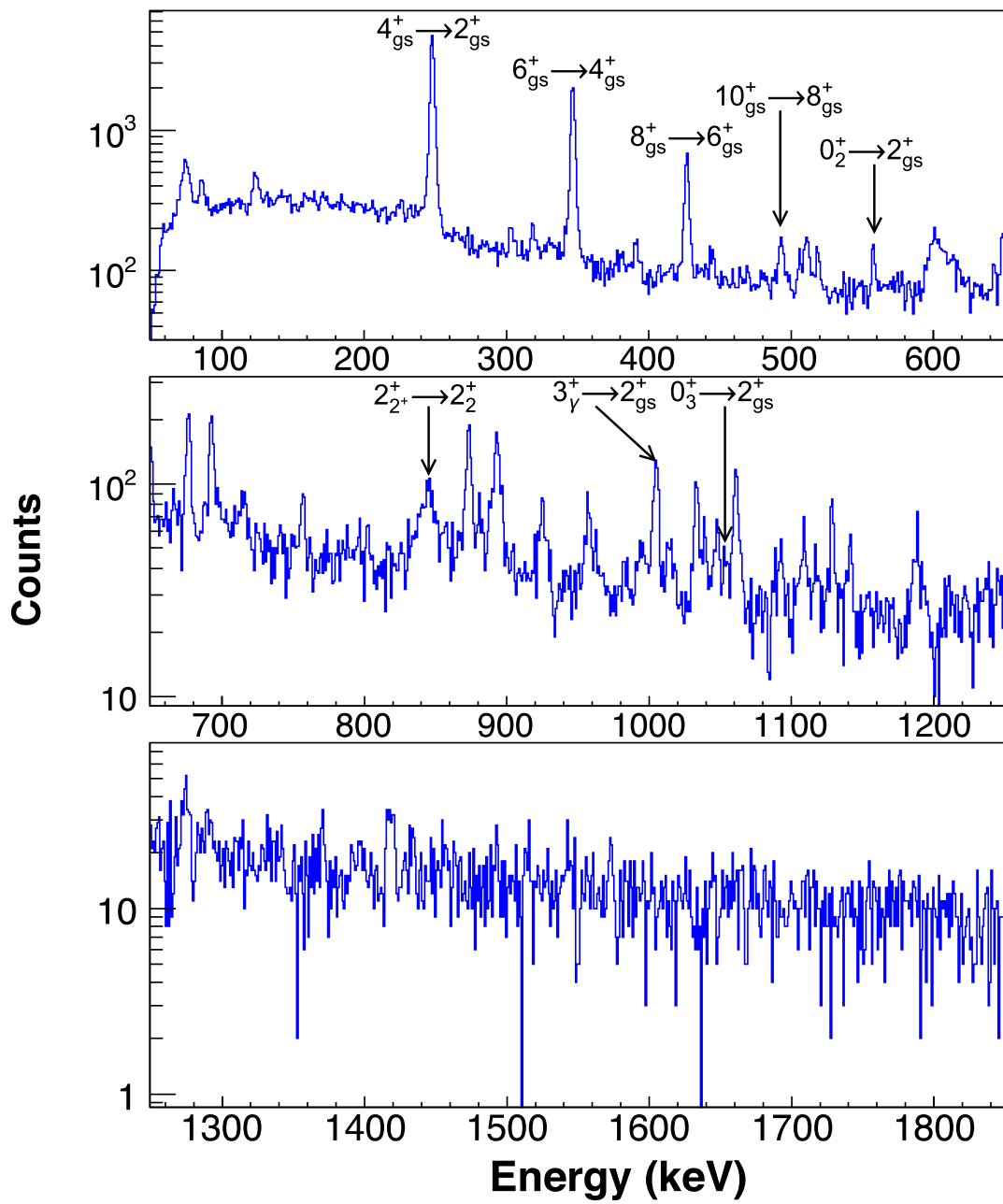
Figure 4.4(a) Level Scheme of ^{154}Gd . The gate on the $2_{gs}^+ \rightarrow 0_{gs}^+$ transition (123 keV) γ -component in the ground state. The lines shown are in coincidence. The levels are organized by band. The lower levels of the band, unseen by gamma rays in this gate, are in blue. (b) Gamma spectrum gated on 123 keV, corresponding to the $2_{gs}^+ \rightarrow 0_{gs}^+$ transition. Several transitions have been labeled, corresponding to the level scheme.

90I



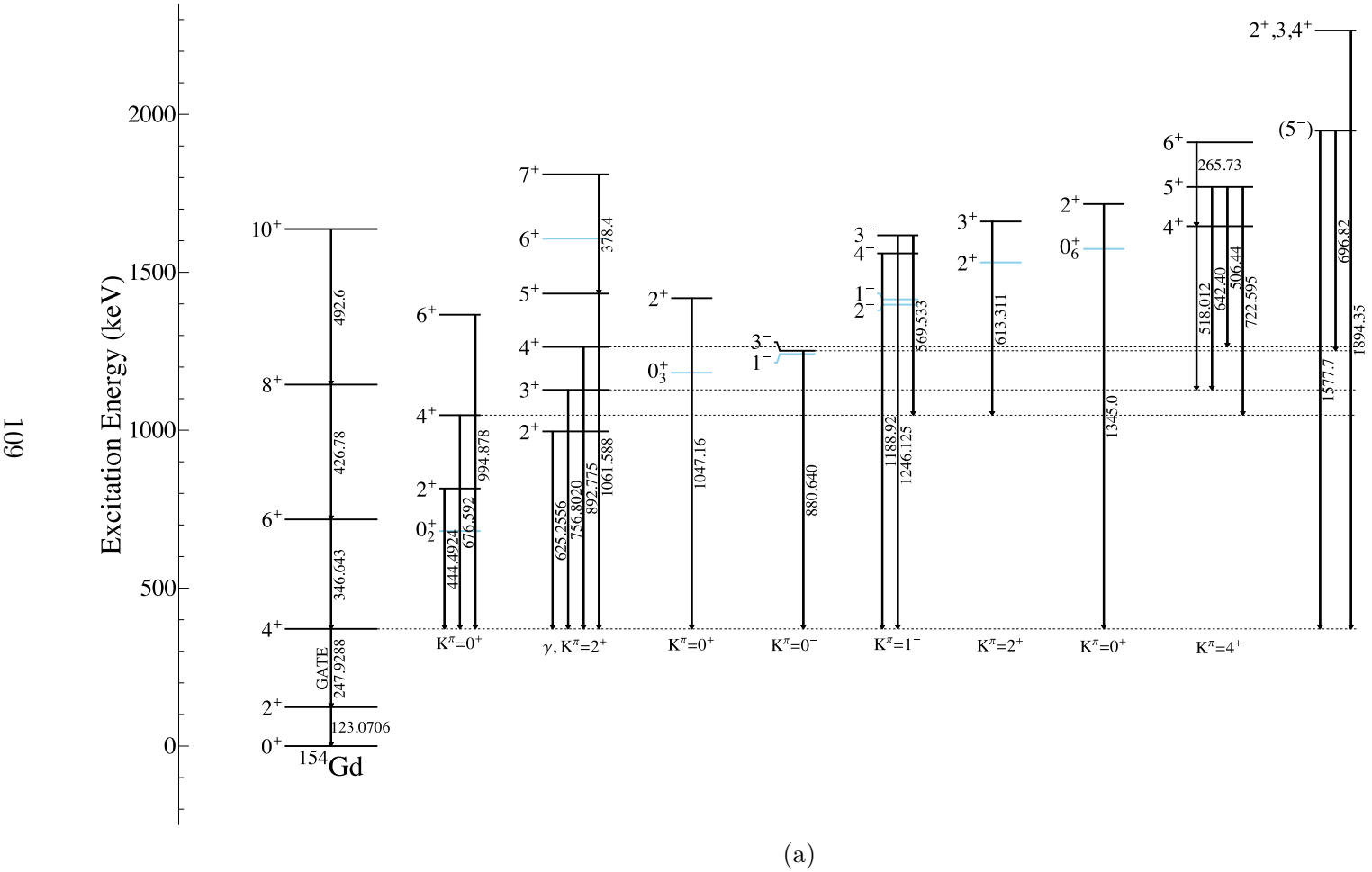
(a)

123 keV gated spectra

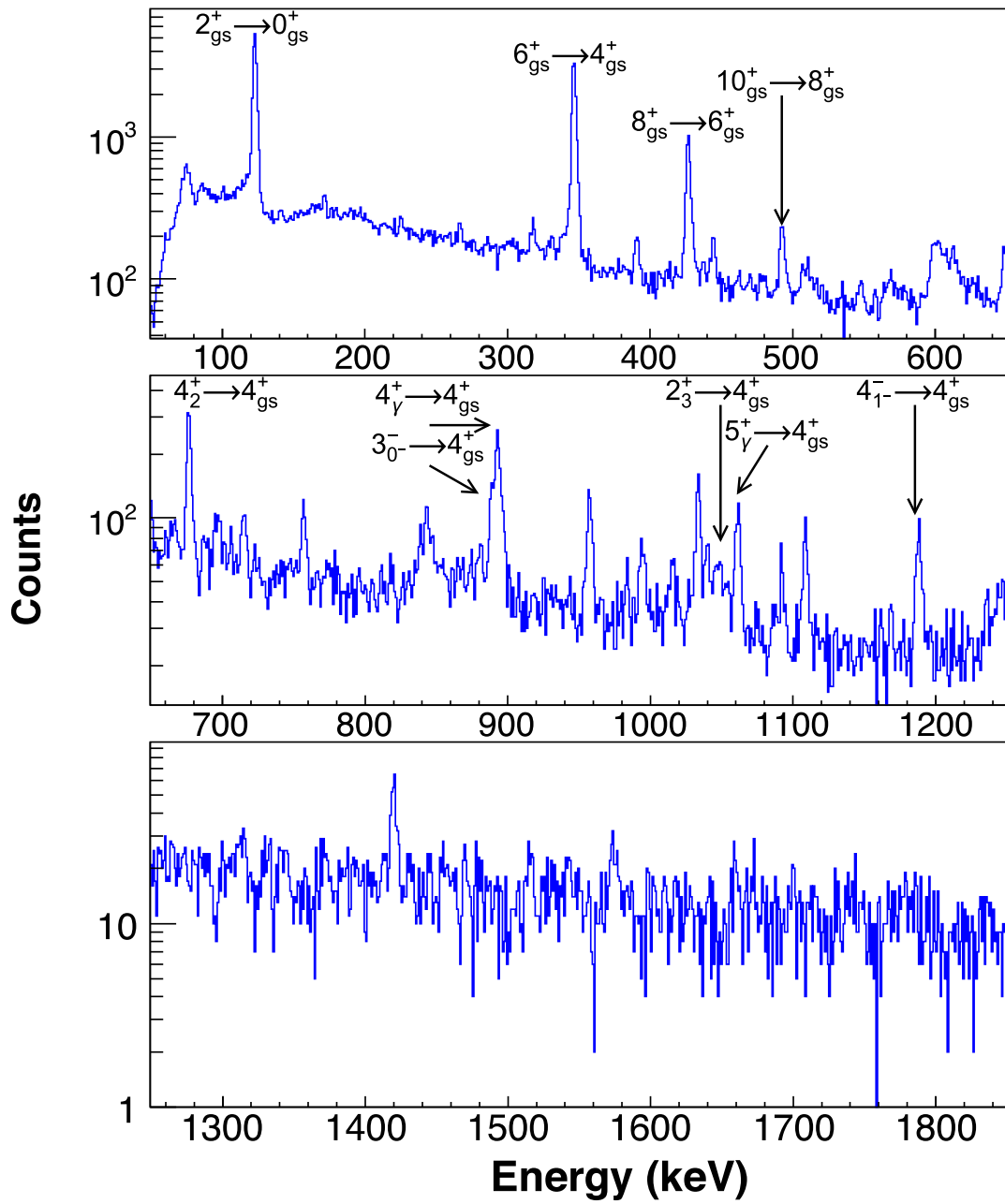


(b)

Figure 4.5(a) Level Scheme of ^{154}Gd . The gate on the $4_{gs}^+ \rightarrow 2_{gs}^+$ transition (247 keV) γ -component in the ground state. The lines shown are in coincidence. The levels are organized by band. The lower levels of the band, unseen by gamma rays in this gate, are in blue. (b) Gamma spectrum gated on 247 keV, corresponding to the $4_{gs}^+ \rightarrow 2_{gs}^+$ transition. Several transitions have been labeled, corresponding to the level scheme.

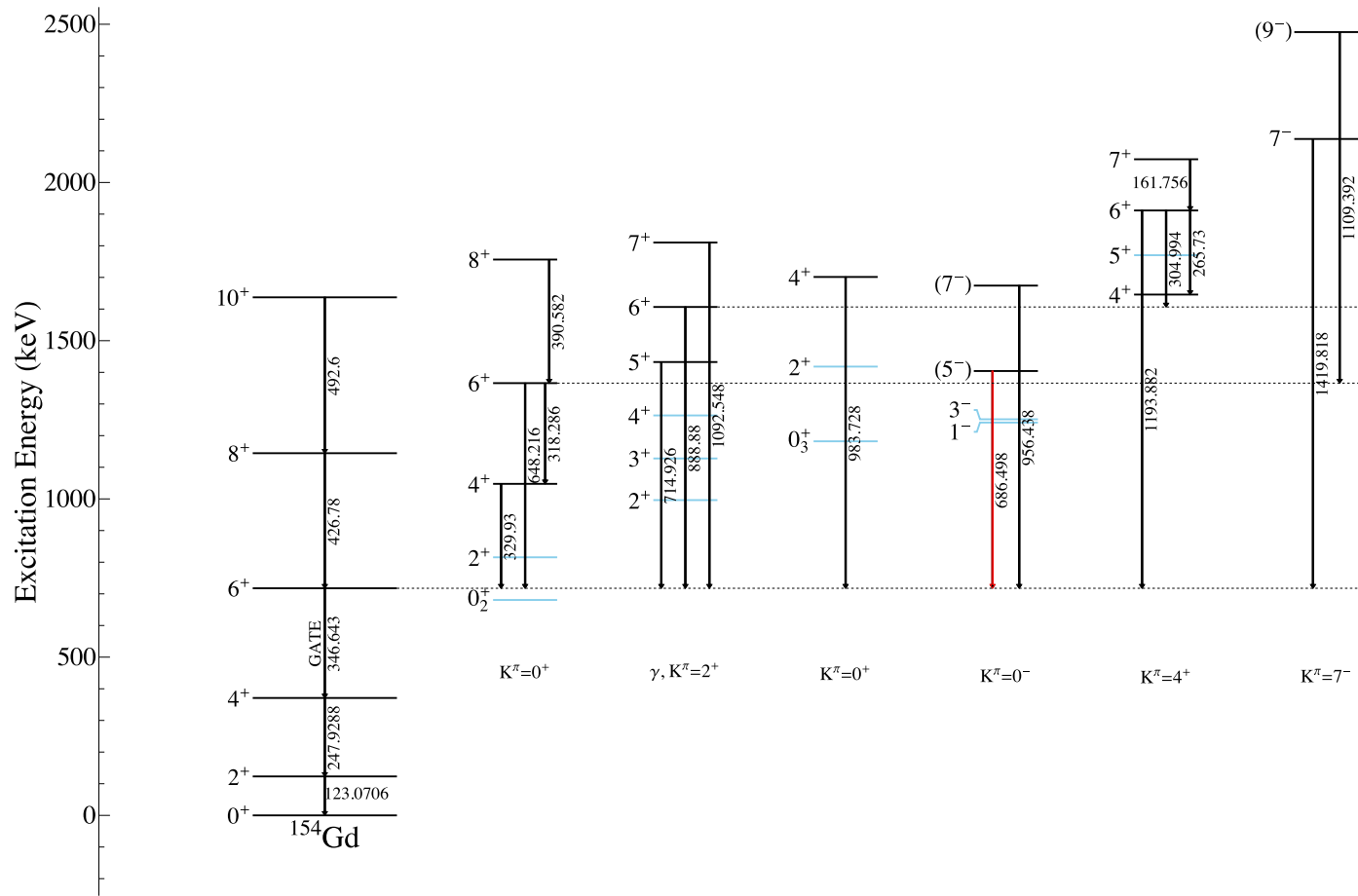


247 keV gated spectra



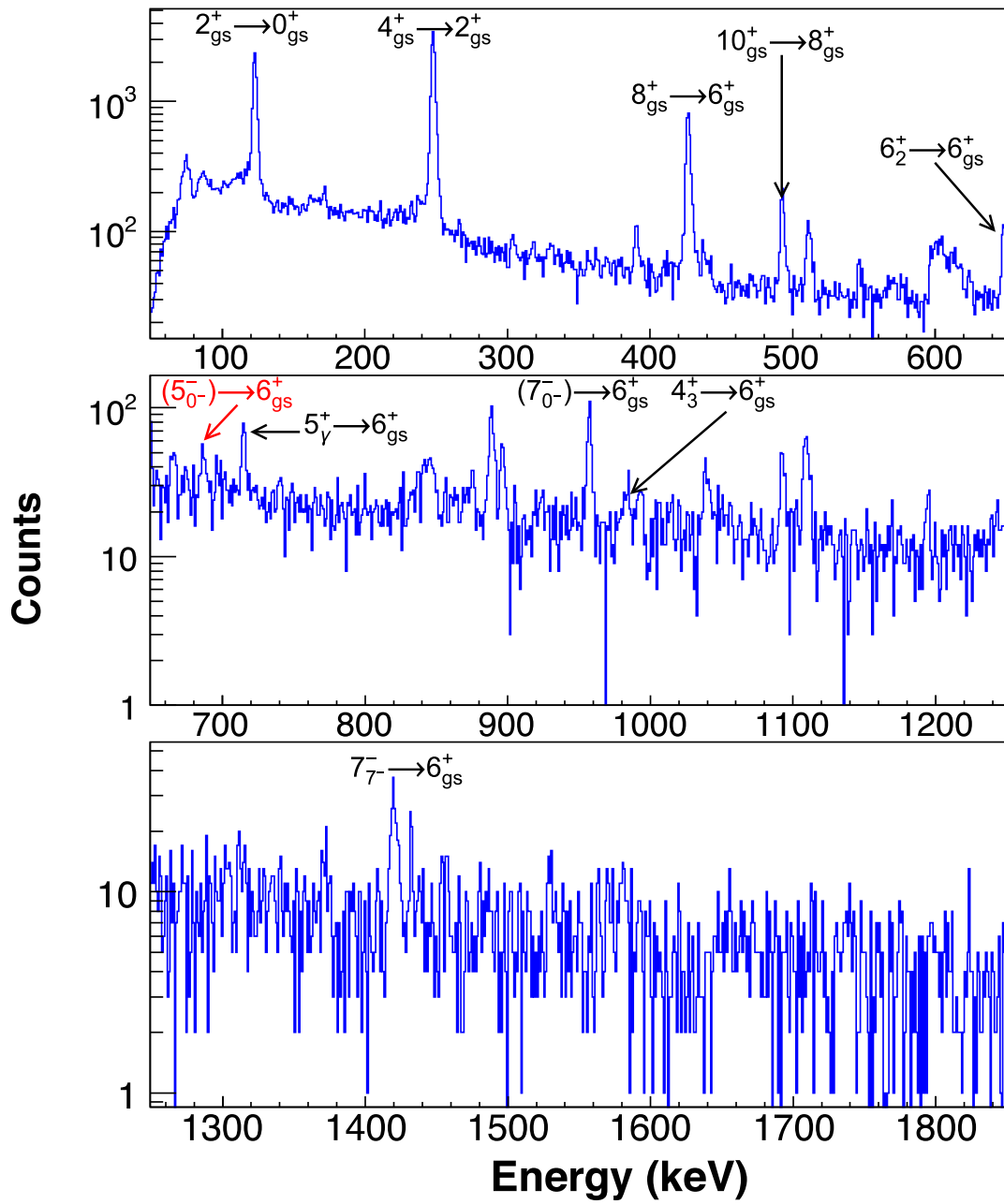
(b)

Figure 4.6(a) Level Scheme of ^{154}Gd . The gate on the $6_{gs}^+ \rightarrow 4_{gs}^+$ transition (346 keV) γ -component in the ground state. The lines shown are in coincidence. The levels are organized by band. The lower levels of the band, unseen by gamma rays in this gate, are in blue. (b) Gamma spectrum gated on 346 keV, corresponding to the $6_{gs}^+ \rightarrow 4_{gs}^+$ transition. Several transitions have been labeled, corresponding to the level scheme.



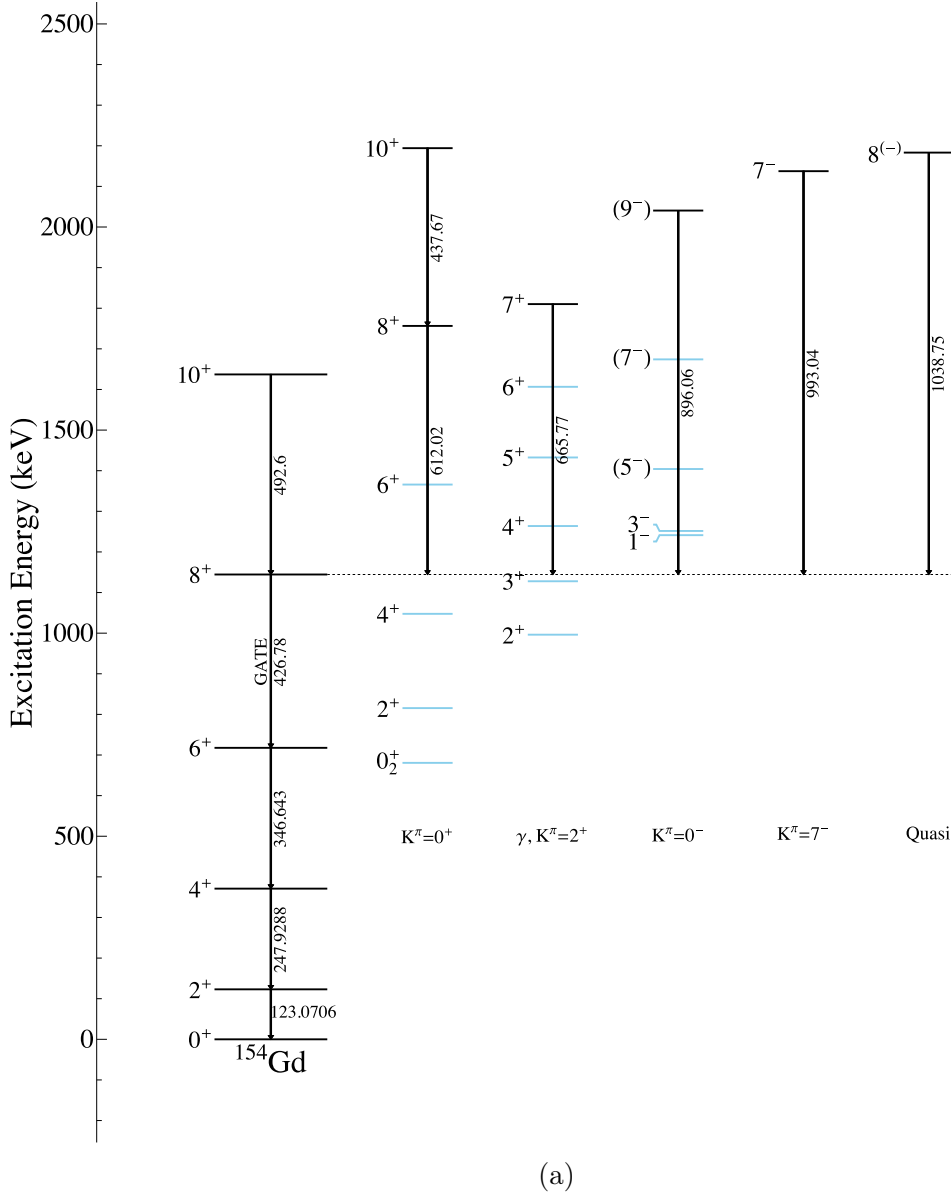
(a)

346 keV gated spectra



(b)

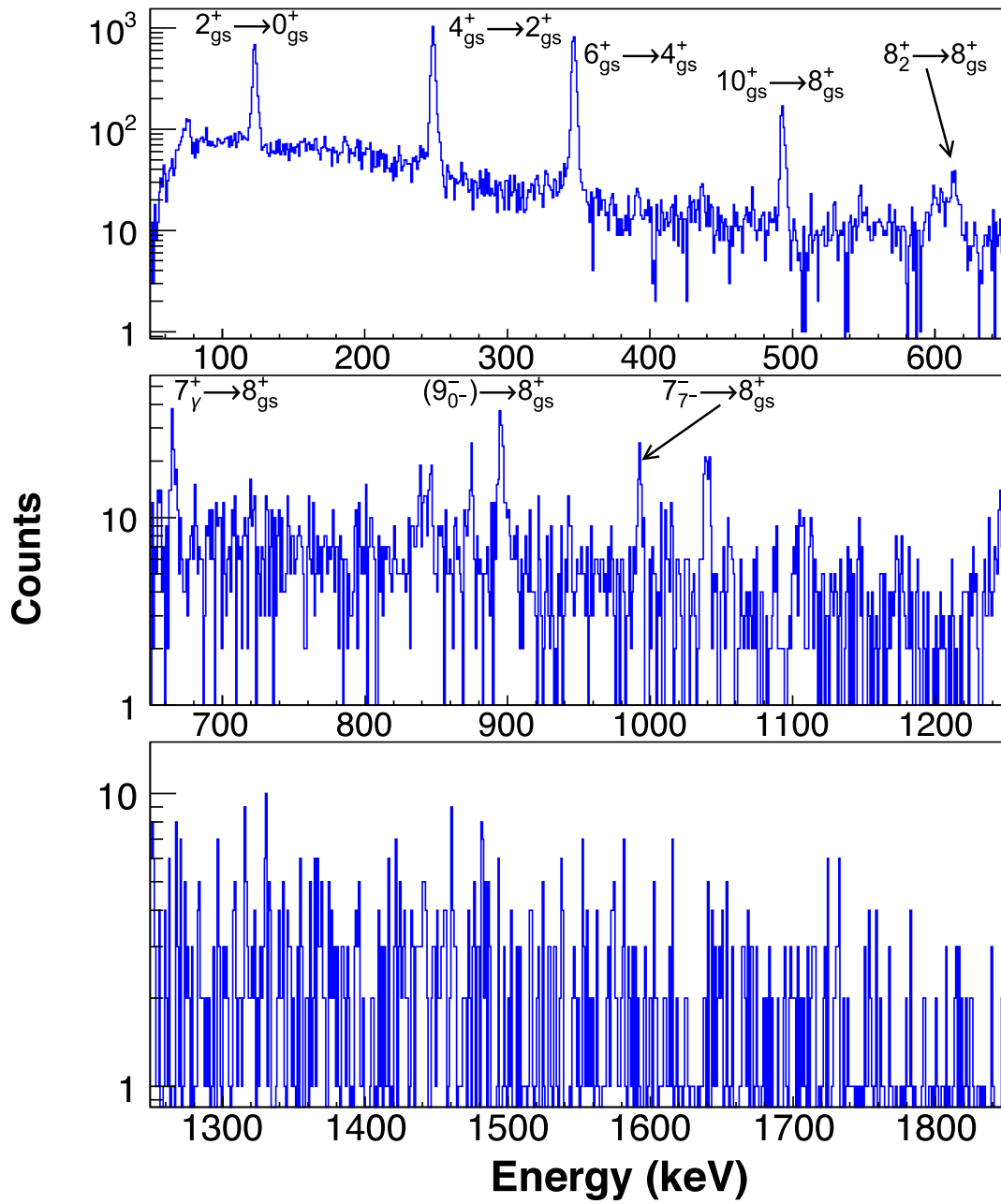
Figure 4.7(a) Level Scheme of ^{154}Gd . The gate on the $8_{gs}^+ \rightarrow 6_{gs}^+$ transition (426 keV) γ -component in the ground state. The lines shown are in coincidence. The levels are organized by band. The lower levels of the band, unseen by gamma rays in this gate, are in blue. (b) Gamma spectrum gated on 426 keV, corresponding to the $8_{gs}^+ \rightarrow 6_{gs}^+$ transition. Several transitions have been labeled, corresponding to the level scheme.



where α_{exp} is the uncorrected conversion coefficient, $C_\angle(\delta)$ is the angular distribution correction as a function of the mixing ratio, and $\alpha(E2), \alpha(M1)$ are the theoretical conversion coefficients from BrICC[40]. Two possible mixing ratios, $\delta = -1.68^{+30}_{-43}$ or 1.18^{+24}_{-19} were found.

Table 4.5 contains the conversion coefficients that could not be corrected because the transition has no multipole assignment. It contains allowable and reasonable theoretical conversion coefficients to compare the values against, calculated using

426 keV gated spectra



(b)

TABLE 4.3

 ^{154}GD INTERNAL CONVERSION COEFFICIENTS FROM SINGLES

(a)

E (keV)	$J^\pi \rightarrow J^\pi$	E_i (keV)	E_f (keV)	$T_{1/2}$ (fs)	Multipolarity	δ
232.44	$4_{0_2^+}^+ \rightarrow 2_{0_2^+}^+$	1047.592	815.4917	7600	E2	
329.49	$4_{0_2^+}^+ \rightarrow 6_{gs}^+$	1047.592	717.662	7600	E2	
349.89	$2_{2_2^+}^+ \rightarrow 0_{gs}^+$	1531.305	1182.091		[E2]	
416.79	$4_{0_6^+}^+ \rightarrow 3_{2_2^+}^+$	2080.23	1660.903		(M1)	
444.19	$2_{0_2^+}^+ \rightarrow 4_\gamma^+$	815.4917	370.9998	6400	E2	
506.41	$5_{4_1^+}^+ \rightarrow 4_\gamma^+$	1770.187	1263.778		E2	
515.92	$4_{4_1^+}^+ \rightarrow 3_\gamma^+$	1645.814	1127.802		E2+M1	-7 (3)
557.58	$0_{0_2^+}^+ \rightarrow 2_{gs}^+$	680.6673	123.0709	4560	E2	
610.71	$8_{0_2^+}^+ \rightarrow 8_{gs}^+$	1756.49	1144.44		E0+M1+E2	-0.69 (14)
676.70	$4_{0_2^+}^+ \rightarrow 4_{gs}^+$	1047.592	370.9998	7600	E0+M1+E2	+2.9 (4)
693.47	$2_{0_2^+}^+ \rightarrow 2_{gs}^+$	815.4917	123.0709	6400	E2+M1+E0	7.5 (4)
873.54	$2_\gamma^+ \rightarrow 2_{gs}^+$	996.2568	123.0709	950	E2+M1+E0	-9.4 (4)
889.61	$6_\gamma^+ \rightarrow 6_{gs}^+$	1606.55	717.662		E2+M1	> 1.8
894.40	$4_\gamma^+ \rightarrow 4_{gs}^+$	1263.778	370.9998		E0+M1+E2	-3.8 (3)
924.85	$4_{0_2^+}^+ \rightarrow 2_{gs}^+$	1047.592	123.0709	7600	E2	
996.33	$2_\gamma^+ \rightarrow 0_{gs}^+$	996.2568	0	950	E2	
1005.12	$3_\gamma^+ \rightarrow 2_{gs}^+$	1127.8018	123.0709		E2+M1	-7.4 (4)

TABLE 4.3 (CONTINUED)

(b)

E (keV)	Shell	α (This Work)	α (Th)[40]	α (Spits)[75]	α (Gono)[31]
232.44	K	0.287 (103) $^{+83}_{-82}$	0.0982 (14)	0.100 (8)	
	LM	0.0450 (46) (13)	0.0288 (4)		
329.49	K	0.1573 (89) (17)	0.0352 (5)	0.034 (3)	
349.89	K	0.0298 (8) $^{+8}_{-7}$	0.0296 (5)	< 0.097	
416.79	K	0.0334 (47) (6)	0.03442 (5)		
444.19	K	0.0525 (32) (6)	0.01543 (22)	0.014 (1)	
506.41	K	0.0071 (4) (1)	0.01098 (16)	0.0100 (11)	
515.92	K	0.0069 (5) (1)	0.0107 (4)	0.0113 (9)	
557.58	K	0.0486 (42) (6)	0.00864 (12)	0.009 (1)	0.0091 (16)
610.71	K	0.0258 (10) (7)	0.0110 (6)		0.053 (7)
	L	0.0167 (9) (4)	0.00158 (7)		
676.70	K	0.0283 (4) (10)	0.00593 (17)	0.0460 (46)	0.040 (7)
693.47	K	0.0017 (2) (1)	0.00522 (8)	0.0421 (4)	
873.54	K	0.0021 (3) (1)	0.00311 (5)	0.0035 (1)	
889.61	K	0.0043 (6) (2)	0.00349 (5)	0.0033 (2)	
894.40	K	0.0019 (2) (1)	0.00307 (5)	0.0039 (3)	
924.85	K	0.0033 (9) (1)	0.00273 (4)	0.0031 (1)	
996.33	K	0.0021 (4) (1)	0.00234 (4)	0.0025 (1)	
1005.12	K	0.0019 (1) (1)	0.00233 (4)	0.0024 (1)	

Table 4.3: A list of conversion coefficients from ^{154}Gd . Table (a) lists transition information. Multipolarities and mixing ratios were taken from the nuclear data sheets[64]. Table (b) lists the conversion coefficients. Unless otherwise stated, the α values are α_K . An angular distribution correction has been applied based on multipolarities for pure transitions, and those with known mixing ratios. The first error is statistical, the second is systematic. Numbers are compared with Spits et al.[75] and Gono et al.[31] The starred value was used as an absolute calibration of the conversion electron detector in the Gono work. The bands for each level are listed as subscripts.

TABLE 4.4

 UNCORRECTED ^{154}GD INTERNAL CONVERSION COEFFICIENTS
 FROM SINGLES

(a)

E (keV)	$J^\pi \rightarrow J^\pi$	E_i (keV)	E_f (keV)	Multipolarity	δ
198.311	$3_{1-}^- \rightarrow 2_{0_3^+}^+$ $(9)_{4_1^+}^+ \rightarrow (8)_{4_1^+}^+$	1617.123 2453.29	1418.16 2254.12	[E1]	
313.21	$3_\gamma^+ \rightarrow 2_{0_2^+}^+$	1127.802	815.492	[M1,E2]	
641.92	$5_{4_1^+}^+ \rightarrow 3_\gamma^+$	1770.187	1127.8018	M1,E2	
648.951	$6_{0_2^+}^+ \rightarrow 6_{gs}^+$	1365.87	717.662	E0+M1+E2	+1.30 (20)
715.198	$2_{2_2^+}^+ \rightarrow 2_{0_2^+}^+$	1531.305	815.492	E0+M1+E2	
1061.59	$0_{0_3^+}^+ \rightarrow 2_{gs}^+$ $5_\gamma^+ \rightarrow 4_{gs}^+$	1182.091 1432.588	123.0709 370.9998	E2 E2+M1	-4.3_{-26}^{+12}

TABLE 4.4 (CONTINUED)

(b)

E (keV)	Shell	α (This Work)		α (Th)[40]	α (Spits)[75]	α (Gono)[31]
		Uncorrected	Corrected			
198.311	K	0.0842 (26) (19)	0.0568 (18) (13)	0.0393 (6)		
			[M1] 0.0986 (30) (22)	[M1] 0.248 (4)		
			[E2] 0.1144 (35) (26)	[E2] 0.1587 (23)		
313.21	K	0.0805 (47) (20)	[M1] 0.0543 (32) (13)	[M1] 0.0723 (11)		
			[E2] 0.0832 (49) (21)	[E2] 0.0407 (6)		
641.92	K	0.0303 (7) (8)	0.0249 (6) (2)	0.00615 (9)	0.0086 (8)	
648.951		0.0079 (5)	0.0082 (5)	0.0079 (5)		0.039 (7)
715.198	K	0.0199 (5) (5)	[M1] 0.0299 (8) (8)	[M1] 0.00879 (13)	0.0070 (5)	
			[E2] 0.0150 (4) (4)	[E2] 0.00479 (7)		
		0.0041 (4) (1)	[M1] 0.0061 (6) (2)			
1061.59	K	0.0022 (3) (1)	0.0046 (6) (2)	0.0021 (1)		
			0.0021 (1)	0.0014 (1)	0.0019 (4)	

Table 4.4: A list of conversion coefficients from ^{154}Gd . Table (a) lists transition information. Multipolarities and mixing ratios were taken from the nuclear data sheets[64]. Table (b) lists the conversion coefficients. Unless otherwise stated, the α values are α_K . An angular distribution correction has been applied in the second column of this work, with both the pure M1 and E2 coefficients listed in the cases where the transition does not have a mixing ratio. No M1 information is listed for the $5_{4+}^+ \rightarrow 3_\gamma^+$, as that is not a possible transition by selection rules. The theoretical value for the $6_{0_2^+}^+ \rightarrow 6_{gs}^+$ transition assumes no E0 component. None of the above transitions have known half-lives. The first error is statistical, the second is systematic. Numbers are compared with Spits et al.[75]. The bands for each level are listed as subscripts.

TABLE 4.5

^{154}GD INTERNAL CONVERSION ELECTRONS WITHOUT ASSIGNED
MULTIPOLEARITIES

(a)			
E (keV)	$J_i \rightarrow J_f$	E_i (keV)	E_f (keV)
266.37	$6_{4_1^+}^+ \rightarrow 4_{4_1^+}^+$	1911.544	1645.814
303.89	$(7^+)_{4_1^+} \rightarrow 5_{4_1^+}^+$	2073.30	1770.187
318.382	$6_{0_2^+}^+ \rightarrow 4_{0_2^+}^+$	1365.87	1047.592
379.55	$7_\gamma^+ \rightarrow 5_\gamma^+$	1810.21	1432.588
433.12	$4_{0_6^+}^+ \rightarrow 4_{4_1^+}^+$	2080.23	1645.814
687.05	$(5^-)_{0-} \rightarrow 6_{gs}^+$	1404.16	717.662
722.64	$5_{4_1^+}^+ \rightarrow 4_{0_2^+}^+$	1770.187	1047.592
1033.91	$3^- \rightarrow 4_{0_2^+}^+$	2080.791	1047.592

TABLE 4.5 (CONTINUED)

(b)

E (keV)	Shell	α (This Work)		Theory[40]			α (Spits)[75]
		Uncorrected	Corrected	$\alpha(M1)$	$\alpha(E2)$	$\alpha(E1)$	
266.37	K	0.2074 (74) (50)	0.1684 (60) (41)		0.0654 (10)		
303.89	K	0.1183 (40) $^{+30}_{-29}$	0.0954 (32) $^{+24}_{-23}$		0.0444 (7)		
318.382	K	0.0736 (18) (18)	0.0600 (15) (15)		0.0388 (6)		
	L	0.0371 (12) (9)	0.0301 (10) (7)		0.00892 (13)		
379.55	K	0.1120 (60) (31)	0.0903 (48) (25)		0.0236 (4)		
433.12	K	0.0571 (42) (15)	[M1] 0.0777 (57) (20) [E2] 0.0351 (26) (9)	0.0310 (5)	0.01650 (24)		0.0220 (45)
687.05	K	0.3538 (116) (90)	0.6435 (211) (163)			0.00203 (3)	
722.64	K	0.0166 (12) (42)	[M1] 0.0107 (8) (27) [E2] 0.0185 (13) (47)	0.00856 (12)	0.00468 (7)		
1033.91	K	0.0015 (4) (1)	0.0028 (7) (2)			0.000916 (13)	

Table 4.5: A list of conversion coefficients from ^{154}Gd without known multipolarities. Table (a) lists transition information. Table (b) lists the conversion coefficients and theoretical values. As a result, an angular distribution correction term cannot be applied to compare with theory, except in the case of pure multipoles. None of the above transitions have known half-lives. The first error is statistical, the second is systematic. Numbers are compared with theoretical coefficients for allowed and reasonable polarities, as well as results from Spits et al. [75] The bands for each level are listed as subscripts. The 3^- for $E = 1033.91$ keV has no band placement.

BrIcc [40].

In Table 4.3, there are several conversion coefficients that are high, not only compared to theory, but compared to previous measurements (232, 329, 444, and 557 keV). For the 232 keV transition, the large error hints at a lack of statistics. For the other three transitions, the transition indicates a change from smaller to larger J^π . The angular distribution correction for such transitions is less than 1, inflating the value. This may be an indication the angular distribution correction is not wholly accurate. Further, due to these values being from singles data, unknown contaminants to the electron spectrum cannot be ruled out. While these transitions were identified clearly and separably, low-intensity gamma-rays may have not have had enough statistics to appear in gated spectra. There are also three transitions that are lower than the theoretical values (515, 873 and 894 keV). In all of these cases, δ is negative. Finally, there are several $J^\pi \rightarrow J^\pi$ transitions seen in the singles. For the $4_{0_2^+}^+ \rightarrow 4_{gs}^+$ between the first excited 0^+ band and the ground state band at 676 keV, there is clearly an E0 component, although not as big at that seen by Spits or Gono [31, 75]. It is a similar situation for the $8_{0_2^+}^+ \rightarrow 8_{gs}^+$ at 610 keV compared to Gono. Additionally, there is a $6_\gamma^+ \rightarrow 6_{gs}^+$ transition at 889 keV that is higher than number from Spits and the theoretical conversion coefficient. The $4_\gamma^+ \rightarrow 4_{gs}^+$ was also found in gating, as will be discussed in the next section.

In Table 4.4, the $2_{2_2^+}^+ \rightarrow 2_{0_2^+}^+$ transition at 715 keV appears to have a large E0 component. This transition is examined in the next section. For the two entangled transitions around 645 keV, the $6_{0_2^+}^+ \rightarrow 6_{gs}^+$ transition is likely the dominant contribution, as the measured value in the singles is in good agreement with the measured value in the gated data, see Table 4.10. Two separate α values are listed in this part of Table 4.4, as the gamma-rays were separable, but the conversion electron peaks were not.

In Table 4.5, the $4_{0_6^+}^+ \rightarrow 4_{4_1^+}^+$ transition at 433 keV either indicates a mixed transi-

tion with an E0 component. The angular correction for a pure E2 transition would make the conversion coefficient approximately double the theoretical conversion coefficient from BrICC [40]. This angular correction is the largest correction that can be made. Mixed component angular corrections result in values larger than the theoretical M1 transition. Together, this points toward an E0 component to the transition. Unfortunately, these transitions could not be found in gates, as the levels are too high in energy to be populated significantly enough for gates.

4.4 $J^\pi \rightarrow J^\pi$ Transitions

4.4.1 $0^+ \rightarrow 0^+$ Identification and Population

With the large number of 0^+ states in ^{154}Gd , our first priority was to identify which bands were populated. Table 4.6 contains a list of 0^+ states from Meyer et al, with indications as to which 0^+ have been observed outside of the discovery paper, and which have been previously observed in the reaction used in this work [54].

Many of the states were left unseen in this work as is to be expected. We have seen all states that were observed previously in $(\alpha, 2n)$ experiments, in addition to three other 0^+ excited states. The energy of the 12^+ in the ground state band, 2184.69 keV, is the rough cut off for populating states. The levels seen in this work exceed previous $(\alpha, 2n)$ experiments and agree with the levels seen in Spits et al, a thermal neutron capture experiment[75]. Until Spits, there was no known spectroscopy for the 1182, 1573 and 1650 keV states, having only been seen previously in (p, t) and (t, p) experiments. No $(\alpha, 2n)$ experiments with $\gamma - \gamma$ coincidence, looking for such levels have been run since Spits et al was published in 1996. The energies of the $0^+ \rightarrow 0^+$ transitions from these states are marked in the electron singles in Figure 4.8. The most prominent is the $0_2^+ \rightarrow 0_{gs}^+$ transition. The $0_7^+ \rightarrow 0_3^+$ transition is at the energy of the $10_{gs}^+ \rightarrow 8_{gs}^+$ K-electron energy, and the $0_6^+ \rightarrow 0_3^+$ transition is

TABLE 4.6

 0^+ STATES IN ^{154}GD

Energy (keV)	Seen Previously [54]	Seen in $(\alpha, 2n)$	Seen in This Work
0	×	×	×
680.4(3)	×	×	×
1181.9(3)	×		×
1352.9(3)			
1497.7(3)			
1573.7(3)	×		×
1650.6(4)	×		×
1836.7(4)			
1899.3(4)			
1942.9(4)			
2039.8(4)			
2299.9(5)	×		
2485.1(5)			
2585.3(5)			
2744.5(5)	×		
2855.0(5)	×		

Table 4.6: A list of all 0^+ states in ^{154}Gd . All the states listed were seen in Meyer et al, a (p, t) experiment[54]. 0^+ states above approximately 2184 keV would not be seen in this experiment, the energy of the 12^+ ground state, as that is the energy cut off in the nucleus for state population, discussed in the text. The levels seen in this exceed previous $(\alpha, 2n)$ experiments and agree with the levels seen in Spits [75]. Until Spits, there was no known spectroscopy for the 1182, 1573 and 1650 keV states, having only been seen previously in (p, t) and (t, p) experiments. No $(\alpha, 2n)$ experiments with $\gamma - \gamma$ coincidence, looking for such levels have been run since Spits et al was published.

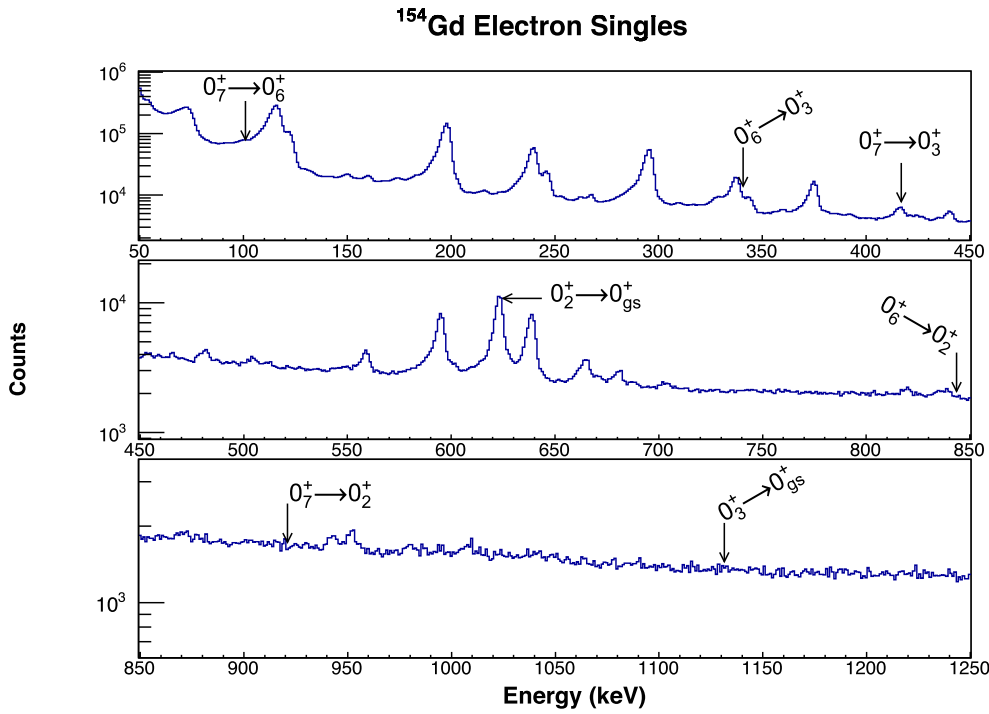


Figure 4.8. Electron singles for ^{154}Gd . The energies of transitions between 0^+ states are marked in the plot. The most prominent is the $0_2^+ \rightarrow 0_{gs}^+$ transition. The $0_7^+ \rightarrow 0_3^+$ transition is at the energy of the $10_{gs}^+ \rightarrow 8_{gs}^+$ K-electron energy, and the $0_6^+ \rightarrow 0_3^+$ transition is between the $8_{gs}^+ \rightarrow 6_{gs}^+$ L and M electron energies. The $0_7^+ \rightarrow 0_6^+$ transition may be present, but sits on the low energy tail of the $2_{gs}^+ \rightarrow 0_{gs}^+$ L electron peak.

between the $8_{gs}^+ \rightarrow 6_{gs}^+$ L and M electron energies. The $0_7^+ \rightarrow 0_6^+$ transition may be present, but sits on the low energy tail of the $2_{gs}^+ \rightarrow 0_{gs}^+$ L electron peak. To obtain information in these areas, and for possible $J^\pi \rightarrow J^\pi$ transitions, energy gates were used. A full list of gates and spectra can be found in Appendix ??.

4.4.2 $J^\pi \rightarrow J^\pi$ Transitions

After identification of the bands and transitions, gates were put on the outgoing and incoming transitions of states of interest, namely even- J^+ states. Gates on

incoming transitions did not have enough statistics to extract data on transitions of interest from the resulting spectra. However, gates on outgoing transitions allowed enough statistics to look for transitions from states of the same J^π . In many cases, two separate outgoing transition gates could be used to look at the same state. To look for these transitions of interest, other electron peaks, namely those of the ground state band, were subtracted from the regions of interest as described in Section 3.4. This subtraction technique causes the results to be treated as limits. Tables 4.7 - 4.10 are the tabulated results. Where previous measurements have been taken, they are listed. Additionally, the theoretical conversion coefficients have been listed for $M1$ and $E2$ transitions, as taken from BrIcc [40].

As is expected, Table 4.7 is only lower limits. A lower limit in this table is an indication of the noise in the gamma spectrum that acts as the limit for the ability to see a line in the spectrum. Although $M1$ and $E2$ transitions are not allowed, they have been included in the table for the sake of comparison. The lower limits, expectedly, rule out the $M1$ and $E2$ transitions. The measured limits agree with the ones seen by Spits [75].

In Tables 4.8, 4.9 and 4.10 many of the transitions could be seen in two different gates. In many cases, only lower limits could be seen due to the noise limit in the gamma spectrum. In other cases, only upper limits could be seen due to the same effect in the electron spectrum.

The majority of these states do not have lifetimes, so $B(E0)$ values cannot be calculated. However, the relative intensities of these values can be compared, assuming they are coming from the same state, as the lifetime would divide out (see equation 1.36 and 1.37). The contributions from the individual components of the transition must be separated out.

To compare the $E0$ components, the other two major contributing components ($M1$ and $E2$) had to be subtracted out. This was done by calculating ϵ^2 via equation

TABLE 4.7

 $0^+ \rightarrow 0^+$ TRANSITIONS IN ^{154}GD

E_i (keV)	Band	E_f (keV)	Band	E (keV)	Gate	α (This Work)	Theory[40]		
							α (M1)	α (E2)	α (Spits)[75]
1182.091	0_3^+	680.6673	0_2^+	501.427	557.581	> 0.0283	0.0213 (3)	0.01126 (16)	> 0.2
1573.9	0_6^+	680.6673	0_2^+	893.9	557.581	> 0.0183	0.00510 (8)	0.00294 (5)	
1573.9	0_6^+	1182.091	0_3^+	391.9	1059.033	> 0.0529	0.0402 (6)	0.0216 (3)	> 0.1
1650.3	0_7^+	680.6673	0_2^+	970.3	557.581	> 0.0209	0.00419 (6)	0.00247 (4)	> 0.027
1650.3	0_7^+	1182.091	0_3^+	468.3	1059.033	> 0.0922	0.0254 (4)	0.01343 (19)	

Table 4.7: A list of conversion coefficients from ^{154}Gd for $0^+ \rightarrow 0^+$ transitions seen in the gated data. All are lower limits. Numbers are compared with Spits et al.[75] and theoretical coefficients for M1 and E2 transitions. All coefficients are K-electrons.

TABLE 4.8

 $2^+ \rightarrow 2^+$ TRANSITIONS IN ^{154}GD

E_i (keV)	Band	E_f (keV)	Band	E (keV)	Gate	α (This Work)	Theory[40]		
							α (M1)	α (E2)	α (Spits)[75]
815.4917	0_2^+	123.0709	GS	692.4205	123.0706	0.0430 (3) (9)	0.00952 (14)	0.00516 (8)	0.0421 (4)
996.264	γ	815.4917	0_2^+	180.72	692.4205	> 1.0570	0.320 (5)	0.210 (3)	
					444.4924	> 0.9718			
1418.16	0_3^+	815.4917	0_2^+	602.688	692.4205	> 0.0125	0.01343 (19)	0.00715 (10)	0.025 (3)
					444.4924	> 0.0093			
1418.16	0_3^+	996.2568	γ	421.893	873.1834	> 0.0367	0.0332 (5)	0.01170 (25)	0.114 (16)
					625.2556	> 0.0463			
1531.305	2_2^+	815.4917	0_2^+	715.819	692.4205	$0.0146 (40)^{+43}_{-33}$	0.00877 (13)	0.00478 (7)	0.0070 (4)
					444.4924	$0.0234(80)^{+68}_{-52}$			
1531.305	2_2^+	996.2568	γ	535.050	873.1834	$0.0204 (70)^{+54}_{-41}$	0.0181 (3)	0.00956 (14)	0.093 (11)
					625.2556	> 0.0183			
1716.050	0_6^+	815.4917	0_2^+	900.5583	692.4205	< 0.0105	0.00501 (7)	0.00289 (4)	

TABLE 4.8 (CONTINUED)

E_i (keV)	Band	E_f (keV)	Band	E (keV)	Gate	α (This Work)	Theory[40]		
							α (M1)	α (E2)	α (Spits)[75]
					444.4924	< 0.0531			
1716.050	0_6^+	996.2568	γ	719.80	873.1834 625.2556	0.0113 (46) $^{+33}_{-25}$ 0.0501 (260) $^{+147}_{-113}$	0.00865 (13)	0.00472 (7)	
1775.429	0_7^+	815.4917	0_2^+	960.05	692.4205 444.4924	> 0.0221 > 0.0231	0.00430 (6)	0.00253 (4)	
1775.429	0_7^+	996.2568	γ	779.165	873.1834 625.2556	0.0206 (112) $^{+60}_{-46}$ 0.0745 (521) $^{+217}_{-165}$	0.00712 (10)	0.00396 (6)	

Table 4.8: A list of conversion coefficients from ^{154}Gd for $2^+ \rightarrow 2^+$ transitions seen in the gated data. The first error is statistical, the second is systematic. Numbers are compared with theoretical K-shell conversion coefficients for M1 and E2 transitions, as well as results from Spits et al.[75] All coefficients are K-electrons.

TABLE 4.9

 $4^+ \rightarrow 4^+$ TRANSITIONS IN ^{154}GD

E_i (keV)	Band	E_f (keV)	Band	E (keV)	Gate	α (This Work)	Theory[40]		α (Spits)[75]	α (Gono)[31]
							α (M1)	α (E2)		
1047.592	0_2^+	370.9998	GS	676.593	247.9288	0.0550 (2) $^{+12}_{-11}$ 0.0131 (1) (3)	0.01007 (15) 0.001384 (20)	0.00544 (8) 0.000870 (13)	0.0460 (46)	0.040 (7)
1263.778	γ	1047.592	0_2^+	216.186	676.593 924.55	< 0.1250 < 0.1033	0.196 (3)	0.1222 (18)		
1645.814	4_1^+	1047.592	0_2^+	598.22	676.593 924.55	< 0.0092 < 0.0142	0.01368 (20)	0.00728 (11)	< 0.067	
1645.814	4_1^+	1263.778	γ	382.025	892.775 1140.702	< 0.0360 < 0.0494	0.0429 (6)	0.0232 (4)	0.033 (5)	
1701.39	0_3^+	1047.592	0_2^+	653.7	676.593 924.55	< 0.0093 < 0.0301	0.01097 (16)	0.00590 (9)	0.0220 (62)	
1701.39	0_3^+	1263.778	γ	437.612	892.775 1140.702	< 0.0585 < 0.0511	0.0302 (5)	0.01605 (23)		

TABLE 4.9 (CONTINUED)

E_i (keV)	Band	E_f (keV)	Band	E (keV)	Gate	α (This Work)	Theory[40]		α (Spits)[75]	α (Gono)[31]
							α (M1)	α (E2)		
1789.17	2_2^+	1047.592	0_2^+	740.91	676.593	< 0.0124	0.00806 (12)	0.00443 (7)		
					924.55	< 0.0447				
1789.17	2_2^+	1263.778	γ	525.392	892.775	< 0.0168	0.0190 (3)	0.01001 (14)		
					1140.702	< 0.0161				

Table 4.9: A list of conversion coefficients from ^{154}Gd for $4^+ \rightarrow 4^+$ transitions seen in the gated data. The first error is statistical, the second is systematic. Numbers are compared with theoretical K-shell conversion coefficients for M1 and E2 transitions, as well as results from Spits et al.[75] and Gono et al.[31] All coefficients are K-electrons, except for the transition from 1047 keV. The second value is the LM peak.

TABLE 4.10

 $6^+ \rightarrow 6^+$ TRANSITIONS IN ^{154}GD

E_i (keV)	Band	E_f (keV)	Band	E (keV)	Gate	α (This Work)	Theory[40]		α (Gono)[31]
							α (M1)	α (E2)	
1365.878	0_2^+	717.662	GS	648.3	346.643	0.0778 (4) (16)	0.01120 (16)	0.00601 (9)	0.039 (7)
1606.55	γ	1365.878	0_2^+	240.672	648.3 994.9	> 0.9065 > 1.1070	0.1462 (21)	0.0885 (13)	
1911.544	4_1^+	1365.878	0_2^+	545.7	648.3 994.9	< 0.0209 < 0.0189	0.01723 (25)	0.00911 (13)	
1911.544	4_1^+	1606.55	γ	304.75	888.69	< 0.0794	0.0777 (11)	0.0440 (7)	0.042 (6)

Table 4.10: A list of conversion coefficients from ^{154}Gd for $6^+ \rightarrow 6^+$ transitions seen in the gated data. The first error is statistical, the second is systematic. Numbers are compared with theoretical K-shell conversion coefficients for M1 and E2 transitions, as well as results from Gono et al.[31] All coefficients are K-electrons.

1.38. Transitions with known δ mixing ratios are in Table 4.13. Transitions without known δ mixing ratios, had δ assumed to be 1. In some cases, this left a negative value, which has been excluded from the table of results. These values are listed in Table 4.11. The $0^+ \rightarrow 0^+$ transitions are in Table 4.12. This subtraction was not done for the 0^+ transitions, as $M1$ and $E2$ transitions are not allowed. Most of the values calculated are upper or lower limits, as the original α obtained was an upper or lower limit.

The transitions with prominent E0 components are the $J_{0_2^+}^\pi \rightarrow J_{gs}^\pi$, $2_\gamma^+ \rightarrow 2_{0_2^+}^+$, $2_{0_2^+}^+ \rightarrow 2_\gamma^+$, $2_{0_6^+}^+ \rightarrow 2_\gamma^+$, $2_{0_7^+}^+ \rightarrow 2_\gamma^+$, $2_{0_7^+}^+ \rightarrow 2_{0_2^+}^+$ and $6_\gamma^+ \rightarrow 6_{0_2^+}^+$ transitions. Several others transitions may have further E0 components, as the upper limit does not rule an E0 component out or a lower limit doesn't give a clear indication of an E0 component.

With these values, two transitions from the same level can be compared using the $B(E0)$ formula to take the energy adjustment into account (equation 1.37). This ratio must then be corrected by the ratio of the gate efficiencies, as the intensities of the transitions are unknown, and the efficiency correction gives absolute numbers to compare. Because some transitions could be seen in multiple gates, these ratios could be calculated using several corrected numbers. These results are summarized in Table 4.14.

4.4.2.1 $K^\pi = 0_2^+$, First Excited 0^+ Band, 680.6673 keV

The $J^\pi \rightarrow J^\pi$ transitions between the first excited 0^+ band and the ground state band appear to be quite strong. Lifetimes beyond the 4^+ state in the band are unknown, inhibiting the ability to calculate ρ^2 for these transitions. In gating, the $2_{0_2^+}^+ \rightarrow 2_{gs}^+$, $4_{0_2^+}^+ \rightarrow 4_{gs}^+$, and $6_{0_2^+}^+ \rightarrow 6_{gs}^+$ transitions were seen. All three transitions indicated a strong E0 component. The $0_{0_2^+}^+ \rightarrow 0_{gs}^+$ and $8_{0_2^+}^+ \rightarrow 8_{gs}^+$ transitions could be seen in the singles, but not enough statistics were present in gates, viewable in Appendix ?? (the relevant gates for the $0_{0_2^+}^+ \rightarrow 0_{gs}^+$ transition are 134.8 keV and 850

TABLE 4.11

E0 CONTRIBUTIONS FOR $J^\pi \rightarrow J^\pi$ TRANSITIONS

E_i (keV)	Band	E_f (keV)	Band		E (keV)	Gate	$q^2\alpha(E2)$
$2^+ \rightarrow 2^+$							
996.264	γ	815.4917	0_2^+	602.688	692.4205		> 1.584
				444.4924			> 1.414
1418.16	0_3^+	815.4917	0_2^+	602.688	692.4205		> 0.0044
1418.16	0_3^+	996.2568	γ	421.893	625.2556		> 0.0477
				873.1834			> 0.0285
1531.305	2^+	815.4917	0_2^+	715.819	692.4205		$0.0157 (43)^{+46}_{-35}$
				444.4924			$0.0333 (114)^{+97}_{-74}$
1531.305	2^+	996.2568	γ	535.050	873.1834		$0.0131 (45)^{+35}_{-26}$
				625.2556			> 0.0089
1716.050	0_6^+	815.4917	0_2^+	900.5583	692.4205		< 0.0131
				444.4924			< 0.0983
1716.050	0_6^+	996.2568	γ	719.80	873.1834		$0.0092 (38)^{+19}_{-20}$
				625.2556			$0.0868 (451)^{+255}_{-196}$
1775.429	0_7^+	815.4917	0_2^+	960.05	692.4205		> 0.0374
				444.4924			> 0.0394
1775.429	0_2^+	996.2568	γ	779.165	873.1834		$0.0301 (164)^{+88}_{-67}$
				625.2556			$0.1379 (965)^{+401}_{-305}$
$4^+ \rightarrow 4^+$							
1645.814	4^+	1263.778	γ	382.025	892.775		< 0.0059
				1140.702			< 0.0033
1701.39	0_3^+	1047.592	0_2^+	653.7	676.593		< 0.0017

E_i (keV)	Band	E_f (keV)	Band	E (keV)	Gate	$q^2\alpha(E2)$
				924.55		< 0.0433
1701.39	0_3^+	1263.778	γ	437.612	892.775	< 0.0708
					1140.702	< 0.0560
1789.17	2^+	1047.592	0_2^+	740.91	676.593	< 0.0123
					924.55	< 0.0769
1789.17	2^+	1263.778	γ	525.392	892.775	< 0.0046
					1140.702	< 0.0319
$6^+ \rightarrow 6^+$						
1606.55	γ	1365.878	0_2^+	240.672	648.3	> 1.5783
					994.9	> 1.9793
1911.544	4^+	1365.878	0_2^+	545.7	648.3	< 0.0155
					994.9	< 0.0115
1911.544	4^+	1606.55	γ	304.75	888.69	< 0.0371

Table 4.11: A list of $E0$ contributions in ^{154}Gd , assuming a mixing ratio between the E2 and M1 contributions of $\delta = 1$. These values have not been normalized, as the lifetime of the states are unknown. Table 4.14 compares values between two transitions of the same initial state. Only non-negative values are listed in the table, and δ was assumed to be 1, as no mixing ratios are known for these transitions. For $\alpha(\text{exp})$, $\alpha(M1)$, and $\alpha(E2)$ used in these calculations, please refer to Tables 4.8-4.10. Bands are listed.

TABLE 4.12

 $q_K^2(E0/E2)$ FOR $0^+ \rightarrow 0^+$ TRANSITIONS

E_i (keV)	Transition	$E0$ (keV)	Transition	$E2$ (keV)	$q_K^2(E0/E2)$
1182.091	$0_3^+ \rightarrow 0_2^+$	501.427	$0_3^+ \rightarrow 2_{gs}^+$	1059.033	0.0023 (5)
1573.9	$0_6^+ \rightarrow 0_3^+$	391.85	$0_6^+ \rightarrow 2_{gs}^+$	1451.7	0.0521 (119)
1573.9	$0_6^+ \rightarrow 0_2^+$	893.9	$0_6^+ \rightarrow 2_{gs}^+$	1451.7	0.0168 (77)
1650.3	$0_7^+ \rightarrow 0_3^+$	468.3	$0_7^+ \rightarrow 2_{gs}^+$	1527.1	0.2082 (345)
1650.3	$0_7^+ \rightarrow 0_2^+$	970.3	$0_7^+ \rightarrow 2_{gs}^+$	1527.1	0.0402 (192)

Table 4.12: A list of $q_K^2(E0/E2)$ contributions in ^{154}Gd for the $0^+ \rightarrow 0^+$ transitions. These values cannot be converted to nuclear strengths, ρ^2 as the lifetimes are unknown.

TABLE 4.13

E0 CONTRIBUTIONS FOR $J^\pi \rightarrow J^\pi$ TRANSITIONS WITH KNOWN
MIXING RATIOS

E_i (keV)	Band	E_f (keV)	Band	E (keV)	δ	$t_{1/2}$ (ps)	Gate	ϵ^2	$\rho^2(E0)$
$2^+ \rightarrow 2^+$									
815.4917	0_2^+	123.0709	GS	692.4205	7.5 (4)	6.4 (4)	123.0706	1.9211 (1112) (402)	53.74 (900) (112)
$4^+ \rightarrow 4^+$									
1047.592	0_2^+	370.9998	GS	676.593	2.9 (4)	7.6 (4)	247.9288	0.4274 (60) $^{+93}_{-85}$	14.46 (335) $^{+31}_{-29}$
1645.814	4^+	1047.592	0_2^+	598.22	0.65 (20)		676.593	< 0.00003	
$6^+ \rightarrow 6^+$									
1365.878	0_2^+	717.662	GS	648.3	1.30 (20)		346.643	0.1843 (286) (38)	

Table 4.13: A list of $E0$ contributions in ^{154}Gd for data with known mixing ratios, δ . These values have not been normalized, as the lifetime of the states are unknown. Table 4.14 compares values between two transitions of the same initial state. Lifetimes are from [76]. For $\alpha(\text{exp})$, $\alpha(M1)$, and $\alpha(E2)$ used in these calculations, please refer to Tables 4.8-4.10.

TABLE 4.14

 $B(E0)$ RATIOS FOR $J^\pi \rightarrow J^\pi$ TRANSITIONS

E_i (keV)	Band	$E_{0_2^+}$ (keV)	Gate $_{0_2^+}$	$E_{0_3^+}$ (keV)	Gate $_{0_3^+}$	$B(E0)$ Ratio
$0^+ \rightarrow 0^+$						
1573.9	0_6^+	680.6673	557.581	1182.091	1059.033	0.219
1650.3	0_7^+	680.6673	557.581	1182.091	1059.033	0.090
E_i (keV)	Band	$E_{0_2^+}$ (keV)	Gate $_{0_2^+}$	E_γ (keV)	Gate $_\gamma$	$B(E0)$ Ratio
$2^+ \rightarrow 2^+$						
1418.16	0_3^+	815.4917	692.4205	996.2568	625.2556	0.068
					873.1834	0.099
1531.305	2^+	815.4917	444.4924	996.2568	625.2556	< 2.416
					873.1834	$1.438 (698)^{+565}_{-431}$
			692.4205		625.2556	< 1.363
					873.1834	$0.812 (358)^{+321}_{-245}$
1716.050	0_6^+	815.4917	444.4924	996.2568	625.2556	< 0.786
					873.1834	< 6.473
			692.4205		625.2556	< 0.126
					873.1834	< 0.786
1775.429	0_7^+	815.4917	444.4924	996.2568	625.2556	> 0.201
					873.1834	> 0.807
			692.4205		625.2556	> 0.229
					873.1834	> 0.912
$4^+ \rightarrow 4^+$						
1645.814	4^+	1047.592	924.55	1263.778	892.775	0.817
					1140.702	0.133

E_i (keV)	Band	$E_{0_2^+}$ (keV)	Gate $_{0_2^+}$	E_γ (keV)	Gate $_\gamma$	$B(E0)$ Ratio
1701.39	0_3^+	1047.592	676.593 924.55	1263.778	892.775	0.015
					1140.702	0.0167
					892.775	0.416
					1140.702	0.474
1789.17	2^+	1047.592	676.593 924.55	1263.778	892.775	1.702
					1140.702	2.207
					892.775	12.052
					1140.702	15.622
$6^+ \rightarrow 6^+$						
1911.544	4^+	1365.878	648.3 994.9	1606.55	888.69	0.205
						0.181

Table 4.14: Ratios of the $B(E0)$ values in ^{154}Gd . Only ratios between two transitions of the same state are listed, as the lifetime of the states are unknown. Table 4.11 lists the values that were used in the calculation. The gates are included, as an efficiency correction was made on the ratio based on the gates. In many cases, only upper or lower limits for the values could be used for this calculation. Errors are not given on these values. Those values marked with errors or as limits had defined values instead of limits.

keV, while the relevant gates for the $8_{0_2^+}^+ \rightarrow 8_{gs}^+$ transition are 426.8 keV and 437.7 keV). The $2_{0_2^+}^+ \rightarrow 2_{gs}^+$ transition agreed with previous measurements from Spits [75]. The $4_{0_2^+}^+ \rightarrow 4_{gs}^+$ transition appears to be higher than the measurements from Spits and Gono [31]. Similarly, the $6_{0_2^+}^+ \rightarrow 6_{gs}^+$ transition appears to be larger than Gono.

Looking at Table 4.13, the first 0^+ excited band to the ground state has several transitions with known mixing ratios and lifetimes. The E0 mixing ratio, ϵ^2 and the matrix element $\rho^2(E0)$ are calculated.

4.4.2.2 $K^\pi = 0_3^+$, Second Excited 0^+ Band, 1182.091 keV

All of the measurements of transitions coming out of the second excited state were limits. For the 0^+ state (1182.091 keV), the gates were used to look for the transition to the first excited 0^+ state. The lower limit on the transition is lower than that previously measured by Spits. The limit in this work comes from the background of the HPGe detector. No further transitions could be seen above 4^+ , as the band is only known up to this J^π .

For the 2^+ state (1418.16 keV), two transitions were examined, one to the 2^+ in the first 0^+ excited state and one to the head of the γ -band. Each of these transitions was measured with two different gates. The lower limits are consistent with the Spits data. For the transition to the γ -band, there appears to be an E0 component. The lower limit in the transition to the first excited 0^+ state is not conclusive.

For the 4^+ state (1701.39 keV), two transitions were examined, one to the 4^+ in the first 0^+ excited state and one to the head of the γ -band. Each of these transitions was measured with two different gates. These transitions only have upper limits. For the transition to the γ -band, the upper limit is not close to the M1 conversion coefficient, indicating there may be some E0 strength. This cannot be stated conclusively, as it is only an upper limit. The upper limits in the transition to the first excited 0^+ state from the two different gates disagree. One upper limit agrees with the previous measurement from Spits, and would indicate there may be E0 strength [75]. The other upper limit indicates a mixed M1+E2 transition with no or very little E0 strength.

Looking at Table 4.14, the second 0^+ excited band seems to strongly favor transitioning to the γ -band, over transitioning to the first 0^+ excited band. None of the transitions examined have known mixing ratios, so the q^2 and αq^2 can be found in Tables 4.11 and 4.12.

4.4.2.3 $K^\pi = 0_6^+$, Fifth Excited 0^+ Band, 1573.9 keV

For the 0^+ state (1573.9 keV), the gates were used to look for the transition to the first and second excited 0^+ states. The lower limit on the transition to the second excited 0^+ state is lower than that previously measured by Spits. The limit in this work comes from the background of the HPGe detector. The transition to the first excited 0^+ state had not previously been measured, making this lower limit the first measurement. No further transitions could be seen above 4^+ , as the band is only known up to this J^π . The 4^+ state is not seen, as it is at approximately the same energy as the population cut off.

For the 2^+ state (1716.050 keV), two transitions were examined, one to the 2^+ in the first 0^+ excited state and one to the head of the γ -band. Each of these transitions was measured with two different gates. The upper limits to the first excited 0^+ band would indicate a small E0 component if one exists. For the transition to the γ -band, the values were measurable. The conversion coefficients found in both gates indicate an E0 component. Not enough statistics were present to see any transition between this 2^+ state and the 2^+ state of the second excited 0^+ band.

Looking at Table 4.14, the fifth 0^+ excited band seems to favor transitioning to the γ -band, over transitioning to the first 0^+ excited band. None of the transitions examined have known mixing ratios, so the q^2 and αq^2 can be found in Tables 4.11 and 4.12.

4.4.2.4 $K^\pi = 0_7^+$, Sixth Excited 0^+ Band, 1650.3 keV

For the 0^+ state (1650.3 keV), the gates were used to look for the transition to the first and second excited 0^+ states. The transition to the fifth state would emit an electron lower than the thresholds on the detectors, making the measurement infeasible with the current set up. The lower limit on the transition to the first excited 0^+ state is lower than that previously measured by Spits, but of similar

magnitude. The transition to the second excited 0^+ state had not previously been measured, making this lower limit the first measurement. No further transitions could be seen above 2^+ , as the band is only known up to this J^π , as proposed by Spits[75].

For the 2^+ state (1775.429 keV), two transitions were examined, one to the 2^+ in the first 0^+ excited state and one to the head of the γ -band. Each of these transitions was measured with two different gates. The lower limits to the first excited 0^+ band are in good agreement, and would indicate an E0 component if one exists. For the transition to the γ -band, the values were measurable. The conversion coefficients found in both gates indicate an E0 component. Not enough statistics were present to see any transition between this 2^+ state and the 2^+ state of the second excited 0^+ band.

Looking at Table 4.14, the sixth 0^+ excited band seems to favor transitioning to the γ -band, over transitioning to the first 0^+ excited band, but as the ratio is a lower limit, this cannot be confirmed. None of the transitions examined have known mixing ratios, so the q^2 and αq^2 can be found in Tables 4.11 and 4.12.

4.4.2.5 $K^\pi = 2^+, \gamma$ Band, 996.264 keV

Transitions for the 2^+ (996.264 keV), 4^+ (1263.778 keV), and 6^+ (1606.55 keV) to the first excited 0^+ band could be seen in the gates. The $2_\gamma^+ \rightarrow 2_{0_2^+}^+$ transition are lower limits, indicating a large E0 component. The $6_\gamma^+ \rightarrow 6_{0_2^+}^+$ transition shows a similar lower limit, indicating a large E0 component. Conversely, the $4_\gamma^+ \rightarrow 4_{0_2^+}^+$ transition has upper limits pointing to a largely E2 transition. This makes conclusions difficult to draw.

None of the states in the γ -band had multiple outgoing transitions measured. No transitions examined have known mixing ratios, so the q^2 and αq^2 can be found in Table 4.11.

4.4.2.6 $K^\pi = 2_2^+$, Second Excited 2^+ Band, 1531.305 keV

Transitions for the 2^+ (1531.305 keV) and 4^+ (1789.17 keV) to the first excited 0^+ band and γ -band could be seen in the gates. For the 2^+ transition to the first excited 0^+ band, the values are large for both gates, disagreeing with the value found by Spits [75]. It is worth noting the large error on the values from this work indicates the disagreement may be purely statistical. This would indicate a small E0 component if true. For the transition to the γ -band, there is one value and one lower limit. The lower limit agrees with the measured value, which is much smaller than Spits, but would indicate an E0 component, as Spits' value does.

The transitions for the 4^+ state are all upper limits. To the first excited 0^+ band, the upper limits do not rule out the possibility of an E0 component. For the transition to the γ -band, the upper limits from the two gates agree, firmly placing the transition as an M1+E2 transition, if not a pure E2.

Looking at Table 4.14, the second 2^+ excited band seems to either not favor transitioning to the γ -band over the first 0^+ excited band, or prefer the first excited 0^+ band. None of the transitions examined have known mixing ratios, so the q^2 and αq^2 can be found in Table 4.11.

4.4.2.7 $K^\pi = 4_1^+$, First Excited 4^+ Band, 1645.814 keV

Transitions for the 4^+ (1645.814 keV) and 6^+ (1911.544 keV) to the first excited 0^+ band and γ -band could be seen in the gates. All the values are upper limits. For the 4^+ transition to the first excited 0^+ band, the upper limits are lower than the one set by Spits [75]. The lower of the two upper limits would indicate a mostly E2 transition. The higher of the two would indicate a mixed M1+E2, with little to no E0 component. The upper limits on the transition to the γ -band agrees with the value measured by Spits, which would indicate a mixed M1+E2 transition. Without a known mixing ratio, it is not possible to tell if there is an E0 component.

For the 6^+ state, the upper limits on the transition to the first excited 0^+ band indicate there may be a small E0 component, as both upper limits are higher than the M1 theory strength. Only one gate could be used to look at the transition to the γ -band. The upper limit agrees with the previous measurement from Gono, which would indicate an E2 transition [31]. This work's upper limit does not eliminate the possibility of a mixed transition.

Looking at Table 4.14, the first 4^+ excited band seems to favor transitioning to the γ -band over the first 0^+ excited band. One of the transitions examined has a known mixing ratio, δ^2 , which allows for the calculation of the E0 mixing ratio, ϵ^2 , listed in Table 4.13. For the other transitions, the q^2 and αq^2 can be found in Table 4.11.

CHAPTER 5

^{156}Gd RESULTS

^{156}Gd is one of the most well studied nuclei in the rare-earth region. It has a large number of known lifetimes, having been studied by both (n, γ) and (n, e^-) [41]. Only two other nuclei, ^{162}Dy and ^{168}Er have been studied to a similar extent. It is known to have 6 excited 0^+ states, three with known lifetimes, enabling the direct calculation of the nuclear matrix element with the observation of an E0. This nucleus has not been studied by (p, t) since 1973, long before the renaissance of 0^+ states being discovered via (p, t) in the early 2000s [30, 47, 54]. Further lifetimes and known δ mixing ratios enable similar calculations for E0 components of $J^\pi \rightarrow J^\pi$ transitions.

This data was taken with ICEBall and GEORGINA. The experiment used an enriched ^{154}Sm target of 1.7 mg/cm^2 thickness, as discussed in Chapter 2 and shown in Table 2.10. A complete catalog of spectra used in analysis can be found in Appendix ??.

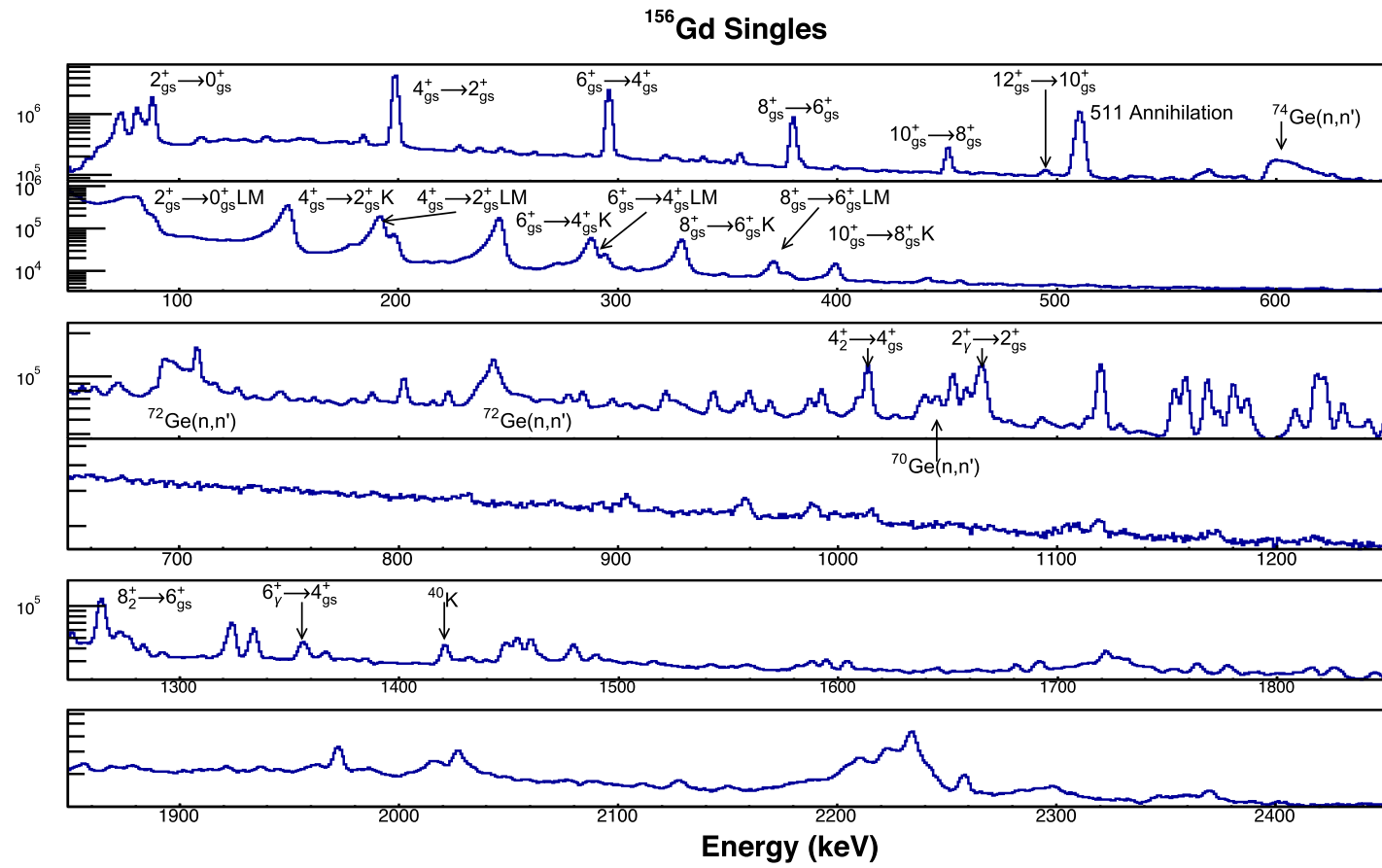
5.1 Ground State Band Confirmation

The singles spectra show several prominent peaks in Figure 5.1. In the γ -spectrum on top, there are three prominent peaks from 100 to 400 keV. These peaks are the ground state band transitions from the 2^+ state up to the 8^+ state. The transition from the 2^+ state to the ground state is 89 keV, and while visible, suffers from a steep efficiency drop-off due to attenuation at that energy, and a large background due to x-rays. The peak just beyond 500 keV is the 511 keV annihilation peak. The

Figure 5.1. Singles spectra of ^{156}Gd . Spectra are labeled with the particles being detected, the energies of the γ and electron spectra aligned for identification. In the γ spectrum, several lines of note are labeled. The large peak in the electron spectrum at low energy is cut off due to the threshold. It is a combination of background and the 89L peak. Transitions in the higher energy regime of the γ spectrum cannot be determined without gating, due to additional background from the experimental room. The electron spectrum only goes to 1250 keV, as that is the limit of the detectors.

149

Counts

 γ e^- γ e^- γ γ

conversion electron spectrum beneath has distinguishable *K*-shell and *L*-shell peaks corresponding to these ground state band transitions.

The transitions in the ground state band are used as a diagnostic of the data. The ground state band transitions should all be pure E2 multipole transitions and have been measured as such, making them an excellent comparison and calibration with the theoretical coefficients from BrIcc[40]. Singles data had to be corrected for angular distribution effects, discussed in section 3.3.3. The transitions from 2^+ to 10^+ are summarized and compared with theory in Table 5.1.

There do not appear to be contaminants in these ground state lines, outside of the $2_{gs}^+ \rightarrow 0_{gs}^+$ transition, unlike the ^{154}Gd data. The $2_{gs}^+ \rightarrow 0_{gs}^+$ transition is considered unreliable, as the low energy of the γ -ray puts it in the energy region where the efficiency decreases due to the attenuation of the photon before it reaches the active region of the detector. The change in efficiency in the HPGe detectors is steep in this region, leading to large uncertainty.

5.2 Gates on the Ground State Band

The transitions of the ground state band are the most prominent peaks in the spectra (Figure 5.1). The γ -rays of these transitions were gated onto confirm the levels populated in the reaction. Figures 5.2, 5.3, 5.4, and 5.5 are the result of these gates. The $4_{gs}^+ \rightarrow 2_{gs}^+$ gate has the most statistics to work with, due to the challenges the attenuation of the $2_{gs}^+ \rightarrow 0_{gs}^+$ transition posed.

Determining which transitions went uniquely into a given ground state level was done by comparing the outgoing ground state transition for that level with the incoming transitions, i.e. the $4_{gs}^+ \rightarrow 2_{gs}^+$ (199 keV) gate was compared directions with the $6_{gs}^+ \rightarrow 4_{gs}^+$ (296 keV) gate. The γ -spectra corresponding to gates of two of these lines can be seen in Figure 5.6. Lines in the gamma spectrum that were present only in the outgoing spectrum, but not the incoming spectrum, are going into that level

TABLE 5.1

¹⁵⁶GD GROUND STATE BAND INTERNAL CONVERSION
COEFFICIENTS FROM SINGLES

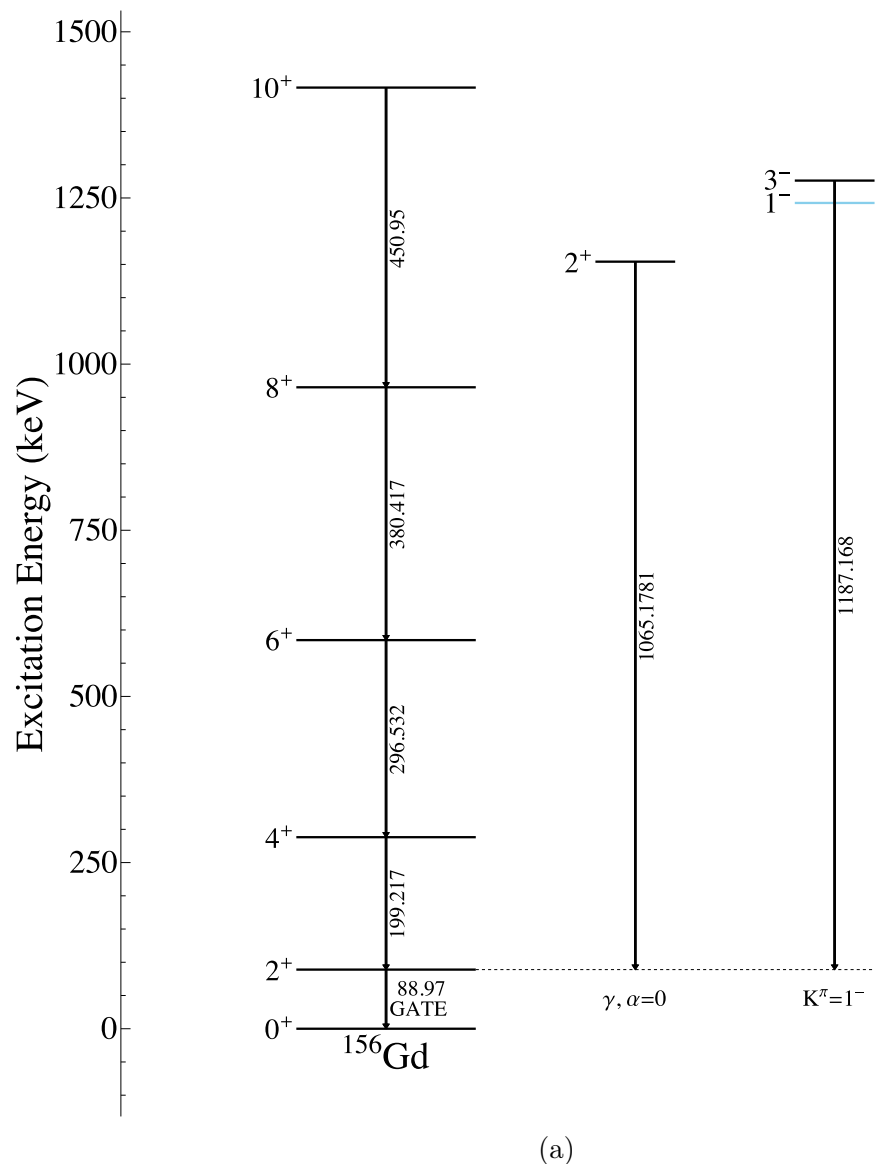
E (keV)	$J^\pi \rightarrow J^\pi$	E_i (keV)	E_f (keV)	$T_{1/2}$ (fs)	Multipolarity	Shell	α (This Work)	α (Th)	α (Konijn)
198.58	$4^+ \rightarrow 2^+$	288.187	88.97	111900	E2	K	$0.1667 (4)^{+46}_{-45}$	0.1565 (22)	0.199 (36)
						L	$0.0537 (1)^{+16}_{-15}$	0.0531 (8)	
						M	0.0170 (1) (5)	0.0122 (2)	
296.04	$6^+ \rightarrow 4^+$	584.715	288.187	15800	E2	K	0.0572 (1) (18)	0.0477 (7)	0.04683*
						L	0.0121 (1) (4)	0.0115 (2)	
						M	0.0036 (1) (1)	0.0026 (1)	
379.92	$8^+ \rightarrow 6^+$	965.134	584.715	4320	E2	K	0.0274 (1) (9)	0.0235 (4)	0.038 (10)
						L	0.0050 (1) (2)	0.0048 (1)	
						M	0.0013 (1) (1)	0.0011 (1)	

TABLE 5.1 (CONTINUED)

E (keV)	$J^\pi \rightarrow J^\pi$	E_i (keV)	E_f (keV)	$T_{1/2}$ (fs)	Multipolarity	Shell	α (This Work)	α (Th)	α (Konijn)
450.64	$10^+ \rightarrow 8^+$	1416.078	965.134	1900	E2	K	0.0152 (2) (5)	0.01483 (21)	0.0145*
						L	0.0028 (1) (1)	0.00279 (4)	
						M	0.0010 (1) (1)	0.000621 (9)	

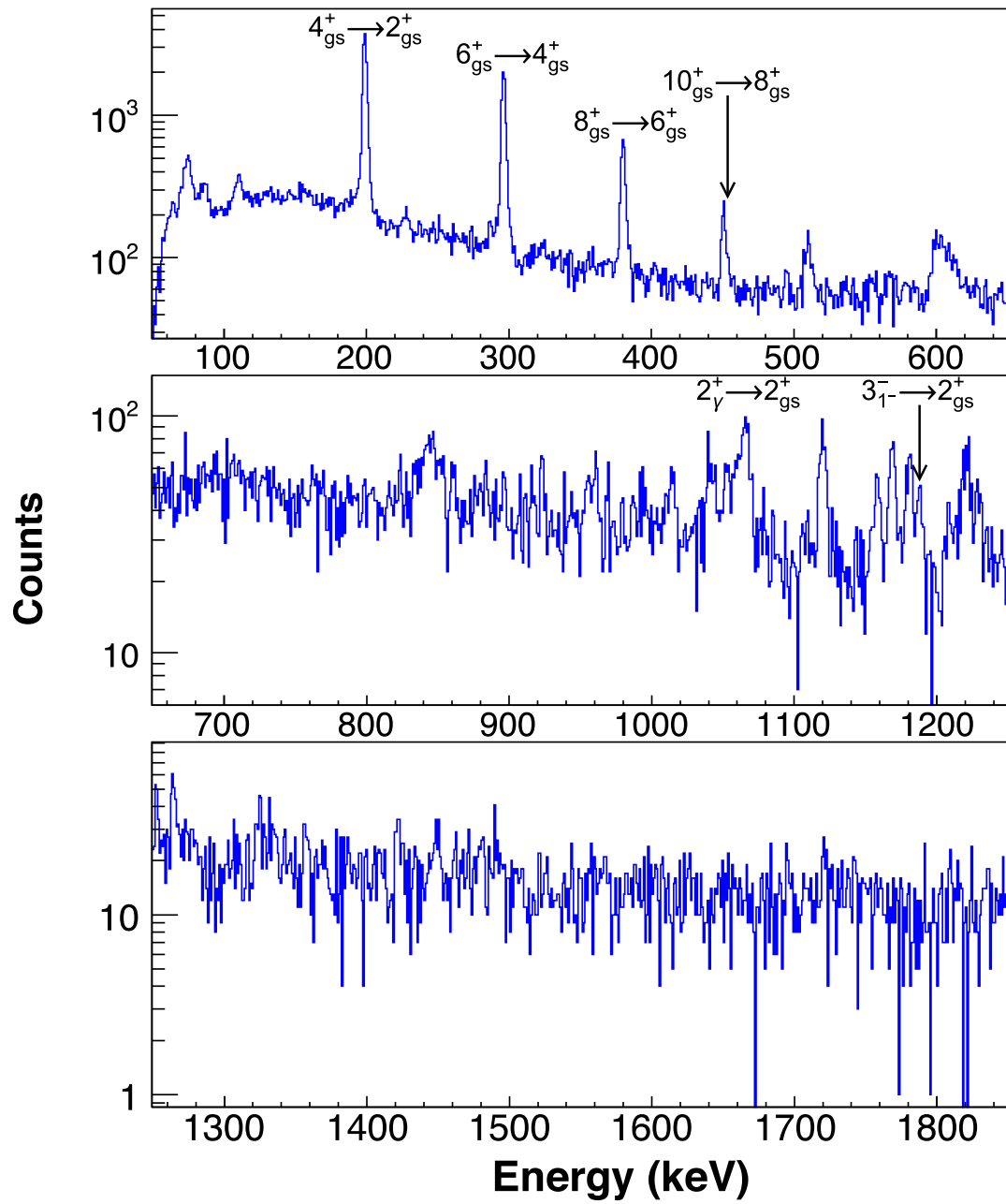
A list of the ground state conversion coefficients from ^{156}Gd . Multipolarities and mixing ratios were taken from the nuclear data sheets[65]. Unless otherwise stated, the α values are α_K . An angular distribution correction has been applied based on multipolarities for pure transitions, and those with known mixing ratios. The first error is statistical, the second is systematic. Numbers are compared with Konijn et al. [43] Starred values in the Konijn data were used as calibration points.

Figure 5.2(a) Level Scheme of ^{156}Gd . The gamma ray of the $2_{gs}^+ \rightarrow 0_{gs}^+$ (89 keV) transition in the ground state was gated on. It was then compared with the gated spectrum from the gamma ray of the $4_{gs}^+ \rightarrow 2_{gs}^+$ (199 keV) transition in the ground state. Peaks only appearing in the first gate were assumed to go into the 2_{gs}^+ state, and assignments were made. Due to the low energy of the $2_{gs}^+ \rightarrow 0_{gs}^+$ transition, the efficiency was lower, and it is likely that transitions into the 2_{gs}^+ state were missed. The levels are organized by band. The lower levels of the band, unseen by gamma rays in this gate, are in blue. (b) Gamma spectrum gated on 89 keV, corresponding to the $2_{gs}^+ \rightarrow 0_{gs}^+$ transition. Several transitions are marked according to the level scheme.



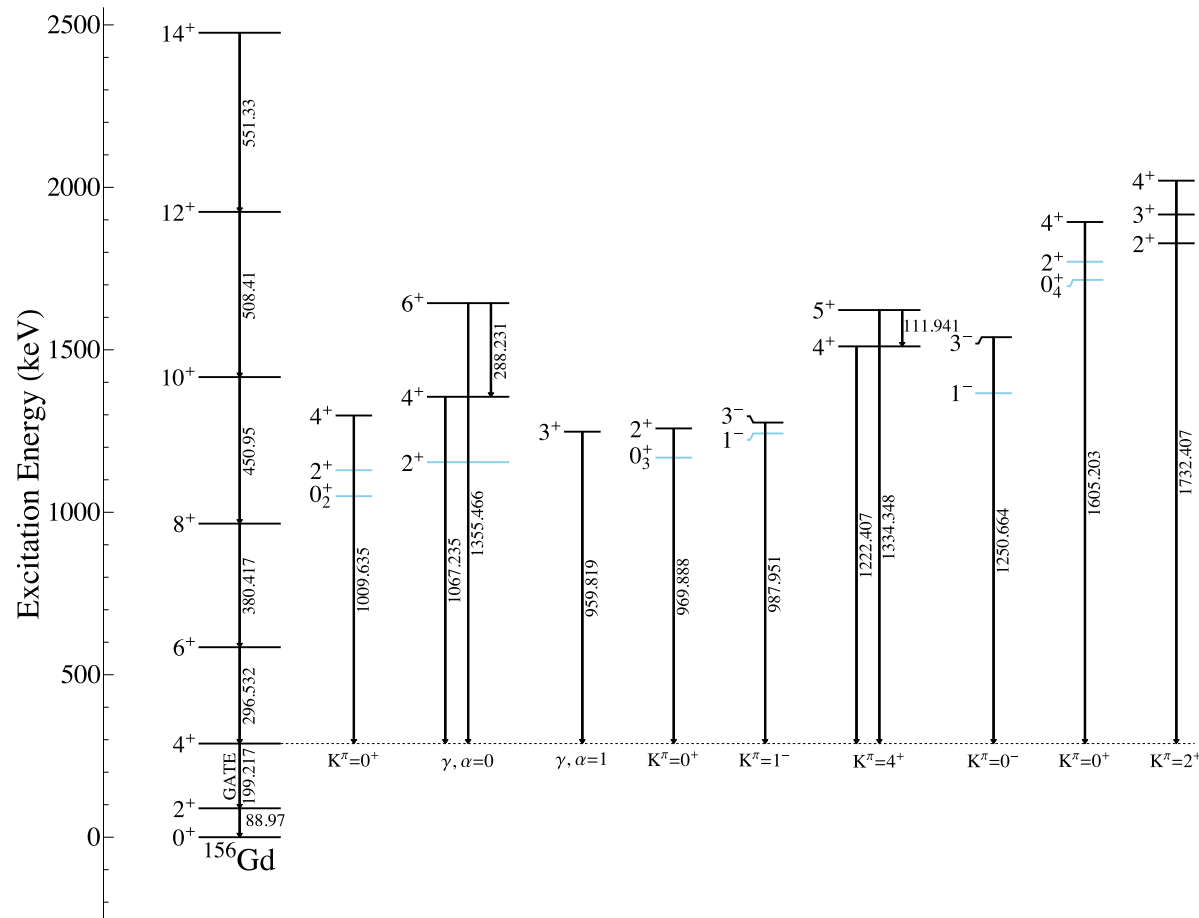
(a)

89 keV gated spectra



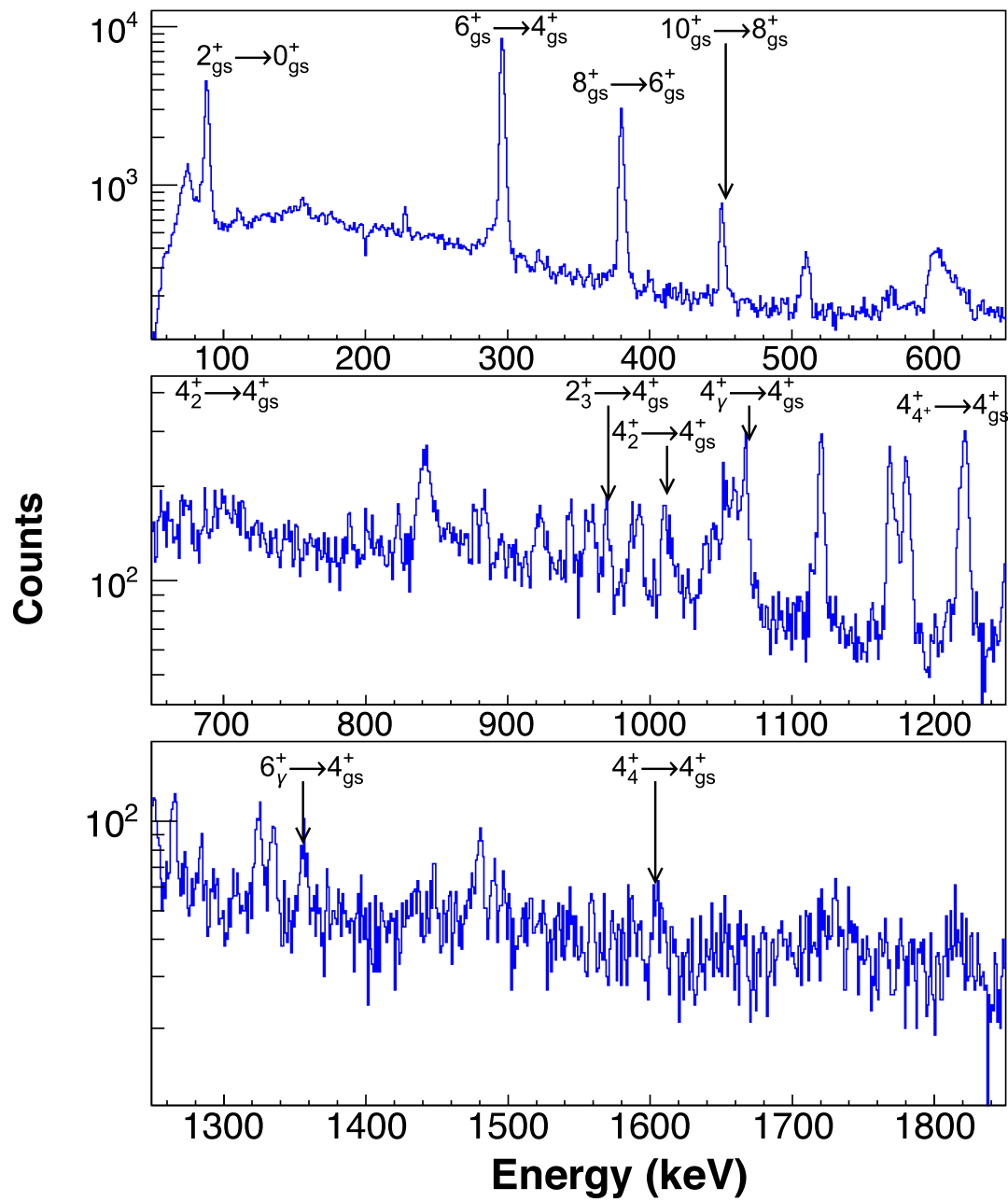
(b)

Figure 5.3(a) Level Scheme of ^{156}Gd . The gamma ray of the $4_{gs}^+ \rightarrow 2_{gs}^+$ (199 keV) transition in the ground state was gated on. It was then compared with the gated spectrum from the gamma ray of the $6_{gs}^+ \rightarrow 4_{gs}^+$ (296 keV) transition in the ground state. Peaks only appearing in the first gate were assumed to go into the 4_{gs}^+ state, and assignments were made. Additionally, these peaks were also gated on, to look for cascades leading into the 4_{gs}^+ state, which were found in several cases. The levels are organized by band. The lower levels of the band, unseen by gamma rays in this gate, are in blue. (b) Gamma spectrum gated on 199 keV, corresponding to the $4_{gs}^+ \rightarrow 2_{gs}^+$ transition. Several transitions are marked according to the level scheme.



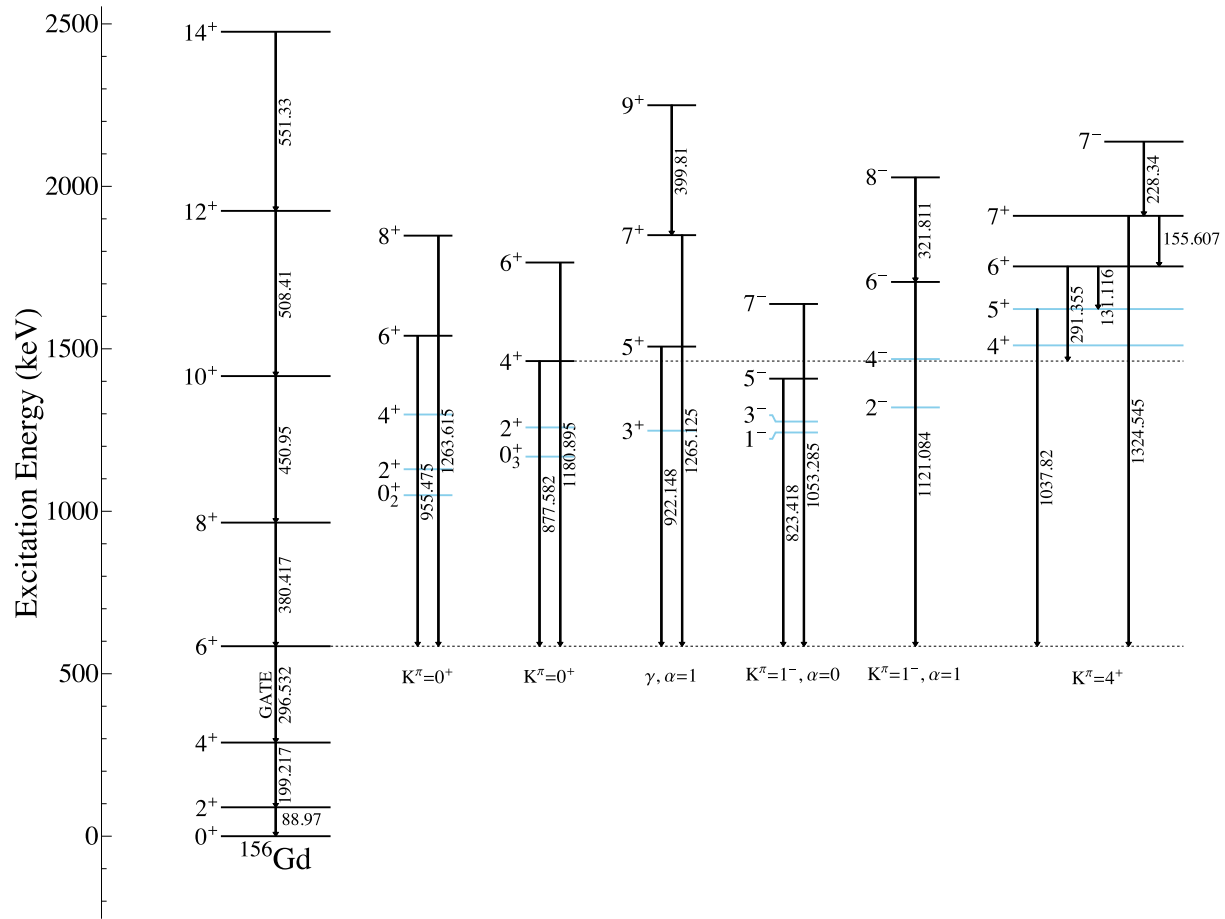
(a)

199 keV gated spectra



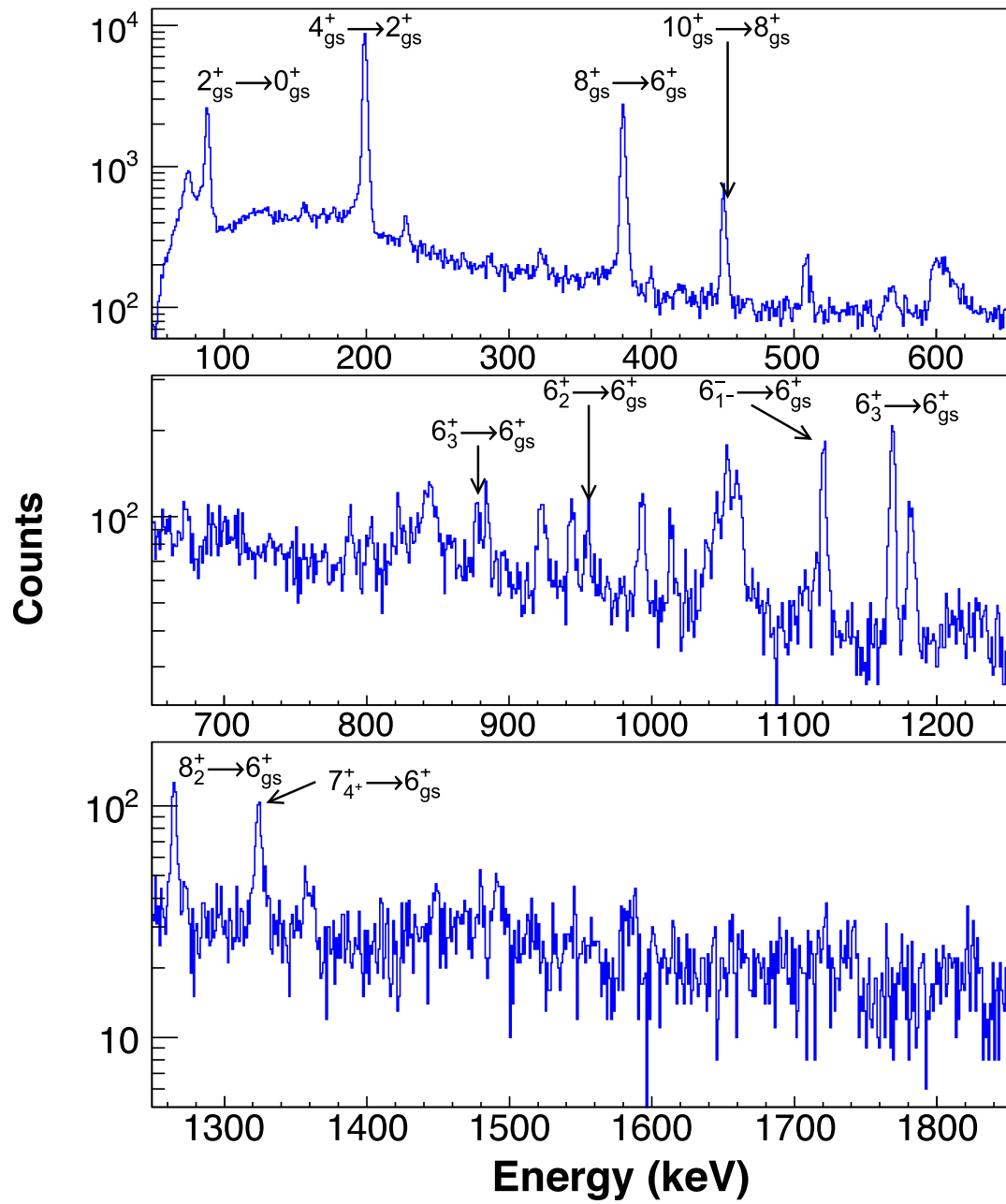
(b)

Figure 5.4(a) Level Scheme of ^{156}Gd . The gamma ray of the $6_{gs}^+ \rightarrow 4_{gs}^+$ (296 keV) transition in the ground state was gated on. It was then compared with the gated spectrum from the gamma ray of the $8_{gs}^+ \rightarrow 6_{gs}^+$ (380 keV) transition in the ground state. Peaks only appearing in the first gate were assumed to go into the 6_{gs}^+ state, and assignments were made. Additionally, these peaks were also gated on, to look for cascades leading into the 6_{gs}^+ state, which were found in several cases. The levels are organized by band. The lower levels of the band, unseen by gamma rays in this gate, are in blue. (b) Gamma spectrum gated on 296 keV, corresponding to the $6_{gs}^+ \rightarrow 4_{gs}^+$ transition. Several transitions are marked according to the level scheme.



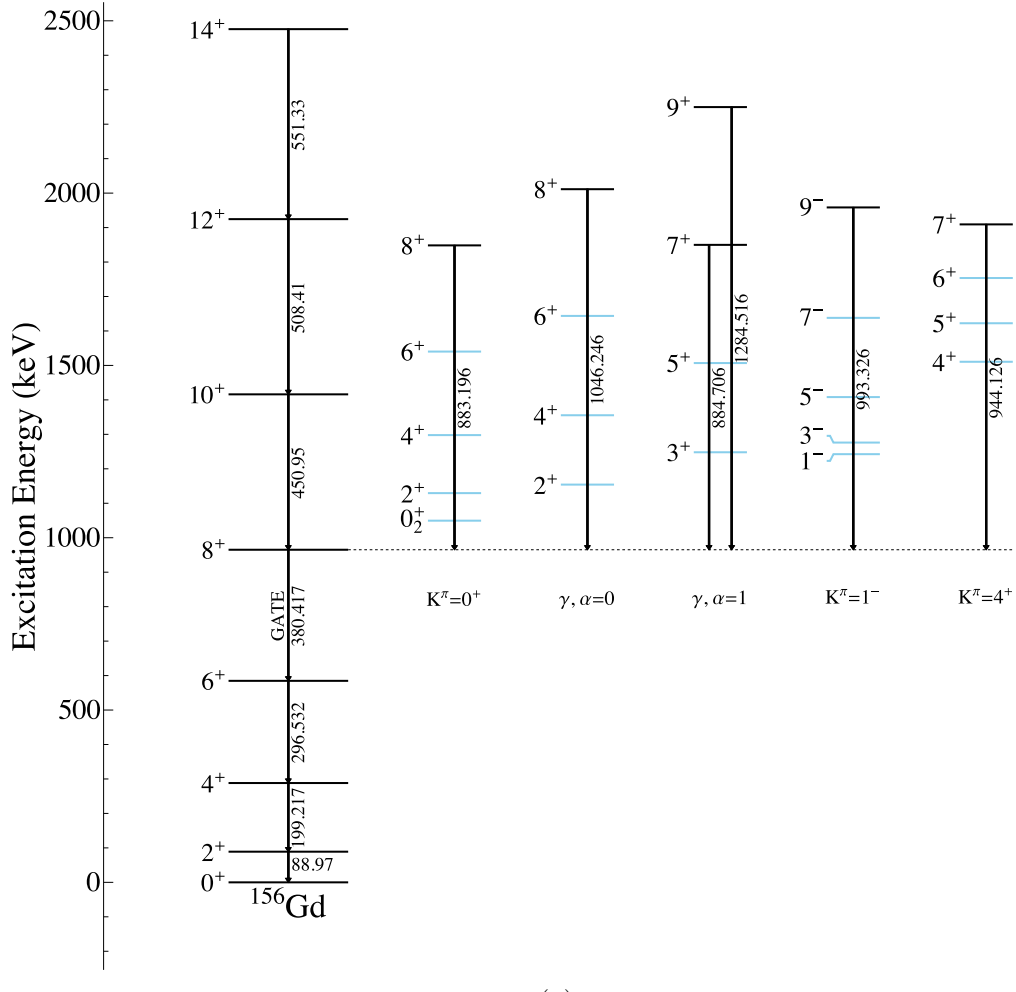
(a)

296 keV gated spectra



(b)

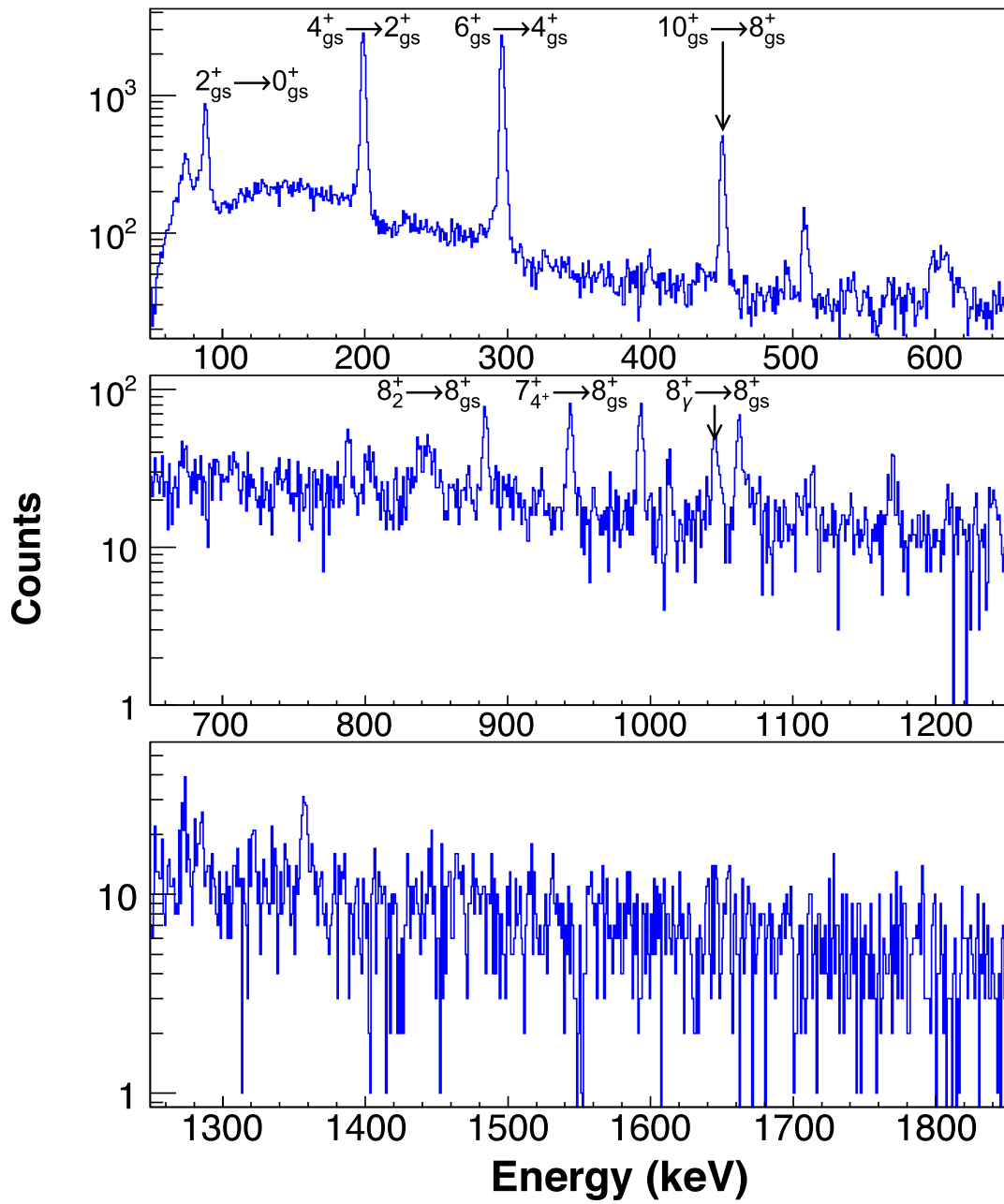
Figure 5.5(a) Level Scheme of ^{156}Gd . The gamma ray of the $8_{gs}^+ \rightarrow 6_{gs}^+$ (380 keV) transition in the ground state was gated on. It was then compared with the gated spectrum from the gamma ray of the $10_{gs}^+ \rightarrow 8_{gs}^+$ (451 keV) transition in the ground state. Peaks only appearing in the first gate were assumed to go into the 8_{gs}^+ state, and assignments were made. Additionally, these peaks were also gated on, to look for cascades leading into the 8_{gs}^+ state, which were found in several cases. The levels are organized by band. The lower levels of the band, unseen by gamma rays in this gate, are in blue. (b) Gamma spectrum gated on 380 keV, corresponding to the $8_{gs}^+ \rightarrow 6_{gs}^+$ transition. Several transitions are marked according to the level scheme.



(a)

(the 4_{gs}^+ in the example above). Several areas have been circled to demonstrate this effect. Identified transitions were then gated on to confirm assignments and search for cascades from higher energy states.

380 keV gated spectra



(b)

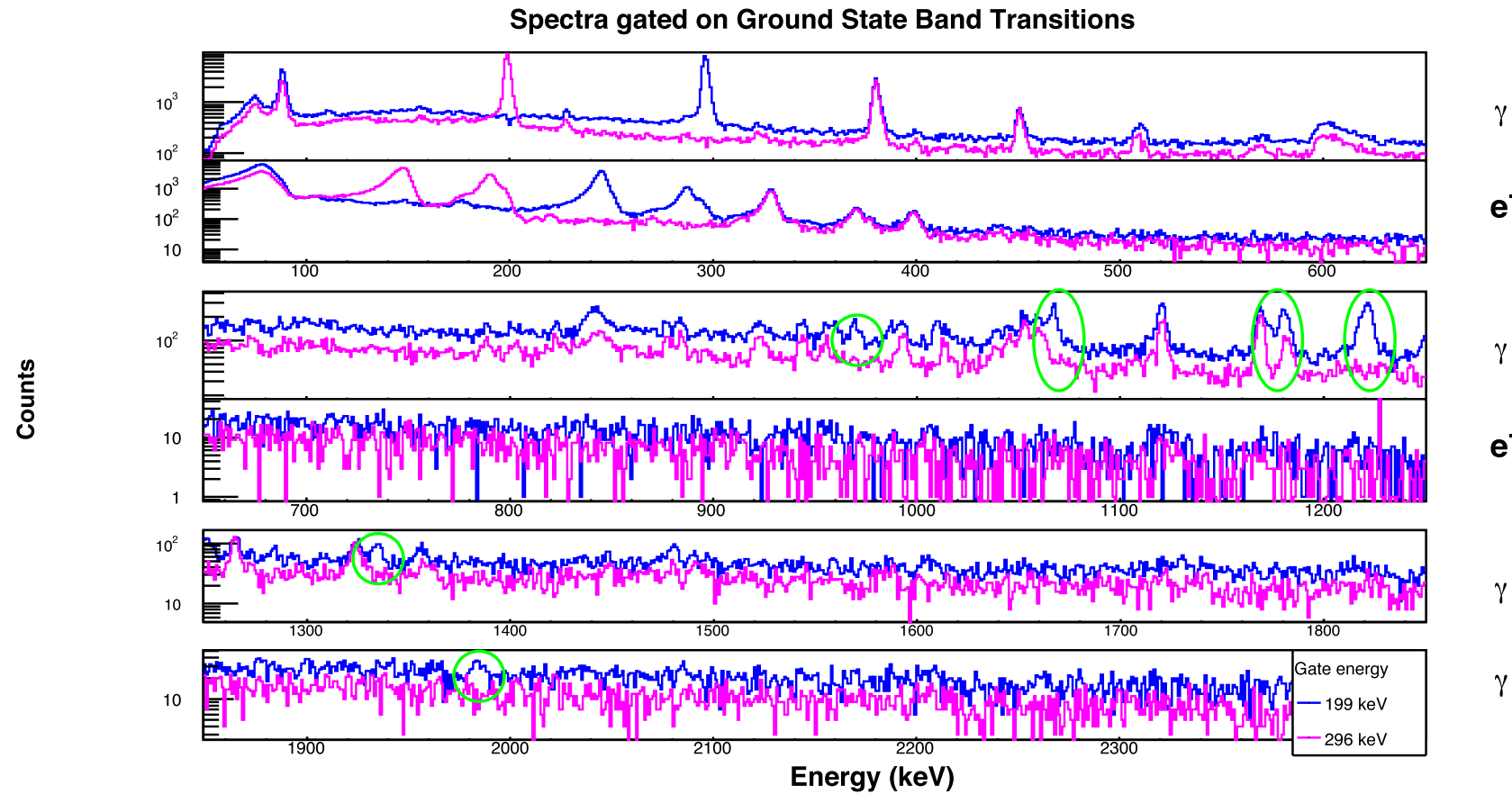


Figure 5.6. Spectra gated on two of the ground state band lines of ^{156}Gd . As highlighted in green, some lines do not appear in different gates. Comparison of these gates yields a list of transitions that directly populate the interim level.

The secondary gate check is important, as the attenuation of the $2_{gs}^+ \rightarrow 0_{gs}^+$ transition meant weaker lines going into the 2_{gs}^+ state could be falsely assigned going into the 4_{gs}^+ state. As the ground state band transitions are so intense, the transitions showed up when gating on weaker peaks in the spectra, while the inverse was not always true. The spectra from these gates are available in Appendix ??.

Few transitions could be seen in the $2_{gs}^+ \rightarrow 0_{gs}^+$ (89 keV) gate, as is reflected in Figure 5.2. The $4_{gs}^+ \rightarrow 2_{gs}^+$ (199 keV) gate shows a larger number of γ -rays, seen in Figure 5.3, including evidence of populating 3 excited 0^+ bands. In total, nine bands were seen in the gating. The number of bands seen populated drops off with higher gates, both due to the drop off in populating higher energy states and the drop off in populating higher J states. Studies have shown the $(\alpha, 2n)$ reaction to stop populating spin states with a significant cross section beyond about $J^\pi = 12^+$ [81]. In the ground state band of ^{156}Gd , the 12_{gs}^+ state sits at 1924.49 keV, giving an approximate cut off for populating higher energy states in the nucleus. Additionally, due to the lack of known higher spin states in the higher energy 0^+ bands, identification of populating the bands in the higher gates becomes difficult.

5.3 Conversion Coefficients from Singles

With the gamma-rays now identified through gates, conversion coefficients could be calculated from singles spectra. Tables 5.3, 5.4, and 5.5 are these results. Where available, results are compared with Konijn et al[43], which also examined the nucleus via an $(\alpha, 2n)$ reaction.

Transitions that could be clearly identified and distinguished are found in Table 5.3. These transitions all have known multipole assignments and mixing ratios as needed, allowing for angular corrections. Two transitions with possible E0 components are seen in this table. One, the $2_{0_2^+}^+ \rightarrow 2_{gs}^+$ transition, appears to have a clear E0 component. Although this transition was not seen in Figure 5.2, the band the state

exists in is populated, as seen in Figures 5.3, 5.4, and 5.5. The $6_{\gamma}^{+} \rightarrow 6_{gs}^{+}$ transition does not appear to have an E0 component. While the value agrees with Konijn[43], it does not agree with the theoretical value for an E2, the multipole the transition has been assigned.

Table 5.4 holds conversion coefficients that have been left uncorrected for angular distribution in the singles for one of two reasons: either there were multiple known assignments to the gamma-ray energy, or the exact multipole mixing-ratio δ was unknown. Several of these transitions are high energy $J^{\pi} \rightarrow J^{\pi}$ transitions, including a $0^{+} \rightarrow 0^{+}$ transition. The Si(Li) efficiency at these energies was too low to see the conversion electrons in gated spectra.

Table 5.5 has conversion coefficients that could not be corrected for angular distribution due to the transitions having unknown multipole assignments. Allowable and reasonable theoretical conversion coefficients from BrIcc[40] are listed in the table. Assuming pure multipole assignments, corrected coefficients have also been listed for comparison. The $7_{4+}^{+} \rightarrow 8_{gs}^{+}$ transition sits within the theoretical bounds of the conversion coefficients when corrected. Using equation 4.1, the E2+M1 mixing ratio delta comes out to be < 0.61 or -0.55^{+51}_{-8} . This value is small enough to indicate this transition may be a pure E2 transition.

5.4 $J^{\pi} \rightarrow J^{\pi}$ Transitions

5.4.1 $0^{+} \rightarrow 0^{+}$ Identification and Population

With the large number of 0^{+} states in ^{156}Gd , our first priority was to identify which bands were populated. Table 5.2 contains a list of 0^{+} states from the nuclear data sheets [65], with notes as to which 0^{+} states have been previously observed in the reaction used in this work.

We have seen all 0^{+} states observed previous in $(\alpha, 2n)$ experiments in addition

TABLE 5.2

 0^+ STATES IN ^{156}Gd

Energy (keV)	Seen in $(\alpha, 2n)$	Seen in This Work
0	×	×
1049.487(2)	×	×
1168.186(7)	×	×
1715.211(4)		×
1851.278(7)		×
1988.5(2)		
2082.0		

Table 4.6: A list of all 0^+ states in ^{156}Gd . 0^+ states above approximately 1924 keV would not be seen in this experiment, the energy of the 12^+ ground state, as that is the energy cut off in the nucleus for state population, discussed in the text. The levels seen in this exceed previous $(\alpha, 2n)$ experiments.

TABLE 5.3

 ^{156}GD INTERNAL CONVERSION COEFFICIENTS FROM SINGLES

E (keV)	$J^\pi \rightarrow J^\pi$	E_i (keV)	E_f (keV)	$T_{1/2}$ (fs)	Multipolarity	δ	Shell	α (This Work)	α (Th)	α (Konijn)
227.90	$7_{7-}^- \rightarrow 7_{4+}^+$	2137.6	1909.26	13000000000	E1		K	0.4687 (50) $^{+85}_{-84}$	0.0272 (4)	0.063 (13)
							LM	0.1073 (20) (20)	0.0049 (6)	
321.92	$8_{1-}^- \rightarrow 6_{1-}^-$	2027.1	1705.799		E2		K	0.0290 (13) (9)	0.0378 (6)	0.025 (7)
355.87	$4_{4+}^+ \rightarrow 2_\gamma^+$	1510.594	1154.152	189000	E2		K	0.0158 (6) (5)	0.0281 (4)	
399.56	$9_\gamma^+ \rightarrow 7_\gamma^+$	2249.65	1849.84		E2		K	0.0077 (8) (3)	0.0205 (3)	0.026 (5)
921.83	$5_\gamma^+ \rightarrow 6_{gs}^+$	1506.863	584.715	400	E2		K	0.0041 (9) (5)	0.0028 (1)	0.0030 (7)
1040.470	$2_{0_2^+}^+ \rightarrow 2_{gs}^+$	1129.437	88.970		E2+E0+M1	-5.9^{+14}_{-28}	K	0.0152 (10) (2)	0.0022 (1)	0.014 (3)
1059.31	$6_\gamma^+ \rightarrow 6_{gs}^+$	1643.653	584.715		E2		K	0.0013 (5) (1)	0.0021 (1)	0.0013 (8)

A list of conversion coefficients from ^{156}Gd . Multipolarities and mixing ratios were taken from the nuclear date sheets[65]. Unless otherwise stated, the α values are α_K . An angular distribution correction has been applied based on multipolarities for pure transitions, and those with known mixing ratios. The first error is statistical, the second is systematic. Numbers are compared with Konijn et al[43].

TABLE 5.4

 UNCORRECTED ^{156}GD INTERNAL CONVERSION COEFFICIENTS
 FROM SINGLES

(a)

E (keV)	$J^\pi \rightarrow J^\pi$	E_i (keV)	E_f (keV)	$T_{1/2}$ (fs)	Multipolarity	δ
154.94	$4_{4+}^+ \rightarrow 4_\gamma^+$	1510.594	1355.422	189000	M1+E2	0.48
	$7_{4+}^+ \rightarrow 6_{4+}^+$	1909.26	1753.653		(M1+E2)	0.29
883.86	$8_{0_2^+}^+ \rightarrow 8_{gs}^+$	1848.33	965.134		E0+E2	
	$7_\gamma^+ \rightarrow 8_{gs}^+$	1849.84	965.134		E2(+M1)	
955	$6_{0_2^+}^+ \rightarrow 6_{gs}^+$	1540.19	584.715		E0+E2	
959.88	$0_{0_2^+}^+ \rightarrow 2_{gs}^+$	1049.487	88.97	1800	E2	
	$3_\gamma^+ \rightarrow 4_{gs}^+$	1248.006	288.197	580	E2+M1	-12
1009.33	$4_{0_2^+}^+ \rightarrow 4_{gs}^+$	1297.822	288.197	1600	E0+E2,M1	
1045.48	$8_\gamma^+ \rightarrow 8_{gs}^+$	2011.38	965.134		E2(+M1)	
1052.61	$7_{1-}^- \rightarrow 6_{gs}^+$	1638	584.715		E1	
1065.74	$2_\gamma^+ \rightarrow 2_{gs}^+$	1154.152	88.97	568	E2+M1	-16
	$4_\gamma^+ \rightarrow 4_{gs}^+$	1355.422	288.187	540	E2+M1	-4
1158.65	$2_\gamma^+ \rightarrow 0_{gs}^+$	1154.152	0	568	E2	
	$3_\gamma^+ \rightarrow 2_{gs}^+$	1248.006	88.97	580	E2+M1	-11.8
1168.69	$0_{0_3^+}^+ \rightarrow 0_{gs}^+$	1168.186	0	5000	E0	
	$2_{0_3^+}^+ \rightarrow 2_{gs}^+$	1258.075	88.97	1540	E2+M1+E0	0.38

TABLE 5.4 (CONTINUED)

(a)

E (keV)	$J^\pi \rightarrow J^\pi$	E_i (keV)	E_f (keV)	$T_{1/2}$ (fs)	Multipolarity	δ
1222.22	$4_{4+}^+ \rightarrow 4_{gs}^+$	1510.594	288.197	189000	M1+E2	-1.7
	$5_\gamma^+ \rightarrow 4_{gs}^+$	1506.863	288.197	400	E2	
1264.85	$4_\gamma^+ \rightarrow 2_{gs}^+$	1355.422	88.97	540	E2	
	$8_2^+ \rightarrow 6_{gs}^+$	1848.33	584.715			
	$7_\gamma^+ \rightarrow 6_{gs}^+$	1849.84	584.715			

TABLE 5.4 (CONTINUED)

(b)

E (keV)	Shell	α (This Work)		α (Th)[40]	α (Konijn)[43]
		Uncorrected	Corrected		
154.94	K	0.4635 (183) ⁺⁹⁸ ₋₉₇	0.3462 (137) ⁺⁷³ ₋₇₂	0.460 (7)	
	K	0.4879 (193) ⁺¹⁰³ ₋₁₀₂	0.474 (7)		
883.86	K	0.0057 (7) (1)	0.0034 (4) (1)	0.0030 (1)	> 0.0092
	K		[M1] 0.0102 (13) (2)	[M1] 0.0052 (1)	< 0.0052
			[E2] 0.0073 (9) (1)	[E2] 0.0030 (1)	
955	K	0.0065 (4) (5)	0.0039 (2) (3)	0.0026 (1)	0.020 (8)
959.88	K		0.0136 (8) (10)	0.0025 (1)	0.0045 (24)
	K		0.0120 (7) (9)	0.0025 (1)	
1009.33	K	0.0173 (9) (4)	[M1] 0.0234 (12) (5)	[M1] 0.0038 (1)	0.0164 (29)
			[E2] 0.0107 (6) (2)	[E2] 0.0023 (1)	
1045.48	K	0.0012 (2) (2)	[M1] 0.0015 (3) (3)	[M1] 0.0035 (1)	0.0025 (6)
			[E2] 0.0007 (1) (1)	[E2] 0.0021 (1)	
1052.61	K		0.0008 (1) (1)	0.0009 (1)	
1065.74	K		0.0034 (3) (1)	0.0021 (1)	0.0025 (9)
	K		0.0029 (3) (1)	0.0021 (3)	0.0021 (1)
1158.65	K	0.0020 (3) (1)	0.0020 (3) (1)	0.0017 (1)	0.0023 (3)
	K	0.0014 (2) (1)	0.0017 (1)		
1168.69	K	0.0045 (3) (1)	0.0045 (3) (1)	0.0026 (1)	> 0.0035
	K	0.0038 (3) (1)			
1222.22	K	0.0028 (4) (1)	0.0031 (4) (1)	0.0018 (1)	0.00174*
	K	0.0031 (4) (1)	0.001560 (22)		
1264.85	K	0.0017 (3) (1)	0.0014 (2) (1)	0.0014 (1)	
	K	[E2] 0.0014 (2) (1)	[E2] 0.0014 (1)		

TABLE 5.4 (CONTINUED)

(b)

E (keV)	Shell	α (This Work)		α (Th)[40]	α (Konijn)[43]
		Uncorrected	Corrected		
	K		[M1] 0.0011 (2) (1) [E2] 0.020 (3) (1)	[M1] 0.0022 (1) [E2] 0.0014 (1)	

Table 5.4: A list of conversion coefficients from ^{156}Gd . Multipolarities and mixing ratios were taken from the nuclear data sheets[65]. Unless otherwise stated, the α values are α_K . No angular distribution correction has been applied, either due to unknown mixing ratios, or multiple assignments of the gamma-ray. The first error is statistical, the second is systematic. Numbers are compared with Konijn et al. [43] Starred values were used as calibration points in the Konijn paper. All coefficients are K-shell electrons.

TABLE 5.5

$$^{156}\text{GD INTERNAL CONVERSION ELECTRONS WITHOUT ASSIGNED}$$

$$\text{MULTIPOLEARITIES}$$

E (keV)	$J^\pi \rightarrow J^\pi$	E_f (keV)	E_i (keV)	α (This Work)		Theory			α (Konijn)
				Uncorrected	Corrected	$\alpha(\text{M1})$	$\alpha(\text{E2})$	$\alpha(\text{E1})$	
671.41	$7_{1-}^- \rightarrow 8_{gs}^+$	1638	965.134	0.0064 (6) (2)	0.0115 (11) (4)			0.00213 (3)	
838.83	$9_\gamma^+ \rightarrow 10_{gs}^+$	2249.65	1416.078	0.0009 (3) (1)	[M1] 0.0016 (5) (2) [E2] 0.0011 (4) (1)	0.00595 (9)	0.00337 (5)		
943.732	$7_{4+}^+ \rightarrow 8_{gs}^+$	1909.26	965.134	0.0022 (6) (1)	[M1] 0.0040 (11) (12) [E2] 0.0028 (8) (1)	0.00448 (7)	0.00262 (4)		0.0025 (3)

A list of conversion coefficients from ^{156}Gd without known multipolarities. As a result, an angular distribution correction term has not been applied. None of the states have known half lives. The first error is statistical, the second is systematic. Numbers are compared with theoretical values for allowed multipolarities and results from Konijn et al. [43]. All coefficients are K-shell electrons.

to two more of higher energy. The energies of the possible $0^+ \rightarrow 0^+$ transitions from these states are marked in the electron singles in Figure 5.7. In this spectrum, the $0_3^+ \rightarrow 0_{gs}^+$ transition is the most prominent. The $0_2^+ \rightarrow 0_{gs}^+$ and $0_4^+ \rightarrow 0_3^+$ transitions appears to have some strength, but are obscured by other conversion electrons in the data. The $0_3^+ \rightarrow 0_2^+$ transition is at too low an energy to distinguish from the high background at low energies.

To obtain information in these areas, and for possible $J^\pi \rightarrow J^\pi$ transitions, energy gates were used. A full list of gates and spectra can be found in Appendix ??.

5.4.2 $J^\pi \rightarrow J^\pi$ Transitions

After identification of the bands and transitions, gates were put on the incoming and outgoing transitions of states of interest, namely even- J^+ states. Incoming transitions did not have enough statistics to yield information. For the 0^+ states, this is unfortunate, as only incoming transitions can be used for transitions to the ground state. Outgoing transitions had more statistics, and results could be obtained. To look for these transitions of interest, other transitions, namely those of the ground state band, were subtracted from the regions of interest as described in Section 3.4. This subtraction technique causes the results to be treated as limits. $J^\pi \rightarrow J^\pi$ transitions up to 4^+ were seen. Tables 5.6, 5.7, and 5.8 are the tabulated results. These values are compared with Konijn[43] where available. Additionally, the theoretical conversion coefficients have been listed for the $M1$ and $E2$ transitions, as taken from BrIcc[40].

Due to the lack of lifetimes of these states, $B(E0)$ values cannot be calculated. However, the relative intensities of these values can be compared, assuming they are coming from the same state, as the lifetime would divide out (see equations 1.36 and 1.37). The contributions from the individual components of the transition must be separated out for the 2^+ and 4^+ transitions. This was done by getting the q^2 values

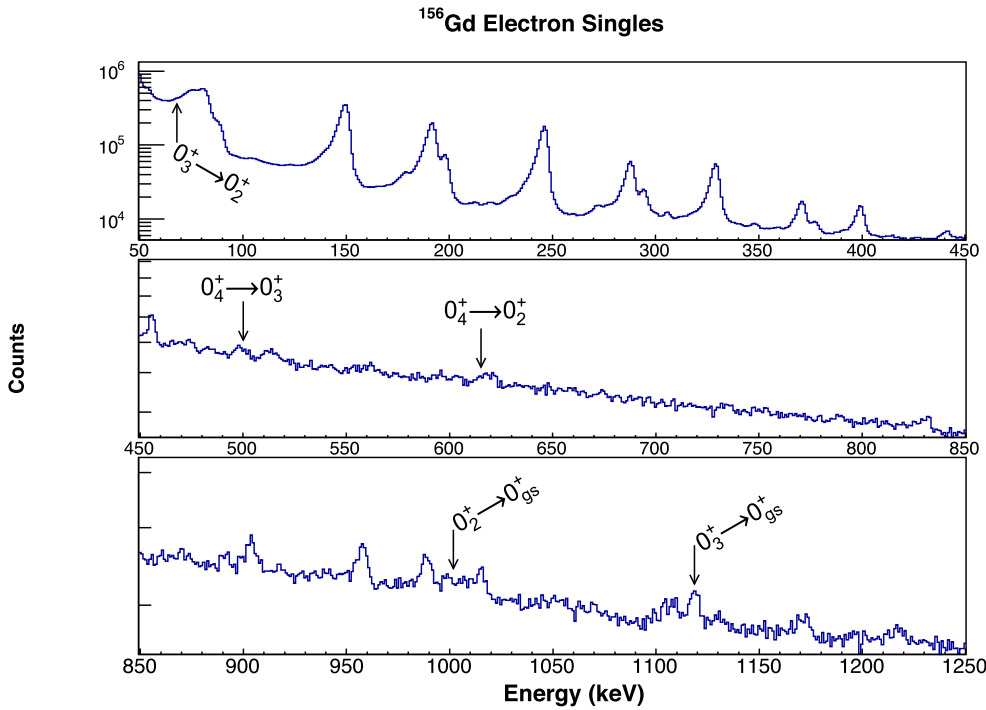


Figure 5.7. Electron singles for ^{156}Gd . The energies of transitions between 0^+ states are marked in the plot. In this spectrum, the $0_3^+ \rightarrow 0_{gs}^+$ transition is the most prominent. The $0_2^+ \rightarrow 0_{gs}^+$ and $0_4^+ \rightarrow 0_3^+$ transitions appear to have some strength, but are obscured by other conversion electrons in the data. The $0_3^+ \rightarrow 0_2^+$ transition is at too low an energy to distinguish from the high background at low energies.

TABLE 5.6

 $0^+ \rightarrow 0^+$ TRANSITIONS IN ^{156}GD

E_i (keV)	Band	E_f (keV)	Band	E (keV)	Gate	α (This Work)	Theory	
							$\alpha(M1)$	$\alpha(E2)$
1168.186	0_3^+	1049.487	0_2^+	118.71	960.50771	> 1.1970	1.042 (15)	0.726 (11)

A list of conversion coefficients from ^{156}Gd for $0^+ \rightarrow 0^+$ transitions seen in the gated data. All listed theoretical values are for the K-shell internal conversion coefficient. Numbers are compared with theoretical values for illustration. All coefficients are K-shell electrons.

TABLE 5.7

 $2^+ \rightarrow 2^+$ TRANSITIONS IN ^{156}GD

E_i (keV)	Band	E_f (keV)	Band	E (keV)	Gate	α (This Work)	Theory		
							$\alpha(\text{M1})$	$\alpha(\text{E2})$	α (Konijn)
1258.075	0_3^+	1129.437	0_2^+	128.638	1040.470	> 0.5325	0.830 (12)	0.578 (8)	
1258.075	0_3^+	1154.152	γ	103.92	1065.1781	> 2.9695	1.524 (22)	1.049 (15)	
1827.841	2_2^+	1129.437	0_2^+	698.407	1040.470	< 0.0208	0.00932 (13)	0.00506 (7)	
1827.841	2_2^+	1154.152	γ	673.684	1065.1781	< 0.0228	0.01018 (15)	0.00550 (8)	
1827.841	2_2^+	1258.075	0_3^+	569.771	1169.087	< 0.0013	0.01545 (22)	0.00819 (12)	0.006 (4)

A list of conversion coefficients from ^{156}Gd for $2^+ \rightarrow 2^+$ transitions seen in the gated data. All listed theoretical values are for the K-shell internal conversion coefficient. Numbers are compared with Konijn et al.[43] All coefficients are K-shell electrons.

TABLE 5.8

 $4^+ \rightarrow 4^+$ TRANSITIONS IN ^{156}GD

E_i (keV)	Band	E_f (keV)	Band	E (keV)	Gate	α (This Work)	Theory	
							$\alpha(M1)$	$\alpha(E2)$
1462.297	0_3^+	1297.822	0_2^+	164.469	1009.649	> 0.4870	0.416 (6)	0.279 (4)
1462.297	0_3^+	1355.422	γ	106.88	1067.2325	> 0.7233	1.405 (20)	0.972 (14)
1510.594	4_1^+	1297.822	0_3^+	212.771	1009.649	> 0.0704	0.204 (3)	0.1282 (18)
1510.594	4_1^+	1355.422	γ	155.168	1067.2325	> 0.0981	0.490 (7)	0.333 (5)

A list of conversion coefficients from ^{156}Gd for $4^+ \rightarrow 4^+$ transitions seen in the gated data. All listed theoretical values are for the K-shell internal conversion coefficient. Numbers are compared with Konijn et al. [43] All coefficients are K-shell electrons.

multiplied by the theoretical $\alpha(E2)$, which gives an estimate of $E0$ intensity (see Section 1.3.1). None of the transitions have known δ mixing ratios, so δ was assumed to be 1, and the theoretical mixed $M1$ and $E2$ α was subtracted. In some cases, this left a negative value, which has been excluded from the table of results, Table 5.9. All values calculated are upper or lower limits, as the α calculated in the previous tables were upper and lower limits.

With these values, two transitions from the same level can be compared using the $B(E0)$ formula to take the energy adjustment into account. It is also adjusted by the ratio of the gate efficiencies. Only one 2^+ level had transitions to other 2^+ states that could be compared. This ratio is in Table 5.10.

The first excited 0^+ band and the γ band are not discussed, as no $J^\pi \rightarrow J^\pi$ transitions could be observed leaving these levels.

5.4.2.1 $K^\pi = 0_3^+$, Second Excited 0^+ Band, 1168.186 keV

Transitions from this band to both the first 0^+ band (0_2^+) and the γ band could be observed. All values observed are lower limits. The 0^+ state in the band has a known lifetime, allowing for the $0_3^+ \rightarrow 0_2^+$ nuclear matrix element to the first excited 0^+ state be calculated[4]. Table 5.11 contains the calculated q^2 and ρ^2 value for the $0_3^+ \rightarrow 0_2^+$ transition.

For the other transitions to the first excited 0^+ band, the $2_{0_3^+}^+ \rightarrow 2_{0_2^+}^+$ transition lower limit did not allow for any conclusions to be drawn as to the nature of the transition. The $4_{0_3^+}^+ \rightarrow 4_{0_2^+}^+$ transition lower limit indicates an $E0$ component. Assuming both transitions have an $E0$ component and δ is 1, Table 5.9 has the lower limits tabulated for the $q^2\alpha(E2)$ values.

For the transitions to the γ band, the $2_{0_3^+}^+ \rightarrow 2_{0_2^+}^+$ transition lower limit indicates an $E0$ component. The $4_{0_3^+}^+ \rightarrow 4_{0_2^+}^+$ transition lower limit did not allow for any conclusions to be drawn as to the nature of the transition.

TABLE 5.9

E0 CONTRIBUTIONS FOR $J^\pi \rightarrow J^\pi$ TRANSITIONS

E_i (keV)	Band	E_f (keV)	Band	E (keV)	Gate	$q^2\alpha(E2)$
$2^+ \rightarrow 2^+$						
1258.075	0_3^+	1154.152	γ	103.92	1065.1781	> 3.366
1827.841	2_2^+	1129.437	0_2^+	698.407	1040.47	< 0.02722
1827.841	2_2^+	1154.152	γ	673.684	1065.1781	< 0.02992
$4^+ \rightarrow 4^+$						
1462.297	0_3^+	1297.822	0_2^+	164.469	1009.649	> 0.279

A list of $E0$ contributions in ^{156}Gd , assuming a mixing ratio between the E2 and M1 contributions of $\delta = 1$. These values have not been normalized, as the lifetime of the states are unknown. Table 5.10 compares values between two transitions of the same initial state. Only non-negative values are listed in the table, and δ was assumed to be 1, as no mixing ratios are known for these transitions. For $\alpha(\text{exp})$, $\alpha(M1)$, and $\alpha(E2)$ used in these calculations, please refer to Tables 5.7-5.8.

TABLE 5.10

B(E0) RATIOS FOR $J^\pi \rightarrow J^\pi$ TRANSITIONS

E_i (keV)	Band	$E_{0_2^+}$ (keV)	Gate $_{0_2^+}$	E_γ (keV)	Gate $_\gamma$	$B(E0)$ Ratio
$2^+ \rightarrow 2^+$						
1827.841	2_2^+	1129.437	1040.47	1154.152	1065.1781	1.128

Ratios of the $B(E0)$ values in ^{156}Gd . Only ratios between two transitions of the same state are listed, as the lifetime of the states are unknown. Table 5.9 lists the values that were used in the calculation. The gates are included, as an efficiency correction was made on the ratio based on the gates. In many cases, only upper or lower limits for the values could be used for this calculation. Errors are not given on these values.

TABLE 5.11

E0 CONTRIBUTIONS FOR $J^\pi \rightarrow J^\pi$ TRANSITIONS

E_i (keV)	Transition	$E0$ (keV)	Transition	$E2$ (keV)	$t_{1/2}$ (ps)	$q_K^2(E0/E2)$	$\rho^2(E0)$
1168.186	$0_3^+ \rightarrow 0_2^+$	118.71	$0_3^+ \rightarrow 2_{gs}^+$	1079.216	$0.9031 < t_{1/2} < 4.4221$	1.995 (15)	$22.78 < \rho^2 < 111.53$

Table 5.11: A list of $q_K^2(E0/E2)$ and $\rho^2(E0)$ contributions in ^{156}Gd for the $0^+ \rightarrow 0^+$ transitions. Lifetime from [4].

5.4.2.2 $K^\pi = 2_2^+$, Second Excited 2^+ Band, 1827.841 keV

The transitions from the head of this band to the 2^+ states of the γ band and the first and second 0^+ excited states were observed. All three coefficients are upper limits. The transitions to the γ band and the first excited 0^+ band may have E0 components, as the upper limits do not rule them out. Assuming both transitions have an E0 component and δ is 1, Table 5.9 has the upper limits tabulated for the $q^2\alpha(E2)$ values. The values are quite small. Table 5.10 compares the strengths of the two transitions as a ratio. The ratio is close to 1, indicating similar transition strengths from this 2^+ excited band to the γ band the first excited 0^+ band.

The upper limit on the transition to the second excited 0^+ band does rule out an E0 component. The upper limit is lower than the measurement by Konijn, although not significantly so when looking at the error on the conversion coefficient[43].

5.4.2.3 $K^\pi = 4_1^+$, First Excited 4^+ Band, 1510.594 keV

The transitions from the head of this band to the 4^+ states of the γ band and the first excited state were observed. Both coefficients are lower limits. No conclusions can be drawn for the transitions, as the lower limits do not rule any type of transition out.

CHAPTER 6

DISCUSSION

Understanding the nature of collective bands in nuclei requires the use of multiple tools. Energies, transition characterization including strengths and multipolarities, and lifetime information is all vital. Combining this data together creates a story to understand the nature of the band.

6.1 Dynamic Symmetries in Nuclei

Dynamical symmetries are a way to describe physical properties of nuclear systems with explicit analytical form [33]. The most notable example of a dynamical system is that of the interacting boson model (IBM). The standard interacting boson triangle of symmetries is in Figure 6.1. The three corners represent the vibrator, rotor, and γ -soft (or γ -unstable) models of nuclei. A nucleus can rest anywhere within the triangle. The points E(5) and X(5) are the critical points of phase transition. Introduced by Iachello in 2000 [33], with first evidence noted later that year [19], properties of these critical point nuclei can be described analytically, predicting differences in energies of excited states in the nucleus, for example [34].

The predicted ratios for the X(5) critical point symmetry agree well with the ratios for ^{154}Gd [76]. However, these ratios were determined not to be robust enough to definitively classify ^{154}Gd as an X(5) nucleus, and a more stringent test of the X(5) predictions, the absolute B(E2) values was used. The nucleus showed good agreement with theory. Importantly, one of the assumptions Iachello made when developing these critical point symmetries was shape coexistence between the two

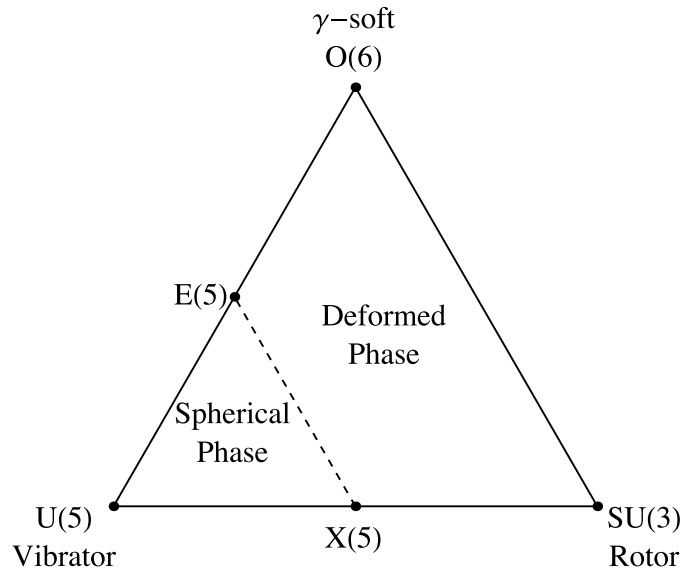


Figure 6.1. The interacting boson model symmetry triangle. The critical point symmetries described by Iachello[33] are marked.

lowest 0^+ states in the nucleus. The IBM predicted the deformations of these two excited 0^+ states will become similar as the deformed limit is reached[78]. While ^{156}Gd has also been examined through the lens of the interacting boson model, it is a rotor in the axially-deformed limit.

6.2 Dynamic Moments of Inertia

Identical bands in neighboring nuclei are a phenomenon that was discovered in the 1990s [7]. These identical bands indicate identical moments of inertia in two different nuclei. Baktash[7] defines two different moments of inertia: kinematic ($\mathcal{J}^{(1)}$) and dynamic ($\mathcal{J}^{(2)}$), specifically identifying $\mathcal{J}^{(2)}$ as being identical in both bands. These

moments of inertia can be approximated for rotational bands as

$$\begin{aligned}\mathcal{J}^{(1)} &\equiv I/\omega \approx 2I/E_\gamma \\ \mathcal{J}^{(2)} &\equiv (d^2E/dI^2)^{-1} = dI/d\omega \approx 4/\delta E_\gamma\end{aligned}\tag{6.1}$$

where I is the spin of the level being depopulated, E_γ is the energy of the gamma depopulating level I , δE_γ is the difference between two separate energies of gamma transitions, and ω us the rotational frequency such that

$$\hbar\omega(I) = dE_I/dI \approx [E(I+1) - E(I-1)]/2 = E_\gamma(I+1)/2\tag{6.2}$$

As $\mathcal{J}^{(2)}$ is a derivative of the spin, it eliminates any single particle component of the aligned angular momentum, making it a better indicator if the collective properties of the band. There is still a slowly changing component that is seen with increasing spin.

While Baktash discussed the identical band phenomenon between two different nuclei, it can also be used to compare bands within the same nucleus, giving insight into the relative nature of the collective bands [4]. Combining the dynamic moment of inertia with measures of the ρ^2 of E0 transitions can give further insight into the nuclear matrix element. While the E0 matrix element is generally seen as a change in the radius of the nucleus between two states of the same J^π , it is, more accurately, a combination of this radial change and a measure of the overlap of the nuclear states. Comparing the dynamic moments of inertia of the two bands involved in an E0 transition can aid in examining the strength of the nuclear overlap.

To examine the structure of the bands seen in this experiment, the dynamic moments of inertia can be compared. This is usually done with higher spins, but examination at lower spins can allow for more bands to be compared. The energy difference tracks linearly, with the slope being directly correlated to the moment of

inertia of the band, as seen in Figures 6.2, 6.3, 6.4, and 6.5. The slopes of these bands are summarized in Tables 6.1 and 6.15. Slopes will vary with spin, and slopes with an error had enough points to calculate the error on the slope based on the fit. Those without error had only two points or, in the case of the second excited 2^+ band, one point and the origin. These points each require two levels of the band to be known for calculation. The intercept was left to float, but not included, as it was in agreement with 0 in all cases where error could be calculated.

6.3 ^{154}Gd Results

In Chapter 4, the results of this work on the nucleus ^{154}Gd were detailed. From the singles data multipole assignments were confirmed for two transitions, conversion coefficients were measured for 30 transitions, and δ was measured for one. A new transition, from $5_{0-}^- \rightarrow 6_{gs}^+$ was seen. Five pure E0 transitions were measured via coincidence (Table 4.7), with two of these transitions having been measured for the first time in this work ($0_6^+ \rightarrow 0_2^+$ and $0_7^+ \rightarrow 0_3^+$). None of these 0^+ states had lifetimes, but the $q_K^2(E0/E2)$ value was calculated for all the transitions (Table 4.12).

A total of 22 $J^\pi \rightarrow J^\pi$ transitions were measured for 2^+ (Table 4.8), 4^+ (Table 4.9), and 6^+ (Table 4.10) states, 11 of these transitions for the first time. Of these 22 transitions, 11 have conversion coefficients indicating evidence of E0 components. Four of these transitions had known δ mixing ratios, allowing for the calculation of ϵ , the E0/E2 mixing ratio (Table 4.13), and in two cases with known lifetimes, the nuclear strength parameter $\rho^2(E0)$. For the rest of the transitions, δ was assumed to be 1, so $q^2\alpha(E2)$ and $B(E0)$ ratios were calculated for transitions depopulating the same level (Tables 4.11 and 4.14). Combining these ratios with the dynamic moments of inertia can give some insight into the strength of $\rho^2(E0)$.

The γ -band, seen in Figure 6.2 is a vibration built on the ground state, leading to a nearly identical dynamic moment of inertia. The $K = 4^+$ band has a nearly

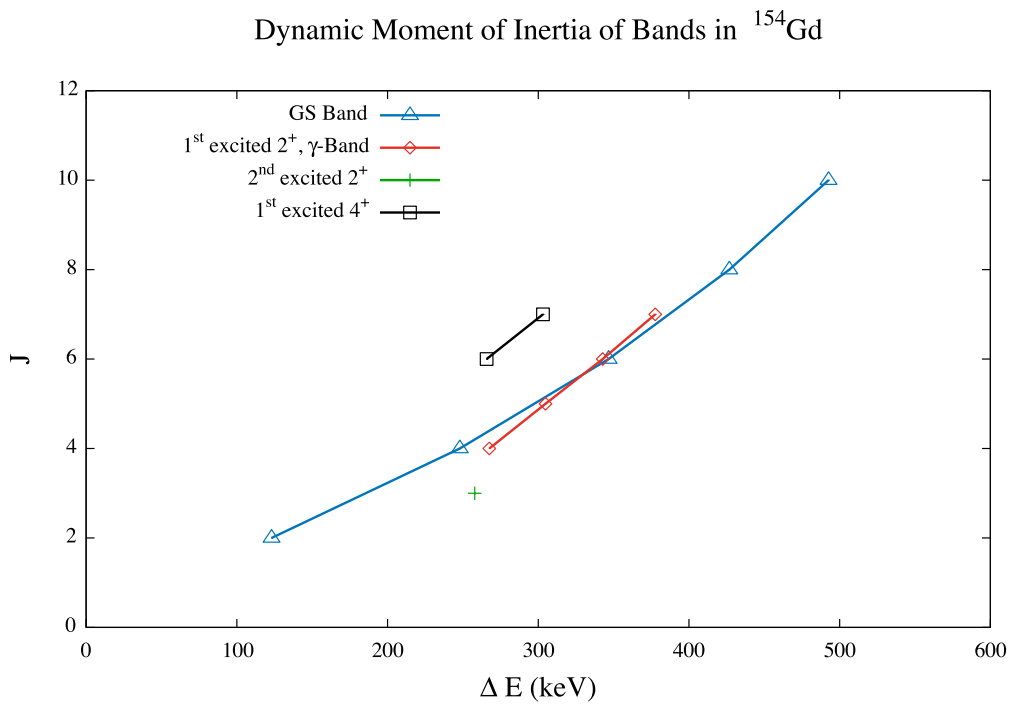


Figure 6.2. The dynamic moments of inertia of the non- 0^+ bands seen in the experiment. As is seen visually and with the slopes, the ground state band and the γ band have similar moments of inertia. However, they do not overlap within their standard deviations.

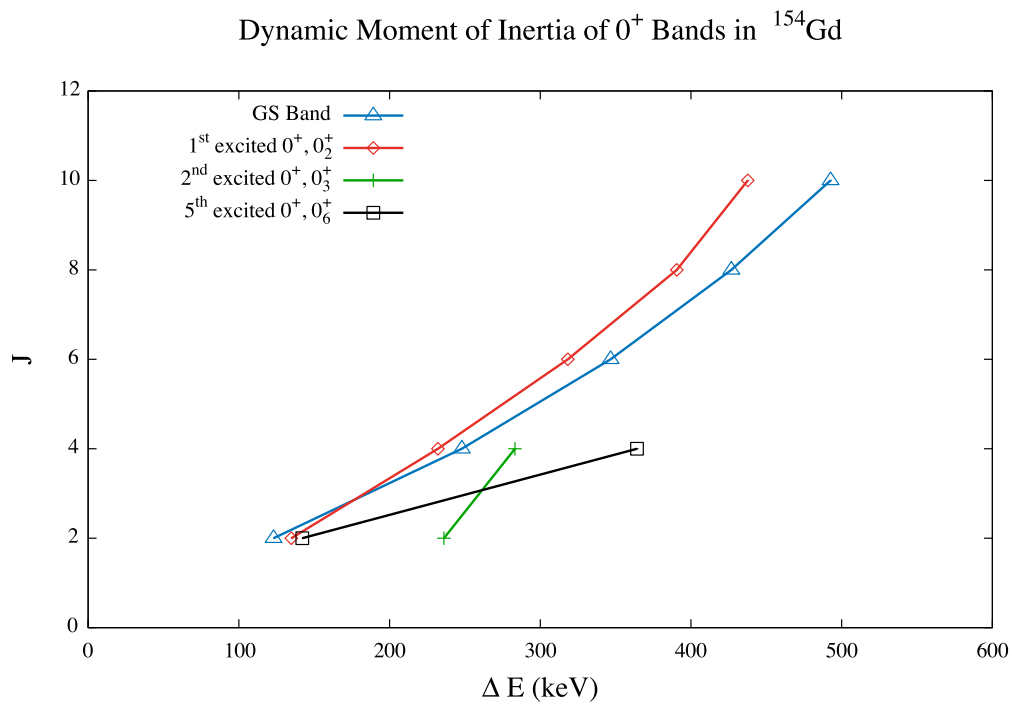


Figure 6.3. The dynamic moments of inertia of the four 0^+ bands seen in the experiment. As is seen visually and with the slopes, the ground state band and the first excited 0^+ band have very similar moments of inertia.

TABLE 6.1
DYNAMIC MOMENTS OF INERTIA OF BANDS SEEN IN ^{154}GD

Band	Moment of Inertia
Ground State	0.0214 (15)
1st excited 0^+ , 0_2^+	0.0258 (19)
2nd excited 0^+ , 0_3^+	0.0424
5th excited 0^+ , 0_6^+	0.0090
1st excited 2^+ , γ -band	0.0271 (3)
2nd excited 2^+	0.0155
1st excited 4^+	0.0267

Table 6.1: List of the moments of inertia of the bands seen in ^{154}Gd in this experiment. The moment of inertia is the slope in a least-squares linear regression. Those without error only had one or two points of energy difference, so the standard deviation of the slope could not be calculated. The ground state band and the first excited 0^+ band agree within two standard deviations.

identical moment of inertia to the γ -band, indicating it, too, may be a vibration built on the same structure as the ground state. The first excited 0^+ state 0_2^+ , seen in Figure 6.3, agrees with the γ -band within 1σ . The variation in the error of slopes has to do with the slow change in $\mathcal{J}^{(2)}$ due to the increase in spin.

6.3.1 $K^\pi = 0_2^+$, First Excited 0^+ Band, 680.6673 keV

The conversion coefficients for the singles and gated data originating from the first excited 0^+ band are in Tables 6.2 and 6.3, respectively. The first excited 0^+ band is the only band with lifetimes and mixing ratios such that ρ^2 could be calculated, seen in Table 4.12. The first excited 0^+ band has a very similar slope to the ground state band, as seen both in Figure 6.3 and Table 6.1, indicating similar moments of inertia. Lifetimes beyond the 4^+ state are unknown, so the ρ^2 value cannot be calculated for the 6^+ state, but could be calculated for the 2^+ and 4^+ states. With the large ρ^2 values calculated for the $2_{0_2^+}^+ \rightarrow 2_{gs}^+$ and $4_{0_2^+}^+ \rightarrow 4_{gs}^+$ transitions to the ground state, the small change in the moment of inertia would indicate a large overlap in the nuclear states.

TABLE 6.2

^{154}GD $K_i = 0_2^+$ INTERNAL CONVERSION COEFFICIENTS FROM
SINGLES

(a)

E (keV)	$J^\pi \rightarrow J^\pi$	E_i (keV)	E_f (keV)	$T_{1/2}$ (fs)	Multipolarity	δ
557.58	$0_{0_2^+}^+ \rightarrow 2_{gs}^+$	680.6673	123.0709	4560	E2	
444.19	$2_{0_2^+}^+ \rightarrow 4_\gamma^+$	815.4917	370.9998	6400	E2	
693.47	$2_{0_2^+}^+ \rightarrow 2_{gs}^+$	815.4917	123.0709	6400	E2+M1+E0	7.5 (4)
232.44	$4_{0_2^+}^+ \rightarrow 2_{0_2^+}^+$	1047.592	815.4917	7600	E2	
329.49	$4_{0_2^+}^+ \rightarrow 6_{gs}^+$	1047.592	717.662	7600	E2	
676.70	$4_{0_2^+}^+ \rightarrow 4_{gs}^+$	1047.592	370.9998	7600	E0+M1+E2	+2.9 (4)
924.85	$4_{0_2^+}^+ \rightarrow 2_{gs}^+$	1047.592	123.0709	7600	E2	
610.71	$8_{0_2^+}^+ \rightarrow 8_{gs}^+$	1756.49	1144.44		E0+M1+E2	-0.69 (14)

(b)

E (keV)	Shell	α (This Work)	α (Th)[40]	α (Spits)[75]	α (Gono)[31]
557.58	K	0.0486 (42) (6)	0.00864 (12)	0.009 (1)	0.0091 (16)
444.19	K	0.0525 (32) (6)	0.01543 (22)	0.014 (1)	
693.47	K	0.0017 (2) (1)	0.00522 (8)	0.0421 (4)	
232.44	K	0.287 (103) $^{+83}_{-82}$	0.0982 (14)	0.100 (8)	
	LM	0.0450 (46) (13)	0.0288 (4)		
329.49	K	0.1573 (89) (17)	0.0352 (5)	0.034 (3)	
676.70	K	0.0283 (4) (10)	0.00593 (17)	0.0460 (46)	0.040 (7)
924.85	K	0.0033 (9) (1)	0.00273 (4)	0.0031 (1)	
610.71	K	0.0258 (10) (7)	0.0110 (6)		0.053 (7)
	L	0.0167 (9) (4)	0.00158 (7)		

Table ??: A list of conversion coefficients from ^{154}Gd , originating in the $K_i = 0_2^+$ band. Table (a) lists transition information. Multipolarities and mixing ratios were taken from the nuclear data sheets[64]. Table (b) lists the conversion coefficients. Unless otherwise stated, the α values are α_K . An angular distribution correction has been applied based on multipolarities for pure transitions, and those with known mixing ratios. The first error is statistical, the second is systematic. Numbers are compared with Spits et al.[75] and Gono et al.[31] The starred value was used as an absolute calibration of the conversion electron detector in the Gono work. The bands for each level are listed as subscripts.

TABLE 6.3

 $J^\pi \rightarrow J^\pi$ TRANSITIONS FOR $K_i = 0_2^+$ IN ^{154}GD

E_i (keV)	Band	E_f (keV)	Band	E (keV)	Gate	α (This Work)	Theory[40]		α (Spits)[75]	α (Gono)[31]
							α (M1)	α (E2)		
815.4917	$2_{0_2^+}^+$	123.0709	2_{gs}^+	692.4205	123.0706	0.0430 (3) (9)	0.00952 (14)	0.00516 (8)	0.0421 (4)	
1047.592	$4_{0_2^+}^+$	370.9998	4_{gs}^+	676.593	247.9288	0.0550 (2) ₋₁₁ ⁺¹²	0.01007 (15)	0.00544 (8)	0.0460 (46)	0.040 (7)
						0.0131 (1) (3)	0.001384 (20)	0.000870 (13)		
1365.878	$6_{0_2^+}^+$	717.662	6_{gs}^+	648.3	346.643	0.0778 (4) (16)	0.01120 (16)	0.00601 (9)		0.039 (7)

Table 6.3: A list of conversion coefficients from ^{154}Gd for $J^\pi \rightarrow J^\pi$ transitions for $K_i = 0_2^+$ seen in the gated data. The first error is statistical, the second is systematic. Numbers are compared with theoretical K-shell conversion coefficients for M1 and E2 transitions, as well as results from Spits et al.[75] and Gono et al.[31] All coefficients are K-electrons, except for the transition from 1047 keV. The second value is the LM peak.

The similarity in the dynamic moment of inertia, coupled with the large ρ^2 values, indicate a β -vibration. The γ -vibration band dynamic moment of inertia behaves very similarly to the ground state in much the same way, also favoring this interpretation.

6.3.2 $K^\pi = 0_3^+$, Second Excited 0^+ Band, 1182.091 keV

The conversion coefficients for the gated data originating from the second excited 0^+ band are in Table 6.17. All of the measurements from the $K = 0_3^+$ band were limits, and connected to either the 0_2^+ band or the γ -band. All the transitions were measured with two different gates. The 2^+ state transitions only had lower limits, with the lower limit on the γ -band indicating an E0 component. For the 4^+ state transitions, the limits were upper limits. The upper limit to the 0_2^+ transition indicated little to no E0 component, while the upper limit on the transition to the γ -band allows for a larger E0 component. The transitions, in agreement with Table 4.14, indicate the 0_3^+ band favors populating the γ -band. This band also has a much larger dynamic moment of inertia, compared to the ground state, first excited 0^+ state and γ -bands. None of the transitions examined have known mixing ratios, so the q^2 and αq^2 can be found in Tables 4.11 and 4.12.

TABLE 6.4

 $J^\pi \rightarrow J^\pi$ TRANSITIONS FOR $K_i = 0_3^+$ IN ^{154}GD

E_i (keV)	Band	E_f (keV)	Band	E (keV)	Gate	α (This Work)	Theory[40]		α (Spits)[75]
							α (M1)	α (E2)	
1182.091	0_3^+	680.6673	0_2^+	501.427	557.581	> 0.0283	0.0213 (3)	0.01126 (16)	> 0.2
1418.16	$2_{0_3^+}^+$	815.4917	$2_{0_2^+}^+$	602.688	692.4205	> 0.0125	0.01343 (19)	0.00715 (10)	0.025 (3)
					444.4924	> 0.0093			
1418.16	$2_{0_3^+}^+$	996.2568	2_γ^+	421.893	873.1834	> 0.0367	0.0332 (5)	0.01170 (25)	0.114 (16)
					625.2556	> 0.0463			
1701.39	$4_{0_3^+}^+$	1047.592	$4_{0_3^+}^+$	653.7	676.593	< 0.0093	0.01097 (16)	0.00590 (9)	0.0220 (62)
					924.55	< 0.0301			
1701.39	$4_{0_3^+}^+$	1263.778	4_γ^+	437.612	892.775	< 0.0585	0.0302 (5)	0.01605 (23)	
					1140.702	< 0.0511			

Table 6.17: A list of conversion coefficients from ^{154}Gd for $J^\pi \rightarrow J^\pi$ transitions for $K_i = 0_3^+$ seen in the gated data. The first error is statistical, the second is systematic. Numbers are compared with theoretical K-shell conversion coefficients for M1 and E2 transitions, as well as results from Spits et al.[75]. All coefficients are K-electrons, except for the transition from 1047 keV. The second value is the LM peak.

6.3.3 $K^\pi = 0_6^+$, Fifth Excited 0^+ Band, 1573.9 keV

The conversion coefficients for the singles and gated data originating from the fifth excited 0^+ band are in Tables 6.5 and 6.6, respectively. Transitions between the 0_6^+ band and the 0_2^+ and 0_3^+ bands could be seen in the gates, specifically for the 0^+ states. ρ^2 could not be calculated due to a lack of lifetime, but the two transitions could be compared, in Table 4.14, indicating a stronger connection to the 0_3^+ band. Comparisons between the 0_2^+ and γ -band were also done using the 2^+ state, generally indicating a stronger connection to the γ -band than the 0_2^+ band. None of the transitions examined have known mixing ratios, so the q^2 and αq^2 can be found in Tables 4.11 and 4.12. The fifth excited 0^+ band has the smallest slope of all the bands looked at in this nucleus, the strongly different moment of inertia gives an indication this band is likely not built on the γ -band or 0_2^+ band.

TABLE 6.5

^{154}GD $K_i = 0_6^+$, INTERNAL CONVERSION COEFFICIENTS FROM
SINGLES

(a)

E (keV)	$J^\pi \rightarrow J^\pi$	E_i (keV)	E_f (keV)	$T_{1/2}$ (fs)	Multipolarity	δ
416.79	$4_0^+ \rightarrow 3_2^+$	2080.23	1660.903		(M1)	

(b)

E (keV)	Shell	α (This Work)	α (Th)[40]	α (Spits)[75]	α (Gono)[31]
416.79	K	0.0334 (47) (6)	0.03442 (5)		

Table 6.5: A list of conversion coefficients from ^{154}Gd , originating in the $K_i = 0_6^+$ band. Table (a) lists transition information. Multipolarities and mixing ratios were taken from the nuclear data sheets[64]. Table (b) lists the conversion coefficients. Unless otherwise stated, the α values are α_K . An angular distribution correction has been applied based on multipolarities for pure transitions, and those with known mixing ratios. The first error is statistical, the second is systematic. Numbers are compared with Spits et al.[75] and Gono et al.[31] The starred value was used as an absolute calibration of the conversion electron detector in the Gono work. The bands for each level are listed as subscripts.

TABLE 6.6

 $J^\pi \rightarrow J^\pi$ TRANSITIONS FOR $K_i = 0_6^+$ IN ^{154}GD

E_i (keV)	Band	E_f (keV)	Band	E (keV)	Gate	α (This Work)	Theory[40]		α (Spits)[75]
							α (M1)	α (E2)	
1573.9	0_6^+	680.6673	0_2^+	893.9	557.581	> 0.0183	0.00510 (8)	0.00294 (5)	
1573.9	0_6^+	1182.091	0_3^+	391.9	1059.033	> 0.0529	0.0402 (6)	0.0216 (3)	> 0.1
1716.050	$2_{0_2^+}^+$	815.4917	$2_{0_2^+}^+$	900.5583	692.4205 444.4924	< 0.0105 < 0.0531	0.00501 (7)	0.00289 (4)	
1716.050	$2_{0_6^+}^+$	996.2568	2_γ^+	719.80	873.1834 625.2556	0.0113 (46) $^{+33}_{-25}$ 0.0501 (260) $^{+147}_{-113}$	0.00865 (13)	0.00472 (7)	

Table 6.6: A list of conversion coefficients from ^{154}Gd for $J^\pi \rightarrow J^\pi$ transitions for $K_i = 0_6^+$ seen in the gated data. The first error is statistical, the second is systematic. Numbers are compared with theoretical K-shell conversion coefficients for M1 and E2 transitions, as well as results from Spits et al.[75]. All coefficients are K-electrons, except for the transition from 1047 keV. The second value is the LM peak.

6.3.4 $K^\pi = 0_7^+$, Sixth Excited 0^+ Band, 1650.3 keV

The conversion coefficients for the gated data originating from the sixth excited 0^+ band are in Table 6.17. Transitions between the 0_7^+ band and the 0_2^+ and 0_3^+ bands could be seen in the gates, specifically for the 0^+ states. ρ^2 could not be calculated due to a lack of lifetime, but the two transitions could be compared, in Table 4.14, indicating a stronger connection to the 0_3^+ band. Comparisons between the 0_2^+ and γ -band were also done using the 2^+ state, generally indicating a stronger connection to the γ -band than the 0_2^+ band, although with this ratio being a limit, this could be untrue. None of the transitions examined have known mixing ratios, so the q^2 and αq^2 can be found in Tables 4.11 and 4.12. This band did not have enough information to calculate the dynamic moment of inertia, hence its omission from Figure 6.3 and Table 6.1.

TABLE 6.7

 $J^\pi \rightarrow J^\pi$ TRANSITIONS FOR $K_i = 0_7^+$ IN ^{154}GD

E_i (keV)	Band	E_f (keV)	Band	E (keV)	Gate	α (This Work)	Theory[40]		α (Spits)[75]
							α (M1)	α (E2)	
1650.3	0_7^+	680.6673	0_2^+	970.3	557.581	> 0.0209	0.00419 (6)	0.00247 (4)	> 0.027
1650.3	0_7^+	1182.091	0_3^+	468.3	1059.033	> 0.0922	0.0254 (4)	0.01343 (19)	
1775.429	$2_{0_7^+}^+$	815.4917	$2_{0_2^+}^+$	960.05	692.4205	> 0.0221	0.00430 (6)	0.00253 (4)	
1775.429	$2_{0_7^+}^+$	996.2568	2_γ^+	779.165	873.1834	0.0206 (112) $^{+60}_{-46}$	0.00712 (10)	0.00396 (6)	
					625.2556	0.0745 (521) $^{+217}_{-165}$			

Table 6.7: A list of conversion coefficients from ^{154}Gd for $J^\pi \rightarrow J^\pi$ transitions for $K_i = 0_7^+$ seen in the gated data. The first error is statistical, the second is systematic. Numbers are compared with theoretical K-shell conversion coefficients for M1 and E2 transitions, as well as results from Spits et al.[75]. All coefficients are K-electrons, except for the transition from 1047 keV. The second value is the LM peak.

6.3.5 $K^\pi = 2^+$, γ Band, 996.264 keV

The conversion coefficients for the singles and gated data originating from the first excited 2^+ band, the γ -vibrational band are in Tables 6.8 and 6.9, respectively. The γ band has a very similar slope to the ground state band, as seen both in Figure 6.2 and Table 6.1, indicating similar moments of inertia, although the slope is higher than that seen by the ground state band or first excited 0^+ band. While measures of the transitions between the γ band and ground state band could not be done in this work, measures between the γ -band and first excited 0^+ were done. The $2^+ \rightarrow 2^+$ and $6^+ \rightarrow 6^+$ transitions indicate potentially large E0 components for the conversion coefficients. The $4^+ \rightarrow 4^+$ transition indicates small E0 components. Of these transitions, the $2^+ \rightarrow 2^+$ has a previously measured relative γ -intensity of 0.043 (6)% [64]. The low intensities of these transitions and the lack of mixing and branching ratios make it difficult to draw conclusions. None of the transitions examined have known mixing ratios, so the q^2 and αq^2 can be found in Table 4.11.

TABLE 6.8

^{154}GD $K_i = 2_1^+$, γ INTERNAL CONVERSION COEFFICIENTS FROM
SINGLES

(a)

E (keV)	$J^\pi \rightarrow J^\pi$	E_i (keV)	E_f (keV)	$T_{1/2}$ (fs)	Multipolarity	δ
873.54	$2_\gamma^+ \rightarrow 2_{gs}^+$	996.2568	123.0709	950	E2+M1+E0	-9.4 (4)
996.33	$2_\gamma^+ \rightarrow 0_{gs}^+$	996.2568	0	950	E2	
889.61	$6_\gamma^+ \rightarrow 6_{gs}^+$	1606.55	717.662		E2+M1	> 1.8
894.40	$4_\gamma^+ \rightarrow 4_{gs}^+$	1263.778	370.9998		E0+M1+E2	-3.8 (3)
1005.12	$3_\gamma^+ \rightarrow 2_{gs}^+$	1127.8018	123.0709		E2+M1	-7.4 (4)

(b)

E (keV)	Shell	α (This Work)	α (Th)[40]	α (Spits)[75]	α (Gono)[31]
873.54	K	0.0021 (3) (1)	0.00311 (5)	0.0035 (1)	
889.61	K	0.0043 (6) (2)	0.00349 (5)	0.0033 (2)	
894.40	K	0.0019 (2) (1)	0.00307 (5)	0.0039 (3)	
996.33	K	0.0021 (4) (1)	0.00234 (4)	0.0025 (1)	
1005.12	K	0.0019 (1) (1)	0.00233 (4)	0.0024 (1)	

Table 6.8: A list of conversion coefficients from ^{154}Gd , originating in the $K_i = 2_1^+$, γ band. Table (a) lists transition information. Multipolarities and mixing ratios were taken from the nuclear data sheets[64]. Table (b) lists the conversion coefficients. Unless otherwise stated, the α values are α_K . An angular distribution correction has been applied based on multipolarities for pure transitions, and those with known mixing ratios. The first error is statistical, the second is systematic. Numbers are compared with Spits et al.[75] and Gono et al.[31] The starred value was used as an absolute calibration of the conversion electron detector in the Gono work. The bands for each level are listed as subscripts.

TABLE 6.9

 $J^\pi \rightarrow J^\pi$ TRANSITIONS FOR $K_i = 2_1^+$, γ IN ^{154}GD

E_i (keV)	Band	E_f (keV)	Band	E (keV)	Gate	α (This Work)	Theory[40]		α (Spits)[75]
							α (M1)	α (E2)	
996.264	2_γ^+	815.4917	$2_{0_2^+}^+$	180.72	692.4205	> 1.0570	0.320 (5)	0.210 (3)	
					444.4924	> 0.9718			
1263.778	4_γ^+	1047.592	$4_{0_2^+}^+$	216.186	676.593	< 0.1250	0.196 (3)	0.1222 (18)	
					924.55	< 0.1033			
1606.55	6_γ^+	1365.878	$6_{0_2^+}^+$	240.672	648.3	> 0.9065	0.1462 (21)	0.0885 (13)	
					994.9	> 1.1070			

Table 6.9: A list of conversion coefficients from ^{154}Gd for $J^\pi \rightarrow J^\pi$ transitions for $K_i = 2_1^+$, γ seen in the gated data. The first error is statistical, the second is systematic. Numbers are compared with theoretical K-shell conversion coefficients for M1 and E2 transitions, as well as results from Spits et al.[75]. All coefficients are K-electrons, except for the transition from 1047 keV. The second value is the LM peak.

6.3.6 $K^\pi = 2_2^+$, Second Excited 2^+ Band, 1531.305 keV

The conversion coefficients for the singles and gated data originating from the second excited 2^+ band are in Tables 6.10 and 6.19, respectively. The dynamic moment of inertia of the 2nd excited 2^+ state is very different from any of the previously discussed bands. This band has indications of E0 components to both the γ -band and the first excited 0^+ band for the $2^+ \rightarrow 2^+$ transition, but only indications to the first excited 0^+ band for the $4^+ \rightarrow 4^+$ transition. Comparisons of the transitions between the two bands in Table 4.14 indicate a stronger connection to the first excited 0^+ band than the γ -band. This does not confirm it to be built on the first excited 0^+ band, though evidence points to this, including the branching ratios to the ground state and the first excited 0^+ band. With ^{154}Gd considered to be an X(5) critical point nucleus by some, the 0_2^+ state is thought to be a sign of shape coexistence. Should this be the case, this second excited 2^+ band may be a vibration built on this state. It seems unlikely the band is a $\gamma\gamma$ -vibration. None of the transitions examined have known mixing ratios, so the q^2 and αq^2 can be found in Tables 4.11 and 4.12.

TABLE 6.10

^{154}GD $K_i = 2_2^+$, INTERNAL CONVERSION COEFFICIENTS FROM
SINGLES

(a)

E (keV)	$J^\pi \rightarrow J^\pi$	E_i (keV)	E_f (keV)	$T_{1/2}$ (fs)	Multipolarity	δ
349.89	$2_{2^+}^+ \rightarrow 0_{gs}^+$	1531.305	1182.091		[E2]	

(b)

E (keV)	Shell	α (This Work)	α (Th)[40]	α (Spits)[75]	α (Gono)[31]
329.49	K	0.1573 (89) (17)	0.0352 (5)	0.034 (3)	

Table 6.10: A list of conversion coefficients from ^{154}Gd , originating in the $K_i = 2_2^+$ band. Table (a) lists transition information. Multipolarities and mixing ratios were taken from the nuclear data sheets[64]. Table (b) lists the conversion coefficients. Unless otherwise stated, the α values are α_K . An angular distribution correction has been applied based on multipolarities for pure transitions, and those with known mixing ratios. The first error is statistical, the second is systematic. Numbers are compared with Spits et al.[75] and Gono et al.[31] The starred value was used as an absolute calibration of the conversion electron detector in the Gono work. The bands for each level are listed as subscripts.

TABLE 6.11

 $J^\pi \rightarrow J^\pi$ TRANSITIONS FOR $K_i = 2_2^+$ IN ^{154}GD

E_i (keV)	Band	E_f (keV)	Band	E (keV)	Gate	α (This Work)	Theory[40]		α (Spits)[75]
							α (M1)	α (E2)	
1531.305	$2_{2_2^+}^+$	815.4917	$2_{0_2^+}^+$	715.819	692.4205	$0.0146(40)^{+43}_{-33}$	0.00877 (13)	0.00478 (7)	0.0070 (4)
					444.4924	$0.0234(80)^{+68}_{-52}$			
1531.305	$2_{2_2^+}^+$	996.2568	2_γ^+	535.050	873.1834	$0.0204(70)^{+54}_{-41}$	0.0181 (3)	0.00956 (14)	0.093 (11)
					625.2556	> 0.0183			
1789.17	$4_{2_2^+}^+$	1047.592	$4_{0_2^+}^+$	740.91	676.593	< 0.0124	0.00806 (12)	0.00443 (7)	
					924.55	< 0.0447			
1789.17	$4_{2_2^+}^+$	1263.778	4_γ^+	525.392	892.775	< 0.0168	0.0190 (3)	0.01001 (14)	
					1140.702	< 0.0161			

Table 6.19: A list of conversion coefficients from ^{154}Gd for $J^\pi \rightarrow J^\pi$ transitions for $K_i = 2_2^+$ seen in the gated data. The first error is statistical, the second is systematic. Numbers are compared with theoretical K-shell conversion coefficients for M1 and E2 transitions, as well as results from Spits et al.[75]. All coefficients are K-electrons, except for the transition from 1047 keV. The second value is the LM peak.

6.3.7 $K^\pi = 4^+$, First Excited 4^+ Band, 1645.814 keV

The conversion coefficients for the singles and gated data originating from the first excited 4^+ band are in Tables 6.12 and 6.13, respectively. The dynamic moment of inertia for the first excited 4^+ band is almost identical to the γ -band dynamic moment of inertia. The ratios in Table 4.14 indicate a stronger connection to the γ band. The E0 components would not be large for these transitions, indicating a potentially small ρ^2 . The large connection but small ρ^2 would make sense if the first excited 4^+ band is the 4^+ component of the $\gamma\gamma$ excitations. One of the transitions examined has a known mixing ratio, but not a lifetime, and q^2 and ϵ^2 can be found in Table 4.13. The rest, without known mixing ratios, can be found in Table 4.11.

TABLE 6.12

^{154}GD $K_i = 4_1^+$, INTERNAL CONVERSION COEFFICIENTS FROM SINGLES

(a)

E (keV)	$J^\pi \rightarrow J^\pi$	E_i (keV)	E_f (keV)	$T_{1/2}$ (fs)	Multipolarity	δ
506.41	$5_{4_1^+}^+ \rightarrow 4_\gamma^+$	1770.187	1263.778		E2	
515.92	$4_{4_1^+}^+ \rightarrow 3_\gamma^+$	1645.814	1127.802		E2+M1	-7 (3)

(b)

E (keV)	Shell	α (This Work)	α (Th)[40]	α (Spits)[75]	α (Gono)[31]
506.41	K	0.0071 (4) (1)	0.01098 (16)	0.0100 (11)	
515.92	K	0.0069 (5) (1)	0.0107 (4)	0.0113 (9)	

Table 6.12: A list of conversion coefficients from ^{154}Gd , originating in the $K_i = 4_1^+$ band. Table (a) lists transition information. Multipolarities and mixing ratios were taken from the nuclear data sheets[64]. Table (b) lists the conversion coefficients. Unless otherwise stated, the α values are α_K . An angular distribution correction has been applied based on multipolarities for pure transitions, and those with known mixing ratios. The first error is statistical, the second is systematic. Numbers are compared with Spits et al.[75] and Gono et al.[31] The starred value was used as an absolute calibration of the conversion electron detector in the Gono work. The bands for each level are listed as subscripts.

TABLE 6.13

 $J^\pi \rightarrow J^\pi$ TRANSITIONS FOR $K_i = 4_1^+$ IN ^{154}GD

E_i (keV)	Band	E_f (keV)	Band	E (keV)	Gate	α (This Work)	Theory[40]		α (Spits)[75]
							α (M1)	α (E2)	
1645.814	$4_{4_1^+}^+$	1047.592	$4_{0_2^+}^+$	598.22	676.593	< 0.0092	0.01368 (20)	0.00728 (11)	< 0.067
					924.55	< 0.0142			
1645.814	$4_{4_1^+}^+$	1263.778	4_γ^+	382.025	892.775	< 0.0360	0.0429 (6)	0.0232 (4)	0.033 (5)
					1140.702	< 0.0494			
1911.544	$6_{4_1^+}^+$	1365.878	$6_{0_2^+}^+$	545.7	648.3	< 0.0209	0.01723 (25)	0.00911 (13)	
					994.9	< 0.0189			
1911.544	$6_{4_1^+}^+$	1606.55	6_γ^+	304.75	888.69	< 0.0794	0.0777 (11)	0.0440 (7)	0.042 (6)

Table 6.13: A list of conversion coefficients from ^{154}Gd for $J^\pi \rightarrow J^\pi$ transitions for $K_i = 4_1^+$ seen in the gated data. The first error is statistical, the second is systematic. Numbers are compared with theoretical K-shell conversion coefficients for M1 and E2 transitions, as well as results from Spits et al.[75]. All coefficients are K-electrons, except for the transition from 1047 keV. The second value is the LM peak.

6.3.8 Summary and Conclusions

Table 6.14 contains a summary of relevant data for the 0^+ states in ^{154}Gd . Lifetimes are unknown for most of the 0^+ states. This nucleus has not been measured via (n, n') since the 1970s. It would benefit from more lifetime measurements.

6.4 ^{156}Gd Results

In Chapter 5, the results of this work on the nucleus ^{156}Gd were detailed. From the singles data a multipole assignment was made for one transition ($7_{4+}^+ \rightarrow 8_{gs}^+$) of E2+M1, with a δ of < 0.61 or -0.55_{-8}^{+51} , and conversion coefficients were measured for 21 transitions. The newly measured multipole assignment indicates a small M1 component, if not a pure E2 transition. One pure E0 transition was measured via coincidence (Table 4.7). This 0^+ state has a measured lifetime, so $\rho^2(E0)$ was calculated (Table 5.11).

A total of 9 $J^\pi \rightarrow J^\pi$ transitions were measured for 2^+ (Table 5.7) and 4^+ (Table 5.8) states, 8 of these transitions for the first time. Of these 9 transitions, 2 have conversion coefficients indicating evidence of E0 components, with 4 more that have lower limits that may indicate E0 components. None of these transitions had known δ mixing ratios. For the transitions, δ was assumed to be 1, so $q^2\alpha(E2)$ and $B(E0)$ ratios were calculated for transitions depopulating the same level (Tables 5.9 and 5.10). Combining these ratios with the dynamic moments of inertia can give some insight into the strength of $\rho^2(E0)$.

The γ -band, seen in Figure 6.4 is a vibration built on the ground state, leading to a nearly identical dynamic moment of inertia. The $K = 4^+$ band has a nearly identical moment of inertia to the γ -band, indicating it, too, may be a vibration built on the same structure as the ground state. The first excited 0^+ state, 0_2^+ , seen in Figure 6.5, agrees with the γ -band within 1σ . The variation in the error of slopes

TABLE 6.14

SUMMARY OF 0^+ STATE INFORMATION IN ^{154}GD

E (keV)	(p, t) (mb/sr)[54]	τ (ps)	Conv. Elec
0.0	2.37 (1)	Stable	Ground State
680.4(3)	0.513(2)	4.56(27)	×
1181.9(3)	0.0099(9)		×
1352.9(3)	0.0053(7)		
1497.7(3)	0.0032(7)		
1573.7(3)	0.0228(8)		×
1650.6(4)	0.071(1)		×
1836.7(4)	0.0099(5)		
1899.3(4)	0.0030(3)		
1942.9(4)	0.0038(4)		
2039.8(4)	0.0186(7)		
2299.9(5)	0.0200(8)		
2485.1(5)	0.0037(4)		
2585.3(5)	0.0337(9)		
2744.5(5)	0.0131(6)		
2855.0(5)	0.004(2)		

Table 6.14: The current state of information for the 0^+ states in ^{154}Gd . The (p, t) cross section is the 5 from Meyer et al[54]. The lifetime is from Wollersheim and Elze using coulomb excitation[79]. Conversion electron measurements are from this work and Spits et al. [75].

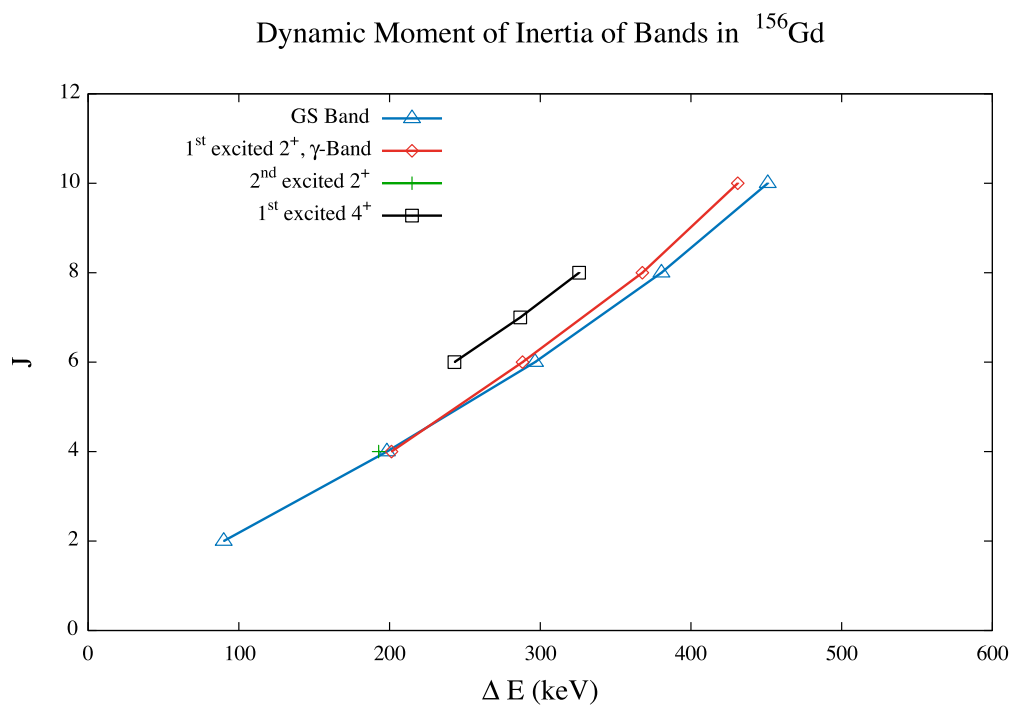


Figure 6.4. The dynamic moments of inertia of the non- 0^+ bands seen in the experiment. As is seen visually and with the slopes, the ground state band and the γ band have similar moments of inertia, and overlap within two standard deviations.

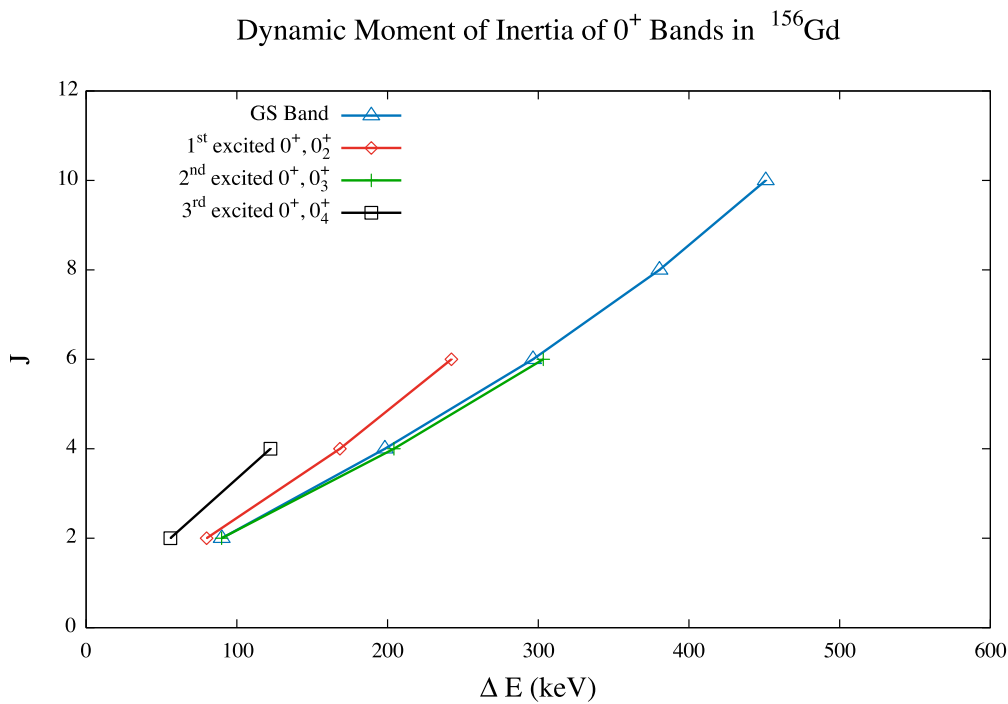


Figure 6.5. The dynamic moments of inertia of the four 0^+ bands seen in the experiment. As is seen visually and with the slopes, the ground state band and the first excited 0^+ band have very similar moments of inertia.

TABLE 6.15
DYNAMIC MOMENTS OF INERTIA OF BANDS SEEN IN ^{156}Gd

Band	Moment of Inertia
Ground State	0.0220 (11)
1st excited 0^+ , 0_2^+	0.0245 (13)
2nd excited 0^+ , 0_3^+	0.0187 (8)
3rd excited 0^+ , 0_4^+	0.0301
1st excited 2^+ , γ -band	0.0259 (13)
2nd excited 2^+	0.0208
1st excited 4^+	0.0242 (10)

Table 6.15: List of the moments of inertia of the bands seen in ^{156}Gd in this experiment. The moment of inertia is the slope in a least-squares linear regression. Those without error only had one or two points of energy difference, so the standard deviation of the slope could not be calculated. The ground state band and the first excited 0^+ band agree within two standard deviations. The same is true of the ground state band and both the γ -band and first excited 4^+ band.

has to do with the slow change in $\mathcal{J}^{(2)}$ due to the increase in spin.

6.4.1 $K^\pi = 0_2^+$, First Excited 0^+ Band, 1049.487 keV

The conversion coefficients for the singles data originating from the first excited 0^+ band are in Table 6.16. The first excited 0^+ band has a very similar slope to the ground state band, as seen both in Figure 6.5 and Table 6.15. The two bands agree within 2σ . Without more statistics, data could not be collected for outgoing transitions from the first excited 0^+ band.

TABLE 6.16

$$^{156}\text{GD}$$
 $K_i = 0_2^+$ INTERNAL CONVERSION COEFFICIENTS FROM
SINGLES

E (keV)	$J^\pi \rightarrow J^\pi$	E_i (keV)	E_f (keV)	Multipolarity	δ	Shell	α (This Work)	α (Th)	α (Konijn)
1040.470	$2_{0_2^+}^+ \rightarrow 2_{gs}^+$	1129.437	88.970	E2+E0+M1	-5.9_{-28}^{+14}	K	0.0152 (10) (2)	0.0022 (1)	0.014 (3)

Table ??: A list of conversion coefficients from ^{156}Gd , originating in the $K_i = 0_2^+$ band.. Multipolarities and mixing ratios were taken from the nuclear date sheets[65]. Unless otherwise stated, the α values are α_K . An angular distribution correction has been applied based on multipolarities for pure transitions, and those with known mixing ratios. The first error is statistical, the second is systematic. Numbers are compared with Konijn et al[43].

6.4.2 $K^\pi = 0_3^+$, Second Excited 0^+ Band, 1168.186 keV

The conversion coefficients for the gated data originating from the second excited 0^+ band are in Table ???. The second excited 0^+ band could be seen going to both the γ band and first excited 0^+ band. It has a very different dynamic moment of inertia compared to those two. This change in shape may account for the large ρ^2 value between the first and second 0^+ excited states, in Table 5.9. In this data, transitions for the 2^+ and 4^+ states in this band were inconclusive about E0 components to the first excited 0^+ state, and the 2^+ state may have an E0 component to the γ -band. The 2^+ and 4^+ transitions examined do not have known mixing ratios, so αq^2 can be found in 5.9.

TABLE 6.17

 $J^\pi \rightarrow J^\pi$ TRANSITIONS FOR $K_i = 0_3^+$ IN ^{154}Gd

E_i (keV)	Band	E_f (keV)	Band	E (keV)	Gate	α (This Work)	Theory[40]		α (Spits)[75]
							α (M1)	α (E2)	
1182.091	0_3^+	680.6673	0_2^+	501.427	557.581	> 0.0283	0.0213 (3)	0.01126 (16)	> 0.2
1418.16	$2_{0_3^+}^+$	815.4917	$2_{0_2^+}^+$	602.688	692.4205	> 0.0125	0.01343 (19)	0.00715 (10)	0.025 (3)
					444.4924	> 0.0093			
1418.16	$2_{0_3^+}^+$	996.2568	2_γ^+	421.893	873.1834	> 0.0367	0.0332 (5)	0.01170 (25)	0.114 (16)
					625.2556	> 0.0463			
1701.39	$4_{0_3^+}^+$	1047.592	$4_{0_3^+}^+$	653.7	676.593	< 0.0093	0.01097 (16)	0.00590 (9)	0.0220 (62)
					924.55	< 0.0301			
1701.39	$4_{0_3^+}^+$	1263.778	4_γ^+	437.612	892.775	< 0.0585	0.0302 (5)	0.01605 (23)	
					1140.702	< 0.0511			

Table 6.17: A list of conversion coefficients from ^{154}Gd for $J^\pi \rightarrow J^\pi$ transitions for $K_i = 0_3^+$ seen in the gated data. The first error is statistical, the second is systematic. Numbers are compared with theoretical K-shell conversion coefficients for M1 and E2 transitions, as well as results from Spits et al.[75]. All coefficients are K-electrons, except for the transition from 1047 keV. The second value is the LM peak.

6.4.3 $K^\pi = 2^+$, γ Band, 1065.1781 keV

The conversion coefficients for the singles data originating from the first excited 2^+ band, the γ -vibrational band are in Table 6.16. The γ band has a very similar slope to the ground state band, as seen both in Figure 6.3 and Table 6.15, indicating similar moments of inertia, although the slope is higher than that seen by the ground state band or first excited 0^+ band. The transitions between the first excited 0^+ band and the γ band are not energetically capable of conversion electrons for the $2_\gamma^+ \rightarrow 2_{0_2^+}^+$ transition, and below the energy threshold of the detectors in this work for the $4_\gamma^+ \rightarrow 4_{0_2^+}^+$ transition.

TABLE 6.18

^{156}GD $K_i = 2_1^+$, γ INTERNAL CONVERSION COEFFICIENTS FROM
SINGLES

E (keV)	$J^\pi \rightarrow J^\pi$	E_i (keV)	E_f (keV)	$T_{1/2}$ (fs)	Multipolarity	Shell	α (This Work)	α (Th)	α (Konijn)
399.56	$9_\gamma^+ \rightarrow 7_\gamma^+$	2249.65	1849.84		E2	K	0.0077 (8) (3)	0.0205 (3)	0.026 (5)
921.83	$5_\gamma^+ \rightarrow 6_{gs}^+$	1506.863	584.715	400	E2	K	0.0041 (9) (5)	0.0028 (1)	0.0030 (7)
1059.31	$6_\gamma^+ \rightarrow 6_{gs}^+$	1643.653	584.715		E2	K	0.0013 (5) (1)	0.0021 (1)	0.0013 (8)

Table ???: A list of conversion coefficients from ^{156}Gd , originating in the $K_i = 2_1^+$, γ band. Multipolarities and mixing ratios were taken from the nuclear date sheets[65]. Unless otherwise stated, the α values are α_K . An angular distribution correction has been applied based on multipolarities for pure transitions, and those with known mixing ratios. The first error is statistical, the second is systematic. Numbers are compared with Konijn et al[43].

6.4.4 $K^\pi = 2^+$, Second Excited 2^+ Band, 1827.841 keV

The conversion coefficients for the gated data originating from the second excited 2^+ band are in Table ???. The second excited 2^+ band has a smaller slope than the ground state band, first excited 0^+ band and the γ band. It is a slightly larger moment of inertia than the second excited 0^+ band. Transitions to the 0_3^+ band do not indicate an E0 component. Transitions to the first excited 0^+ band and the γ band may have an E0 component, but with only upper limits, it is inconclusive. These limits indicate approximately equal strengths to both bands, as seen in Table 5.10, a possible indication it may be a mix of the two bands. The transitions examined do not have known mixing ratios, so αq^2 can be found in 5.9.

TABLE 6.19

 $J^\pi \rightarrow J^\pi$ TRANSITIONS FOR $K_i = 2_2^+$ IN ^{154}GD

E_i (keV)	Band	E_f (keV)	Band	E (keV)	Gate	α (This Work)	Theory[40]		α (Spits)[75]
							α (M1)	α (E2)	
1531.305	$2_{2_2^+}^+$	815.4917	$2_{0_2^+}^+$	715.819	692.4205	$0.0146(40)^{+43}_{-33}$	0.00877 (13)	0.00478 (7)	0.0070 (4)
					444.4924	$0.0234(80)^{+68}_{-52}$			
1531.305	$2_{2_2^+}^+$	996.2568	2_γ^+	535.050	873.1834	$0.0204(70)^{+54}_{-41}$	0.0181 (3)	0.00956 (14)	0.093 (11)
					625.2556	> 0.0183			
1789.17	$4_{2_2^+}^+$	1047.592	$4_{0_2^+}^+$	740.91	676.593	< 0.0124	0.00806 (12)	0.00443 (7)	
					924.55	< 0.0447			
1789.17	$4_{2_2^+}^+$	1263.778	4_γ^+	525.392	892.775	< 0.0168	0.0190 (3)	0.01001 (14)	
					1140.702	< 0.0161			

Table 6.19: A list of conversion coefficients from ^{154}Gd for $J^\pi \rightarrow J^\pi$ transitions for $K_i = 2_2^+$ seen in the gated data. The first error is statistical, the second is systematic. Numbers are compared with theoretical K-shell conversion coefficients for M1 and E2 transitions, as well as results from Spits et al.[75]. All coefficients are K-electrons, except for the transition from 1047 keV. The second value is the LM peak.

6.4.5 $K^\pi = 4^+$, First Excited 4^+ Band, 1510.594 keV

The conversion coefficients for the singles and gated data originating from the first excited 4^+ band are in Tables ?? and 6.21, respectively. Only the first state in the first excited 4^+ band was able to get electron spectroscopy. This band has a similar slope to the ground state band, first excited 0^+ band and the γ band, although it is least like the ground state band dynamic moment of inertia. The lower limits on the conversion coefficients to the first excited 0^+ band and the γ band tell very little, as all forms of multipolarity, including a pure E2, are still accessible. Further, the lack of information on transition to the ground state band obfuscates interpretation. The transitions examined do not have known mixing ratios, so αq^2 can be found in 5.9.

TABLE 6.20

$$^{156}\text{GD } K_i = 2_1^+, \gamma \text{ INTERNAL CONVERSION COEFFICIENTS FROM}$$

SINGLES

E (keV)	$J^\pi \rightarrow J^\pi$	E_i (keV)	E_f (keV)	$T_{1/2}$ (fs)	Multipolarity	Shell	α (This Work)	α (Th)
355.87	$4_{4+}^+ \rightarrow 2_\gamma^+$	1510.594	1154.152	189000	E2	K	0.0158 (6) (5)	0.0281 (4)

Table ??: A list of conversion coefficients from ^{156}Gd , originating in the $K_i = 4_1^+$ band. Multipolarities and mixing ratios were taken from the nuclear date sheets[65]. Unless otherwise stated, the α values are α_K . An angular distribution correction has been applied based on multipolarities for pure transitions, and those with known mixing ratios. The first error is statistical, the second is systematic.

TABLE 6.21

 $J^\pi \rightarrow J^\pi$ TRANSITIONS FOR $K_i = 4_1^+$ IN ^{156}GD

E_i (keV)	J_i^π	E_f (keV)	Band	E (keV)	Gate	α (This Work)	Theory	
							α (M1)	α (E2)
1510.594	$4_{4_1^+}^+$	1297.822	$2_{0_3^+}^+$	212.771	1009.649	> 0.0704	0.204 (3)	0.1282 (18)
1510.594	$4_{4_1^+}^+$	1355.422	2_γ^+	155.168	1067.2325	> 0.0981	0.490 (7)	0.333 (5)

A list of conversion coefficients from ^{156}Gd for $J^\pi \rightarrow J^\pi$ transitions for $K_i = 4_1^+$ seen in the gated data. All listed theoretical values are for the K-shell internal conversion coefficient. Numbers are compared with theoretical values for illustration. All coefficients are K-shell electrons.

6.4.6 Summary and Conclusions

Table 6.22 contains a summary of relevant data for the 0^+ states in ^{156}Gd . For the low-lying levels, there is a good amount of information known. The cross sections from (p, t) are from Fleming et al.[30]. These measurements were done in 1973, and are the most recent (p, t) measurements for ^{156}Gd . With new high-precision spectroscopy and the discovery of so many 0^+ states in the rare-earth region, this nucleus should be revisited via the reaction.

TABLE 6.22
SUMMARY OF 0^+ STATE INFORMATION IN ^{156}Gd

E (keV)	(p, t) ($\mu\text{b}/\text{sr}$)	τ (ps)[4]	Conv. Elec
0.0	624	Stable	Ground State
1049.487(2)	64	$1.81 < \tau < 4.75$	\times
1168.186(7)	12	$3.00 < \tau < 14.7$	\times
1715.211(4)		$0.02 < \tau < 7.08$	\times
1851.278(7)			
1988.5(2)			
2082.0			

Table 6.22: The current state of information for the 0^+ states in ^{156}Gd . The (p, t) cross section is the 30 from Fleming et al.[30]. The lifetimes are from Aprahamian et al.[4]. Conversion electron measurements are from this work, Bäcklin et al.[6], Yamada et al.[83], Ewan et al.[28], and Peek et al.[59].

CHAPTER 7

FUTURE WORK

Throughout the course of this experiment, there have been a variety of areas that were adjusted to try and optimize the data. In this chapter, continued work and optimizations for future experiments are discussed.

7.1 Detector Upgrades

In a given experiment, the detectors are one of the single most important pieces of equipment. Two different styles of HPGe detectors were used, to varying success, and different magnetic configurations were used to optimize efficiency, discussed in Section 2.4.1.1. Further steps are being taken for the future of conversion electron experiments at Notre Dame in both areas to improve the quality of data.

7.1.1 fIREBAll

The La Crosse Internal ConveRsion Electron Ball Array (fIREBAll) will be the next generation of ICEBall[46]. The Major Research Instrumentation (MRI) proposal to the National Science Foundation (NSF) for funding has been approved. The University of Wisconsin-La Crosse submitted the proposal. The ICEBall beamline at the NSL will become the fIREBAll beamline. The focus of the proposal was detector upgrades, both for the Si(Li) detectors, and the HPGe detectors.

With this proposal, there will be dedicated HPGe detectors for the array, with two Bismuth Germanate (BGO) anti-Compton suppression shields. The current Si(Li)

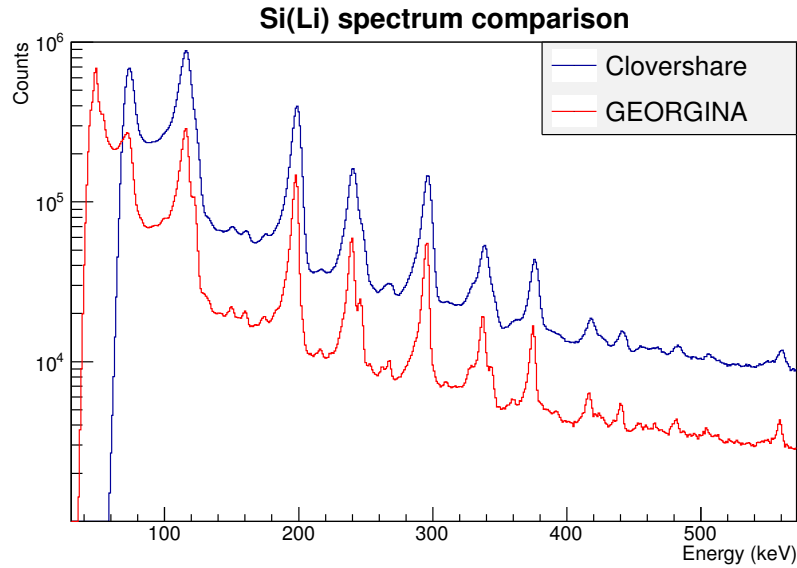


Figure 7.1. A comparison of the singles spectrum of one Si(Li) detector between the GEORGINA and Clovershare experiments. The resolution of the Si(Li) detector has deteriorated between the two experiments (the GEORGINA one was performed first). The LM peaks at ~ 240 keV and ~ 330 keV show this most clearly. The peaks are distinguishable in the GEORGINA data, but not in the Clovershare data.

detectors would be replaced with two Si(Li) detectors, for a total of twelve detectors each. There would still be six detection planes, as the Si(Li) detectors would be stacked in a telescope formation, to allow for the measurement of higher energy conversion electron transitions, including E0 transitions. The current Si(Li) detectors in use are 5 mm thick. All of the new detectors would be 5 mm thick, making for an active stopping depth of 10 mm when stacked. Additionally, the detectors would be 800 mm^2 surface area instead of 750 mm^2 of the current detectors. Over the past 25 years of use, the current Si(Li) detectors have begun to deteriorate. As seen in Figure 7.1, there is a clear decline in the resolution of the detector between the different experiments.

7.1.2 Magnet Designs

To improve the detection efficiency of the conversion electrons, the magnetic configurations can be changed. This was done in the experiments to optimize for higher energies. When the experiments in this work were performed, the permanent magnets used were $36 \times 36 \times 5$ mm SmCo₅ squares. These thin squares are not, necessarily, creating the most optimal magnetic field.

Using GEANT4 and COMSOL, a variety of magnetic shapes were modeled, varying the cross-shape profile, the thickness, and the number of magnets used [1, 26]. Figure 7.2 shows what the magnetic fields look like when modelled in COMSOL. This figure is of the original magnets used in this work. Efficiencies of the new shapes were modeled from 0.1 to 1.0 MeV. The magnets were assumed to have a maximal side length of 37 mm. All of the magnets simulated were assumed to be Neodymium, specifically Nd₂Fe₁₄B. In all of the shape testing, the number of magnets was varied to find idealized scenarios, with the magnets symmetrically spaced. The first variation was the cross-shape profile. Two extremes would be chosen, with intermediate steps between the extremes modelled and tested, as shown in Figure 7.3. Several hybrids of the intermediate steps were also examined, seen in Figure 7.4. The number of magnets was varied from 3 to 6 for each design, and evenly spaced.

After picking the best cross-shapes, the thickness was varied between uniform and a gradient. Initially, this was a linear, uniform gradient. As simulations continued, variations in the form of the gradient were tested, including a step function, and a piecewise linear design, seen in Figure 7.5. As with the cross-shape, the number of magnets was varied for each design, ranging from 3 to 6 magnets.

Three designs were chosen after extensive simulations, to maximize efficiencies at low energies (0.2 to 0.4 MeV), high energies (0.7-1.0 MeV), and overall (0.2 to 1.0 MeV). These designs are shown in Figure 7.6 with simulated efficiencies for six magnet configurations. These designs have been ordered for testing with the detectors.

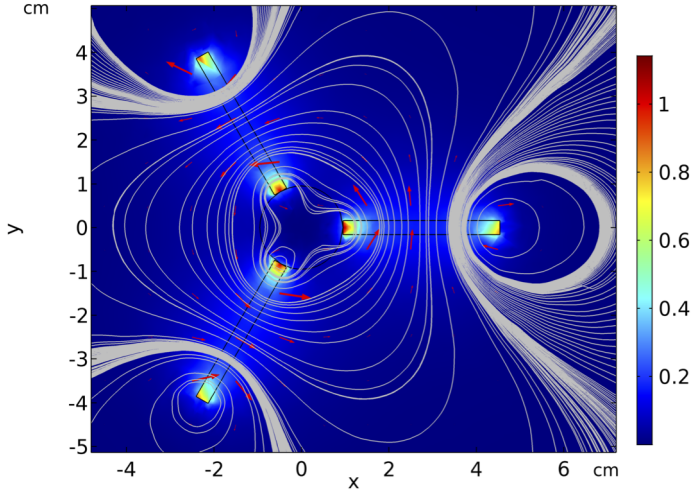


Figure 7.2. Map of the magnetic field lines, created through the use of COMSOL, for the original magnetic design [26].

7.2 Target Upgrades

One of the concerns and limitations of the original experiments was the thickness of the target. Ideally, the target being used would be less than $500 \mu\text{g}/\text{cm}^2$, but the ones used were $1.7 \text{ mg}/\text{cm}^2$ and $1.44 \text{ mg}/\text{cm}^2$. While these targets were self-supporting, they were thick enough that electron straggling occurred, smearing out the spectrum.

To create a thinner target, it was decided to explore a carbon-backing. The Sm was evaporated onto a backing $20 \mu\text{g}/\text{cm}^2$ thick. In the targets made, the Sm was measured to be $170 \mu\text{g}/\text{cm}^2$, ten times thinner than the original targets used.

To compare the old and new targets, an experiment was run with both targets inside of ICEBall. The data compared was taken with the same electronics (discussed in the next section) and setup, to minimize differences that could impact the data.

The new targets could be run with higher beam currents to get similar rates in the detectors, at what appeared to be a proportional rate to the target thickness. At

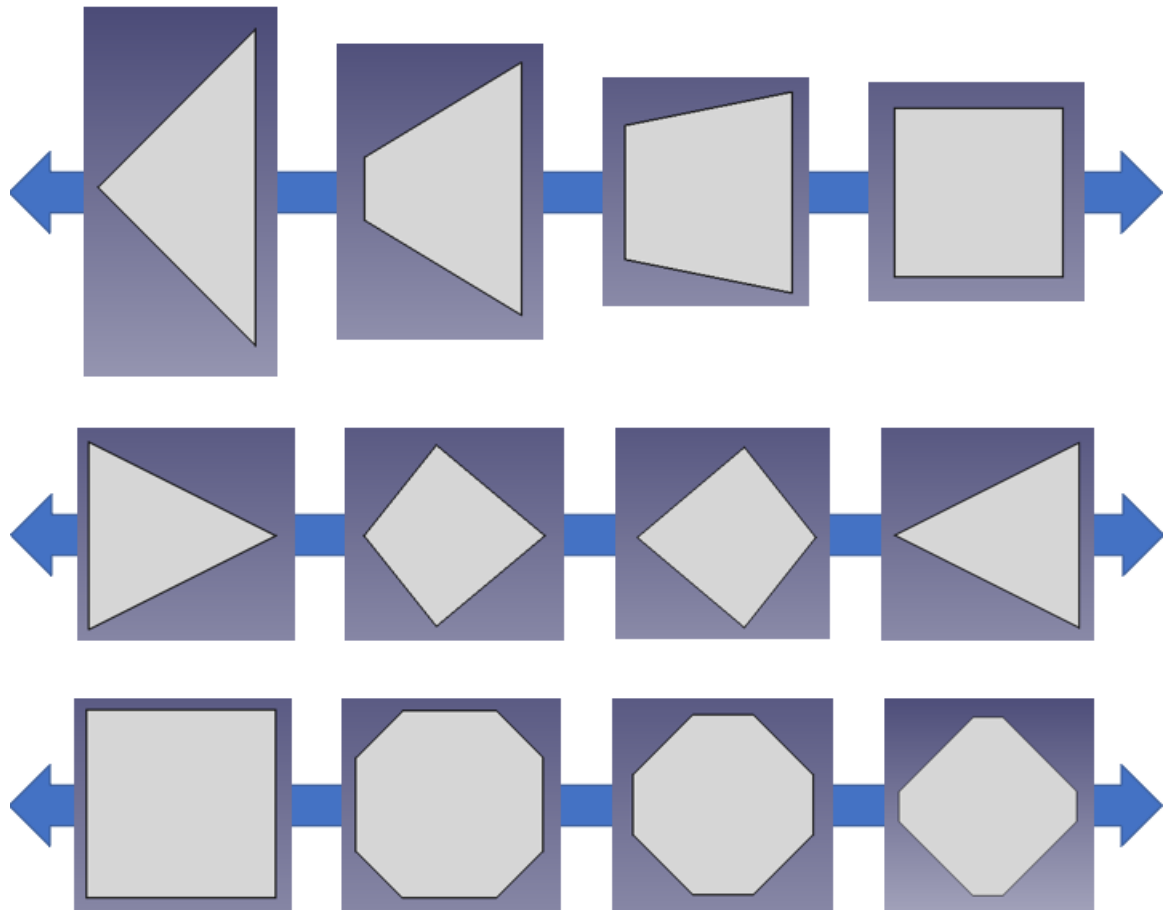


Figure 7.3. Initial tests of the cross shapes. The left-side of the shape would be the side against the blocker. Two extremes were chosen, with intermediate steps being tested between the two. These are the three sets of extremes used: large triangle to square, triangle with the base against the blocker to triangle with the point against the blocker, and square to truncated diamond.

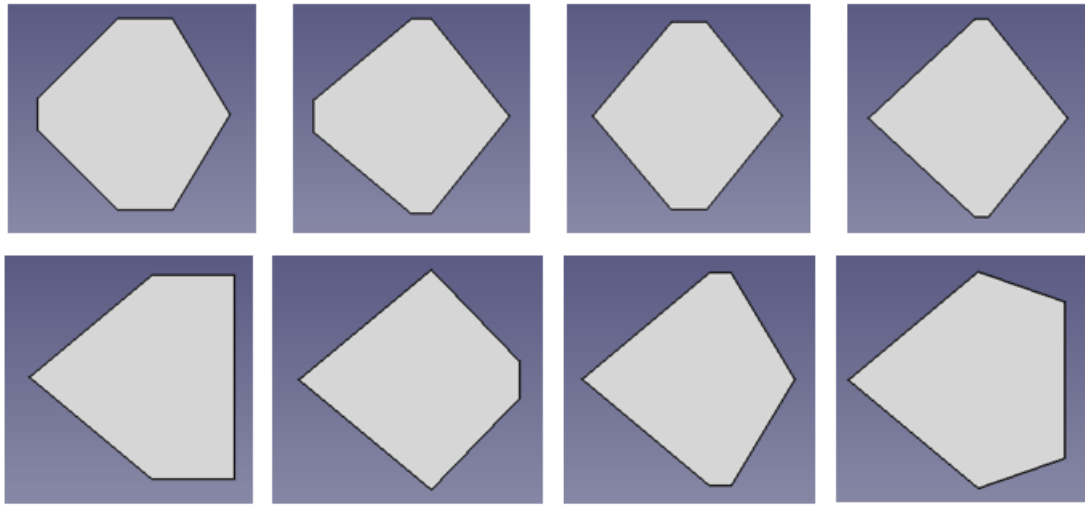


Figure 7.4. Sampling of the different hybrid cross shapes tested while examining magnetic designs. The left side of the shape would be the side against the central blocker.

lower electron energies, the carbon-backed targets had far better resolution, as seen in Figure 7.7. The centroids of the peaks also shifted in comparison between the thick and thin target, which follows logically from the thicker target causing greater energy loss.

Also of note in Figure 7.7, the thin target appears to have a higher background, causing the signal-to-noise ratio to decrease. To understand this increase in background, the beam was cut off and a new run was taken. Figure 7.8 shows the detector trigger rate with respect to time during this background run. The background appears to show an exponential decay with a half-life on the order of two minutes.

It was theorized this decay may be from ^{15}O , which would be created from the $^{12}\text{C}(\alpha, n)$ reaction. Using the cross section, obtained from the EXFOR database, the cross section for this reaction at 20 MeV was obtained [12, 85]. This was used to calculate the rate in the detectors if it was ^{15}O being created. These values matched, providing evidence of the new background element. One way this background can be

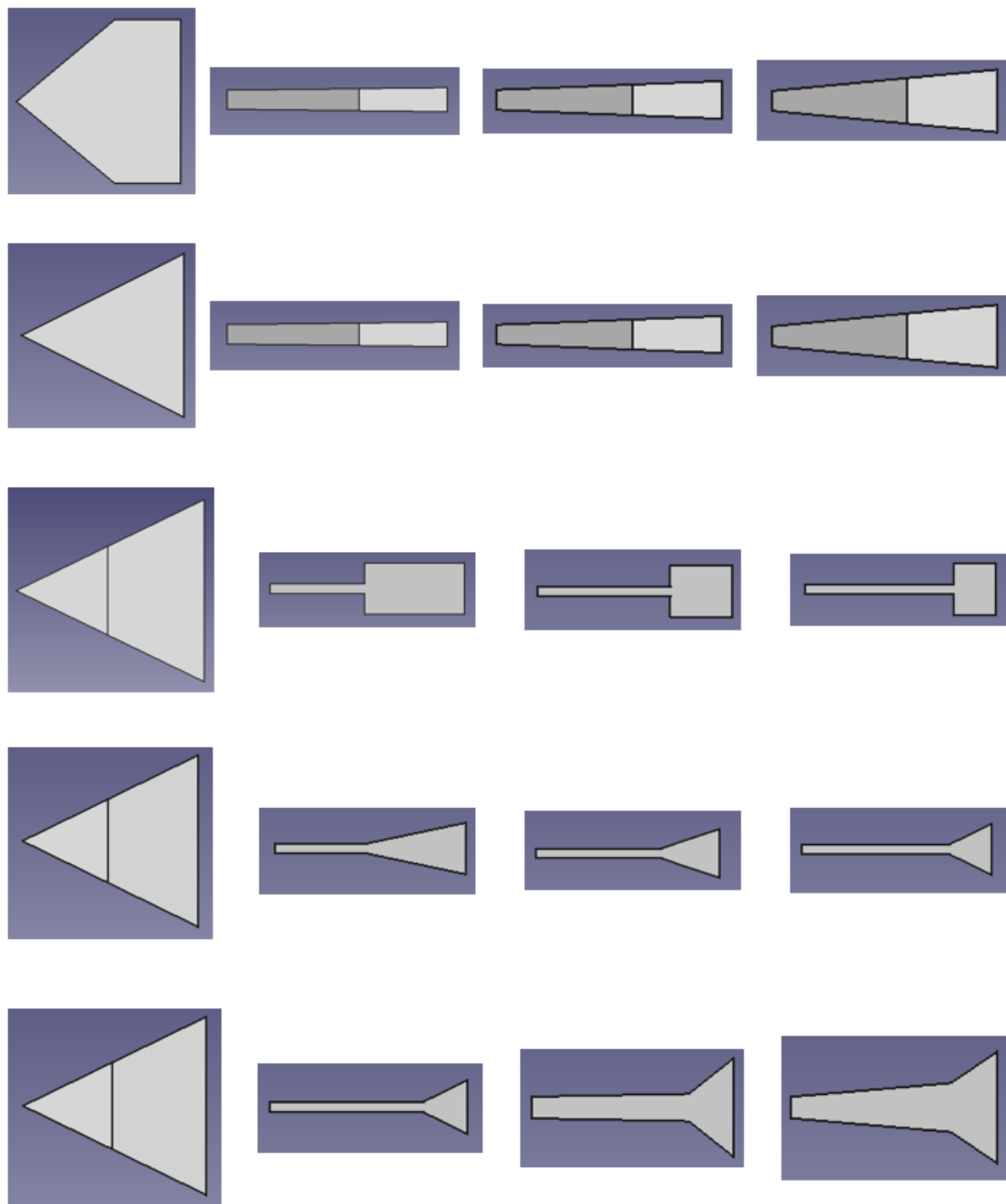


Figure 7.5. Various width profiles tested for the magnets. The left figure shows the cross-shape for the width profiles. The left side goes against the central blocker. Variable gradients were looked at, starting with linear slopes, but evolving into step functions and piecewise linear slopes as the simulations expanded.

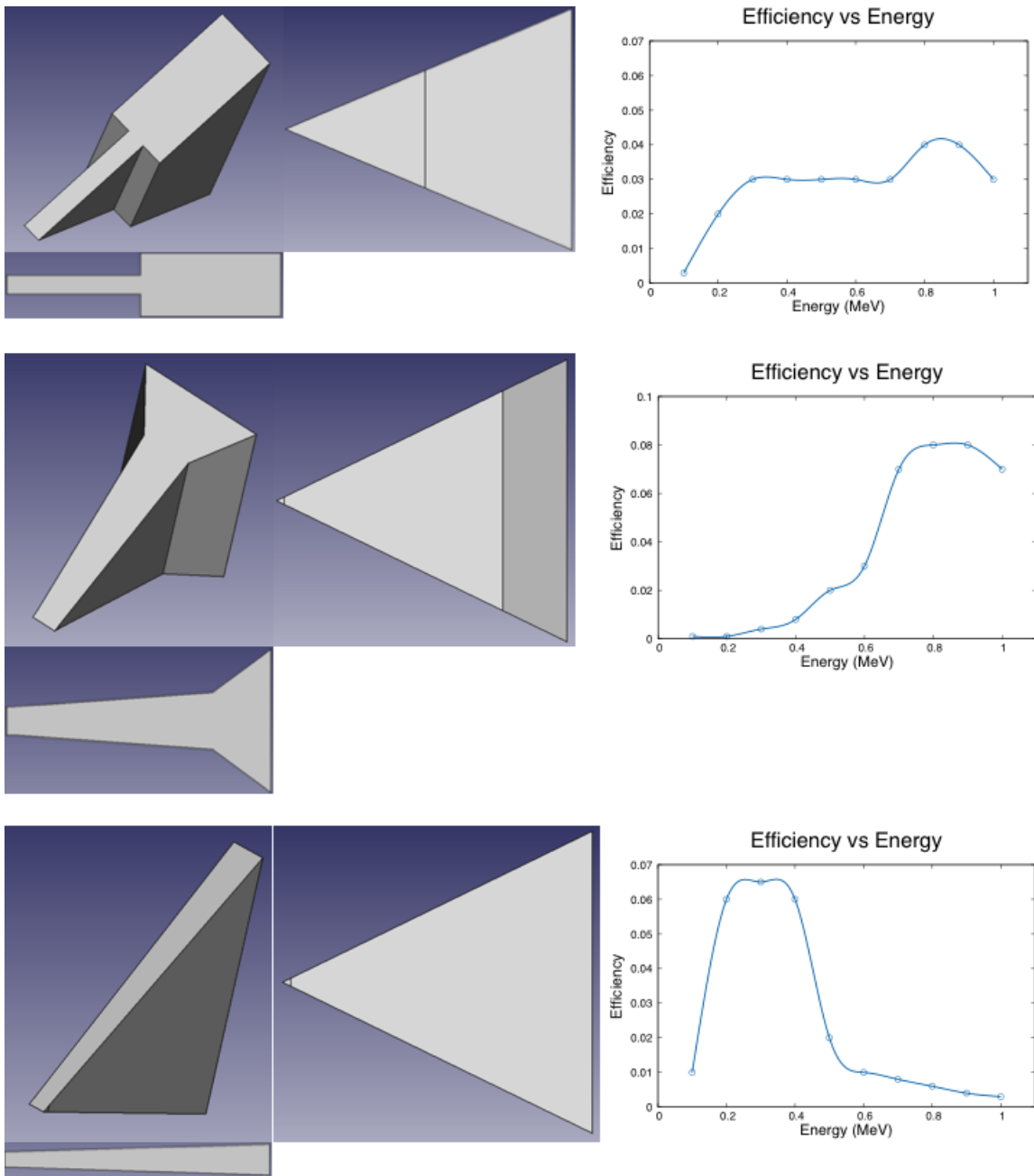


Figure 7.6. The final shapes chosen for testing. The left side goes against the central blocker. The top design has the best overall efficiency, the middle design has the best high energy efficiency, and the bottom design has the best low energy efficiency. These designs have been commissioned for testing.

Target Tests SiLi 3

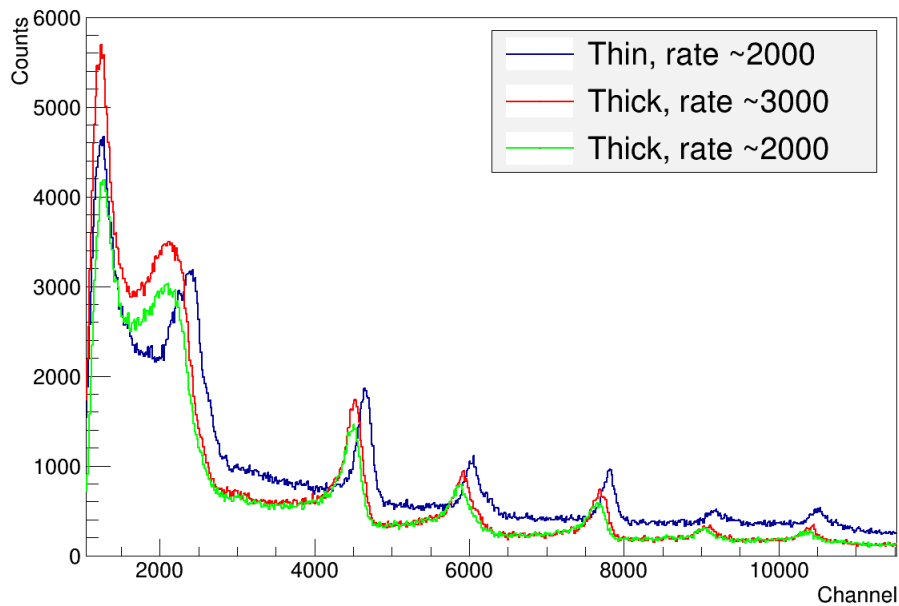


Figure 7.7. Comparison of the thick (self-supporting) and thin (carbon-backed) targets. The spectra were taken during the same experiment. At low energies, the resolution is better in the thin target. Further, the energies of the peaks shift based on which target it is. This spectrum is not energy calibrated.

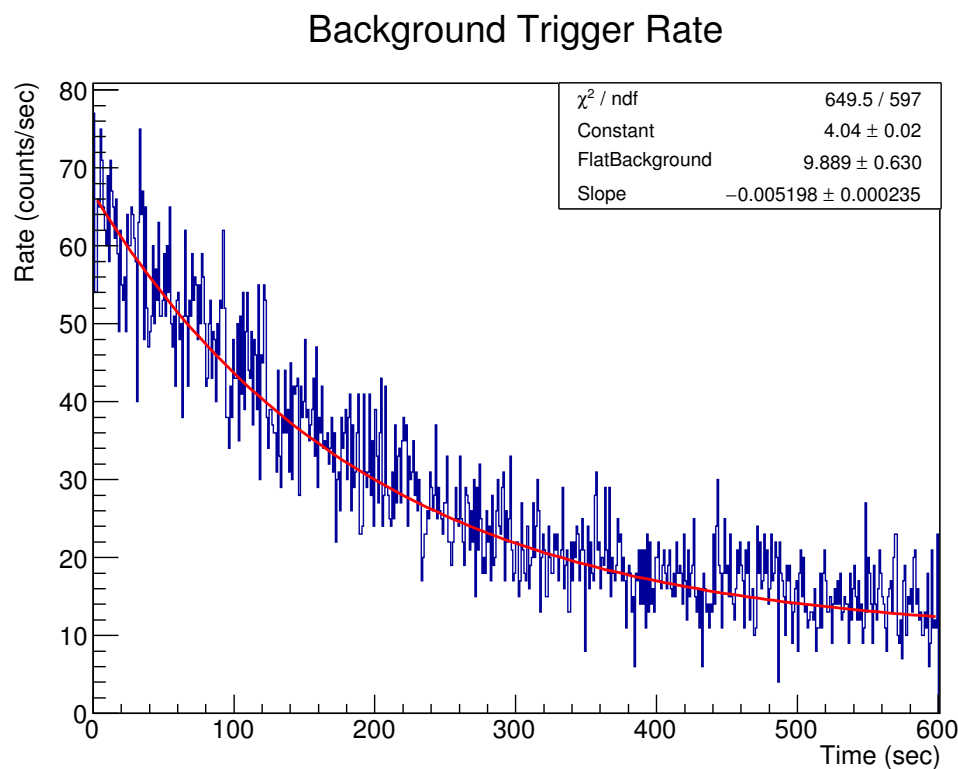


Figure 7.8. Trigger rate of the background with respect to time, after running on one of the carbon-backed targets. There is a clear indication of an exponential decay, shown by the fit. The slope corresponds to a half-life of 133(5) seconds. ^{15}O has a half-life of 122 seconds, within an acceptable error with the low statistics of the run.

decreased is by using thinner carbon-backing, as $12 \mu\text{g}/\text{cm}^2$ is commercially available. This should reduce the ^{15}O contribution the background by 40 percent.

7.3 Electronics

After experiments with two different electronics set ups, a third electronics set up was used, with the plan for it to become the standard electronics for future FIREBALL experiments. These electronics use the Mesytec MDPP-16 VME module and the Mesytec MVME data acquisition software [50, 51]. The MVME software from Mesytec has built-in online analysis tools, allowing for real time analysis of the data and can be used with multiple types of VMEs. The MDPP-16 modules replace the conventional NIM modules, replacing external CFDs and TDCs. The gain, threshold, shaping time, and signal rise and decay times are all set within the module.

The MDPP-16 modules can be run in multiple modes, depending on the firmware: QDC, SCP, and RCP modes. The firmware can be changed using a switch on the module, allowing a given module to hold all three firmware versions. For these tests, the SCP, or standard charge sensitive preamplifier, mode is used. Figure 7.9 shows the schematic configuration of the module in SCP mode, and Table 7.1 shows the breakdown of the event words in the system.

One of the benefits of the MDPP-16 modules is the compatibility with other VME modules. Scaler values can be read in with a separate module, such as the CAEN V830, as was done with the GEORGINA setup, discussed in Section 2.7.2. Many of the scaler values can be read in using the MDPP-16, but the addition of the V830 allows for more versatility in rates to record, including comparing rates between the MDPP-16 and the V830 for deadtime corrections.

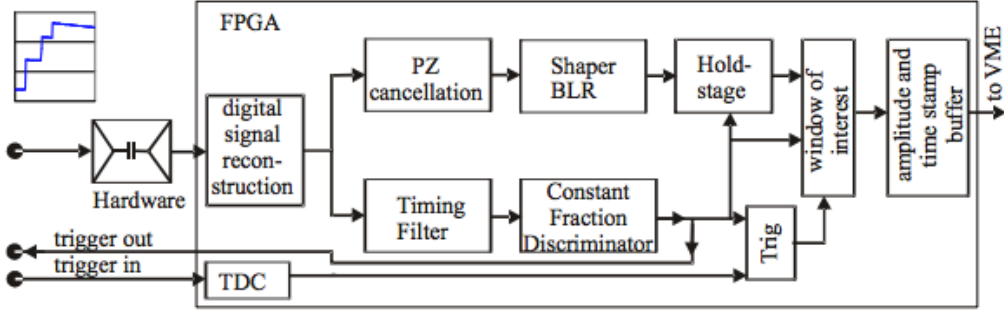


Figure 7.9. A schematic representation of the MDPP-16 software in SCP mode. The amplitude and timing are separated out into individual signals. Signal properties, shaping time, and the threshold can all be adjusted.

Taken from [50].

7.4 Additional Experiments

In Section 1.4, several other spectroscopic fingerprints essential to understanding shape coexistence in this nucleus and other nuclei in the region were mentioned. To that end, for a full and complete understanding of ^{154}Gd , additional spectroscopy experiments would benefit the interpretation of the data. No new gamma spectroscopy has been taken for ^{154}Gd since the discovery of the ten new 0^+ states[54]. The 0^+ states found have no current gamma spectroscopy, and recent experiments of the same (p, t) reaction have not seen these states [2]. Additionally, only one excited 0^+ state in the nucleus has a lifetime, making additional lifetime experiments important.

Unlike ^{154}Gd , ^{156}Gd has not had a large number of states recently found without spectroscopy information, and recent lifetime measurements have been published [4]. ^{156}Gd would benefit from a (p, t) experiment to look for more 0^+ states.

7.5 Outlook

Testing with the new magnetic configurations is currently underway, while the new detectors are being manufactured. The electronics have been tested and used

extensively at the NSL. Future experiments with the new fIREBall system will have greater sensitivity, contributing to the effort to probe the nuclear chart for E0 transitions in the search for understanding collective modes and shape coexistence.

TABLE 7.1

DATA EVENT - MDPP-16 (32 BIT WORD)

Header							
2 header signature	2 subheader	4	8 module id	3 TDC resolution	3 ADC resolution	10 number of following words	
b01	b00	xxxx	module id	bxxx	bxxx	number of 32 bit data words	
Data Word							
2 data-sig	2	4	2	1	5	16	
b00	01	xxxx	(pu,ov)	Trigger Flag	channel number	ADC Value	
2 data-sig	2	6		1	5	16	
b00	01	xxxxxx		Trigger Flag	channel number + 16	TDC time difference	
End of Event							
2				30			
b11				Event counter/time stamp			

Table of the 32-bit word data structures of the Mesytec MDPP-16 in the SCP Firmware. The headers, event word structure, and end of event structure, where needed, are all listed. In the tables, the first row in a given block is the number of bits used by that piece of data, while the second row is a description of the data. Bits go in descending order from left to right. Data has two words, one for the amplitude and one for the corresponding timing. The (pu,ov) bits are for pile up, underflow, and overflow flags.

BIBLIOGRAPHY

1. J. Allison, K. Amako, J. Apostolakis, P. Arce, M. Asai, T. Aso, E. Bagli, A. Bagulya, S. Banerjee, G. Barrand, B. R. Beck, A. G. Bogdanov, D. Brandt, J. M. C. Brown, H. Burkhardt, P. Canal, D. Cano-Ott, S. Chauvie, K. Cho, G. A. P. Cirrone, G. Cooperman, M. A. Cortés-Giraldo, G. Cosmo, G. Cuttone, G. Depaola, L. Desorgher, X. Dong, A. Dotti, V. D. Elvira, G. Folger, Z. Francis, A. Galoyan, L. Garnier, M. Gayer, K. L. Genser, V. M. Grichine, S. Guatelli, P. Guèye, P. Gumplinger, A. S. Howard, I. Hřivnáčová, S. Hwang, S. Incerti, A. Ivanchenko, V. N. Ivanchenko, F. W. Jones, S. Y. Jun, P. Kaitaniemi, N. Karakatsanis, M. Karamitros, M. Kelsey, A. Kimura, T. Koi, H. Kurashige, A. Lechner, S. Lee, F. Longo, M. Maire, D. Mancusi, A. Mantero, E. Mendoza, B. Morgan, K. Murakami, T. Nikitina, L. Pandola, P. Paprocki, J. Perl, I. Petrović, M. G. Pia, W. Pokorski, J. M. Quesada, M. Raine, M. A. Reis, A. Ribon, A. R. Fira, F. Romano, G. Russo, G. Santin, T. Sasaki, D. Sawkey, J. I. Shin, I. I. Strakovský, A. Taborda, S. Tanaka, B. Tomé, T. Toshito, H. N. Tran, P. R. Truscott, L. Urban, V. Uzhinsky, J. M. Verbeke, M. Verderi, B. Wendt, H. Wenzel, D. H. Wright, D. M. Wright, T. Yamashita, J. Yarba, and H. Yoshida. Recent developments in Geant4. *Nuclear Instruments and Methods in Physics Research Section A: Accelerators, Spectrometers, Detectors and Associated Equipment*, 835:186 – 225, 2016. ISSN 0168-9002. doi: <https://doi.org/10.1016/j.nima.2016.06.125>. URL <http://www.sciencedirect.com/science/article/pii/S0168900216306957>.
2. J. M. Allmond, C. W. Beausang, T. J. Ross, P. Humby, M. S. Basunia, L. A. Bernstein, D. L. Bleuel, W. Brooks, N. Brown, J. T. Burke, B. K. Darakchieva, K. R. Dudziak, K. E. Evans, P. Fallon, H. B. Jeppesen, J. D. Leblanc, S. R. Lesher, M. A. McMahan, D. A. Meyer, L. Phair, J. O. Rasmussen, N. D. Scielzo, S. R. Stroberg, and M. Wiedeking. Particle- γ coincidence spectroscopy of the $n = 90$ nucleus ^{154}gd by ($p, t\gamma$). *European Physical Journal. A*, 53(3), 2017. ISSN 1434-6001.
3. AMETEK ORTEC. 579 Fast-Filter Amplifier. <https://www.ortec-online.com/products/electronics/amplifiers/579>.
4. A. Aprahamian, R. C. de Haan, S. R. Lesher, C. Casarella, A. Stratman, H. G. Börner, H. Lehmann, M. Jentschel, and A. M. Bruce. Lifetime measurements in ^{156}Gd . *Phys. Rev. C*, 98:034303, September 2018. doi: 10.1103/PhysRevC.98.034303. URL <https://link.aps.org/doi/10.1103/PhysRevC.98.034303>.

5. Autodesk. Inventor professional-grade 3d cad software for product design and engineering. <https://www.autodesk.com/products/inventor/overview>.
6. A. Bäcklin, G. Hedin, B. Fogelberg, M. Saraceno, R. Greenwood, C. Reich, H. Koch, H. Baader, H. Breitig, O. Schult, K. Schreckenbach, T. V. Egidy, and W. Mampe. Levels in ^{156}gd studied in the (n, γ) reaction. *Nuclear Physics A*, 380(2):189 – 260, 1982. ISSN 0375-9474. doi: [https://doi.org/10.1016/0375-9474\(82\)90104-X](https://doi.org/10.1016/0375-9474(82)90104-X). URL <http://www.sciencedirect.com/science/article/pii/037594748290104X>.
7. C. Baktash, B. Haas, and W. Nazarewicz. Identical bands in deformed and superdeformed nuclei. *Annual Review of Nuclear and Particle Science*, 45(1): 485–541, 1995. doi: 10.1146/annurev.ns.45.120195.002413. URL <https://doi.org/10.1146/annurev.ns.45.120195.002413>.
8. A. Battaglia. *Conversion Coefficients Measurements of ^{176}Lu Using ICEBall*. PhD thesis, University of Notre Dame, May 2015.
9. C. Beausang, C. Barton, M. Caprio, R. Casten, J. Cooper, R. Krücken, B. Liu, J. Novak, Z. Wang, M. Wilhelm, A. Wilson, N. Zamfir, and A. Zilges. The YRAST Ball array. *Nuclear Instruments and Methods in Physics Research Section A: Accelerators, Spectrometers, Detectors and Associated Equipment*, 452(3):431 – 439, 2000. ISSN 0168-9002. doi: [https://doi.org/10.1016/S0168-9002\(00\)00449-6](https://doi.org/10.1016/S0168-9002(00)00449-6). URL <http://www.sciencedirect.com/science/article/pii/S0168900200004496>.
10. P. R. Bevington and D. K. Robinson. *Data Reduction and Error Analysis for the Physical Sciences*. McGraw-Hill, 3rd edition, 2003. ISBN 0-07-247227-8.
11. L. C. Biedenharn and M. E. Rose. Theory of angular correlation of nuclear radiations. *Reviews of Modern Physics*, 25(3):729–777, July 1953.
12. J. Black, W. Caelli, D. Livesey, and R. Watson. Search for the lowest $T = 2$ state of ^{8}Be : Experimental. *Physics Letters B*, 30(2):100 – 102, 1969. ISSN 0370-2693. doi: [https://doi.org/10.1016/0370-2693\(69\)90408-0](https://doi.org/10.1016/0370-2693(69)90408-0). URL <http://www.sciencedirect.com/science/article/pii/0370269369904080>.
13. J. M. Blatt and V. F. Weisskopf. *Theoretical Nuclear Physics*. Springer-Verlag New York Inc., 1979.
14. A. Bohr and B. Mottelson. Moments of Inertia of Rotating Nuclei. *Kgl. Danske Videnskab. Selskab, Mat.-fys. Medd.*, 30(1), 1955.
15. D. M. Brink and G. R. Satchler. *Angular Momentum*. Oxford Science Publications, 3rd edition, 2015.
16. R. Brun and F. Rademakers. Root - an object oriented data analysis framework. *Nuclear Instruments and Methods in Physics Research Section A: Accelerators*,

Spectrometers, Detectors and Associated Equipment, 389(1):81 – 86, 1997. ISSN 0168-9002. doi: [https://doi.org/10.1016/S0168-9002\(97\)00048-X](https://doi.org/10.1016/S0168-9002(97)00048-X). URL <http://www.sciencedirect.com/science/article/pii/S016890029700048X>. New Computing Techniques in Physics Research V.

17. CAEN. CAEN V775. <https://www.caen.it/products/v775/>, .
18. CAEN. CAEN V830. <https://www.caen.it/products/v830/>, .
19. Casten and Zamfir. Evidence for a possible e(5) symmetry in ^{134}ba . *Physical review letters*, 85(17):3584, 2000. ISSN 00319007.
20. R. F. Casten. *Nuclear Structure from a Simple Perspective*. Oxford University Press, Inc., 1st edition, 1990.
21. E. Caurier, J. Menéndez, F. Nowacki, and A. Poves. Coexistence of spherical states with deformed and superdeformed bands in doubly magic ^{40}Ca : A shell-model challenge. *Phys. Rev. C*, 75:054317, May 2007. doi: 10.1103/PhysRevC.75.054317. URL <https://link.aps.org/doi/10.1103/PhysRevC.75.054317>.
22. G. Choppin, J.-O. Liljenzin, J. Rydberg, and C. Ekberg. *Radiochemistry and Nuclear Chemistry*. Academic Press, Oxford, 4th edition, 2013.
23. E. L. Church and J. Weneser. Electric-monopole transitions in atomic nuclei. *Physical Review*, 103(4):1035–1044, August 1956.
24. E. L. Church, M. E. Rose, and J. Weneser. Electric-monopole directional-correlation experiments. *Physical Review*, 109(4):1299–1306, February 1958.
25. S. Clifford, X. Guo-ji, C. Ingelbrecht, and M. J. Pomeroy. Processes for the production of ultra-pure metals from oxide and their cold rolling to ultra-thin foils for use as targets and as reference materials. *Nuclear Instruments and Methods in Physics Research A*, (480):29–35, 2002.
26. COMSOL Inc. COMSOL Multiphysics Software. <https://www.comsol.com/comsol-multiphysics>.
27. J. P. Delaroche, M. Girod, J. Libert, H. Goutte, S. Hilaire, S. Péru, N. Pillet, and G. F. Bertsch. Structure of even-even nuclei using a mapped collective hamiltonian and the d1s gogny interaction. *Physical Review C*, 81:014303, Jan 2010.
28. G. Ewan, R. Graham, and J. Geiger. Levels in gd156 fed in the β -decay of eu156. *Nuclear Physics*, 29:153 – 176, 1962. ISSN 0029-5582. doi: [https://doi.org/10.1016/0029-5582\(62\)90173-6](https://doi.org/10.1016/0029-5582(62)90173-6). URL <http://www.sciencedirect.com/science/article/pii/0029558262901736>.
29. U. Fano. Ionization yield of radiation ii. the fluctuations of the number of ions. *Physical Review*, 72(1):26–29, July 1947.

30. D. G. Fleming, C. Günther, G. Hagemann, B. Herskind, and P. O. Tjøm. Study of the (p, t) reaction on the even gadolinium nuclei. *Phys. Rev. C*, 8:806–818, Aug 1973. doi: 10.1103/PhysRevC.8.806. URL <https://link.aps.org/doi/10.1103/PhysRevC.8.806>.
31. Y. Gono and T. T. Sugihara. Electric monopole admixtures in interband transitions of ^{154}Gd . *Physical Review C*, 10(6):2460–2466, 1974.
32. K. Heyde and J. L. Wood. Shape coexistence in atomic nuclei. *Reviews of Modern Physics*, 83:1467–1521, 2011.
33. Iachello. Dynamic symmetries at the critical point. *Physical review letters*, 85(17):3580, 2000. ISSN 00319007.
34. F. Iachello. Analytic description of critical point nuclei in a spherical-axially deformed shape phase transition. *Physical Review Letters*, 87(5):52502–1–52502–4, 2001. ISSN 00319007.
35. G. Ilie and R. F. Casten. $E0$ transitions in deformed nuclei. *Physical Review C*, 84:064320, 2011.
36. Institute for Nuclear Astrophysics. GEORGINA A compact Ge-detector Array. <https://isnap.nd.edu/research/facility/experimental/georgina/>, 2018.
37. J. Van Klinken and K. Wissak. Conversion Electrons Separated from High Background. *Nuclear Instruments and Methods*, 98:1–8, 1972.
38. J. Van Klinken, S. J. Feenstra, K. Wissak and H. Faust. Mini-Orange Spectrometers for In- and Off-Beam Observation of Conversion Electrons. *Nuclear Instruments and Methods*, 130:427–441, 1975.
39. J. D. Jackson. *Classical Electrodynamics*. John Wiley & Sons Inc., 3rd edition, 1999.
40. T. Kibédi, T. W. Burrows, M. B. Trzhaskovskaya, P. M. Davidson, and C. W. N. Jr. Evaluation of theoretical conversion coefficients using bricc. *Nuclear Instrumentation and Methods A*, 589:202–229, 2008.
41. J. Klora, H. G. Börner, T. von Egidy, R. Georgii, J. Jolie, S. Judge, V. A. Khitrov, B. Krusche, V. A. Libman, H. Lindner, L. L. Litvinsky, U. Mayerhofer, A. V. Murzin, S. J. Robinson, A. M. Sukhovojo, and H. Trieb. Nuclear structure of ^{156}Gd studied with (n, γ) , (n, e^-) , (d, p) , (d, t) reactions and lifetime measurements. *Nuclear Physics A*, 561(1):1 – 73, 1993. ISSN 0375-9474. doi: [https://doi.org/10.1016/0375-9474\(93\)90165-T](https://doi.org/10.1016/0375-9474(93)90165-T). URL <http://www.sciencedirect.com/science/article/pii/037594749390165T>.
42. G. F. Knoll. *Radiation Detection and Measurement*. John Wiley & Sons Inc., 3rd edition, 2000.

43. J. Konijn, F. W. N. D. Boer, A. V. Poelgeest, W. H. A. Hesselink, M. J. A. D. Voigt, and H. Verheul. The level structure of ^{156}Gd studied by means of the $(\alpha, 2n\gamma)$ reaction. *Nuclear Physics A*, 352:191–220, 1981.
44. A. J. Koning, S. Hilaire, and M. C. Duijvestijn. Talys-1.0. In O. Bersillon, F. Gunsing, E. Bauge, R. Jacqmin, and S. Leray, editors, *Proceedings of the International Conference on Nuclear Data for Science and Technology*, pages 211–214, Nice, France, April 22-27 2007. EDP Sciences.
45. K. S. Krane and R. M. Steffen. Theory of Angular Correlation of Nuclear Radiations. *Reviews of Modern Physics*, 25(3):729–777, July 1953.
46. S. Lesher, A. Aprahamian, and W. Tan. MRI: Acquisition of Si(Li) Detectors and Two BGO Compton Suppression Shields for the Development of the La Crosse FIREBALL. NSF Major Research Instrumentation Award Number 1919364, 2019.
47. S. R. Lesher, A. Aprahamian, L. Trache, A. Oros-Peusquens, S. Deyliz, A. Gollwitzer, R. Hertenberger, B. D. Valnion, and G. Graw. New 0^+ states in ^{158}Gd . *Physical Review C*, 66:051305, Nov 2002.
48. Mesytec. Mesytec MADC-32. <https://www.mesytec.com/products/nuclear-physics/MADC-32.html>, .
49. Mesytec. Mesytec MPD-4. <https://www.mesytec.com/products/nuclear-physics/MPD-4.html>, .
50. Mesytec. Mesytec MDPP-16. <https://www.mesytec.com/products/nuclear-physics/MDPP-16.html>, .
51. Mesytec. mvme - Mesytec VME data acquisition. <https://www.mesytec.com/downloads/mvme.html>, .
52. M. P. Metlay. *Development Of A Multiple-Element Conversion-Electron Spectrometer Array And Investigation Of Transition Multipolarities In ^{130}Ce* . PhD thesis, University of Pittsburgh, May 1992.
53. M. P. Metlay, J. X. Saladin, I. Y. Lee, and O. Dietzsch. The ICEBall: a multiple element array for in-beam internal conversion electron spectroscopy. *Nuclear Instruments and Methods in Physics Research Section A: Accelerators, Spectrometers, Detectors and Associated Equipment*, 336(1):162–170, November 1993.
54. D. A. Meyer, V. Wood, R. F. Casten, C. R. Fitzpatrick, G. Graw, D. Bucurescu, J. Jolie, P. von Brentano, R. Hertenberger, H.-F. Wirth, N. Braun, T. Faestermann, S. Heinze, J. L. Jerke, R. Krücken, M. Mahgoub, O. Möller, D. Mücher, and C. Scholl. Enhanced density of low-lying 0^+ states: A corroboration of shape phase transitional behavior. *Physics Letters B*, 638(1):44 – 49, 2006.
55. National Electrostatics Corporation. Pelletron Charging System. <http://www.pelletron.com/products/pelletron-charging-chains/>.

56. National Superconducting Cyclotron Laboratory. NSCL Data Acquisition Documentation. <http://docs.nscl.msu.edu/daq/>.
57. N. Nica. Nuclear data sheets for $a=158$. *Nuclear Data Sheets*, 141:1 – 326, 2017. ISSN 0090-3752. doi: <https://doi.org/10.1016/j.nds.2017.03.001>. URL <http://www.sciencedirect.com/science/article/pii/S009037521730025X>.
58. R. K. Osborn and M. E. Rose. $1-3\gamma$ correlation with mixtures and polarization. Technical Report 1560, Oak Ridge National Laboratory, June 1953.
59. N. F. Peek, J. A. Jungerman, and C. G. Patten. Nuclear energy levels of gd^{156} as populated by β emission from eu^{156} . *Phys. Rev.*, 136:B330–B340, Oct 1964. doi: 10.1103/PhysRev.136.B330. URL <https://link.aps.org/doi/10.1103/PhysRev.136.B330>.
60. C. Prokop, S. Liddick, B. Abromeit, A. Chemey, N. Larson, S. Suchyta, and J. Tompkins. Digital data acquisition system implementation at the National Superconducting Cyclotron Laboratory. *Nuclear Instruments and Methods in Physics Research Section A: Accelerators, Spectrometers, Detectors and Associated Equipment*, 741:163 – 168, 2014. ISSN 0168-9002. doi: <https://doi.org/10.1016/j.nima.2013.12.044>. URL <http://www.sciencedirect.com/science/article/pii/S0168900213017488>.
61. D. C. Radford. Notes on the use of the program gf3. <http://radware.phy.ornl.gov/gf3/>, May 2000.
62. S. RAMAN, C. NESTOR, and P. TIKKANEN. Transition probability from the ground to the first-excited $2+$ state of even-even nuclides. *Atomic Data and Nuclear Data Tables*, 78(1):1 – 128, 2001. ISSN 0092-640X. doi: <https://doi.org/10.1006/adnd.2001.0858>. URL <http://www.sciencedirect.com/science/article/pii/S0092640X01908587>.
63. C. Reich. Nuclear data sheets for $a=160$. *Nuclear Data Sheets*, 105(3):557 – 774, 2005. ISSN 0090-3752. doi: <https://doi.org/10.1016/j.nds.2005.08.001>. URL <http://www.sciencedirect.com/science/article/pii/S0090375205000530>.
64. C. Reich. Nuclear data sheets for $a = 154$. *Nuclear Data Sheets*, 110(10):2257 – 2532, 2009. ISSN 0090-3752. doi: <https://doi.org/10.1016/j.nds.2009.09.001>. URL <http://www.sciencedirect.com/science/article/pii/S0090375209000805>.
65. C. Reich. Nuclear data sheets for $a = 156$. *Nuclear Data Sheets*, 113(11):2537 – 2840, 2012. ISSN 0090-3752. doi: <https://doi.org/10.1016/j.nds.2012.10.003>. URL <http://www.sciencedirect.com/science/article/pii/S0090375212000798>.
66. C. S. Reingold, O. Olivas-Gomez, A. Simon, J. Arroyo, M. Chamberlain, J. Wurzer, A. Spyrou, F. Naqvi, A. C. Dombos, A. Palmisano, T. Anderson,

- A. M. Clark, B. Frentz, M. R. Hall, S. L. Henderson, S. Moylan, D. Robertson, M. Skulski, E. Stech, S. Y. Strauss, W. P. Tan, and B. Vande Kolk. High efficiency total absorption spectrometer hector for capture reaction measurements. *The European Physical Journal A*, 55(77), 2019. doi: 10.1140/epja/i2019-12748-8.
67. M. E. Rose. Supplementary remarks on angular correlation. Technical Report 1555, Oak Ridge National Laboratory, June 1953.
 68. M. E. Rose, G. H. Goertzel, B. I. Spinrad, J. Harr, and P. Strong. The internal conversion coefficients. i. the k -shell. *Physical Review*, 83(1):79–87, July 1951.
 69. M. E. Rose, L. C. Biedenharn, and G. B. Arfken. Internal conversion angular correlations. *Physical Review*, 85(1):5–16, January 1952.
 70. D. J. Rowe. *Nuclear Collective Motion Models and Theory*. World Scientific, 2010.
 71. D. J. Rowe and J. L. Wood. *Fundamentals of Nuclear Models*. World Scientific, 2010.
 72. R. R. Roy and B. P. Nigam. *Nuclear Physics Theory and Experiment*. John Wiley & Sons Inc., 1st edition, 1967.
 73. E. Segré. *Nuclei and Particles*. Basic Books, 2nd edition, 1977.
 74. K. Smith. evt2root Package. <https://github.com/ksmith0/evt2root/>, March 2014.
 75. A. M. J. Spits, P. H. M. V. Assche, H. G. Börner, W. F. D. K. Schreckenbach, G. G. Colvin, R. C. Greenwood, C. W. Reich, P. O. Lipas, J. Suhonen, P. Sinkko, and A. Bäcklin. Spectroscopy of the ^{153}Gd and ^{154}Gd Isotopes, 1996. in BLG-703, edited by A. M. J. Spits and A. Bäcklin.
 76. D. Tonev, A. Dewald, T. Klug, P. Petkov, J. Jolie, A. Fitzler, O. Möller, S. Heinze, P. von Brentano, and R. F. Casten. Transition probabilities in ^{154}Gd : Evidence for X(5) critical point symmetry. *Phys. Rev. C*, 69:034334, Mar 2004. doi: 10.1103/PhysRevC.69.034334. URL <https://link.aps.org/doi/10.1103/PhysRevC.69.034334>.
 77. W. H. Trzaska. Recommended data on selected gamma-ray and conversion-electron calibration sources. *Nuclear Instruments and Methods in Physics Research A*, 297(2):223–229, 1990.
 78. V. Werner, E. Williams, R. Casperson, R. Casten, C. Scholl, and P. Von Brentano. Deformation crossing near the first-order shape-phase transition in gd152-156. *Physical Review C - Nuclear Physics*, 78(5), 2008. ISSN 05562813.

79. H. J. Wollersheim and T. W. Elze. E2 and e3 transition strengths in some rare-earth nuclei. *Zeitschrift für Physik*, A280:277, 1977.
80. J. L. Wood, E. F. Zganjar, C. D. Coster, and K. Heyde. Electric monopole transitions from low energy excitations in nuclei. *Nuclear Physics A*, (651):323–368, 1999.
81. X. Wu. *Investigation of Multiphonon Vibrational States in Deformed Nuclei*. PhD thesis, University of Notre Dame, December 1993.
82. Xia. Pixie-16, 16-channel pxi digital pulse processor. https://www.xia.com/DGF_Pixie-16.html, 2016.
83. H. Yamada, T. Katoh, M. Fujioka, M. Sekikawa, S. H. Ahn, J. H. Hamilton, N. R. Johnson, and J. J. Pinajian. Electric monopole transitions from excited 0^+ states in ^{156}gd . *Journal of the Physical Society of Japan*, 41(6):1843–1850, 1976. doi: 10.1143/JPSJ.41.1843. URL <https://doi.org/10.1143/JPSJ.41.1843>.
84. A. Zangwill. *Modern Electrodynamics*. Cambridge University Press, 1st edition, 2013.
85. V. Zerkin and B. Pritychenko. The experimental nuclear reaction data (EXFOR): Extended computer database and Web retrieval system. *Nuclear Instruments and Methods in Physics Research Section A: Accelerators, Spectrometers, Detectors and Associated Equipment*, 888:31 – 43, 2018. ISSN 0168-9002. doi: <https://doi.org/10.1016/j.nima.2018.01.045>. URL <http://www.sciencedirect.com/science/article/pii/S0168900218300627>.
86. J. F. Ziegler, M. Ziegler, and J. Biersack. SRIM - The stopping and range of ions in matter (2010). *Nuclear Instruments and Methods in Physics Research Section B: Beam Interactions with Materials and Atoms*, 268(11):1818 – 1823, 2010. ISSN 0168-583X. doi: <https://doi.org/10.1016/j.nimb.2010.02.091>. URL <http://www.sciencedirect.com/science/article/pii/S0168583X10001862>. 19th International Conference on Ion Beam Analysis.

*This document was prepared & typeset with pdfL^AT_EX, and formatted with
NDDiss2_ε classfile (v3.2017.2[2017/05/09])*